PROBING THE PHOTOCHEMICAL REACTIVITY OF OCEANIC DISSOLVED ORGANIC CARBON

by

LEANNE POWERS

(Under the Direction of William L. Miller)

ABSTRACT

After 20 years of research in aquatic photochemistry, there remains a need to identify and constrain many photochemical reactions involving colored dissolved organic matter (CDOM). This thesis uses laboratory and field studies in diverse marine systems to examine the photochemical efficiency and reaction rates for carbon monoxide (CO), carbon dioxide (CO_2), superoxide (O_2^-) and hydrogen peroxide (H_2O_2), all important photoproducts, and improves quantitative understanding of photochemistry's significance in biogeochemical cycles. Input of these results to ocean color-based models allowed estimation of photochemical rates on regional and global scales. Direct photo-oxidation of dissolved organic carbon (DOC) to CO_2 and CO is a significant, albeit poorly constrained, DOC removal mechanism. Working in the Northern Gulf of Mexico, we amassed the largest cohesive CO apparent quantum yield (AQY) data set for any marine region (n=99; 18 paired with CO_2), defining distinct inshore and offshore AQY spectra for improved regional photochemical rate models. Analytical limitations for determining CO_2 AQY spectra forced the use of ill-defined coastal CO_2:CO ratios (~6 − 66) for blue water CO_2 calculations, highlighting the need for new direct methods or better proxies to

quantify CO_2 photochemistry in marine waters. Significant photochemical removal of biologically refractory DOC (RDOC), well-mixed in the ocean but isolated at depth, is not compatible with its ^{14}C age. Reevaluation of RDOC photochemical reactivity using paired O_2^- and H_2O_2 photoproduction studies for abyssal Gulf of Alaska samples showed declining O_2^- steady-state concentrations during long-term exposure, with little or no H_2O_2 accumulation past ~6 − 12 hours. This is consistent with a loss of O_2^- source, a shift to oxidative pathways for O_2^- decay, and a lack of long-term photochemical reactivity for RDOC. Because H_2O_2 formation is a thermal reaction involving O_2^-, blending remotely sensed sea surface temperature and color allowed correction of H_2O_2 AQY spectra and production of the first global H_2O_2 and O_2^- photoproduction rate maps from remotely sensed data. Further analysis of paired H_2O_2 and CO_2 photoproduction experiments indicated that H_2O_2 is a far better proxy for CO_2 photoproduction than CO (CO_2:H_2O_2 ratio = 6.89 ± 1.64), and will lead to constrained estimates for global CO_2 photochemical fluxes.

INDEX WORDS: Photochemistry, dissolved organic carbon, apparent quantum yield, colored dissolved organic matter, carbon dioxide, carbon monoxide, hydrogen peroxide, superoxide, ocean color

PROBING THE PHOTOCHEMICAL REACTIVITY OF OCEANIC DISSOLVED ORGANIC CARBON

by

LEANNE POWERS

BA, Colby College, 2008

A Dissertation Submitted to the Graduate Faculty of The University of Georgia in Partial Fulfillment of the Requirements for the Degree

DOCTOR OF PHILOSOPHY

ATHENS, GEORGIA

2014

PROBING THE PHOTOCHEMICAL REACTIVITY OF OCEANIC DISSOLVED ORGANIC CARBON

by

LEANNE POWERS

Major Professor: William L. Miller
Committee: James T. Hollibaugh
Patricia M. Medeiros
Aron Stubbins
Richard G. Zepp

Electronic Version Approved:

Julie Coffield
Interim Dean of the Graduate School
The University of Georgia
December 2014

DEDICATION

This work is dedicated to my parents for their love of the sea.

ACKNOWLEDGEMENTS

There is no way I could adequately thank everyone who has helped me with my dissertation. I would like to first thank my committee members, Tim Hollibaugh, Patricia Medeiros, Aron Stubbins, and Richard Zepp, for their useful critiques, challenging insights, and overall greatly improving my work. I'd also like to thank my advisor, Bill Miller, for his support throughout this entire process, especially in helping me become a more confident scientist. And even when all of our sample bottles rolled off the dock and floated off to sea, he always had a great attitude. And of course, I'm am so grateful to the other members of the Miller lab, especially Heather Reader, Fang Cao and Lydia (Meg) Babcock-Adams, for everything you have helped me with, and for how much fun we've had while working in the lab (not to mention the 90s dance music and Steve Spangler videos…). None of this would have been possible if it weren't for all of the additional support I've received here at UGA and in the field, so thank you all!

I'd quickly like to acknowledge my family and friends, both here and away, for your continual love and support. I would have never made it without you!

TABLE OF CONTENTS

Page

LIST OF TABLES

Page

LIST OF FIGURES

Page

CHAPTER 1

INTRODUCTION AND LITERATURE REVIEW

1.1 CDOM and Marine Photochemistry

Zafiriou (1977) was one of the first to note that the marine chemical literature did not contain any photochemical systems for which we know the structures of the reactants and products, the production rates, and the basics of the mechanism. Some early reviews in the field outlined basic principles of photochemistry in natural waters as well as the various important photoreactions possible from dissolved humic materials (Hoigné et al., 1989; Zepp, 1988; Zika, 1981). The most fundamental principle remains that in order for a photochemical reaction to take place, sunlight must be absorbed by the system. Light absorption is described by an inherent optical property (IOP), the absorption coefficient ($a(\lambda)$; m^{-1}) spectrum, meaning that it depends on the constituents in the water column but it is independent of the incident light field. Like other IOPs, the total $a(\lambda)$ spectrum can be described by a sum of the contributions of its individual components with the following equation (Mobley, 1994)

$$a(\lambda) = a_w(\lambda) + a_g(\lambda) + a_{ph}(\lambda) + a_d(\lambda) \quad (1.1)$$

where $a_w(\lambda)$ is the absorption coefficient spectrum of seawater, $a_g(\lambda)$ is that of chromophoric dissolved organic matter (CDOM), $a_{ph}(\lambda)$ is that of living phytoplankton particles and $a_d(\lambda)$ is that of nonphytoplankton and/or detrital particles. CDOM dominates the total absorption spectrum in seawater in the blue and ultraviolet (UV)

regions of solar radiation, with CDOM accounting for 50% of the total absorption at 400 nm and increasing to about 70% of the total absorption at 300 nm (Nelson and Siegel, 2013). Because radiation in the blue and UV has the highest available energy, absorption of this higher energy radiation, primarily by CDOM, should drive photochemical reactions in the surface ocean. There is evidence that photochemistry can occur from particles (Xie and Zafiriou, 2009), but particles reactions were reported to be only 11 – 35% of CDOM photochemistry based on the photoproduction of carbon monoxide (CO). Because $a_g(\lambda)$ is responsible for the majority of seawater absorption below ~440 nm (Nelson and Siegel 2013), most studies of natural organic mater (NOM) photoreactions have focused on its dissolved fraction (DOM), and hence on photoreactions of CDOM. These studies have implicated photoreactions of CDOM in a variety of important biogeochemical and redox cycles, reviewed in detail by Mopper and Kieber (2002), Blough and Zepp (1995), and Sharpless and Blough (2014), among others.

While modern techniques (e.g. nuclear magnetic resonance spectroscopy and ion cyclotron mass spectrometry) can be used to help characterize DOM (Mopper et al., 2007; Sulzberger and Durisch-Kaiser, 2009, references therein), it is still difficult to differentiate the molecular composition of CDOM from that of bulk DOM. While a number of researchers are working towards understanding functional groups in marine CDOM and molecular level changes via photochemical reactions, CDOM is still most often operationally defined as the light absorbing fraction that passes through a 0.2 μm filter. Measurements of $a_g(\lambda)$ spectra using standard benchtop spectrophotometers (Bricaud et al., 1981; Twardowski et al., 2004) or long pathlength (50 – 200 cm) liquid capillary cells (D'Sa et al., 1999; Nelson et al., 2007) generally have featureless shapes

that decrease exponentially with increasing wavelength. Del Vecchio and Blough (2002) presented a model for CDOM absorption in which charge transfer interactions between electron donating groups and electron accepting groups within CDOM broaden the spectrum. The optical (i.e. absorbance and fluorescence phenomena) and photochemical evidence that supports this physical model over one that describes a featureless spectrum by a superposition of multiple chromophores has been recently reviewed by Sharpless and Blough (2014).

Because $a_g(\lambda)$ spectra appear an have an exponential shape, they are often described with the following equation

$$a_g(\lambda) = a_g(\lambda_{ref})e^{-S(\lambda - \lambda ref)} \quad (1.2)$$

where λ_{ref} is the reference wavelength and S (nm^{-1}) is the spectral slope coefficient. Differences in S between studies depend less on the method used for its determination (nonlinear curve fitting to solve for S vs. log-linearizing a_g spectra to solve for S) and more on the wavelength region over which S is determined (Sharpless and Blough, 2014). In that regard, S is often reported over shorter wavelength regions, like 275 – 295 nm or 350 – 400 nm. Helms et al. (2008) demonstrated that S(275 – 295 nm) and the slope ratio (S_R; S determined over 275 – 295 nm divided by that from 350 – 400 nm) were correlated to molecular weight of DOM for a variety of samples. Lower values of S are often associated with high molecular weight (HMW) DOM and high values of S are associated with low molecular weight (LMW) DOM (Helms et al., 2008). For S determined over larger wavelength regions (e.g. 300 – 700 nm), it is typically higher for offshore samples (> 0.020 nm^{-1}), lower for coastal/inshore samples (0.014 – 0.018 nm^{-1}) and lowest for

fresh water humic and fulvic acids (< 0.014 nm^{-1}) (Sharpless and Blough, 2014, references therein).

Again, because CDOM is a complex mixture of multiple chromophores and there is currently no way to measure its concentration, *S* from 275 – 295 nm has also been used as a proxy for DOC concentrations in river influenced coastal zones (Fichot and Benner, 2011). CDOM absorption coefficients at certain wavelengths have been used as proxies for CDOM photochemical efficiencies for that of CO (Stubbins et al., 2011; Zhang et al., 2006). Furthermore, specific UV absorption (the absorption coefficient or absorbance, usually at 254 nm, divided by DOC concentration) has been correlated to both the percent aromaticity in DOC (Weishaar et al., 2003) and CO photoproduction (Stubbins et al., 2008; Zhang et al., 2006). These relationships have been demonstrated for dark fresh waters or inshore estuarine waters, and therefore may not be representative or simply may not work for CDOM in the global ocean.

While CDOM absorption and DOC concentration tend to have a linear relationship for the high DOC and CDOM gradients found in coastal margins (Del Vecchio and Blough, 2004), this relationship is usually region specific and falls apart in the open ocean. In an extensive compilation of CDOM survey data, Nelson and Siegel (2013) demonstrated that marine DOC and the $a_g(\lambda)$ at 325 nm were not correlated and varied over 2 orders of magnitude in the open ocean. Because of the analytical difficulty in accurately measuring small changes in open ocean DOC loss during irradiations without sample pre-concentration, the photoreactivity of open ocean marine DOC is largely unstudied when compared to coastal and inshore environments.

With continued irradiation, CDOM absorption decreases at all wavelengths, though it is typically faster in the UVA (300 – 320 nm) and visible, with corresponding increases in spectral slope coefficients with photobleaching (e.g. Del Vecchio and Blough, 2002; Moran et al., 2000; Sharpless and Blough, 2014). Because not all DOM is colored, and the loss of color does not mean the loss of carbon, samples typically fade faster than the loss of dissolved organic carbon (DOC). During irradiations of riverine water samples lasting several weeks, nearly all of the CDOM was lost but ~60% of the DOC remained (Moran et al., 2000; Spencer et al., 2009). Interestingly, in a recent study, during a 110 day irradiation of swamp water where far more DOC (74 – 88%) was lost, photoreactions caused this terrestrial DOM to better resemble marine DOM in terms of its molecular level signatures (Helms et al., 2014). It is well known that upon irradiation, allochthonous CDOM, largely delivered to marine systems via river inputs, loses its terrestrial character in terms of terrestrial biomarkers (e.g lignin phenols) and ^{13}C isotopic signatures (Dittmar et al., 2007; Helms et al., 2014; Opsahl et al., 2001; Stubbins et al., 2010). It has been suggested that terrestrial DOM is almost entirely remineralized at the coast because terrestrial DOM is only a small fraction of that in the open ocean (Opshal and Benner, 1997). There is also evidence that marine CDOM is largely derived autochthonously, by microbial processing of marine organic matter (Rochelle-Newall and Fisher, 2002) or by direct release from phytoplankton and zoonplankton (Romera-Castillo et al., 2010; Steinberg et al., 2004). Since terrestrial biomarkers, like lignin phenols, are lost during irradiations, there is no way to distinguish marine DOM from terrestrial DOM that is highly degraded. Helms et al. (2014) suggest that markers other than lignins would be useful in tracking terrestrial DOM into the marine environment, but

this is currently challenging in that distinguishing between aliphatic DOM present before irradiation and that produced during irradiation is not possible, even with high resolution techniques (e.g. solid state ^{13}C NMR and FTIR mass spectrometry).

There have been a number of advances in understanding the importance of photochemical processes on chemical and biological systems in natural waters since the subject was first reviewed and previewed (Zafiriou, 1977; Zafiriou et al., 1984; Zika, 1981). However, areas remain where estimates of photochemical reactions are poorly defined or missing so critical data is still needed to improve our current understanding, and consequently our modeling accuracy, of photochemistry's importance in marine biogeochemical and redox cycles. Because the nature of marine CDOM and its photochemical transformations still remain enigmatic, this dissertation focuses on a study of several important photoproducts in diverse, yet understudied marine environments. The basic approach involves laboratory determinations of the photochemical efficiency for inorganic carbon species, namely carbon monoxide (CO) and carbon dioxide (CO_2), and the reactive oxygen species (ROS), hydrogen peroxide (H_2O_2).

Photochemical efficiency is the probability that absorption of solar radiation by CDOM will lead to a photochemical product. This is typically determined as the spectral apparent quantum yield (AQY; $\phi(\lambda)$), defined as the ratio of the moles of product produced to the moles of photons absorbed by the sample

$$\phi(\lambda) = (\text{moles product})/(\text{moles photons absorbed}) = P/Q_a(\lambda) \qquad (1.3)$$

where P (mol m^{-3} s^{-1}) is the photoproduction rate and $Q_a(\lambda)$ (mol(photons) m^{-3} s^{-1}) is the rate of photon absorption. Photoproduction rates in natural waters are controlled by the reaction efficiency (AQY) and $Q_a(\lambda,z)$ at a given wavelength (λ; m) and depth (z; m).

$Q_a(\lambda,z)$ is a function of the $a_g(\lambda)$ spectrum, the solar spectral scalar irradiance ($E_0(\lambda,0^-)$; mol (photons) m^{-2} s^{-1} nm^{-1}), and its attenuation in the water column ($K_d(\lambda)$; m^{-1}). This is quantified as

$$Q_a(\lambda,z) = E_0(\lambda,0^-)e^{-K_d(\lambda)z}a_g(\lambda,z) \quad (1.4)$$

Assuming active photochemical production is confined to the 290 – 490 nm wavelength range (Fichot and Miller, 2010), *in situ* production rates of any photochemical product in sunlit waters can be modeled as follows,

$$P = \int_{290}^{490} Q_a(\lambda,z)\phi(\lambda,z)d\lambda \quad (1.5)$$

This general approach is appropriate for any scale for which the optical and photochemical variables above can be defined and has been used to describe results ranging from laboratory irradiations in quartz containers (Reader and Miller, 2012), used extensively throughout this dissertation, to global ocean calculations (Fichot and Miller, 2010) from satellite data. This latter development is critical for the examination of the importance of photochemical reactions over large spatio-temporal scales. In this dissertation, new AQY spectra and ocean color-based optical models (Cao et al., 2014; Fichot et al., 2008) are used to calculate CO and CO_2 photoproduction rates on regional spatial scales in Chapter 2. Chapter 3 expands photochemical flux estimates of H_2O_2 to global scales and uses chemical rate constants for its precursor, superoxide (O_2^-), to estimate photochemical production rates for both H_2O_2 and O_2^- in the surface ocean. Chapter 4 expands the database for the photochemical production of H_2O_2 and that for the largely under-studied ROS, O_2^- in both deep and surface waters of the North Pacific to better evaluate the photochemical reactivity of these waters. Chapter 5 then uses relationships between the photoproducts studied here, primarily between CO_2 and H_2O_2,

to emphasize links between their photochemical efficiency. Specific areas studied are outlined in detail in the following sections.

1.2 Photochemistry and Coastal Carbon Cycling

Most global ocean CO_2 flux studies are in agreement that the ocean acts as a net sink for atmospheric CO_2, removing about 2 Pg C yr^{-1} (Takahashi et al., 2009; Wanninkhof et al., 2013), but there are still large uncertainties associated with this estimate (~ 0.6 Pg C yr^{-1} reported by Wanninkhof et al. 2013). A primary source of the uncertainty in air-sea CO_2 fluxes lies in coastal zones. Studies have shown that there can be large deviations from atmospheric equilibrium in the surface water partial pressure of CO_2 (pCO_2) and imbalances in the carbon budget in the coastal ocean (Hales et al. 2008). Hales et al. (2008) further argues that despite their small surface area, the coastal ocean contributes significantly to global CO_2 fluxes. High inputs of organic carbon and nutrients from land or upwelling in these areas create active sites of biogeochemical cycling so resolving the air-sea CO_2 flux term in coastal regions may change our current understanding of global carbon budget (Borges et al., 2005; Cai et al., 2006).

Since coastal carbon cycling is extremely complex, resolving coastal ocean carbon dynamics has become an active area of research. An early study suggested that, like the global ocean, three coastal zones are sinks for CO_2 from estimations of carbon loading off the continental slopes of the mid-Atlantic Bight, the southeastern Bering Sea, and the Peru coast (Walsh et al. 1985). A later study suggested the same, based on carbon and nitrogen cycling models, for the Chukchi Sea and the Northern Gulf of Mexico and concluded that atmospheric CO_2 is sequestered by temperate and polar shelf ecosystems (Walsh and Dieterie 1994). Around the same time, however, Smith and

Hollibaugh (1993) found that the coastal ocean can also be a source of CO_2 to the atmosphere. They based their estimates on terrigenous organic matter delivery to coastal zones and the portion of that organic matter that can be readily oxidized to CO_2. They also considered how primary production consumes CO_2 and respiration produces CO_2. In fact, a combination of physical, chemical, and biological factors associated with the balance of organic matter inputs from land, organic matter production and respiration, and retention or export from the shelf all influence the net air-sea CO_2 flux in the coastal environment (Bates and Mathis 2009).

In more recent years, additional studies have shown that the coastal ocean can be either a source (Zhai et al. 2004) or sink (Arrigo et al. 2008; Wesslander et al. 2011) of atmospheric CO_2. Available estimates of CO_2 flux in shelf seas converge toward a sink of about ~0.3 Pg C yr^{-1}, but based on the sparse data available, this estimate is highly biased towards mid latitudes in the Northern hemisphere and by poor spatio-temporal coverage (Borges, 2011). Including more data from Asian and Antarctic environments, with CO_2 flux estimates from 165 estuaries and 87 continental shelves, Chen et al. (2013) estimated that estuaries release 0.1 Pg C yr^{-1} while shelves absorb 0.4 Pg C yr^{-1}. Currently, the factors controlling CO_2 fluxes in coastal environments are too complex to include in global models (Chen et al., 2013) even though understanding theses controls is essential to fully understanding their impact on global carbon budgets. Coupled circulation-biogeochemical models have made progress in estimating carbon fluxes in continental margins (Hofmann et al., 2011), but model results are heavily dependent on the selection of model inputs and parameterizations (Hofmann et al., 2011). Almost surprisingly, photochemical oxidation of organic carbon has not been considered in these

CO_2 flux estimates although it has been recognized as a major process affecting carbon sources and fluxes in the coastal zones (Bauer et al., 2013). In particular, the photodegradation of CDOM in the ocean is a significant process in the oxidation of organic carbon to CO_2, CO, and a number of low molecular weight organic molecules (Miller and Zepp, 1995; Mopper and Kieber, 2002). In particular, terrestrial biomass transported to the coast via river export is rich in aromatic compounds, like lignin phenols, that are highly photoreactive (Miller and Zepp, 1995; Opsahl and Benner, 1998; Stubbins et al., 2010).

It is likely that CDOM photodegradation is an important process in a variety of coastal areas receiving fresh water inputs, well illustrated for long-term (i.e. >50 day) photochemical loss experiments where solar radiation decomposed ~40% of the dissolved organic carbon (DOC) and almost all of the CDOM in riverine waters exposed to sunlight (Moran et al., 2000; Spencer et al., 2009). However, when compared to estimates of DOC inputs via river systems, recent studies have indicated that direct photochemical oxidation of DOC to CO_2 may only be a small (about 3%) contributor to DOC remineralization in estuarine environments (Bélanger et al., 2006; Reader and Miller, 2012; White et al., 2010). Large scale multi-season studies are needed to better address the impact of direct photochemistry on coastal carbon cycling, especially in river-dominated systems.

For instance, the Northern Gulf of Mexico and the Mississippi River System, comprised of the Mississippi and Atchafalaya Rivers, is of particular interest because high nutrient loading causes a decrease in water quality as large phytoplankton blooms eventually lead to an annual summer hypoxic zone (Rabalais et al., 2002). This area also receives large and variable fluxes of terrigenous DOC, amounting to about 3 Tg C yr^{-1}

(Bianchi et al., 2004; Shen et al., 2012). Evidence suggests that in situ production, bacterial utilization and photo-oxidation could all aid in regulating the removal of DOC in this region based on the high variability in organic carbon concentrations, both in the particulate and dissolved fractions, along with the variability observed in isotopic and elemental signatures (Wang et al. 2004). The primary factor controlling CDOM in this region may be the quantity of fresh water runoff from the river system (Chen and Gardner, 2004; Conmy et al., 2004), but as the authors note, the complexity in circulation patterns, variability in river flow and multiple river sources makes observation of both biological and photochemical effects challenging in this region. Chapter 2 of this dissertation focuses on the pressing need to better understand the mechanisms controlling carbon cycling in the Northern Gulf of Mexico by fully considering the extent to which photochemical carbon oxidation contributes to regional CO_2 flux estimates with a large photochemical study of both CO_2 and CO photochemical efficiency over 4 different sampling campaigns.

1.3 Photochemistry as a Sink for Marine Dissolved Organic Carbon

The marine dissolved organic carbon (DOC) pool contains 662 ± 32 Pg C (Hansell et al., 2009) and is therefore one of Earth's largest active carbon reservoirs, on the same order of the carbon stored in the atmosphere. Marine DOC has often been classified based on somewhat qualitative assessments based on its reactivity, with labile DOC turned over on a time scale of days and refractory DOC (RDOC) overturned on a time scale of millennia (Kirchman et al., 1993; Carlson 2002). RDOC is largely biologically refractory, with a mean radiocarbon age of 4000 – 6000 years (Williams and Druffel, 1987), and comprises the majority of this carbon pool (~642 Pg C, Hansell,

2013). Currently, a quantitative assessment of the turnover of this DOC pool has been hampered by the fact that the sources and sinks of RDOC are still not completely understood (Hansell, 2013). This, in turn, might hinder our understanding of how changes in this pool may play a role in past and future climates (Sexton et al., 2011). For instance, DOC release from the ocean's interior by ventilation has been implicated in rapid hyperthermal warming events (Sexton et al., 2011). General circulation models indicate the with these warming events, convection significantly increases in areas having strong haloclines like the North Pacific and the Southern Ocean, suggesting that a warm ocean is one that is better ventilated (de Boer et al., 2007). RDOC is ubiquitous in the ocean, but deep sea (>1000 m) refractory organic carbon (DORC) is almost entirely refractory and represents ~70% of the entire DOC pool (Hansell et al., 2009). Unfortunately, carbon dynamics in the deep sea have been largely under studied, primarily due to the difficulty in sampling the deep sea on large spatial and temporal scales.

As more bulk DOC concentration data has become available, an average RDOC removal rate of ~0.003 μmol C kg^{-1} yr^{-1} in the deep ocean was determined based on models of DOC concentration gradients and radiocarbon ages (Hansell et al., 2012, 2009). However, a more recent analysis suggests that RDOC is conserved during circulation but unknown local sinks exist in both the deep far North Pacific and mid depth subtropical South Pacific (Hansell and Carlson, 2013). On the other hand, one identified sink for RDOC appears to be via its photo-oxidation in the surface ocean (Mopper et al., 1991; Stubbins et al., 2012). Removal of RDOC by photochemistry is at odds with its ^{14}C age because it implies that this pool of carbon has passed through sunlight waters several times before its eventual removal. However, the Mopper et al.

(1991) study found that samples collected from the deep ocean in the Sargasso Sea were more photoreactive than surface samples in terms of the photoproduction of low molecular weight organic carbon species. Based on their results, they estimated a residence time for photolabile biorefractory DOC of ~500 – 2100 years, well below its average age, arguing photochemistry was capable of removing all RDOC in about 1 to 2 oceanic mixing cycles. This calculation is somewhat flawed because it assumes the entire DOC pool is photoreactive, and as noted above, only a fraction of DOC can absorb sunlight and is therefore available to participate in photoreactions.

Furthermore, the calculation of Mopper et al. (1991) is based on first order kinetics, while more recent evidence suggests that apparent second order kinetics better describe the photoreactivity of heterogeneous mixtures such as DOC (Beaupré and Druffel, 2012). The residence time estimates of Mopper et al. (1991) were also based on short (<5 h) irradiations from one location without considering the potential changes in these rates with long exposures. Long term photodegradation has been recently addressed by Stubbins et al. (2012) who found that dissolved black carbon collected in the deep waters (3000 m) of the North Atlantic was very photoreactive, decreasing by 95% in a 28 day irradiation. The high molecular weight fraction of dissolved black carbon has a radiocarbon age of ~18,000 years (Ziolkowski and Druffel, 2010), leading Stubbins et al. (2012) to suggest that this apparent age is not due to its inertness, but rather the rate of ocean turnover and its control on delivering dissolved black carbon to the photic zone. Dissolved black carbon has been recently classified as an ultra-refractory component of marine DOC, containing about 12 Pg C (Hansell, 2013), and is therefore a small component of the entire refractory DOC pool (~642 Pg C for refractory and ultra

refractory together; Hansell, 2013). Additional evidence that dissolved black carbon should not be classified as refractory is that stable compounds in marine DOM tend to have higher H/C and O/C ratios and lower aromatic content than that of dissolved black carbon (Lechtenfeld et al., 2014).

Although direct measurements of DOC loss from irradiations of RDOC is analytically challenging, a reevaluation of the earlier work of Mopper et al. (1991) is warranted in order to assess photochemistry as a RDOC removal mechanism. While direct links between the photoproduction of reactive oxygen species (ROS) and the carbon cycle have not been fully addressed, their formation should be a useful proxy for DOC photoreactivity. Accordingly, Mopper and Zhou (1990) used increased photoproduction of hydroxyl radicals ($^{\bullet}OH$) in deep Sargasso Sea samples relative to surface samples from the same location to argue for increased photoreactivity of deep ocean DOC. H_2O_2 and its precursor O_2^- are products of CDOM photoreactions that are long-lived relative to other ROS (e.g. $^{\bullet}OH$ and $^1O_2$) and have the added benefit that sensitive (sub-nanomolar) chemiluminescent methods exist for their detection (King et al., 2007; Rose et al., 2008). These questions are fully addressed in Chapter 4 of this dissertation, in conjunction with a large project aimed at reevaluating the photoreactivity of deep ocean DOC in the North Pacific. The deep waters of the North Pacific are the most aged and should therefore contain the oldest reservoir of DOC. Measurements of both H_2O_2 and O_2^- during controlled laboratory and ship board irradiations of deep ocean water, containing only RDOC, are compared to those during irradiations of surface and mesopelagic waters, thought to contain more labile fractions of DOC. As mentioned previously, and documented by Swan et al. (2009) for the Pacific ocean, DOC and

CDOM do not correlate in the open ocean. CDOM in the deep North Pacific is likely a very small component of the low (<40 μM) DOC pool, and perhaps the processes controlling CDOM and DOC distributions in this pool are not related. A strong linear relationship between CDOM absorption coefficients and AOU has been reported in the interior of the Pacific Ocean (Swan et al., 2009; Yamashita and Tanoue, 2009), indicating that new CDOM is produced via biological oxidation that appears to be semilabile and photolabile (Helms et al., 2013). Therefore, production rates of these two ROS in deep waters discussed in Chapter 4 may not be reflective of the RDOC pool at all, but rather of a more labile fraction produced in the ocean interior.

1.4 Photoproducts Quantified in this Study

1.4.1 Oxidized Inorganic Carbon Products

The largest identifiable carbon photoproduct thus far is CO_2, with its production typically 15 – 20 times greater than that for the second largest identified carbon photoproduct, CO (Miller and Zepp 1995, White et al. 2010, Reader and Miller 2012). Because of the analytical difficulty in measuring photoproduced CO_2 over background dissolved inorganic carbon (DIC) in marine samples, there is currently limited, and often unclear, information on its formation mechanism(s). Because photodecarboxylation has been well documented in synthetic organic chemistry since the mid 20th century (e.g. Givens and Oettle, 1972), it may be tempting to suspect that the majority of CO_2 photoproduction is via photodecarboxylation of CDOM. Early studies with implications for natural waters demonstrated that photodecarboxylation can occur by irradiating commercially available ligands through ligand to metal charge transfer (Langford et al., 1973; Lockhart Jr. and Blakeley, 1975). The stoichiometry of photodecarboxylation

however requires the consumption of $0.5O_2$ per CO_2 produced but CO_2 photoproduction from riverine DOM has been observed in the absence of O_2, albeit lower than that in air or O_2 saturated systems (Gao and Zepp, 1998). Subsequent work investigating the relationships between O_2 consumption, CO_2 photoproduction, photobleaching and iron redox chemistry during river water irradiations found that the loss of carboxyl groups was too small to account for the much larger production of CO_2, indicating that photodecarboxylation is not the major pathway of CO_2 photoproduction from NOM (Xie et al., 2004). In fact, the stoichiometry of O_2 consumption to CO_2 photoproduction is closer to 1 in air-saturated solutions (Gao and Zepp, 1998; Xie et al., 2004).

Metal catalyzed reactions and pH changes have also been implicated in the photoproduction of CO_2 in natural waters. Decreased pH in fresh water has been reported to accelerate CDOM photoreactions and the loss of DOC (Anesio and Graneli, 2003; Gennings et al., 2001; Wu et al., 2005) as well as the photoproduction of CO_2/DIC (Anesio and Graneli, 2003; Bertilsson and Tranvik, 2000). Conversely, Gao and Zepp (1998) observed that DIC photoproduction rates were higher when Satilla River samples were increased from a pH of 4 to 7 and Miller and Zepp (1995) observed little change in DIC photoproduction rates with varying pH of Mississippi River plume waters. Observed effects may reflect the presence and speciation of metals, especially iron, since DIC photoproduction is reported to be faster with higher iron concentrations (Bertilsson and Tranvik, 2000; Gao and Zepp, 1998; Xie et al., 2004) and the pH effect observed by Gao and Zepp (1998) disappeared when iron was chelated with fluoride.

Similar studies in marine waters are lacking and are still hampered by analytical difficulties in measuring small changes in photoproduced CO_2 over background DIC.

Most methods involve acidifying samples to a pH of 2 – 3 and sparging them with CO_2-free air overnight (Johannessen and Miller, 2001; Miller and Zepp, 1995; White et al., 2008). To minimize the effects of lowered pH on DOM photochemistry, or perhaps those due to changes in metal catalyzed reactions, all samples are returned to their original pH either with sodium borate (Miller and Zepp, 1995; Johannessen and Miller, 2001, Reader and Miller, 2012) or sodium hydroxide (White et al., 2008; White et al., 2010). White et al. (2008) noted that this acidification-rebuffering process could irreversibly alter DOM, potentially influencing the photochemical reactivity of the sample. They cite possible effects on photoreactivity through the precipitation of humic substances at low pH, loss of volatile organic compounds during sparging, and sample concentration caused by evaporation from sparging with dry air. Current information on CO_2 photoefficiencies in marine systems is limited and somewhat contradictory. For example, Johannessen and Miller (2001) reported higher CO_2 photoefficiencies for offshore samples and White et al. (2010) reported the highest CO_2 photoefficiency in the Delaware estuary at the mouth of the river.

CO is the second largest identified carbon based product of marine photochemistry and, like CO_2 photoproduction rates, its photoproduction is accelerated with higher O_2 and iron concentrations (Gao and Zepp, 1998). CO is an important marine photoproduct because its photoproduction creates CO-supersaturation in almost all marine surface waters, driving the net transport of CO across the air-sea interface into the atmosphere (Swinnerton et al., 1970) where it competes with methane to scavenge hydroxyl radicals (Levy, 1971). A study investigating the isotopic compositions of carbon and oxygen in seawater CO found that photochemically produced CO is

isotopically light, depleted in ^{13}C by more than 20 ppt when compared to the total $\delta^{13}C$ value of DOM (Nakagawa et al., 2004). The authors note that the ocean provides a unique source of ^{13}C and ^{18}O depleted CO relative to that from fossil fuel and biomass combustion, which could aid in creating a better isotopic mass balance for both global and local CO budgets. In addition, CO may occupy a key position in oceanic carbon cycling (Zuo and Jones, 1997), acting as an intermediate in the photochemical mineralization of marine DOM as a direct DOC removal pathway and also as a substrate for bacterial DOM mineralization (Moran and Zepp, 1997; Xie et al., 2009; Zafiriou et al., 2008).

CO production measurements (both photochemical and biological) are made using sensitive headspace equilibration methods similar to those of Xie et al. (2002). This approach has led to a number of CO photochemical flux calculations for a variety of marine waters ranging from highly turbid (Reader and Miller, 2012; Stubbins et al., 2011; White et al., 2010; Zhang et al., 2006) to coastal (Xie et al., 2009; Ziolkowski and Miller, 2007) and oligotrophic waters (Stubbins et al., 2006; Zafiriou et al., 2003). Due to the analytical sensitivity of this method and the fact that it requires no sample pretreatment, CO is the most extensively studied marine photoproduct. Current global estimates suggest that in the open ocean, photochemistry is capable of remineralizing ~50 Tg C of DOM as CO annually (Fichot and Miller, 2010; Stubbins et al., 2006; Zafiriou et al., 2003). Despite the body of work on CO AQY spectra, most studies determined CO AQY spectra for less than 20 samples in one or two sampling season (references listed above).

Because AQY spectra for both CO_2 and CO have similar photon dose dependencies and both direct and indirect mechanisms have been implicated in their

photoformation (Gao and Zepp, 1998), it is tempting to assume that the formation of these two photoproducts is related. While it is often assumed that CO_2 photoproduction is 15 – 20 times larger than CO photoproduction (Miller and Zepp, 1995), published photoproduction CO_2:CO ratios range from ~2 to 65 (Miller and Zepp, 1995; Reader and Miller, 2012; White et al., 2010), suggesting that one ratio is not appropriate for global or regional models of CO_2 photochemical fluxes. Albeit from only three samples for CO and six for CO_2, White et al. (2010) found CO AQY spectra that varied with salinity in the Delaware Estuary but CO_2 AQY spectra were similar for all but the lowest salinity sample. These results indicate that CO and CO_2 could arise from different mechanisms and precursors. In fact, the correlation between the CO AQY and salinity has been demonstrated in variety of coastal zones (Stubbins et al. 2011, Zhang et al. 2006, Xie et al. 2009). However, Stubbins et al. (2011) demonstrated that a simple 2 component-mixing model could not be used to predict CO AQY spectra in the Tyne Estuary and when photoproduction was normalized to CDOM absorbance, Reader and Miller (2012) found no correlation between salinity and photochemical production of either CO_2 or CO in an estuary of the South Atlantic Bight. They did observe, however, that there was a seasonal trend in CO photoproduction rates, with lower CO AQY spectra in the spring and summer and higher CO AQY spectra in the fall and winter. While mechanisms involved in CO_2 and CO photoproduction in marine waters remain elusive, again, Chapter 2 gives an extensive investigation of the spatiotemporal variability in both CO_2 and CO photoproduction rates in a fresh water impacted coastal zone.

Additional evidence for a lack of a relationship between CO_2 and CO has been observed with long irradiation experiments. Miller and Zepp (1995) observed slower CO_2

photoproduction rates after prolonged exposure (after about 8 hours) compared to initial rates while CO photoproduction remains a linear function of photon dose, even after hundreds of hours of irradiation (Valentine and Zepp, 1993). The photoproduction of CO has been correlated to CDOM absorption coefficients and DOM aromaticity (Stubbins et al. 2008), which has not been reported for CO_2. Because CO_2 photoproduction is affected by changes in both pH and in the presence or absence of iron (Gao and Zepp, 1998), Sharpless and Blough (2014) suggest that the mechanisms for H_2O_2 and CO_2 may be similar, especially because the extent of electron transfer required for production, in other words, the magnitude of their AQY spectra, are similar for these two photoproducts. This novel, yet somewhat obvious, idea is investigated for marine systems in detail in Chapter 5.

1.4.2 Reactive Oxygen Species (ROS): Hydrogen Peroxide and Superoxide

In the marine environment, photochemical transformations of organic matter in surface waters saturated with oxygen lead to a number of oxidized products. Due to the presence of oxygen, CDOM photoreactions also initiate the formation of an array of ROS. In fact, ROS are involved in the degradation and indirect photobleaching of CDOM and organic pollutants (Chen et al., 2009; Scully et al., 2003; White et al., 2003), the redox cycling of trace metals (Hansard et al., 2011; Kieber et al., 2003; Moffett and Zika, 1987; Rose and Waite, 2005; Voelker and Sulzberger, 1996), and the response to oxidative stress in aquatic organisms (Baltar et al., 2013; Morris et al., 2011; Zepp et al., 2003). The ROS responsible for these biogeochemical processes include singlet oxygen ($^1O_2$), superoxide (O_2^-), hydroxyl radical ($^{\cdot}OH$), hydrogen peroxide (H_2O_2), and a number of additional reactive radicals (Kieber et al., 2003). Of these ROS, H_2O_2 has been widely

studied due to its role in all of these above processes but also due to its high concentration and stability relative to other ROS (O'Sullivan et al., 2005).

Van Baalen and Marler (1966) were the first to detect H_2O_2 in surface seawater samples, but its sources and role in the ocean remained unclear. Now, it is well accepted that the primary source of H_2O_2 in sunlit waters occurs through an abiotic photochemical pathway (Cooper et al., 1994; Kieber et al., 2003). Based on a detailed mechanistic investigation involving borohydrate reduction and triplet state quenchers, Zhang et al. (2012) confirmed that the formation of H_2O_2, and its precursor O_2^-, arises from charge transfer from excited state CDOM to form oxygen reducing intermediates (charged $CDOM^{+\bullet/-\bullet}$) that subsequently donate an electron to O_2 to form O_2^-.

Superoxide subsequently decays through disproportionation via the following reactions (O'Sullivan et al., 2005):

$$HO_2 + O_2^- \rightarrow HO_2^- + O_2 + OH^- \ (k = 9.7 \times 10^7) \quad (1.6)$$

$$HO_2 + HO_2 \rightarrow H_2O_2 + O_2 \ (k = 8.3 \times 10^5) \quad (1.7)$$

where k is the rate constant in $M^{-1}s^{-1}$ (Bielski et al., 1985). Zafiriou (1990) reported similar superoxide dismutation kinetics in seawater, determining a pK_a of 4.60 ± 0.15, defining the overall second order rate law for O_2^- decay via dismutation as

$$\frac{d[O_2^-]}{dt} = k_{dis}[O_2^-][HO_2] \approx 2k_D[O_2^-]^2 \quad (1.8)$$

where k_D for seawater = $(5 \pm 1) \times 10^{12}[H^+]$, confirming a similar direct dependence on pH for O_2^- kinetics that had been described for pure water (Bielski et al., 1985).

In addition to H_2O_2 formation via O_2^- dismutation, metals (e.g. Fe, Cu, and Mn) and CDOM also efficiently react with O_2^- in natural waters (Heller and Croot, 2010a, 2010b; Voelker et al., 2000; Wuttig et al., 2013). Because O_2^- can act as both an oxidant

and a reductant, its decay pathways are far too complex to be described by dismutation alone (Voelker and Sedlak, 1995; Zafiriou, 1990). Reactions of CDOM and/or metals (A) with O_2^- could produce either H_2O_2 or O_2 via the equations

$$A_{ox} + O_2^- \rightarrow A_{red} + O_2 \quad (1.9)$$

$$A_{red} + O_2^- \xrightarrow{2H^+} A_{ox} + H_2O_2 \quad (1.10)$$

where A_{ox} is an oxidant and A_{red} is a reductant. If catalytic O_2^- decay described above is irreversible, then the amount of H_2O_2 generated per O_2^- should be between 0 and 1. On the other hand, if catalytic redox cycling is occurring between A_{ox} and A_{red}, then the same stoichiometry typical of dismutation ($0.5H_2O_2$ per O_2^-) should be maintained, confusing the matter of identifying which pathway (or neither) is dominant. Some work with additions of superoxide dismutase (SOD), which ensures that O_2^- decays through dismutation, has been done to ascertain the amount of O_2^- leading to H_2O_2. H_2O_2 photoproduction in the presence of SOD was indistinguishable from that produced in its absence for irradiations of samples collected in the Gulf of Aqaba (Shaked et al., 2010), leading to estimates of $0.5H_2O_2$ formed per O_2^-, but a ratio of ~0.3 – 0.4 H_2O_2 per O_2^- has also been reported for coastal seawater (Petasne and Zika, 1987). Some rather questionable evidence suggests that the oxidative pathway (Equation 1.9) may dominate O_2^- decay in the open ocean based on direct superoxide steady state ($[O_2^-]_{ss}$) and H_2O_2 measurements (Rusak et al., 2011). These authors observed a ratio of 0.37 H_2O_2 per O_2^- but used unfiltered samples that are not reflective of solely photochemical production and abiotic decay. Even though the fate of superoxide in seawater is complex, Chapters 4 and 5 of this dissertation attempt to resolve these discrepancies by investigating the photochemical production of both O_2^- and H_2O_2 together for marine samples. This is

especially informative in light of the fact that AQY spectra for O_2^- are unavailable, and currently the only option to gain information about the spectral photochemical production efficiency for O_2^- is to infer it from that for H_2O_2.

Additional mechanisms of H_2O_2 production in the ocean include dry and wet deposition and reactions involving trace metals and O_2^- (Kieber et al., 2003). Even though an oxidant to marine microorganisms, it has been shown that biological H_2O_2 production is possible (Vermilyea et al., 2010). Furthermore, based on dark H_2O_2 production measurements, Vermilyea et al. (2010) concluded that biological production was a significant contributor to the H_2O_2 budget in the Gulf of Alaska. On the other hand, since H_2O_2 can be harmful to marine miroorganisms at elevated concentrations, the primary mechanism for H_2O_2 decay in the ocean is through microbial enzymatic removal, via dismutation with catalase or reduction with peroxidase (Kieber et al., 2003; Petasne and Zika, 1997). Morris et al. (2011) showed that the cyanobacterium *Prochlorococcus*, responsible for nearly half of oceanic primary production, lacks the enzyme catalase and therefore cannot efficiently remove H_2O_2. Therefore, *Prochlorococcus* rely heavily on the microbial community's overall ability to remove H_2O_2 from the photic zone. In addition, Clark et al. (2008) noted that while surface concentrations in coastal waters on the order of 100 nM are too low to directly cause fecal indicator bacteria mortality, H_2O_2 still contributes to oxidative stress in these organisms. Furthermore, cells exposed to sunlight may be even more sensitive to surface water concentrations of peroxide. Finally, metal reactions, most notably the pH-dependent photo-Fenton reactions that produce highly reactive $^{\bullet}OH$ radicals, also remove H_2O_2 from natural waters (Zepp et al., 1992). Moffet and Zika (1987) studied the effects of pH, temperature, chelators, and temperature

on the reactions of H_2O_2 with iron and copper in seawater and concluded that Cu(I) and Fe(II) oxidation by H_2O_2 could be an important source of $^{\bullet}OH$ radicals in the ocean.

Changes in seawater temperature and pH, especially in the Arctic where projected decreases in pH could produce a 185% increase in hydrogen ion concentration (Steinacher et al., 2009), will certainly impact ROS production and decay in natural waters. For example, rates of Fe(II) oxidation by H_2O_2 are a function of pH, temperature and salinity (Millero and Sotolongo, 1989). It has also been shown that in the presence of natural organic matter, the rate of Fe(II) oxidation by H_2O_2 markedly decreases (Miller et al., 2009). This experiment was performed at a pH of 8.4 and so the authors concluded that the formation of a Fe(II)-fulvic acid complex prevents oxidation by H_2O_2. On the other hand, Voelker and Sulzberger (1996), in a similar set of experiments, found the Fe(II) oxidation by H_2O_2 was accelerated in the presence of fulvic acids at a pH of 5. Although these studies using model systems with commercially available organic matter may not be fully representative of marine systems, it is possible that decreasing oceanic pH, especially in coastal zones heavily impacted by terrigenous inputs, could shift redox rates involving H_2O_2, and other ROS. This is just one example of the many redox reactions with ROS that can be impacted by the various changes in the marine environment. Impacts of climate change, namely by increased temperatures and ocean acidification, on open ocean superoxide steady state concentrations and H_2O_2 photochemical production is investigated in detail in Chapter 3 of this dissertation.

The mechanisms that produce and remove H_2O_2 from aquatic systems yield a diurnal cycle in H_2O_2 concentrations in the photic zone. Daytime concentrations are in the 10 to 100 nM range, with coastal and mid to low-latitude regions typically having higher

concentrations (Clark et al., 2009; Petasne and Zika, 1997; Zika et al., 1985). However, H_2O_2 production is largely dependent on the intensity of solar radiation and there have been far fewer studies that actually determined the wavelength dependence of photochemical H_2O_2 formation (i.e. AQY spectra). Like other photoproducts, H_2O_2 AQY spectra are highest in the UVB (280 – 300 nm), and AQY data determined for marine waters are in good agreement (Kieber et al., 2014; O'Sullivan et al., 2005; Yocis et al., 2000). Yocis et al. (2000) and Kieber et al. (2014) compared AQY spectra for H_2O_2 photoproduction from a variety of freshwater and marine samples and found that they were quite similar for all regions studied. However, O'Sullivan et al. (2005) reported H_2O_2 quantum yield values for coastal waters at the lower range of those determined for the Orinoco River outflow by Moore et al. (1993). O'Sullivan et al. (2005) also observed correlations between CDOM photobleaching and the AQY spectrum for H_2O_2. H_2O_2 formation has also been correlated to the E2/E3 ratio, an optical indicator of DOM molecular weight, whereby HMW DOM was generally more photoefficient than LMW DOM for H_2O_2 photoproduction (Dalrymple et al., 2010). These results suggest that there may be differences in the efficiency for H_2O_2 photoproduction between terrigenous and marine CDOM sources.

Although differences in CDOM may impact H_2O_2 photoefficiencies, because the rate limiting step in H_2O_2 formation is a thermal process (Equations 1.6, 1.7, and 1.10), its temperature dependence cannot be discounted. An increase in seawater temperature leads to an increase in H_2O_2 production, typically increasing the AQY for H_2O_2 production by a factor of 2 for every 10° C increase in temperature (Kieber et al., 2014). By plotting the natural log of the H_2O_2 production rate versus the reciprocal of temperature, Szymczak

and Waite (1988) demonstrated that H_2O_2 photoproduction follows an Arrhenius rate law and calculated an activation energy of 37.4 kJ mol^{-1}, again concluding that this relationship was likely due to the fact that O_2 reduction to O_2^-/HO_2 and superoxide disproportionation (Equations 1.6 and 1.7) are thermal processes. Furthermore, Kieber et al. (2014) determined wavelength dependent activation energies from Arrhenius plots for H_2O_2 photoproduction. In order to accurately predict photochemical H_2O_2 production rates in seawater, both wavelength and temperature dependent quantum yields for H_2O_2 production are required as inputs in these rate models (Chapter 3).

1.5 Dissertation Overview

By identifying areas in which quantitative estimates of marine photochemical efficiencies are still poorly constrained or missing, the overall aim of this dissertation is to provide the data sets required to improve our current understanding, and consequently our modeling accuracy, of photochemistry's importance in marine biogeochemical and redox cycles. Chapter 2 focuses on the role of photochemistry in coastal carbon cycling in the Northern Gulf of Mexico with the quantification of 18 inshore AQY spectra for CO_2 and 99 inshore to offshore AQY spectra for CO. Challenges in accurately quantifying direct CO_2 fluxes in this region, especially for offshore waters, are also addressed in this study. Chapter 3 uses open ocean AQY spectra for H_2O_2, in conjunction with an Arrhenius relationship to correct H_2O_2 AQY for their temperature dependence (Kieber et al., 2014), to model surface ocean H_2O_2 photoproduction rates using climatologies for remotely sensed ocean color (Fichot and Miller, 2010) and temperature. Using several assumptions based on the relationship between photoproduced H_2O_2 and O_2^-, information about O_2^- photoproduction and steady state concentrations are also

inferred. Because marine photochemical fluxes for O_2^- are poorly studied, Chapter 4 directly quantifies rates of H_2O_2 and O_2^- photoproduction as part of a larger study reevaluating photochemistry as a removal mechanism for refractory DOC. Finally, in attempts to overcome the analytical difficulties in measuring photoproduced CO_2 in offshore waters, Chapter 5 highlights a brief study suggesting that H_2O_2 photoproduction is a useful proxy for that of CO_2 in waters ranging from a dark inshore tidal creek to the Gulf Stream. Broader implications and some ideas for future directions are discussed in the concluding Chapter 6.

References

Anesio, A.M., Graneli, W., 2003. Increased photoreactivity of DOC by acidification : Implications for the carbon cycle in humic lakes. Limnol. Oceanogr. 48, 735–744.

Arrigo, K.R., van Dijken, G., Long, M., 2008. Coastal southern ocean: a strong anthropogenic CO_2 sink. Geophys. Res. Letters. 35, 1–6.

Baltar, F., Reinthaler, T., Herndl, G.J., Pinhassi, J., 2013. Major effect of hydrogen peroxide on bacterioplankton metabolism in the Northeast Atlantic. PLoS One. 8, e61051. doi:10.1371/journal.pone.0061051

Bates, N.R., Mathis, J.T., 2009. The Arctic Ocean marine carbon cycle: evaluation of air-sea CO_2 exchanges, ocean acidification impacts and potential feedbacks. Biogeosciences. 6: 2433–2459.

Bauer, J.E., Cai, W.-J., Raymond, P.A., Bianchi, T.S., Hopkinson, C.S., Regnier, P. A. G., 2013. The changing carbon cycle of the coastal ocean. Nature. 504, 61–70. doi:10.1038/nature12857

Beaupré, S.R., Druffel, E.R.M., 2012. Photochemical reactivity of ancient marine dissolved organic carbon. Geophys. Res. Lett. 39. doi:10.1029/2012GL052974

Bélanger, S., Xie, H., Krotkov, N., Larouche, P., Vincent, W.F., Babin, M., 2006. Photomineralization of terrigenous dissolved organic matter in Arctic coastal waters from 1979 to 2003: Interannual variability and implications of climate change. Global Biogeochem. Cycles. 20. doi:10.1029/2006GB002708

Bertilsson, S., Tranvik, L.J., 2000. Photochemical transformation of dissolved organic matter in lakes. Limnol. Oceanogr. 45, 753–762. doi:10.4319/lo.2000.45.4.0753

Bianchi, T.S., Filley, T., Dria, K., Hatcher, P.G., 2004. Temporal variability in sources of dissolved organic carbon in the lower Mississippi river. Geochim. Cosmochim. Acta 68, 959–967. doi:10.1016/j.gca.2003.07.011

Bielski, B.H.J., Cabelli, D.E., Arudi, R.L., Ross, A.B., 1985. Reactivity of HO_2/O_2^- radicals in aqueous solution. J. hys. Chem. Ref. Data. 14(4), 1041–1100.

Blough, N.V., Zepp, R.G., 1995. Reactive oxygen species in natural waters. In: Active oxygen in chemistry. Springer, Netherlands, pp. 280-333.

Borges, A.V., 2011. Present day carbon dioxide fluxes in the coastal ocean and possible feedbacks under global change. In: Oceans and the atmospheric carbon content. Springer, Netherlands, pp. 47–77. doi:10.1007/978-90-481-9821-4

Borges, A.V., Delille, B., Frankignoulle, M., 2005. Budgeting sinks and sources of CO_2 in the coastal ocean: Diversity of ecosystems counts. Geophys. Res. Lett. 32. doi:10.1029/2005GL023053

Bricaud, A., Morel, A., Prieur, L., 1981. Absorption by dissolved organic matter of the sea (yellow substance) in the UV and visible domains. Limnol. Oceanogr. 26, 43–53.

Cai, W.-J., Dai, M., Wang, Y., 2006. Air-sea exchange of carbon dioxide in ocean margins: A province-based synthesis. Geophys. Res. Lett. 33, L12603. doi:10.1029/2006GL026219

Cao, F., Fichot, C.G., Hooker, S.B., Miller, W.L., 2014. Improved algorithms for accurate retrieval of UV/visible diffuse attenuation coefficients in optically complex, inshore waters. Remote Sens. Environ. 144, 11–27. doi:10.1016/j.rse.2014.01.003

Carlson, C.A., 2002. Production and removal processes. In: Hansell, D.A., Carlson, C.A. (Eds.), Biogeochemistry of Marine Dissolved Organic Matter. Academic, San Diego, pp. 91–151.

Chen, C.-T.A., Huang, T.-H., Chen, Y.-C., Bai, Y., He, X., Kang, Y., 2013. Air–sea exchanges of CO_2 in the world's coastal seas. Biogeosciences 10, 6509–6544. doi:10.5194/bg-10-6509-2013

Chen, R.F., Gardner, G.B., 2004. High-resolution measurements of chromophoric dissolved organic matter in the Mississippi and Atchafalaya River plume regions, in: Marine Chemistry. pp. 103–125. doi:10.1016/j.marchem.2004.02.026

Chen, Y., Hu, C., Hu, X., Qu, J., 2009. Indirect Photodegradation of Amine Drugs in Aqueous Solution under Simulated Sunlight. Environ. Sci. Technol. 43, 2760–2765. doi:10.1021/es803325j

Clark, C.D., De Bruyn, W.J., Jakubowski, S.D., Grant, S.B., 2008. Hydrogen peroxide production in marine bathing waters: Implications for fecal indicator bacteria mortality. Mar. Pollut. Bull. 56, 397–401. doi:10.1016/j.marpolbul.2007.10.017

Clark, C.D., De Bruyn, W.J., Jones, J.G., 2009. Photochemical production of hydrogen peroxide in size-fractionated Southern California coastal waters. Chemosphere 76, 141–146. doi:10.1016/j.chemosphere.2009.01.076

Conmy, R.N., Coble, P.G., Chen, R.F., Gardner, G.B., 2004. Optical properties of colored dissolved organic matter in the Northern Gulf of Mexico. Mar. Chem. 89, 127–144. doi:10.1016/j.marchem.2004.02.010

Cooper, W.J., Shao, C., Lean, D.R.S., Gordon, A.S., Scully, F.E., 1994. Factors affecting the distribution of H_2O_2 in surface waters. In: Baker, L.A., (Ed.), Advances in

Chemistry Series, 237, Environmental Chemistry of Lakes and Reservoirs. American Chemical Society, Washington, D.C., pp. 393–422.

D'Sa, E.J., Steward, R.G., Vodacek, A., Blough, N. V., Phinney, D., 1999. Determining optical absorption of colored dissolved organic matter in seawater with a liquid capillary waveguide. Limnol. Oceanogr. 44, 1142–1148. doi:10.4319/lo.1999.44.4.1142

Dalrymple, R.M., Carfagno, A.K., Sharpless, C.M., 2010. Correlations between dissolved organic matter optical properties and quantum yields of singlet oxygen and hydrogen peroxide. Environ. Sci. Technol. 44, 5824–5829. doi:10.1021/es101005u

de Boer, A.M., Sigman, D.M., Toggweiler, J.R., Russel, J.L., 2007. Effect of global ocean temperature change on deep ocean ventilation. Paleoceanography. 22, PA2210.

Del Vecchio, R., Blough, N. V, 2002. Photobleaching of chromophoric dissolved organic matter in natural waters: kinetics and modeling. Mar. Chem. 78, 231–253. doi:10.1016/S0304-4203(02)00036-1

Del Vecchio, R., Blough, N. V, 2004. Spatial and seasonal distribution of chromophoric dissolved organic matter and dissolved organic carbon in the Middle Atlantic Bight. Mar. Chem. 89, 169–187. doi:10.1016/j.marchem.2004.02.027

Dittmar, T., Whitehead, K., Minor, E.C., Koch, B.P., 2007. Tracing terrigenous dissolved organic matter and its photochemical decay in the ocean by using liquid chromatography/mass spectrometry. Mar. Chem. 107, 378–387. doi:10.1016/j.marchem.2007.04.006

Fichot, C.G., Benner, R., 2011. A novel method to estimate DOC concentrations from CDOM absorption coefficients in coastal waters. Geophys. Res. Lett. 38. doi:10.1029/2010GL046152

Fichot, C.G., Miller, W.L., 2010. An approach to quantify depth-resolved marine photochemical fluxes using remote sensing: Application to carbon monoxide (CO) photoproduction. Remote Sens. Environ. 114, 1363–1377. doi:10.1016/j.rse.2010.01.019

Fichot, C.G., Sathyendranath, S., Miller, W.L., 2008. Sea*UV* and SeaUV_C : Algorithms for the retrieval of UV/Visible diffuse attenuation coefficients from ocean color. Remote Sens. Environ. 112, 1584–1602. doi:10.1016/j.rse.2007.08.009

Gao, H., Zepp, R.G., 1998. Factors Influencing Photoreactions of Dissolved Organic Matter in a Coastal River of the Southeastern United States. Environ. Sci. Technol. 32, 2940–2946. doi:10.1021/es9803660

Gennings, C., Molot, L.A., Dillon, P.J., 2001. Enhanced photochemical loss of organic carbon in acidic waters. Biogeochemistry 52, 339–354.

Givens, R.S., Oettle, W.F., 1972. Mechanistic studies in organic photochemistry. VI. Photodecarboxylation of benzyl esters. J. Org. Chem. 37(26), 4325–4334.

Hales, B., Cai, W.-J., Mitchell, B.G., Sabine, C.L., Schofield, O. (Eds.), 2008. *North American Continental Margins: A synthesis and Planning Workshop*. Report of the North American Continental Margins Working Group for the U.S. Carbon Cycle Scientific Sterring Group and Interagency Working Group, U.S. Carbon Cycle Science Program, Washington, DC, 110 pp

Hansard, S.P., Easter, H.D., Voelker, B.M., 2011. Rapid reaction of nanomolar Mn(II) with superoxide radical in seawater and simulated freshwater. Environ. Sci. Technol. 45, 2811–2817. doi:10.1021/es104014s

Hansell, D.A., 2013. Recalcitrant dissolved organic carbon fractions. Ann. Rev. Mar. Sci. 5, 421–445. doi:10.1146/annurev-marine-120710-100757

Hansell, D.A., Carlson, C.A., 2013. Localized refractory dissolved organic carbon sinks in the deep ocean. Global Biogeochem. Cycles. 27, 705–710. doi:10.1002/gbc.20067

Hansell, D.A., Carlson, C.A., Repeta, D.J., Schlitzer, R., 2009. Dissolved Organic Matter in the Ocean: A Controversy Stimulates New Insights. Oceanography 22, 202–211. doi:doi.org/10.5670/oceanog.2009.109

Hansell, D.A., Carlson, C.A., Schlitzer, R., 2012. Net removal of major marine dissolved organic carbon fractions in the subsurface ocean. Global Biogeochem. Cycles. 26. doi:10.1029/2011GB004069

Heller, M.I., Croot, P.L., 2010a. Superoxide decay kinetics in the southern ocean. Environ. Sci. Technol. 44, 191–196. doi:10.1021/es901766r

Heller, M.I., Croot, P.L., 2010b. Kinetics of superoxide reactions with dissolved organic matter in tropical Atlantic surface waters near Cape Verde (TENATSO). J. Geophys. Res. 115, C12038. doi:10.1029/2009JC006021

Helms, J.R., Mao, J., Stubbins, A., Schmidt-Rohr, K., Spencer, R.G.M., Hernes, P.J., Mopper, K., 2014. Loss of optical and molecular indicators of terrigenous dissolved organic matter during long-term photobleaching. Aquat. Sci. 76, 353–373. doi:10.1007/s00027-014-0340-0

Helms, J.R., Stubbins, A., Perdue, E.M., Green, N.W., Chen, H., Mopper, K., 2013. Photochemical bleaching of oceanic dissolved organic matter and its effect on absorption spectral slope and fluorescence. Mar. Chem. 155, 81–91. doi:10.1016/j.marchem.2013.05.015

Helms, J.R., Stubbins, A., Ritchie, J.D., Minor, E.C., Kieber, D.J., Mopper, K., 2008. Absorption spectral slopes and slope ratios as indicators of molecular weight, source, and photobleaching of chromophoric dissolved organic matter. Limnol. Oceanogr. 53, 955–969. doi:10.4319/lo.2008.53.3.0955

Hoigné, J., Faust, B.C., Haag, W.R., Scully Jr., F.E., Zepp, R.G., 1984. Aquatic humic substances as sources and sinks of photochemically produced transient reactants. Adv. Chem. Series. 219, 363–381.

Hofmann, E.E., Cahill, B., Fennel, K., Friedrichs, M. a M., Hyde, K., Lee, C., Mannino, A., Najjar, R.G., O'Reilly, J.E., Wilkin, J., Xue, J., 2011. Modeling the dynamics of continental shelf carbon. Ann. Rev. Mar. Sci. 3, 93–122. doi:10.1146/annurev-marine-120709-142740

Johannessen, S.C., Miller, W.L., 2001. Quantum yield for the photochemical production of dissolved inorganic carbon in seawater. Mar. Chem. 76, 271–283. doi:10.1016/S0304-4203(01)00067-6

Kieber, D.J., Miller, G.W., Neale, P.J., Mopper, K., 2014. Wavelength and temperature-dependent apparent quantum yields for photochemical formation of hydrogen peroxide in seawater. Environ. Sci. Process. Impacts 16, 777–791. doi:10.1039/c4em00036f

Kieber, D.J., Peake, B.M., Scully, N.M. 2003. Reactive Oxygen Species in Aquatic Ecosystems. In: Helbling, E.V., Zagarese, H. (Eds.), UV Effects in Aquatic Organisms. Royal Chemistry Society. Cambridge, UK, pp. 251–288.

King, D.W., Cooper, W.J., Rusak, S.A., Peake, B.M., Kiddle, J.J., O'Sullivan, D.W., Melamed, M.L., Morgan, C.R., Theberge, S.M., 2007. Flow injection analysis of H2O2 in natural waters using acridinium ester chemiluminescence: method development and optimization using a kinetic model. Anal. Chem. 79, 4169–4176. doi:10.1021/ac062228w

Kirchman, D.L., Lancelot, C., Fasham, M., Legendre, L., Radach, G., Scott, M., 1993. Dissolved organic matter in biogeochemical models of the ocean. In: Evans, G.T., Fasham, M.J.R. (Eds.), Towards a Model of Ocean Biogeochemical Processes. Springer, Berlin, pp. 209–225.

Langford, C.H., Wingham, M., Sastri, V.S., 1973. Ligand photooxidation in copper(II) complexes of nitrilotriacetic acid. Environ. Sci. Technol. 7, 820–822.

Lechtenfeld, O.J., Kattner, G., Flerus, R., McCallister, S.L., Schmitt-Kopplin, P., Koch, B.P., 2014. Molecular transformation and degradation of refractory dissolved organic matter in the Atlantic and Southern Ocean. Geochim. Cosmochim. Acta 126, 321–337. doi:10.1016/j.gca.2013.11.009

Levy, H. II. 1971. Normal Atmosphere: Large Radical and Formaldehyde Concentrations Predicted. Science. 173: 141–143.

Lockhart Jr., H.B., Blakeley, R.V., 1975. Aerobic photodegradiation of Fe(III)-(Ethylenedinitrilo)tetraacetate (Ferric EDTA). Environ. Sci. Technol. 9, 1035–1038.

Miller, C.J., Rose, A.L., Waite, T.D., 2009. Impact of natural organic matter on H_2O_2-mediated oxidation of Fe(II) in a simulated freshwater system. Geochim. Cosmochim. Acta. 72, 2758–2768.

Miller, W.L., Zepp, R.G., 1995. Photochemical production of dissolved inorganic carbon from terrestrial organic matter: Significance to the oceanic organic carbon cycle. Geophys. Res. Lett. 22, 417–420. doi:10.1029/94GL03344

Millero, F.J. Sotolongo, S., 1989. The oxidation of Fe(II) with H_2O_2 in seawater. Geochim. Cosmochim. Acta. 53, 1867–1873.

Mobley, C.D., 1994. Light and Water: Radiative Transfer in Natural Waters. Academic, San Diego, 592 pp.

Moffett, J.W., Zika, R.G., 1987. Reaction kinetics of hydrogen peroxide with copper and iron in seawater. Environ. Sci. Technol. 21, 804–810. doi:10.1021/es00162a012

Moore, C., Farmer, C., Zika, R., 1993. Influence of the Orinoco River on Hydrogen Peroxide Distribution and Production in the Eastern Caribbean. J. Geophys. Res. 98, 2289–2298.

Mopper, K., Kieber, D.J., 2000. Marine photochemistry and its impact on carbon cycling. In: The effects of UV radiation in the marine environment. 10, 101–129.

Mopper, K., Kieber, D.J., 2002. Photochemistry and the Cycling of Carbon, Sulfur, Nitrogen and Phosphorus. In: Hansell, D.A., Carlson, C.A. (Eds.), Biogeochemistry of Marine Dissolved Organic Matter. Academic Press, San Diego, pp. 455–507.

Mopper, K., Stubbins, A., Ritchie, J.D., Bialk, H.M., Hatcher, P.G., 2007. Advanced Instrumental Approaches for Characterization of Marine Dissolved Organic Matter : Extraction Techniques , Mass Spectrometry, and Nuclear Magnetic Resonance Spectroscopy. Chem. Rev. 107, 419–442.

Mopper, K., Zhou, X., 1990. Hydroxyl radical photoproduction in the sea and its potential impact on marine processes. Science. 250, 661–664.

Mopper, K., Zhou, X., Kieber, R.J., Kieber, D.J., Sikorski, R.J., Jones, R.D., 1991. Photochemical degradation of dissolved organic carbon and its impact on the oceanic carbon cycle. Nature. 353, 60–62. doi:10.1038/353060a0

Moran, M.A., Sheldon, W.M., Zepp, R.G., 2000. Carbon loss and optical property changes during long-term photochemical and biological degradation of estuarine dissolved organic matter. Limnol. Oceanogr. 45, 1254–1264.

Moran, M.A., Zepp, R.G., 1997. Role of photoreactions in the formation of biologically compounds from dissolved organic matter. Limnol. Oceanogr. 42, 1307–1316.

Morris, J.J., Johnson, Z.I., Szul, M.J., Keller, M., Zinser, E.R., 2011. Dependence of the cyanobacterium Prochlorococcus on hydrogen peroxide scavenging microbes for growth at the ocean's surface. PLoS One 6, e16805. doi:10.1371/journal.pone.0016805

Nakagawa, F., Tsunogai, U., Gamo, T., Yoshida, N., 2004. Stable isotopic compositions and fractionations of carbon monoxide at coastal and open ocean stations in the Pacific. J. Geophys. Res. 109, C06016. doi:10.1029/2001JC001108

Nelson, N.B., Siegel, D.A., 2013. The global distribution and dynamics of chromophoric dissolved organic matter. Ann. Rev. Mar. Sci. 5, 447–476. doi:10.1146/annurev-marine-120710-100751

Nelson, N.B., Siegel, D.A., Carlson, C.A., Swan, C., Smethie, W.M., Khatiwala, S., 2007. Hydrography of chromophoric dissolved organic matter in the North Atlantic. Deep Sea Res. Part I Oceanogr. Res. Pap. 54, 710–731. doi:10.1016/j.dsr.2007.02.006

O'Sullivan, D.W., Neale, P.J., Coffin, R.B., Boyd, T.J., Osburn, C.L., 2005. Photochemical production of hydrogen peroxide and methylhydroperoxide in coastal waters. Mar. Chem. 97, 14–33. doi:10.1016/j.marchem.2005.04.003

Opsahl, P., Jones, J.W., Zepp, R.G., 2001. Photochemically-induced alteration of stable carbon isotope ratios ($\delta^{13}C$) in terrigenous dissolved organic carbon. Geophys. Res. Lett. 28, 2417–2420.

Opsahl, S., Benner, R., 1998. Photochemical reactivity of dissolved lignin in river and ocean waters. Limnol. Oceanogr. 43, 1297–1304. doi:10.4319/lo.1998.43.6.1297

Petasne, R.G., Zika, R.G., 1987. Fate of superoxide in coastal seawater. Nature. 325, 516–618.

Petasne, R.G., Zika, R.G., 1997. Hydrogen peroxide lifetimes in south Florida coastal and offshore waters. Mar. Chem. 56, 215–225. doi:10.1016/S0304-4203(96)00072-2

Rabalais, N.N., Turner, R.E., Wiseman, W.J., 2002. Gulf of Mexico Hypoxia, a.K.a. "the Dead Zone". Annu. Rev. Ecol. Syst. 33, 235–263. doi:10.1146/annurev.ecolsys.33.010802.150513

Reader, H.E., Miller, W.L., 2012. Variability of carbon monoxide and carbon dioxide apparent quantum yield spectra in three coastal estuaries of the South Atlantic Bight. Biogeosciences 9, 4279–4294. doi:10.5194/bg-9-4279-2012

Rochelle-Newall, E.J., Fisher, T.R., 2002. Production of chromophoric dissolved organic matter fluorescence in marine and estuarine environments : an investigation into the role of phytoplankton. Mar. Chem. 77, 7–21.

Romera-Castillo, C., Sarmento, H., Anton Alvarez-Salgado, X., Gasol, J.M., Marrase, C., 2010. Erratum: Production of chromophoric dissolved organic matter by marine phytoplankton. Limnol. Oceanogr. 55, 1466–1466. doi:10.4319/lo.2010.55.3.1466

Rose, A.L., Moffett, J.W., Waite, T.D., 2008. Determination of superoxide in seawater using 2-methyl-6-(4-methoxyphenyl)-3,7-dihydroimidazo[1,2-a]pyrazin-3(7*H*)-one chemiluminescence. Anal. Chem. 80, 1215–1227.

Rose, A.L., Waite, T.D., 2005. Reduction of organically complexed ferric iron by superoxide in a simulated natural water. Environ. Sci. Technol. 39, 2645–2650.

Rusak, S.A., Peake, B.M., Richard, L.E., Nodder, S.D., Cooper, W.J., 2011. Distributions of hydrogen peroxide and superoxide in seawater east of New Zealand. Mar. Chem. 127, 155–169. doi:10.1016/j.marchem.2011.08.005

Scully, N.M., Cooper, W.J., Tranvik, L.J., 2003. Photochemical effects on microbial activity in natural waters: the interaction of reactive oxygen species and dissolved organic matter. FEMS Microbiol. Ecol. 46, 353–357. doi:10.1016/S0168-6496(03)00198-3

Sexton, P.F., Norris, R.D., Wilson, P.A, Pälike, H., Westerhold, T., Röhl, U., Bolton, C.T., Gibbs, S., 2011. Eocene global warming events driven by ventilation of oceanic dissolved organic carbon. Nature 471, 349–52. doi:10.1038/nature09826

Shaked, Y., Harris, R., Klein-Kedem, N., 2010. Hydrogen peroxide photocycling in the Gulf of Aqaba, Red Sea. Environ. Sci. Technol. 44, 3238–3244.

Sharpless, C.M., Blough, N.V., 2014. The importance of charge-transfer interactions in determining chromophoric dissolved organic matter (CDOM) optical and photochemical properties. Environ. Sci. Process. Impacts. 16(4), 654–671. doi:10.1039/c3em00573a

Shen, Y., Fichot, C.G., Benner, R., 2012. Floodplain influence on dissolved organic matter composition and export from the Mississippi-Atchafalaya River system to the Gulf of Mexico. Limnol. Oceanogr. 57, 1149–1160. doi:10.4319/lo.2012.57.4.1149

Smith, S.V., Hollibaugh, J.T., 1993. Coastal metabolism and the oceanic organic carbon balance. Rev. Geophys. 31(1), 75–89.

Spencer, R.G.M., Stubbins, A., Hernes, P.J., Baker, A., Mopper, K., Aufdenkampe, A.K., Dyda, R.Y., Mwamba, V.L., Mangangu, A.M., Wabakanghanzi, J.N., Six, J., 2009. Photochemical degradation of dissolved organic matter and dissolved lignin phenols from the Congo River. J. Geophys. Res. 114, G03010. doi:10.1029/2009JG000968

Steinacher, M., Joos, F., Frolicher, T.L., Plattner, G.-K., Doney, S.C., 2009. Imminent ocean acidification in the Arctic projected with the NCAR global coupled carbon cycle-climate model. Geophys. Res. Lett. 6, 515–533.

Steinberg, D., Nelson, N., Carlson, C., Prusak, A., 2004. Production of chromophoric dissolved organic matter (CDOM) in the open ocean by zooplankton and the colonial cyanobacterium Trichodesmium spp. Mar. Ecol. Prog. Ser. 267, 45–56. doi:10.3354/meps267045

Stubbins, A., Law, C.S., Uher, G., Upstill-Goddard, R.C., 2011. Carbon monoxide apparent quantum yields and photoproduction in the Tyne estuary. Biogeosciences. 8, 703–713. doi:10.5194/bg-8-703-2011

Stubbins, A., Niggemann, J., Dittmar, T., 2012. Photo-lability of deep ocean dissolved black carbon. Biogeosciences. 9, 1661–1670. doi:10.5194/bg-9-1661-2012

Stubbins, A., Hubbard, V., Uher, G., Law, C.S., Upstill-Goddard, R.C., Aiken, G.R., Mopper, K., 2008. Relating carbon monoxide photoproduction to dissolved organic matter functionality. Environ. Sci. Technol. 42, 3271–3276.

Stubbins, A., Spencer, R.G.M., Chen, H., Hatcher, P.G., Mopper, K., Hernes, P.J., Mwamba, V.L., Mangangu, A.M., Wabakanghanzi, J.N., Six, J., 2010. Illuminated darkness: Molecular signatures of Congo River dissolved organic matter and its photochemical alteration as revealed by ultrahigh precision mass spectrometry. Limnol. Oceanogr. 55, 1467–1477. doi:10.4319/lo.2010.55.4.1467

Stubbins, A., Uher, G., Law, C.S., Mopper, K., Robinson, C., Upstill-Goddard, R.C., 2006. Open-ocean carbon monoxide photoproduction. Deep Sea Res. Part II Top. Stud. Oceanogr. 53, 1695–1705. doi:10.1016/j.dsr2.2006.05.011

Sulzberger, B., Durisch-Kaiser, E., 2009. Chemical characterization of dissolved organic matter (DOM): A prerequisite for understanding UV-induced changes of DOM absorption properties and bioavailability. Aquat. Sci. 71, 104–126. doi:10.1007/s00027-008-8082-5

Swan, C.M., Siegel, D.A., Nelson, N.B., Carlson, C.A., Nasir, E., 2009. Biogeochemical and hydrographic controls on chromophoric dissolved organic matter distribution in the Pacific Ocean. Deep. Res. Part I Oceanogr. Res. Pap. 56, 2175–2192. doi:10.1016/j.dsr.2009.09.002

Swinnerton, J.W., Linnenbom, V.J., Lamontagne, R.A. 1970. The Ocean: A Natural Source of Carbon Monoxide. Science. 167: 984–986.

Szymczak, R., Waite, T., 1988. Generation and decay of hydrogen peroxide in estuarine waters. Aust. J. Mar. Freshw. Res. 39, 289–299. doi:10.1071/MF9880289

Takahashi, T., Sutherland, S.C., Wanninkhof, R., Sweeney, C., Feely, R.A., Chipman, D.W., Hales, B., Friederich, G., Chavez, F., Sabine, C., Watson, A., Bakker, D.C.E., Schuster, U., Metzl, N., Yoshikawa-Inoue, H., Ishii, M., Midorikawa, T., Nojiri, Y., Körtzinger, A., Steinhoff, T., Hoppema, M., Olafsson, J., Arnarson, T.S., Tilbrook, B., Johannessen, T., Olsen, A., Bellerby, R., Wong, C.S., Delille, B., Bates, N.R., de Baar, H.J.W., 2009. Climatological mean and decadal change in surface ocean pCO2, and net sea–air CO2 flux over the global oceans. Deep Sea Res. Part II Top. Stud. Oceanogr. 56, 554–577. doi:10.1016/j.dsr2.2008.12.009

Twardowski, M.S., Boss, E., Sullivan, J.M., Donaghay, P.L., 2004. Modeling the spectral shape of absorption by chromophoric dissolved organic matter. Mar. Chem. 89, 69–88. doi:10.1016/j.marchem.2004.02.008

Valentine, R.L., Zepp, R., 1993. Formation of Carbon Monoxide from the Photodegradation of Terrestrial Dissolved Organic Carbon in Natural Waters. Environ. Sci. Technol. 27, 409–412.

Van Baalen, C., Marler, J.E. 1966. Occurrence of hydrogen peroxide in sea water. Nature. 211, 951.

Vermilyea, A.W., Dixon, T.C., Voelker, B.M., 2010. Use of $H_2{}^{18}O_2$ to measure absolute rates of dark H_2O_2 production in freshwater systems. Environ. Sci. Technol. 44, 3066–3072. doi:10.1021/es100209h

Voelker, B.M., Sedlak, D.L., 1995. Iron reduction by photoproduced superoxide in seawater. Mar. Chem. 50, 93–102.

Voelker, B.M., Sedlak, D.L., Zafiriou, O.C., 2000. Chemistry of Superoxide Radical in Seawater: Reactions with Organic Cu Complexes. Environ. Sci. Technol. 34, 1036–1042. doi:10.1021/es990545x

Voelker, B.M., Sulzberger, B., 1996. Effects of Fulvic Acid on Fe(II) Oxidation by Hydrogen Peroxide. Environ. Sci. Technol. 30, 1106–1114. doi:10.1021/es9502132

Walsh, J.J., Dieterie, D.A., 1994. CO_2 cycling in the coastal ocean. I – A numberical analysis of the southeastern Bering Sea with applications to the Chukchi Sea and the northern Gulf of Mexico. Progr. Oceanogr. 34(4), 335–392.

Walsh, J.J., Premuzic, E.T., Gaffney, J.S., Rowe, G.T., Harbottle, G., Stoenner, R. W., Balsam, W.L., Betzer, P.R., Macko,, S.A., 1985. Organic storage of CO_2 on the

continental slope off the Mid-Atlantic bight, the southeastern Bering Sea, and the Peru coast. Deep-Sea Res. 32, 853–883.

Wanninkhof, R., Park, G.-H., Takahashi, T., Sweeney, C., Feely, R., Nojiri, Y., Gruber, N., Doney, S.C., McKinley, G.A., Lenton, A., Le Quéré, C., Heinze, C., Schwinger, J., Graven, H., Khatiwala, S., 2013. Global ocean carbon uptake: magnitude, variability and trends. Biogeosciences 10, 1983–2000. doi:10.5194/bg-10-1983-2013

Weishaar, J.L., Aiken, G.R., Bergamaschi, B.A., Fram, M.S., Fujii, R., Mopper, K., 2003. Evaluation of specific ultraviolet absorbance as an indicator of the chemical composition and reactivity of dissolved organic carbon. Environ. Sci. Technol. 37, 4702–4708.

Wesslander, K., Hall, P., Hjalmarsson, S., Lefevre, D., Omstedt, A., Rutgersson, A., Sahlée, E., Tengberg, A., 2011. Observed carbon dioxide and oxygen dynamics in a Baltic Sea coastal region. J. Mar. Sys. 86(1-2), 1–9.

White, E.M., Kieber, D.J., Mopper, K., 2008. Determination of photochemically produced carbon dioxide in seawater. Limnol. Oceanogr. Methods. 6, 441–453. doi:10.4319/lom.2008.6.441

White, E.M., Kieber, D.J., Sherrard, J., Miller, W.L., Mopper, K., 2010. Carbon dioxide and carbon monoxide photoproduction quantum yields in the Delaware Estuary. Mar. Chem. 118, 11–21. doi:10.1016/j.marchem.2009.10.001

White, E.M., Vaughan, P.P., Zepp, R.G., 2003. Role of the photo-Fenton reaction in the production of hydroxyl radicals and photobleaching of colored dissolved organic matter in a coastal river of the southeastern United States. Aquat. Sci. - Res. Across Boundaries. 65, 402–414. doi:10.1007/s00027-003-0675-4

Wu, F.C., Mills, R.B., Cai, Y.R., Evans, R.D., Dillon, P.J., 2005. Photodegradation-induced changes in dissolved organic matter in acidic waters 1027, 1019–1027. doi:10.1139/F05-009

Wuttig, K., Heller, M.I., Croot, P.L., 2013. Pathways of superoxide (O_2^-) decay in the Eastern Tropical North Atlantic. Environ. Sci. Technol. 47, 10249–10256. doi:10.1021/es401658t

Xie, H., Andrews, S.S., Martin, W.R., Miller, J., Ziolkowski, L., Taylor, C.D., Zafiriou, O.C., 2002. Validated methods for sampling and headspace analysis of carbon monoxide in seawater. Mar. Chem. 77, 93–108. doi:10.1016/S0304-4203(01)00065-2

Xie, H., Bélanger, S., Demers, S., Vincent, W.F., Papakyriakou, T.N., 2009. Photobiogeochemical cycling of carbon monoxide in the southeastern Beaufort Sea

in spring and autumn. Limnol. Oceanogr. 54, 234–249. doi:10.4319/lo.2009.54.1.0234

Xie, H., Zafiriou, O.C., 2009. Evidence for significant photochemical production of carbon monoxide by particles in coastal and oligotrophic marine waters. Geophys. Res. Lett. 36, L23606. doi:10.1029/2009GL041158

Xie, H., Zafiriou, O.C., Cai, W.-J., Zepp, R.G., Wang, Y., 2004. Photooxidation and Its Effects on the Carboxyl Content of Dissolved Organic Matter in Two Coastal Rivers in the Southeastern United States. Environ. Sci. Technol. 38, 4113–4119. doi:10.1021/es035407t

Yamashita, Y., Tanoue, E., 2009. Basin scale distribution of chromophoric dissolved organic matter in the Pacific Ocean. Limnol. Oceanogr. 54, 598–609. doi:10.4319/lo.2009.54.2.0598

Yocis, B.H., Kieber, D.J., Mopper, K., 2000. Photochemical production of hydrogen peroxide in Antarctic Waters. Deep Sea Res. Part I Oceanogr. Res. Pap. 47, 1077–1099. doi:10.1016/S0967-0637(99)00095-3

Zafiriou, O.C., 1977. Marine Organic Photochemistry Previewed. Mar. Chem. 5, 497–522.

Zafiriou, O.C., 1990. Chemistry of superoxide ion-radical (O_2^-) in seawater. I . pK*a_{sw} (HOO) and uncatalyzed dismutation kinetics studied by pulse radiolysis. Mar. Chem. 30, 31–43.

Zafiriou, O.C., Andrews, S.S., Wang, W., 2003. Concordant estimates of oceanic carbon monoxide source and sink processes in the Pacific yield a balanced global "blue-water" CO budget. Global Biogeochem. Cycles 17. doi:10.1029/2001GB001638

Zafiriou, O.C., Hole, W., Joussot-dubien, J., Zepp, R.G., Zika, R.G., 1984. Photochemistry of Natural Waters. Environ. Sci. Technol. 18, 358–371.

Zafiriou, O.C., Xie, H., Nelson, N.B., Najjar, R.G., Wang, W., 2008. Diel carbon monoxide cycling in the upper Sargasso Sea near Bermuda at the onset of spring and in midsummer. Limnol. Oceanogr. 53, 835–850. doi:10.4319/lo.2008.53.2.0835

Zepp, R.G., 1988. Environmental photoprocesses involving natural organic matter. In: Frimmel, F.H., Christman, R.F. (Eds.), Humic substances and their role in the environment. Wiley, New York, pp. 192–214.

Zepp, R.G., Callaghan, T. V., Erickson III, D.J., 2003. Interactive effects of ozone depletion and climate change on biogeochemical cycles. Photochem. Photobiol. Sci. 2, 51–61. doi:10.1039/b211154n

Zepp, R.G., Faust, B.C., Hoigné, J., 1992. Hydroxyl Radical Formation in Aqueous Reactions (pH 3-8) of Iron(II) with Hydrogen Peroxide: The Photo-Fenton Reaction 26, 313–319.

Zhai,W., Dai, M., Cai, W-J., Wang, Y., Hong, H., 2004. The parial pressure of carbon dioxide and air-sea fluxes in the northern South China Sea in spring, summer, and autumn. Mar. Chem. 96(1-2), 87–97.

Zhang, Y., Del Vecchio, R., Blough, N.V., 2012. Investigating the mechanism of hydrogen peroxide photoproduction by humic substances. Environ. Sci. Technol. 46, 11836–11843. doi:10.1021/es3029582

Zhang, Y., Xie, H., Chen, G., 2006. Factors affecting the efficiency of carbon monoxide photoproduction in the St. Lawrence estuarine system (Canada). Environ. Sci. Technol. 40, 7771–7777. doi:10.1021/es0615268

Zika, R.G., 1981. Marine organic photochemistry. In: Duursman, E.K., Dawson, R. (Eds.), Marine organic chemistry: evolution, composition, interactions and chemistry of organic matter in seawater. Elsevier oceanography series, vol 31. Elsevier, Amsterdam, pp. 299–325.

Zika, R.G., Saltzman, E.S., Cooper, W.J., 1985. Hydrogen peroxide concentrations in the peru upwelling area. Mar. Chem. 17, 265–275.

Ziolkowski, L.A., Druffel, E.R.M., 2010. Aged black carbon identified in marine dissolved organic carbon. Geophys. Res. Lett. 37. doi:10.1029/2010GL043963

Ziolkowski, L.A., Miller, W.L., 2007. Variability of the apparent quantum efficiency of CO photoproduction in the Gulf of Maine and Northwest Atlantic. Mar. Chem. 105, 258–270. doi:10.1016/j.marchem.2007.02.004

Zuo, Y., Jones, R.D., 1997. Photochemistry of natural dissolved organic matter in lake and wetland waters—production of carbon monoxide. Water Res. 31(4), 850–858. doi:10.1016/S0043-1354(96)00316-8

CHAPTER 2

PHOTOCHEMICAL PRODUCTION OF CO AND CO_2 IN THE NORTHERN GULF OF MEXICO: ESTIMATES AND CHALLENGES FOR QUANTIFYING THE IMPACT OF PHOTOCHEMISTRY ON CARBON CYCLES[1]

[1]L.C. Powers and W.L. Miller. Submitted to *Marine Chemistry*, 9/9/14.

Abstract

The photochemical production of carbon dioxide (CO_2) and carbon monoxide (CO), derived from marine colored dissolved organic matter (CDOM), is considered a significant oceanic loss process for the large and variable fluxes of terrigenous dissolved organic carbon (DOC) in river dominated coastal systems. Using samples collected over 4 seasons (2009 – 2010) in a grid centered on the Mississippi-Atchafalaya River system in the Northern Gulf of Mexico, we attempt to improve constraints for these direct photochemical impacts on DOC cycles by contributing the largest coherent set of photochemical apparent quantum yield (AQY) spectra for CO to date (n = 99), 18 of which had CO_2 AQY spectra determined in the same sample for use in calculating CO_2:CO photoproduction ratios. Simple correlations, previously reported from much smaller data sets, between CO photoproduction and CDOM optical properties showed weak or no correlations within our much larger spatio-temporal study. However, grouping samples with an optical transition point ($a_g(320) = 1.3\ m^{-1}$) allowed definition of two distinct inshore and offshore CO AQY spectra. Inputting these in regional photochemical models that use remotely sensed ocean color data and modeled water optical properties dramatically improves results over using a single CO AQY spectrum (modeled vs. measured $r^2 = 0.73$ vs. 0.18 for single AQY) as has been done previously. Monthly average CO photoproduction rates ranged from 6.0 to 17.7 μmole $m^{-2}\ d^{-1}$, amounting to a conservative estimate of 3.35 Gg C yr^{-1} for our study region. With no accessible method for direct determination of CO_2 photoproduction in oligotrophic waters, CO_2 photoefficiency in the Gulf of Mexico was inferred by determining CO_2:CO ratios for use with CO photoproduction estimates. In agreement with previous studies,

CO_2:CO ratios determined here were also poorly constrained, ranging from ~6 to 66 providing a median value of 24.4. This approach estimates that direct photochemical production of CO_2 plus CO can remineralize DOC on the order of 85 Gg C each year. This estimate provides an improvement over the use of a single inshore CO_2 AQY spectrum for a largely blue water system but caution should be used when interpreting CO_2 photochemical flux estimates that rely heavily on the selection of CO AQY spectra and/or poorly constrained relationships between CO_2 and CO photoproduction. Our results stress that the continued expansion of the CO_2:CO ratio database to new oceanic regimes is likely of very limited value and that accessible direct methods or better proxies to quantify CO_2 photochemistry in clear marine waters are needed.

1. Introduction

Terrestrial dissolved organic carbon (DOC) transported to the coast via rivers is photoreactive (Kieber et al., 1990; Miller and Zepp, 1995) and many irradiation studies on a variety of riverine waters suggest that 31 – 45% of this DOC is lost during long term photochemical exposure (Moran et al., 2000; Spencer et al., 2009) Specifically, solar ultraviolet radiation (UVR; 280-400 nm) absorbed by chromophoric dissolved organic matter (CDOM) results in significant oxidation of DOC to form carbon dioxide (CO_2), carbon monoxide (CO), and a variety of low molecular weight organic molecules (Kieber et al., 1990; Miller and Zepp, 1995; Mopper and Kieber, 2002). In the marine environment, the largest identified DOC photoproduct is "CO_2" which is most often analyzed as dissolved inorganic carbon (DIC) (i.e. the sum of dissolved CO_2, HCO_3^-, and CO_3^{2-}) (Bélanger et al., 2006; Miller and Moran, 1997; Miller and Zepp, 1995; White et al., 2010). Analytical challenges inherent in measuring low μM photochemical

production of DIC in seawater containing ~2 mM DIC background concentrations results in almost all published CO_2 photochemical experiments removing DIC prior to irradiation of high CDOM coastal water to create measurable production. Consequently blue water CO_2 photoproduction rates are rare and very close to the analytical detection limit, making any large-scale estimates beyond nearshore environments speculative.

The second largest identifiable marine carbon photoproduct is CO, which also occupies a key position in oceanic carbon cycling (Zuo and Jones 1995), acting both as a direct DOC removal pathway and as a substrate for bacterial DOM mineralization (Moran and Zepp, 1997; Xie et al., 2009; Zafiriou et al., 2008). Due to the analytical sensitivity of well refined headspace equilibration methods (e.g. Xie et al., 2002) and the fact that irradiations require no sample pretreatment beyond filtering, CO has become the most extensively studied marine carbon photoproduct, with flux calculations published for samples ranging from highly turbid (Stubbins et al., 2011; White et al., 2010; Zhang et al., 2006) to coastal (Xie et al., 2009; Ziolkowski and Miller, 2007) and oligotrophic waters (Stubbins et al., 2006; Zafiriou et al., 2003; Ziolkowski and Miller, 2007). Despite the extensive work on CO photochemistry, most studies examine the efficiency of CO photoproduction by determining apparent quantum yield (AQY) spectra using far fewer than 20 samples in only one or two sampling seasons.

For CO, a correlation between salinity and its photochemical production has been demonstrated in a variety of coastal zones (Gao and Zepp, 1998, Reader and Miller, 2012; Stubbins et al., 2011; Xie et al., 2009; Zhang et al., 2006). However, Stubbins et al. (2011) demonstrated that a simple 2 component-mixing model could not be used to predict CO photoefficiency in the Tyne Estuary, demonstrating non-conservative CDOM

photoreactivity in terms of both the removal and addition of reactive and nonreactive CDOM in this coastal zone. Additionally, Reader and Miller (2012) found no correlation between CDOM normalized photoproduction of either CO_2 or CO and salinity in coastal estuaries of the South Atlantic Bight. They did observe, however, that there was a seasonal trend in CO photoproduction rates, with lower CO production efficiency in the spring and summer and higher CO production efficiency in the fall and winter. Considering the contradictory reports and dynamic nature of these estuarine systems, the spatiotemporal variability in both CO_2 and CO photoproduction rates in fresh water impacted coastal zones requires further evaluation.

A recent multi-season coastal study by Reader and Miller (2012) has provided a much larger temporal CO dataset, including 38 paired CO_2 and CO experiments that determine both production rates and the spectral efficiency, as AQY spectra, for both reactions. This attempt to constrain not only the seasonal variability of each photoproduct but to quantify the link between photochemical CO_2 and CO flux estimates builds on previous work that suggests the *total* direct photochemical loss term for marine DOC might be estimated using relationships to the well-studied and analytically accessible CO results (Miller and Zepp, 1995; Reader and Miller, 2012; White et al., 2010) and a robust CO2:CO ratio. Studies reporting CO_2:CO photoproduction ratios, however, have found a range from ~2 to >65 (Miller and Zepp, 1995; Johannessen 2000; White et al., 2010; Reader and Miller, 2012), suggesting that a single ratio is not appropriate for global or regional models of CO_2 photochemical fluxes. White et al. (2010), using only three ratios, explain some of this variability in CO_2:CO ratios noting correlations with AQY spectra and salinity in the Delaware Estuary. CO AQY spectra

decreased with increasing salinity while CO_2 AQY spectra remained unchanged, thus altering the ratio with salinity related changes in CO AQY spectra.

To provide better estimates for the photochemical impact on DOM turnover in river-dominated coastal margins, we have greatly expanded the database for CO and CO_2 photoproduction rates in the Northern Gulf of Mexico. Our focus on this area is based on isotopic and elemental data that indicate *in situ* production, bacterial utilization and photo-oxidation could all regulate the removal of DOC (Wang et al., 2004) in this region of large and variable terrigenous carbon fluxes (~3 Tg C yr^{-1} ; Bianchi et al., 2004; Shen et al., 2012). Collecting over 4 seasons, we have determined CO AQY spectra for 81 stations and CO_2:CO ratios using the photoproduction of both CO_2 and CO in 18 paired samples (99 total CO spectra) to assess the seasonal and spatial variability in AQY spectra appropriate for this region. Our initial goal was to link this CO variability to CO_2 photoproduction. The study reported here represents the largest coherent data set for CO AQY spectra gathered to date, thus allowing a comprehensive evaluation of trends in CO photoproduction in the Northern Gulf of Mexico. Based on these data, we optimized methods to estimate photochemical CO production from remotely sensed ocean color and modeled solar irradiances (Fichot and Miller, 2010). With associated CO_2 AQY spectra and their relationship to CO photoproduction, we estimated the average photochemical fluxes for both species and evaluate their overall role in carbon cycles for the Northern Gulf of Mexico.

2. Methods

2.1 Sampling

Surface water samples for photochemical experiments were collected in the Northern Gulf of Mexico as part of the GulfCarbon project on four separate 12 day research cruises onboard the R/V *Cape Hatteras* in April 2009, July 2009, and March 2010 and onboard the R/V *Sharp* in October/November 2009. 2 or 3 liters of water were collected and 0.2 μm filtered (Whatman Polycap 75 AS nylon membrane) directly from 12 L Niskin bottles into 1 L acid-cleaned (2 M HCl, J.T. Baker) ashed borosilicate glass bottles (Kimax) at 20 stations, with the exception of October/November 2009 when 21 samples were collected, for a total of 81 samples (Figure 2.1). All samples were stored at 4 °C in the dark until use for a period of up to one year. CDOM absorption spectra have been shown to exhibit no significant changes when stored in this manner for up to 12 months (Johannessen and Miller, 2001; Swan et al., 2012).

2.2 Laboratory Irradiations and Optical Measurements

All laboratory irradiation experiments were performed using a Suntest CPS solar simulator equipped with a 1.5 kW xenon lamp (Atlas), as detailed in Reader and Miller (2012). Each water sample was brought to room temperature and partitioned into 15 gas-tight 10 cm cylindrical quartz spectrophotometric cells, and sealed with no headspace using caps fitted with Teflon faced, butyl rubber septa (Microsolv) to minimize diffusion, particularly of CO_2, into the sample. The absorbance in each cell was measured from 250 – 800 nm with a dual beam UV-Vis spectrophotometer (Lambda 40; Perkin Elmer) both prior to and post irradiation. 18.0 MΩ Milli-Q water (Millipore) was used as the absorbance blank. For open ocean samples, absorbance was additionally measured in a 1-m pathlength liquid core waveguide (LWCC-2100 Type II; World Precision Instuments, Inc.) fitted with Premium grade Si fiber optics to a deuterium-

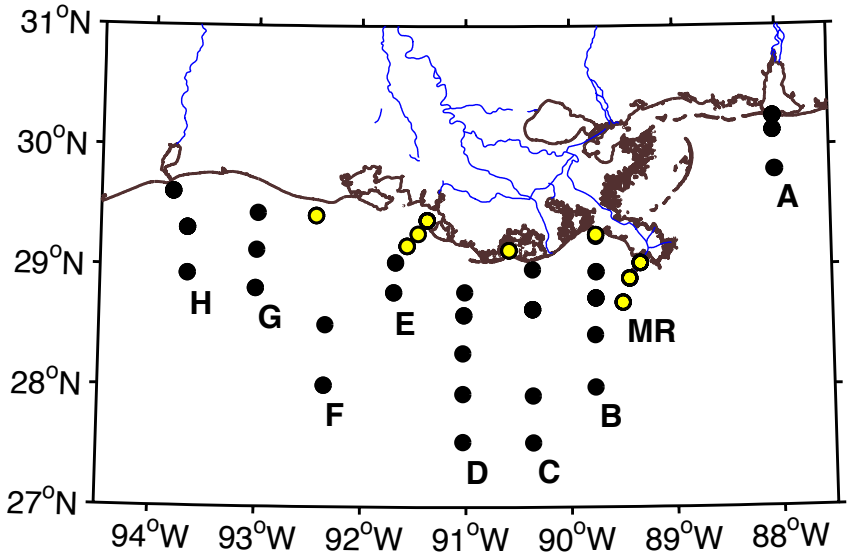

Figure 2.1. Sampling locations in the Northern Gulf of Mexico over 4 separate research cruises between 2009 – 2010, with stations used for both CO_2 and CO AQY spectra determination highlighted in yellow. For CO AQY spectra, 20 or 21 samples were collected each cruise with repeat occupation of 11 stations. Transects MR and E start in the mouth of the Mississippi and Atchafalaya Rivers, respectively.

tungsten light source (DT-Mini GS; Ocean Optics) and a MAYA2000 PRO spectrophotometer (Ocean Optics). Raw absorbance spectra were either fit over the 580 – 800 nm range (Lamda 40) or the 700 – 750 range (LWCC) using the MATLAB® nonlinear curve fitting routine, nlinfit to the equation:

$$A = Fe^{-S\lambda} + O \tag{2.1}$$

where A (unitless) is absorbance, F is a fitting coefficient, S is the spectral slope, and O is the offset (Reader and Miller, 2011). The offset, assumed to correct for scattering, refractive index differences between salt water and the pure water blank, and instrument drift, was subtracted from each spectrum. Absorbance was then converted to Napierian absorption coefficients ($a_g(\lambda)$; m^{-1}) with the equation:

$$a_g(\lambda) = \frac{\ln(10)A}{L} \tag{2.2}$$

over the 280 – 700 nm range, where L (m) is the pathlength of the spectrophotometric cell or capillary cell. Absorption spectra measured both before and after irradiation were averaged for each cell for calculation. Irradiations typically lasted 3 to 6 hours (CO) or 6 to >15 hours (CO_2), and CDOM absorption did not change significantly (≤15% loss in UV absorbance) during any irradiation period.

Spectrophotometric cells were placed vertically in a black water-cooled irradiation block below the solar simulator, which maintained the cells at 15 °C and allowed no transfer of light between samples. Each cell was aligned under a variety of evenly spaced Schott long-band-pass cutoff filters (280, 295, 305, 320, 380, 425, and 480 nm). The irradiation block holds 15 cells and included duplicates of each cutoff filter and one dark. Because CO_2 measurements (analysis described in Section 2.5 below) were

often indistinguishable from the dark under the 380, 425 and 480 nm cutoff filters, these treatments were occasionally omitted from CO_2 AQY determination (Section 2.6). For CO experiments, all cutoff treatments were included (n = 14 for each AQY curve determination). The spectral downwelling irradiance entering each cell, $E_0(\lambda)$ (mole photons m^{-2} s^{-1} nm^{-1}), was quantified on 1 nm intervals with a UV-Vis portable spectroradiometer (OL756; Optronic Laboratories) fitted with a fiber optic cable and integrating sphere, previously calibrated with a NIST standard lamp (OL752-10 irradiance standard; Optronic Laboratories). Photons absorbed by CDOM, $Q_a(\lambda)$ (mol), in each sample were calculated following the recommendations of Hu et al. (2002), correcting for self-shading in optically thick solutions via the equation:

$$Q_a(\lambda) = E_0(\lambda)S(1 - e^{-a_g(\lambda)L})t \quad (2.3)$$

where S (m^2) is the surface area of the irradiated cell, L (m) is the pathlength of the cell and t (s) is irradiation time.

2.3 Derived Optical Properties

Additionally, CDOM spectral slopes (S, nm^{-1}) were calculated from CDOM absorption spectra, prior to irradiation, via the equation

$$a_g(\lambda) = a_g(\lambda_{ref})e^{(-S(\lambda-\lambda_{ref}))} \quad (2.4)$$

where λ_{ref} is the reference wavelength (nm) (Twardowski et al., 2004). S values have been used as a proxy for bulk changes in CDOM characteristics, however, it also strongly depends on the wavelength range over which it is calculated (Helms et al., 2008; Twardowski et al., 2004). The slope values reported here are determined over the 290 – 490 nm range ($S_{290\text{-}490}$), for subsequent use in regional photochemical rate calculations (Equations 2.12 and 2.13, see Section 2.7). Furthermore, Helms et al. (2008) defined the

slope ratio (S_R) parameter by determining the ratio between S values over two distinct wavelength regions, 275 – 295 nm and 350 – 400 nm.

$$S_R = S_{275-295} / S_{350-400} \quad (2.5)$$

Because S_R is inversely related to DOM molecular weight, it also serves as an indicator of photochemically induced changes (Helms et al., 2008). Additionally, $S_{275\text{-}295}$ alone has been linked to % terrigenous DOC (Fichot and Benner, 2012) and photochemical and molecular weight changes in CDOM (Helms et al., 2008).

Aromatic content of DOM has been correlated to both $a_g(350)$ and CO photoproduction rates (Stubbins et al., 2008), as well as the specific UV absorbance at 254 nm ($SUVA_{254}$) (Weishaar et al., 2003). In order to determine whether this optical indicator of aromaticity could be used as a proxy for CO photoproduction rates and AQY spectra from our study, $SUVA_{254}$ (L mg^{-1} m^{-1}) was calculated with the following equation

$$\mathrm{SUVA}_{254} = \frac{a_g(254)}{[\mathrm{DOC}]} \quad (2.6)$$

where $a_g(254)$ is the sample absorption coefficient at 254 nm (m^{-1}) prior to irradiation and [DOC] is the concentration of DOC (mg C L^{-1}). [DOC] (μM) was estimated using the relationship between [DOC] and $S_{275\text{-}295}$ reported for our study region (Fichot and Benner, 2011). Using samples collected during the same field campaigns in the Northern Gulf of Mexico, Fichot and Benner (2011) demonstrated that [DOC] could be estimated with the following equations

$$\ln[\mathrm{DOC}] = 3.4704 + 1.8591 \ln[a_g(275)] - 1.2421 \ln[a_g(295)] \quad (2.7)$$

for samples with $a_g(275) \leq 3.5$ m^{-1} and

$$\ln[\mathrm{DOC}] = 2.9031 + 2.7703 \ln[a_g(275)] - 2.0400 \ln[a_g(295)] \quad (2.8)$$

for samples with $a_g(275) > 3.5\ m^{-1}$.

2.4 CO Analysis

CO production rates in each experiment (Table A1, Appendix A) were determined using a sensitive headspace equilibration method, explained in detail by Xie et al. (2002) and Ziolkowski and Miller (2007). Briefly, 13 to 15 mL of CO-free air (Schutze Reagent) were injected into the cell, removing the same volume of sample to equalize the pressure. The sample was then shaken for approximately two minutes to equilibrate it with the injected headspace. After an additional minute, the CO partitioned into the headspace was drawn into a 10 mL syringe without exposure to the atmosphere. CO in the headspace was measured with a gas chromatograph (GC; Trace Analytical RGA-3) equipped with a reduced gas analyzer. To adequately flush the GC sample loop (1 mL), only duplicate analysis of the same headspace was performed for each sample. To calculate CO produced photochemically in the entire sample, temperature, salinity, Bunsen solubility coefficients and headspace-to-water volume ratios were used with the equations of Wiesenburg and Guinasso (1979). For each experiment, the GC was calibrated with a 1 ppm primary standard (certified master class, Scott Specialty Gas, Air Liquide) and subsequent dilutions with CO-free air scrubbed with Schutze reagent (0 – 1 ppm, $r^2 > 0.98$). This method allows for the analysis of 8 to 12 samples/hr and the limit of the detection, defined as three times the standard deviation of the blank, was ~1 nM.

Photoproduced CO was measured for two types of samples for subsequent AQY determination. A CO AQY experiment was performed on each 0.2 μm filtered and otherwise unamended sample collected over the four field campaigns (n = 81 samples). 18 additional CO AQY spectra were determined for the same samples pretreated for CO_2

AQY experiments (Table A2). During DIC analysis, as each sample was injected into the TOC analyzer, an equivalent volume of CO-free air (scrubbed through a column of Schutze reagent) was drawn into the headspace. Post DIC analysis, additional CO-free air was added to the headspace as needed, and CO was analyzed as described above.

2.5 Sample Pretreatment and "CO_2" Analysis

For 18 inshore samples, photoproduced "CO_2" was measured as DIC using the methods of Johannessen and Miller (2001) and White et al. (2010) (Table A3). In contrast to CO analysis, additional sample pretreatment was required for CO_2 photoproduction measurements. DIC was stripped from the seawater matrix by transferring 0.2 μm filtered samples to a clean glass kettle and acidified to a pH of 2 – 3 with concentrated hydrochloric acid (J.T. Baker), thereby converting all DIC to dissolved CO_2. Samples were then bubbled with hydrated CO_2-free air passed through a soda lime column (indicating, ACS grade, Alfa Aesar) under positive pressure for 10 – 12 hours. DIC removal was confirmed by direct measurement of the sparged and acidified sample using a Shimadzu TOC-V total carbon analyzer run in DIC mode and calibrated with sodium carbonate and bicarbonate standards in Milli-Q water (0 – 250 or 500 μg L^{-1} DIC; r^2 = 0.98 to >0.99). Post sparging, samples were buffered back to their original pH with sodium borate (ACS, Fisher) and immediately transferred to 10 cm spectrophotometer cells and sealed. Although the sample remained under positive pressure, the rebuffering process and filling time required to transfer the sample to individual cells caused slight CO_2 increases in the sample (generally < 1 μM), perhaps from room air or from carbonate in commercially available sodium borate (White et al., 2008). To minimize CO_2 contamination by microbial respiration, all glassware, septa and fittings were UVC-

sterilized in a laminar flow PCR hood (Misonix). Again, because this acidification-rebuffering process could irreversibly alter DOM (White et al., 2008), potentially influencing the photochemical reactivity of the sample, CO photoproduction rates were determined for both pretreated samples and those left unamended as detailed in the previous section.

2.6 Apparent Quantum Yield (AQY) Calculations

For each product (either CO_2 or CO), the production rate is equal to the product of the quantum yield ($\phi(\lambda)$) and the photon absorption rate, $Q_a(\lambda)$ (using CO_2 as an example):

$$\frac{d[CO_2]}{dt} = \phi(\lambda) Q_a(\lambda) \tag{2.9}$$

allowing for the determination of $\phi(\lambda)$. Because irradiations were polychromatic, the spectral quantum yield for each sample is modeled from the CO_2 or CO production rate and $Q_a(\lambda)$ with the following exponential equation (Johannessen and Miller, 2001; Miller and Reader, 2012; White et al., 2010; Ziolkowski and Miller, 2007):

$$\phi(\lambda) = e^{-(m_1 + m_2(\lambda - 290))} \tag{2.10}$$

The fitting parameter m_1 determines the y-intercept of the AQY curve while the fitting parameter m_2 determines its spectral slope coefficient. White et al. (2010) note that there are no chemical or physical mechanisms that would indicate *apriori* that these AQY spectra should be fit to an exponential equation. While these modeled exponential equations have adequately predicted observed photoproduction rates of CO_2 and CO (White et al., 2010), this approach may not provide the best fit of CO_2 or CO AQY spectra. Furthermore, most data sets using an exponential fit for AQY spectra were for

short term irradiations (4 – 8 hours for CO_2, Johannessen and Miller, 2001; Reader and Miller, 2012; White et al., 2010). For irradiation times between 24 and 46 hours, Belanger et al. (2006) employed a modified quasi-exponential function to fit their CO_2 photoproduction data:

$$\phi(\lambda) = k_1 e^{k_2/(\lambda+k_3)} \tag{2.11}$$

where k_1, k_2, and k_3 are fitting parameters. Therefore, we also used this approach to model CO_2 AQY spectra and investigate whether either model better represents the AQY data in our study. Specifically, because irradiations >12 h were required to produce measurable DIC for 8 of our 18 samples, we examined fitting results for short vs. long term irradiations. The fitting parameters (*m* and *k* values above) were again determined using the MATLAB® nonlinear curve fitting routine, *nlinfit*, iteratively finding the best fit to Equations 2.10 and 2.11.

2.7 Estimating Oceanic Photochemical Rates using Ocean Color

Fichot et al. (2008) published a set of algorithms (Sea*UV*/SeaUV_C) for retrieving diffuse attenuation coefficients ($K_d(\lambda)$; m^{-1}) from SeaWiFS remote-sensing reflectances ($R_{rs}(\lambda)$; sr^{-1}). Newly updated Sea*UV* algorithms (Cao et al., 2014) give an estimated relative error of ±16 – 18% at UV wavelengths based on comparison to *in situ* $K_d(\lambda)$ measurements. Fichot and Miller (2010) subsequently used the Sea*UV* model retrievals of $K_d(\lambda)$ with $a_g(\lambda)$ data to estimate global, depth-resolved photochemical fluxes of CO as a demonstration of the model's application. Our general methods for estimating the photochemical production rate of CO_2 and CO in the surface ocean from remotely sensed satellite data very closely follow the approach of Fichot and Miller (2010) for global estimates for CO photoproduction. For full details regarding application, assumptions,

and error analysis for retrieval of UV attenuation data from SeaWiFS imagery using the Sea*UV* algorithms and implementation of this optical data for photochemical calculations on global scales, the reader is referred to the original publications (Cao et al., 2014; Fichot and Miller, 2010; Fichot et al., 2008). We implemented the recently optimized composite Sea*UV* algorithm (Cao et al., 2014) and the "practical" model (section 2.1.2, equation (4), Fichot and Miller, 2010) with the published assumptions that the 290 – 490 nm spectral range captures photochemical activity, that upwelling scalar irradiance can be ignored, and that the attenuation of downwelling scalar irradiance can be described by $K_d(\lambda)$. Knowledge of $\phi(\lambda)$, $a_g(\lambda)$, and the *in situ* light field obtained from the downwelling scalar irradiance just below the surface ($E_{0d}(\lambda,0^-)$; mole photons m^{-2} s^{-1} nm^{-1}) and the average $K_d(\lambda)$ for the depth range in question, allows the photochemical production rate to be calculated for any depth (z; m) or depth interval. We therefore determined total CO_2 and CO photoproduction rates (P_{CO2} or P_{CO}; mol(CO_2 or CO) m^{-3} d^{-1}) with the equation:

$$P_{CO_2/CO} \approx \int_{290}^{490} E_{0d}(\lambda,0^-)e^{-K_d(\lambda)z}a_g(\lambda,z)\phi(\lambda,z)d\lambda \qquad (2.12)$$

The composite Sea*UV* algorithms (Cao et al., 2014) were used to retrieve $K_d(\lambda)$ at 320, 340, 380, 412, 443 and 490 nm from monthly climatologies for SeaWiFS $R_{rs}(\lambda)$ data (September 1997 – December 2010; Level-3, 9 x 9 km spatial resolution; http://oceancolor.gsfc.nasa.gov) to create monthly average $K_d(\lambda)$ climatologies for the Northern Gulf of Mexico. Spectrally resolved $K_d(\lambda)$ (320 – 490 nm) was determined with a cubic interpolation and extended into the UVB (290 – 320 nm) with a spectral slope coefficient determined between $K_d(320)$ and $K_d(340)$. Full $a_g(\lambda)$ spectra (290 – 490 nm) were calculated by first assuming an $a_g(320)/K_d(320)$ ratio of 0.68 (Fichot and Miller,

2010). Higher ratios of $a_g(\lambda)$ to $K_d(\lambda)$ have been reported in the UV (e.g. $a_g(323)/K_d(323)$ = 0.9 for coastal to offshore waters, n = 33; Johannessen et al., 2003), so this estimation should be considered somewhat conservative. A spectral slope coefficient, S_{ag}, of 0.0193 nm^{-1} for pixels with a $a_g(320) > 1.3$ m^{-1} or 0.0227 nm^{-1} for pixels with a $a_g(320) \leq 1.3$ were then used in the following equation (See Section 3.2 and Figure 2.6 for $a_g(320)$ (m^{-1}) transition point determination and Table 2.3 for optical properties for inshore, S_{ag} = 0.0193 nm^{-1}, and offshore, S_{ag} = 0.0227 nm^{-1}, samples):

$$a_g(\lambda) = a_g(320)e^{(-S_{a_g}(\lambda-320))} \tag{2.13}$$

To supply $E_{0d}(\lambda, 0^-)$ for the photochemical model, we started with modeled global clear-sky downwelling irradiance reaching the earth's surface from 280 to 700 nm at 1 nm intervals using the System for Transfer of Atmospheric Radiation (STAR) (Ruggaber et al., 1994). Model inputs included monthly average total ozone concentrations from the Total Ozone Mapping Spectrometer (TOMS) and oceanic values for aerosol, humidity, etc. as described in Fichot and Miller (2010) and a cloud correction for solar irradiance at the sea surface was obtained using monthly averaged TOMS UV reflectivities from 1996 to 2003. The final product from this model is a 7-year climatology for cloud-corrected, daily-integrated, downwelling scalar irradiance, $E_{0d}^{Day}(\lambda,0^-)$, at the sea surface for the 15th of each month. Following Equation 2.12, we combined STAR-modeled $E_{0d}^{Day}(\lambda,0^-)$ with $K_d(\lambda)$ retrieved with Sea*UV* and $a_g(\lambda)$ estimates. Assuming these optical properties do not vary over the temporal and spatial scales of the calculation, we mapped monthly climatologies for average daily photon absorption rates and used them in subsequent photochemical calculations.

3. Results and Discussion

3.1 Photochemical Efficiency Experiments

3.1.1 CO Apparent Quantum Yield Spectra

The apparent quantum yield spectra for CO determined here represent a large spatial range over multiple sampling seasons (n = 81, fitting parameters for Equation 10 are listed in Table A1, Appendix A) but remain in good agreement with published values, especially those for estuarine waters (Reader and Miller, 2012; Stubbins et al., 2011; White et al., 2010; Zhang et al. 2006; Figure 2.2 and Figure A1, Appendix A). Some of our quantum yield spectra determined in oligotrophic water (n = 21) are at the lower end of published values for offshore locations (Figure A1). Our CDOM absorbance spectra for these clear waters were measured using a 100 cm pathlength and this could lead to offsets in AQY calculations relative to comparative work. Zafiriou et al. (2003), Zhang et al. (2006) and Ziolkowski and Miller (2007) used 10 cm cells for CDOM data, even though values in the UVA/visible can near or reach detection limits for benchtop spectrophotometers (Hoge et al., 1993). Stubbins et al. (2006) used a 200 cm liquid capillary cell to overcome possible difficulties from detection limits, however, the "open ocean" CO AQY spectra for that study were calculated from relationships between CDOM and CO AQY spectra in riverine to coastal waters of the Tyne Estuary and the North Sea (Stubbins et al., 2011). Such a calculation may not be universally applicable and, in fact, their derived relationship does not hold when tested for our current Northern Gulf of Mexico data set (Figure A2). Therefore, differences in AQY spectra between our study and those used in current global estimates of CO photochemical fluxes (Fichot and Miller, 2010; Stubbins et al., 2006; Zafiriou et al., 2003) may reflect a larger issue of

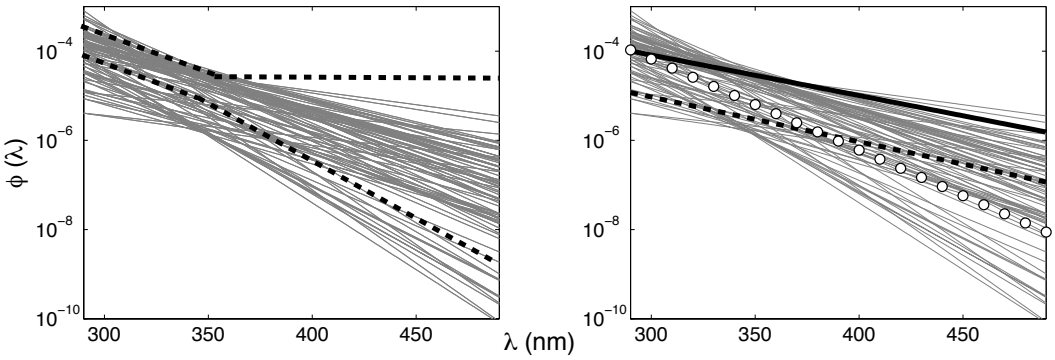

Figure 2.2. CO AQY ($\phi(\lambda)$) spectra (Left) for our study (grey lines) compared to a range of literature values (black dashed lines) reported for other marine studies (Reader and Miller, 2012; Stubbins et al., 2011; White et al., 2010; Zhang et al., 2006; Ziolkowski and Miller, 2007) and (Right) for our study (grey lines) with pooled spectra for the 3 groups identified from the 'average' AQY's (bold black lines). The open circles are the AQY spectral line for samples slightly over predicted by the average AQY spectrum, corresponding to those collected in or near the Mississippi River. The dashed line is the AQY spectrum for samples that were greatly over predicted by the average AQY spectrum, representing blue water samples. The solid line is the AQY fit to remaining samples under predicted by the average AQY spectrum.

differences in the accuracy of absorbance measurements (Reader and Miller, 2011).

Despite differences in offshore CO AQY spectra from those previously reported, all in-cell CO production predicted with AQY spectra match measured CO production in individual experiments with an overall r^2 of 0.97 (Figure 2.3A). As a first approach at defining a single CO AQY spectrum for use in photochemical flux models for this region, a pooled CO AQY spectrum was determined using all paired CO and photon absorbance data (n = 1134). This same approach adequately described CO photoproduction in samples ranging from the Gulf of Maine to the Sargasso Sea (Ziolkowski and Miller, 2007). Comparing our measured CO production data from Gulf of Mexico samples to that modeled with a single pooled AQY spectrum resulted in a bimodal distribution, with an r^2 between measured and modeled CO production of 0.18 (Figure 2.3B and Figure A3). This is a clear indication that a single AQY is a poor choice for photochemical models in this region. The wide range of water types represented in the Northern Gulf of Mexico, ranging from turbid inshore waters to oligotrophic waters sampled offshore, very likely explains this distribution.

To further examine patterns in the dataset for possible improvements in modeled CO photoproduction, CO AQY spectra were pooled for each sampling season. While Reader and Miller (2012) found no correlation between salinity and either CO_2 or CO photoproduction in the South Atlantic Bight, they did observe a seasonal trend in CO photoproduction rates, with lower CO AQY spectra in the spring and summer and higher CO AQY spectra in the fall and winter. Accordingly, we fit a single AQY spectrum to Equation 2.10 for data pooled for each of our sampling seasons (n = 280 for April 2009, July 2009, and March 2010 data sets and n = 294 for the October/November data set).

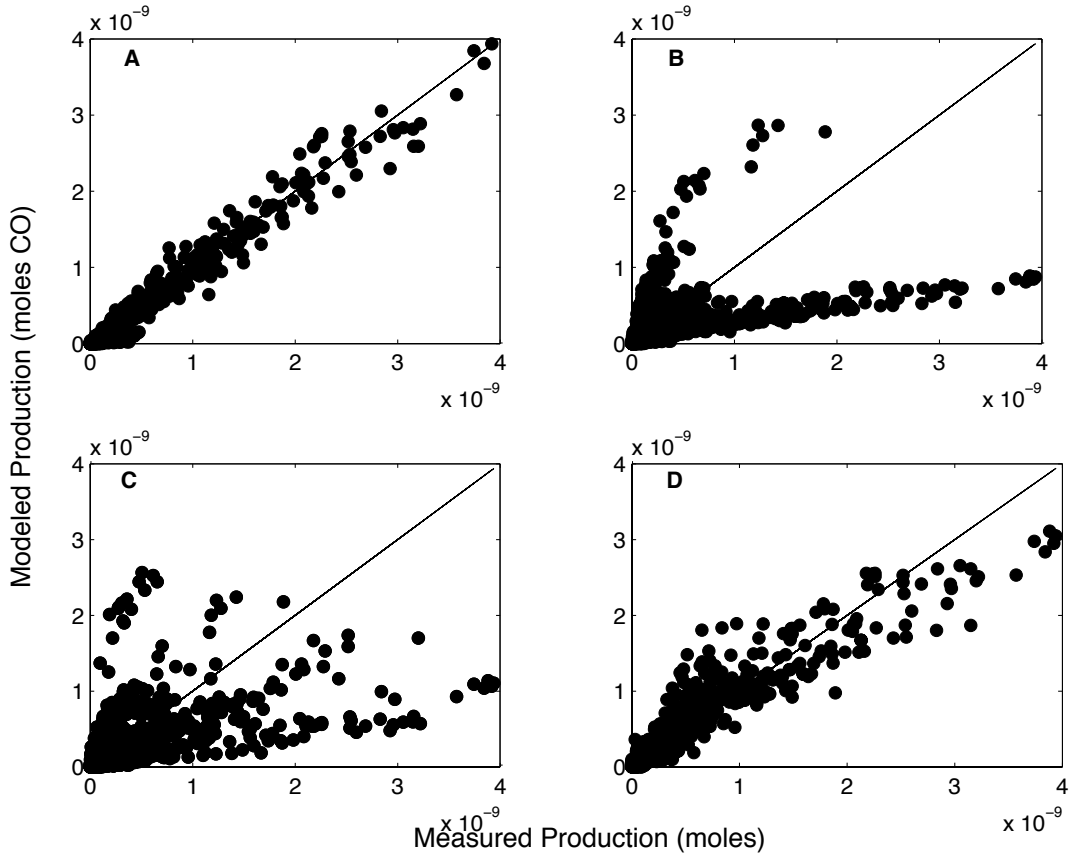

Figure 2.3. Ability of CO AQY spectra to predict experimental results. Modeled photoproduced CO vs. measured photoproduced CO (A) using individual CO AQY curves determined for each experiment (n = 14 for each AQY spectrum, overall r^2 = 0.97); (B) using a single CO AQY spectrum determined from all pooled data (n = 1134 for the pooled AQY spectrum, r^2 = 0.18); (C) using CO AQY spectra pooled for each sampling season (n = 280 for April 2009, July 2009, and March 2010, n = 294 for November 2009, overall r^2 = 0.28), and (D) using 3 separate AQY spectra highlighted in Figure 2.2. Note that calculated vs. measured production no longer shows a bimodal distribution and r^2 improves to 0.89.

The 95% confidence intervals overlap for all AQY fitting parameters determined by season (Table A4) and using a "seasonal" AQY spectrum to predict CO photoproduction provides little improvement over the "average" AQY spectrum for the entire data set (Figure 2.3C). Based on our large data set, it appears that the source of the observed CO AQY distributions are independent of sampling season.

3.1.2 CO_2 Apparent Quantum Yield Spectra

Apparent quantum yield spectra for CO_2 are shown in Figure 2.4A and their corresponding fitting parameters are listed in Table A3. The AQY curves determined here are in good agreement with marine AQY spectra for other inshore and estuarine waters (Reader and Miller 2012, White et al. 2010, Johannessen and Miller 2001; Figure 2.4A). The agreement between CO_2 production measured in each cell under each cutoff filter and that calculated from the AQY curve (Equation 2.10) was good for most samples ($r^2 > 0.8$; n = 14 samples), while others were not as well described by our exponential equation ($r^2 < 0.8$; n = 4 samples). Generally, the AQY spectrum was not well defined for samples collected in the mouth of either the Mississippi (Station MR1) or Atchafalaya (Station E0) Rivers. The quasi-exponential fit (Equation 2.11, e.g. Belanger et al., 2006) was also used to model the AQY spectrum, especially in order to compare our longer (~15 hours) irradiations to those of Belanger et al. (2006) (46 hours), and in some cases improved the agreement between measured and modeled production. However, the CO_2 AQY spectra for these 4 problematic samples were not well described by either equation (Table A3), likely due to errors caused by the difficulty in measuring the very low DIC concentrations produced under longer wavelength cutoff filters (i.e. 380, 425, 480 nm).

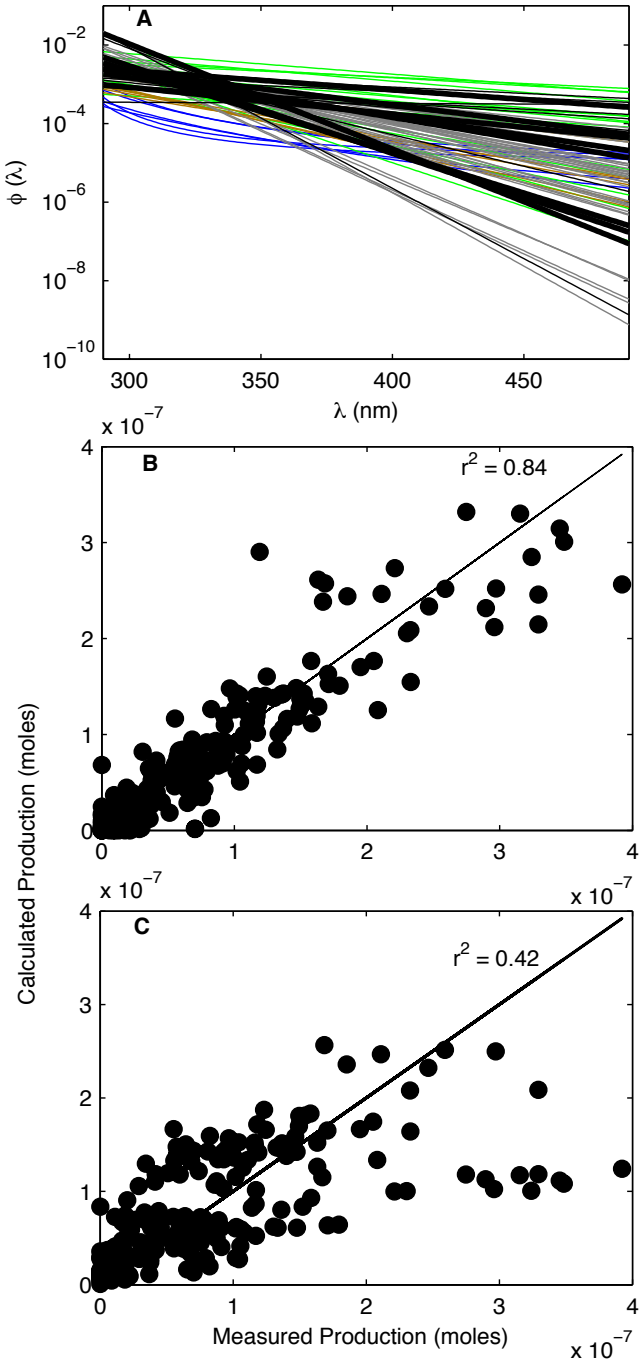

Figure 2.4. (A) CO_2 apparent quantum yield ($\phi(\lambda)$) spectra for our study (black lines, best fits are bold) compared to literature values: green lines - Johannessen and Miller (2001), gold lines - White et al. (2010), gray lines - Reader and Miller (2012), blue lines – Belanger et al. (2006). (B) Modeled DIC photoproduction from individual AQY curves vs. that measured ($r^2 = 0.84$) plotted against a 1:1 line, and (C) Modeled DIC photoproduction from a pooled CO_2 AQY spectrum vs. that measured ($r^2 = 0.43$) plotted against a 1:1 line.

In fact, measured DIC in cells under these cutoff filters was often indistinguishable from the dark controls.

3.1.3 Comparison of CO_2 Photoproduction Efficiency to Literature Values

For comparison of published CO_2 photoefficiency to that in our study region, simulated photoproduction rates (P_{DIC}; μM d^{-1}) were generated by using AQY spectra with "defined" incident spectral irradiance and an average CDOM absorption spectrum as shown in Equation 2.12. This isolates the comparison to only variability in AQY spectra. The calculation used $E_d(\lambda,0)$ (mole photons m^{-2} d^{-1}) estimated for mid-March at 29N and 91W using the STAR model (Ruggaber et al., 1994, as described in section 2.7) and an average $a_g(\lambda)$ (m^{-1}) spectrum from the 18 measured $a_g(\lambda)$ spectra used to determine our CO_2 AQY spectra. Poor AQY fit ($r^2 < 0.8$; n = 4), a flat AQY curve (m_2 values < 0.01; n = 2), and an altered CO AQY spectrum in joint CO/CO_2 experiments relative to their unamended counterpart (see Sect. 3.1.4 below; n = 5; 2 of which also showed poor CO_2 AQY fits) were used as criteria for exclusion from this calculation. In the 8 remaining samples, P_{DIC} ranged from 5.22 to 26.0 μM d^{-1} (median P_{DIC} = 9.87 ± 6.94 μM d^{-1}).

Though weakly correlated, both AQY spectra (Equations 2.10 and 2.11) and P_{DIC} were generally lower for low salinity (S < 5) samples (Figure 2.5). Similarly, Johannessen and Miller (2001) observed increased photoefficiency at higher salinity over an onshore-offshore transect. They explained this trend by suggesting that the aromatic structures in terrestrial carbon that dominate the CDOM signal, and thus the denominator of the AQY calculation, are lost due to photobleaching and/or an increase in marine-derived sources, leading to increased "apparent" efficiency of DIC photoproduction. On the other hand, White et al. (2010) found no correlation between salinity and the AQY

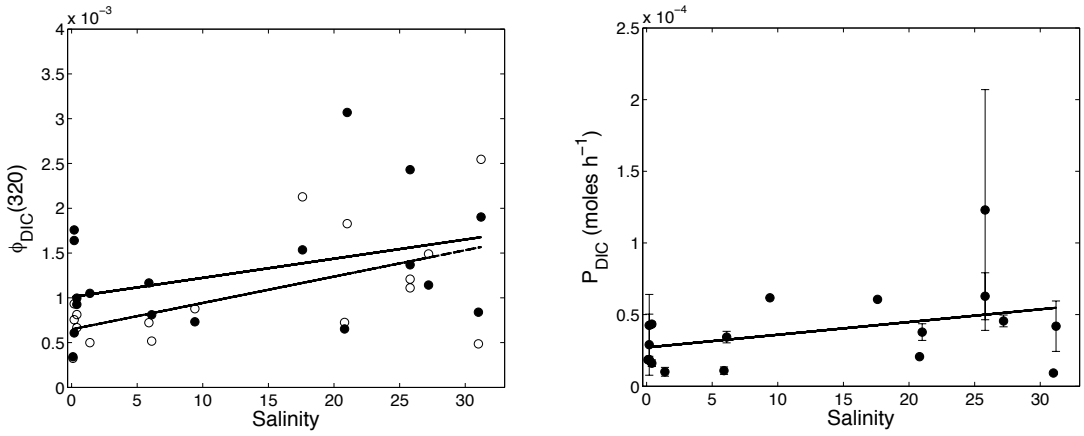

Figure 2.5. (Left) AQY for DIC photoproduction at 320 nm ($\phi_{DIC}(320)$) determined using Equation 10 (black circles) and Equation 11 (open circles) vs. sample salinity with their corresponding linear regressions (black and gray lines, respectively). (Right) In-cell DIC photoproduction rate (P_{DIC} (moles h^{-1})) under the 305 nm cutoff filter using Equation 10 vs. sample salinity.

spectrum for CO_2 in the estuarine waters of the Delaware Bay. Reader and Miller (2012) also observed no relationship between salinity and CO_2 photoproduction when rates were normalized to CDOM absorbance in a freshwater impacted area of the South Atlantic Bight. Because our AQY spectra results are representative of inshore and coastal waters, we cannot say with certainty whether or not a trend of increased photoefficiency with increased salinity is present in the Northern Gulf of Mexico.

While these P_{DIC} values are much lower than those determined with offshore AQY spectra (median P_{DIC} = 47.8 ± 11.7 μM d^{-1}, S > 35, Johannessen and Miller, 2001), they agree well with the median P_{DIC} values of 4.93 ± 1.48 and 16.03 ± 5.78 μM d^{-1} from inshore and coastal AQY spectra, respectively, for the Mid and North Atlantic Bight (Johannessen and Miller, 2001). They also compare favorably to a median P_{DIC} of 8.29 ± 3.75 μM d^{-1} for inshore AQY spectra of the South Atlantic Bight (Reader and Miller, 2012) (Figure A4). Our P_{DIC} values are also in good agreement with those determined for the Delaware River (P_{DIC} = 9.40 μM d^{-1}, White et al., 2010), but are higher than those determined using AQY spectra for the Delaware estuary (White et al., 2010) (median P_{DIC} = 2.69 ± 0.30 μM d^{-1}). P_{DIC} values calculated using AQY spectra determined in the Mackenzie River Estuary and the Amundsen Gulf (median P_{DIC} = 1.76 ± 0.52 μM d^{-1}, Belanger et al., 2006) are the lowest we found, perhaps reflecting the low CO_2 photoefficiency for these water samples. It is also possible that decreases in CO_2 photoefficiency occurred during the long (i.e. 25 – 46 hour) irradiations used in this study, thereby creating non-linear product accumulation and an underestimation of the initial AQY values. Similar decreases of CO_2 photoproduction with increasing irradiation time were first noted by Miller and Zepp (1995).

Despite the larger variability in P_{DIC} values determined for the Northern Gulf of Mexico when compared to those determined for the published values mentioned above, AQY curves from individual experiments do a good job of modeling measured production rates ($r^2 = 0.84$, Figure 2.4B). Because of a small sample size and with no clear difference in the AQY spectra between monthly samples of the river system and those collected inshore, we pooled the results from all DIC production experiments to determine a single CO_2 AQY spectrum describing the entire data set for possible use in regional photoproduction models. Fitting one AQY curve to all production data resulted in an unacceptable fit between modeled and measured production values ($r^2 = 0.41$, n = 197, Figure 2.4C). Consequently the use of this pooled CO_2 AQY spectrum in regional models of CO_2 photoproduction rates would be poorly constrained as well as biased by including data only from inshore waters.

3.1.4 Determination of CO_2:CO Ratios

An alternative approach to the use of average or pooled AQY spectra for direct estimation of regional and/or global CO_2 photoproduction might be to define a robust CO2:CO photoproduction ratio for use in the Northern Gulf of Mexico. For the 18 samples used for CO_2 AQY experiments, two matching sets of CO AQY spectra were also determined with differing pretreatments; one set unamended and one set acidified and rebuffered to match the CO_2 experimental treatment prior to irradiations (Table A2). This effort was to evaluate any potential change in CO photoreactivity from pretreatment since CO_2:CO ratios can, and have been determined using both scenarios (pretreated for both CO_2 and CO data, Miller and Zepp, 1995; pretreated CO_2 and unamended CO data, Reader and Miller, 2012; White et al., 2010).

Following pretreatment, CDOM spectra were very close to starting values ($a_g(320)$ <1 – 15% different) and each sample was returned close to its original pH (± 0.3 pH units). This is an essential step because decreased pH in fresh water has been reported to accelerate CDOM photoreactions and the loss of DOC (Anesio and Graneli, 2003; Gennings et al., 2001; Wu et al., 2005) as well as the photoproduction of DIC (Anesio and Graneli, 2003; Bertilsson and Tranvik, 2000). Conversely, Gao and Zepp (1998) observed that DIC photoproduction rates were higher when Satilla River samples were increased from a pH of 4 to 7 and Miller and Zepp (1995) observed little change in DIC photoproduction rates with varying pH of Mississippi River plume waters. Similar studies in marine waters are lacking. Observed effects may reflect the presence and speciation of metals, especially iron, since DIC photoproduction is reported to be faster with higher iron concentrations (Bertilsson and Tranvik, 2000; Gao and Zepp, 1998) and the pH effect observed by Gao and Zepp (1998) disappeared when iron was chelated with fluoride. Acidifying our samples to a pH ~2 and removing the carbonate system increases the solubility of inorganic Fe(III) (Byrne and Kester, 1976) and could release organically complexed iron, which may be slow to reequilibrate once the sample is rebuffered. Furthermore, White et al. (2008) noted that the acidification and rebuffering process could irreversibly alter the DOM with possible consequences for photochemical reactivity, including the precipitation of humic substances at low pH, loss of volatile organic compounds during sparging, and sample concentration caused by evaporation if sparging is done with dry air.

For unamended samples, CO measured under each cutoff filter agreed well with that modeled by Equation 2.10 ($r^2 = 0.87 – 0.99$ and $r^2 > 0.93$ for all but two samples).

For pretreated samples, the agreement between measured and modeled CO production was more variable ($r^2 = 0.71 – 0.98$). Taking care to minimize potential pretreatment effects discussed above, our data suggests that pretreatment has little effect on the majority of CO AQY spectra. For the few samples where differences in CO AQY spectra were indicated, pretreatment and/or longer irradiation times (~6 hrs for pretreated vs. ~3 hrs for unamended) could have altered DOC photoreactivity, metal speciation, or contaminated the sample (Table A2). The 5 cases where individual CO production values under the 305 nm cutoff filter for unamended samples differed from those for the pretreated samples were excluded from additional ratio calculations.

We calculated CO_2:CO photoproduction ratios in two ways; using measured production values under the 305 nm cutoff filter, which simulates sunlight reaching the surface ocean (Reader and Miller, 2012), and with simulated production from the AQY spectra (for CO_2 or CO) determined for the Northern Gulf of Mexico and Equation 2.12 with the same $E_d(\lambda, 0^-)$ and average $a_g(\lambda)$ spectra used in modeling P_{DIC} (Section 3.1.3). Because CO_2 production values under longer wavelength cutoff filters (380, 425, and 480 nm) were often indistinguishable from dark controls, confidence in AQY spectrum beyond 400 nm was low. Consequently, simulated production values and CO_2:CO ratios were only calculated over the 290 – 400 nm range. All data for CO_2 photoproduction necessarily come from pretreated samples, but ratios were determined using CO production values for both unamended and pretreated samples, as we know of no other study reporting this comparison (Table 2.1). Production ratios agreed with published values (Miller and Zepp, 1995; Reader and Miller, 2012; White et al., 2010) and like previous studies, had a large range. In general, ratios calculated from simulated DIC and

Table 2.1. CO_2:CO Production Ratios.

	Both samples pretreated				CO sample left unamended			
	Range	Ratio Mean	Ratio Median	Standard Deviation	Range	Ratio Mean	Ratio Median	Standard Deviation
In-cell production (305 nm cutoff)	6.13 – 66.1	19.3	12.4	17.4	6.99 – 53.7	29.2	24.4	17.3
Modeled production from AQY curves	4.22 – 16.3	8.67	8.67	3.52	7.54 – 47.8	22.2	11.2	15.8

CO production values (P_{DIC} and P_{CO}, respectively) were better constrained than those calculated from actual measured concentrations in samples irradiated under the 305 nm cutoff filter. Ratios calculated using unamended CO data were higher than those calculated with pretreated CO data.

White et al. (2010) reported a positive correlation between CO_2:CO ratios and salinity driven by CO_2 AQY spectra that did not change with salinity and AQY spectra for CO that decreased with increasing salinity. This relationship, however, used only three paired CO_2 and CO AQY experiments. Using a much larger data set (n = 38), Reader and Miller (2012) could not identify the same AQY trend in estuarine waters along the South Atlantic Bight, but did find riverine ratios to be slightly lower than those in the estuary. For our Gulf of Mexico data, there was also no correlation between CO_2 or CO photoproduction and salinity (Figure 2.5, CO data not shown), supporting the view that a simple salinity relationship cannot be used to further constrain this ratio. As shown in earlier work (Miller and Zepp, 1995; White et al., 2008), exposure issues may account for at least some of the variability reported for CO_2:CO ratios since initial CO_2 photoproduction rates appear to be faster than those measured after prolonged exposure. This same trend has not been observed for CO photoproduction (Valentine and Zepp, 1993), potentially altering the ratio as a function of exposure time.

Based at least partially on the fact that both of these carbon photoproducts derive from CDOM and show a similar exponential decrease in photoefficiency with increasing wavelength, it has been tempting to define a single, robust CO_2:CO production ratio for use in prediction of CO_2 photoproducton rates from the more easily measured CO photochemistry. However, the large reported ranges for CO_2:CO photoproduction ratios

presented in the current study and in the studies listed above tend to support the contention that mechanisms involved in CO_2 and CO photochemistry may be quite different, likely involving both direct and indirect photosensitized reactions (Gao and Zepp, 1998; Pos et al., 1998), and may not have the same relationship to the total photon absorbance that serves as the denominator for the AQY equations, particularly after photochemical fading (Johannessen and Miller, 2001; Reader and Miller, 2012). Consequently, while these ratios currently provide our best constraints on CO_2 photoproduction for most of the ocean where direct CO_2 AQY data are lacking, it is increasingly apparent that a new proxy is needed for marine systems. Until new direct methods to quantify CO_2 photochemistry in clear waters are available, the continued expansion of the CO_2:CO ratio database to new oceanic regimes is likely of very limited value.

3.2 Linking CO Photoproduction to Optical Properties

CDOM absorbance and the derived optical properties discussed in section 2.3 (S, S_R, and $SUVA_{254}$) have all been suggested as indicators of DOM characteristics and as such, potential proxies for photochemical reactivity. We evaluated these optical indicators for correlations to our CO photochemical results using AQY values at specific wavelengths as well as normalized photoproduction rates (P_{CO}; nM d^{-1}) using Equation 2.12 with incident irradiance normalized to $E_d(\lambda, 0^-)$ (mole photons m^{-2} d^{-1}) for mid-March at 29°N and 91°W (STAR model; Ruggaber et al., 1994, as described in section 2.7) and an average $a_g(\lambda)$ (m^{-1}) spectrum from the 81 $a_g(\lambda)$ spectra of all samples used to determine CO AQY spectra (Figs. A2 and A5). Overall, correlations were either weak or nonexistent. This analysis did, however, reveal that the ability of CO AQY spectra to

predict photoproduced CO in our experimental containers was enhanced by pooling data according to CDOM absorbance. Each of these results is discussed in some detail below.

CDOM and salinity generally track together in estuaries (Bowers and Brett, 2008) but Grebel et al. (2009) reported that CDOM photobleaching rates were enhanced by ~40% in the presence of seawater concentrations of chloride and bromide ions. This may explains why Stubbins et al. (2011) found that a simple 2-component mixing model for salinity did not predict CO AQY spectra in the Tyne Estuary. They reported that the CDOM absorption coefficient at 412 nm ($a_g(412)$; m^{-1}) was a better proxy for CO AQY spectra than salinity. As noted previously, neither salinity nor CDOM were useful as photochemical proxies for inshore water along the Georgia coast (Reader and Miller, 2012) and the same was reported for transects from the Gulf of Maine to the Sargasso Sea (Ziolkowski and Miller, 2007). Because *all* of our $a_g(412)$ data fell below the lowest value for the Tyne Estuary study (i.e. < 5 m^{-1}), we also investigated this correlation using $a_g(320)$ which gives stronger absorbance and also represents the wavelength of maximum overlap between the CO AQY and photon absorption in natural waters (i.e. the peak of the CO action spectrum). Our data showed a positive, but weak, correlation between CO photoproduction (represented by $\phi_{CO}(300)$ and P_{CO}, Figure A5) and both $a_g(320)$ and $SUVA_{254}$ (r^2 values ranging from 0.15 – 0.30).

$SUVA_{254}$ has been shown to correlate with DOC aromaticity in a variety of natural waters (Weishaar et al., 2003) and was expected to have a positive correlation to our CO AQY spectra since the aromatic content of DOM has previously been shown to correlate with both $a_g(350)$ and CO photoproduction rates (Stubbins et al., 2008). While $SUVA_{254}$ does not necessarily provide information on the photochemical reactivity of DOC

(Weishaar et al., 2003), Zhang et al. (2006) have shown a relatively strong positive correlation between $SUVA_{254}$ and spectrally integrated CO efficiency values for 6 samples collected in the St. Lawrence Estuary. Our very weak relationships, however, are more similar to results from the more extensive study by Reader and Miller (2012) who found no correlation between CO photoproduction and $SUVA_{254}$ in 38 estuarine samples on the coast of Georgia.

Examination of $S_{R,}$ a proxy for DOM molecular weight and perhaps an indicator of photochemical history (Helms et al., 2008), revealed no relationship with the AQY for CO ($\phi_{CO}(300)$ or P_{CO}, Figure A5). This is not unexpected since CO photoproduction has not previously been linked to either of these properties. Because none of these optical properties provide robust correlations to our CO AQY spectra, it is clear that a basic linear relationship cannot be used for CO photoefficiency in our data set as has been done in other studies focused on much smaller spatial and temporal sample distribution (Stubbins et al., 2011; Zhang et al., 2006). Considering the large spatiotemporal scale of this study and the dynamic river-impacted environment that exhibits rapid turnover and varying source waters for CDOM (Chen and Gardner, 2004), it is perhaps not surprising that these very simple relationships to optical proxies do not exist.

Although the optical properties discussed above did not provide simple correlations for CO photoefficiency in our study area, we found that they could be used to broadly classify water types for improved grouping of data in the determination of CO AQY spectra appropriate for application to the entire study area. After pooling *all* photoproduction data in an effort to determine a single AQY spectrum to predict CO photoproduction (Figure 2.3B and Figure A3), the resulting predictions appear to be

partitioned into three groups across a primarily bimodal distribution. These groups were identified by comparing measured CO photoproduction (CO_{meas}) under the 305nm cutoff filter to that predicted using this "average" AQY curve (CO_{pred}). This evaluation, together with station location information, showed that generally the offshore oligotrophic samples were over-predicted ($CO_{pred} > 2\ CO_{meas}$), while inshore/coastal waters were under-predicted ($CO_{pred} < 0.5\ CO_{meas}$). Samples falling closer to the 1:1 line and between these distinctions were largely from samples strongly influenced by the Mississippi River and were partitioned into a group of their own (Figure A3, details in Appendix A). For each of these three groups, a pooled quantum yield spectrum was determined (Figure 2.2, right, and Table 2.2). Using this three-group approach, the agreement between modeled and measured r^2 improves to 0.89 compared to 0.18 using the single pooled AQY spectrum for the entire data set (Figure 2.3D). It is interesting that the Atchafalaya River end member, with significantly higher CDOM absorbance and DOC concentrations than the Mississippi (Chen and Gardner, 2004; Shen et al., 2012), did not generate an identifiable optical grouping. This likely reflects the Atchafalaya's exchange with coastal wetlands and swamp-bayou systems and/or *in situ* CDOM production which is more typical of the coastal/inshore waters of southern Louisiana than the Mississippi River which is constrained by levees (Chen and Garder, 2004; Shen et al., 2012) and integrates a much larger and very different drainage basin.

3.3 Selecting CO AQY Spectra for Application to Satellite Data

Our methods used to model photochemical rates with ocean color data, as described in Section 2.7, depend heavily on the selection of AQY spectra for the calculation. Accordingly, we have used our examination of different AQY pooling

Table 2.2. Characteristics (general water type, Salinity), optical properties ($S_{290\text{-}490}$, S_R, $a_g(320)$ and $SUVA_{254}$) and AQY fitting parameters (m_1 and m_2, Equation 10) for samples pooled according to their modeled CO production from an "average" AQY (see Fig. 3SI and Supporting Information for details), determined from pooling the entire CO and absorbed photons dataset. Data falls according to a bimodal distribution, with samples either greatly over predicted (CO_{pred}:CO_{meas} > 2.0), well predicted (CO_{pred}:CO_{meas} ~ 1), or under predicted (CO_{pred}:CO_{meas} < 0.5) by the "average" AQY. Values reported here are the median values with standard deviations of each parameter for a given group.

Water type	Salinity	$S_{290\text{-}490}$ (nm^{-1})	S_R	$a_g(320)$ (m^{-1})	$SUVA_{254}$ ($L\ mg^{-1}\ m^{-1}$)	m_1	m_2	r^2
Offshore samples (CO_{pred}:CO_{meas} > 2, n = 294)	33.6 ± 2.3	0.0227 ± 0.0026	1.25 ± 0.47	0.66 ± 0.37	2.77 ± 0.48	11.348 ± 0.317	0.023 ± 0.005	0.80
Inshore/MR River (CO_{pred}:CO_{meas} ~ 1, n = 154)	9.0 ± 10.3	0.0184 ± 0.0007	0.93 ± 0.09	6.49 ± 3.17	6.02 ± 0.94	9.149 ± 0.317	0.047 ± 0.008	0.90
Inshore/Coastal[a] (CO_{pred}:CO_{meas} < 0.5, n = 686)	26.3 ± 8.5	0.0193 ± 0.0029	0.97± 0.24	3.18 ± 3.49	4.68 ± 1.27	9.203 ± 0.170	0.021 ± 0.003	0.88

[a] Sample Oct/Nov E0, with an $a_g(320)$ > 25, was excluded from pooled curve fitting.

options (as discussed above) to guide selection of CO quantum yield spectra for the Northern Gulf of Mexico that will optimize the accuracy of our photochemical estimates. Unfortunately, current satellite algorithms provide simple optical properties ($K_d(\lambda)$ and $a_g(\lambda)$) that cannot distinguish waters impacted by the Mississippi outflow from those for other inshore/coastal waters of the Northern Gulf of Mexico due to overlapping optical qualities (Table 2.2). Consequently, we have focused on determining a simple optical indicator for use in assigning either our offshore or inshore AQY spectrum to a given water type (i.e. pixel) for use in satellite based photochemical rate calculations. In other words, for the waters of the Northern Gulf of Mexico, we have determined a transition point between open ocean samples and inshore samples based on satellite derived $a_g(320)$, resulting in selection of either the offshore AQY spectrum,

$$\phi(\lambda) = e^{-(11.348+0.023(\lambda-290))} \tag{2.13}$$

or the inshore spectrum,

$$\phi(\lambda) = e^{-(9.203+0.021(\lambda-290))} \tag{2.14}$$

based on the rationale discussed in Section 3.2 above.

To determine the best $a_g(320)$ transition point for our entire Gulf of Mexico data set, we systematically evaluated the r^2 between measured and modeled CO photoproduction for transition values between 0.8 and 2.5 m^{-1} over 0.1 m^{-1} increments. Figure 2.6 shows best fit results of this analysis as different transition points are selected. Using our entire data set, Equation 2.13 is used for samples with $a_g(320)$ less than the transition point and Equation 2.14 is used for those above it. As the $a_g(320)$ transition point is increased, r^2 values decrease for the samples modeled with Equation 2.13 while

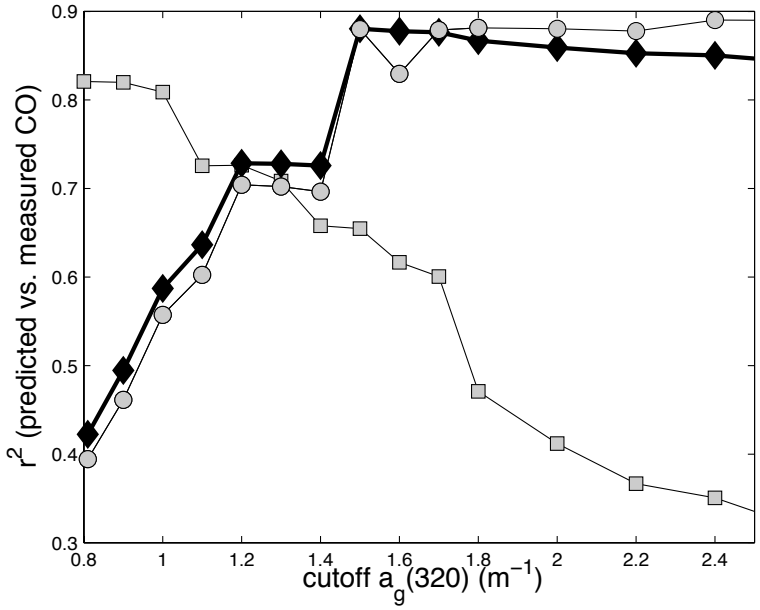

Figure 2.6. The r^2 values for CO photoproduction measured in each experiment vs. that predicted by the AQY spectrum selected using the $a_g(320)$ (m^{-1}) transition point. Samples with $a_g(320)$ (m^{-1}) values less than the transition point are fit to Equation (12) (gray squares) and those with $a_g(320)$ (m^{-1}) values greater than the transition point are fit to Equation (13) (gray circles). The r^2 values for all samples using these two AQY spectra together is shown with black diamonds.

samples modeled with Equation 2.14 showed increasing r^2 values, with the two fits intersecting at $a_g(320)$ =1.3 m^{-1}. Raising the transition point above this value slightly improves the overall fit between measured and modeled CO production but the fit for the more UV transparent waters (those samples less than the transition value) decreases rapidly with an increasing $a_g(320)$ transition point. This reflects the inclusion of samples with $a_g(320)$ values that are simply not representative of blue water (Figure 2.6). Therefore, while the overall fit is best at a transition point of $a_g(320)$ = 1.5 m^{-1}, the intersection point (1.3 m^{-1}) was selected as the $a_g(320)$ (m^{-1}) transition point for use in photochemical flux estimates for this region. This lower value is closer to reported surface open ocean CDOM absorption coefficients that are often much lower in the Pacific Ocean ($a_g(325) < 0.1$ to ~0.2 m^{-1} in the Swan et al., 2009) and the Atlantic Ocean ($a_g(325) < 0.1$ m^{-1} in the Sargasso Sea to ~0.7 m^{-1} along the continental shelves of the North Atlantic, Nelson et al., 2007). Because our "offshore" samples are on the continental shelf, it is not surprising that our CDOM absorption coefficients are somewhat higher (offshore $a_g(320)$ ~0.1 – 1.4 m^{-1}) owing to terrestrial influences here (Siegel et al., 2002). Combining both Equation 2.12 and either Equation 2.13 or 2.14, depending on the sample's $a_g(320)$ transition assignment, CO photochemical rates in our study area were calculated using the appropriate modifications to Equation 2.12 for "offshore" CO photoproduction

$$P_{CO} \approx \int_{290}^{490} E_{0d}(\lambda,0^-)a_g(320,z)e^{-(K_d(\lambda)z+0.0457\lambda+25.282)}d\lambda \qquad (2.15)$$

or "inshore" CO photoproduction

$$P_{CO} \approx \int_{290}^{490} E_{0d}(\lambda,0^-)a_g(320,z)e^{-(K_d(\lambda)z+0.0403\lambda+21.469)}d\lambda \qquad (2.16)$$

3.4 Regional CO Photochemical Flux Estimates from Ocean Color

Maps of regional monthly climatologies for depth-integrated CO photoproduction rates were calculated for the sunlit layer as described above and in Section 2.7. These estimates were made for the area of 27.5 to 31.0 N latitude and 94.5 to 87.0 W longitude, which represents an area covering all stations sampled for CO AQY experiments (Figure 2.1). Estimated CO photoproduction rates over this area had a yearly average of ~12.3 μmole m^{-2} d^{-1} and ranged from 3.56 to 151 μmole m^{-2} d^{-1} (Table 2.3). Photoproduction rates were highest from April - June, a period coincident with peak DOC export from the Mississippi-Atchafalaya River system (1996 – 2010; Shen et al. 2012). The range of monthly average CO photoproduction rate estimates for our study region (6.00 – 17.7 μmole m^{-2} d^{-1}, Table 2.3) is somewhat lower than modeled rates made for the St. Lawrence Estuary and Northwestern Gulf of St. Lawrence, which ranged from 10.63 to 70.86 μmole m^{-2} d^{-1} (Zhang and Xie, 2012). Their calculations used a larger wavelength range (280 – 600 nm) and assumed that CDOM and particles were equally photoefficient for CO photoproduction. Therefore UV absorption would be greater and CO photochemistry was considerably enhanced in these estimates. Based on ratios of CDOM to particulate absorption, Zhang and Xie (2012) estimated that 80% of CO photoproduction is due to CDOM and 20% is due to particles in their study region. Reducing their estimates by 20% for comparison to CO photoproduction rates by CDOM alone gives 8.50 to 56.7 μmole m^{-2} d^{-1}. Our maximum monthly CO production estimates ranged from 60.4 to 151 μmole m^{-2} d^{-1} (Table 2.3), which generally reflects our inshore samples and are higher than the estimates of Zhang and Xie (2012) for the upper St. Lawerence Estuary (22.86 to 70.86 μmole m^{-2} d^{-1}), but are still in good agreement

Table 2.3. Monthly average, maximum and minimum depth-integrated CO photoproduction rates (μmole m^{-2} d^{-1}) calculated for the sunlit layer using 2 AQY spectra for the Northern Gulf of Mexico.

	Jan	Feb	Mar	Apr	May	Jun	Jul	Aug	Sep	Oct	Nov	Dec
Avg	7.39	10.0	15.3	17.7	17.6	16.9	13.5	13.7	12.4	10.1	7.29	6.00
Max	60.3	82.3	115	151	91.3	86.1	114	79.2	73.0	63.0	79.0	62.8
Min	3.84	5.11	6.65	8.13	9.08	8.48	7.90	7.83	6.69	5.88	4.40	3.56

considering the lower incident solar irradiance in the Gulf of St. Lawrence. For comparison to CO photoproduction rates from a more temperate system, modeled CO photoproduction rates by Reader and Miller (2012) averaged 43.2 μmole m^{-2} d^{-1} for inshore waters of the South Atlantic Bight. This is again higher than our average CO photoproduction rate of 12.3 μmole m^{-2} d^{-1} but is not surprising considering the larger range of water types we sampled in the Northern Gulf of Mexico compared to the dark inshore waters sampled along the Georgia coast.

Even though there are many potential errors associated with retrieving seawater optical properties from remote sensing data, Fichot and Miller (2010) demonstrated that the Sea*UV* algorithms (Cao et al., 2014; Fichot et al., 2008) provide a relatively good approximation of UV-visible photon absorption rates. As noted in Fichot and Miller (2010) and demonstrated here (Figure A6), the use of a single AQY spectrum in estimating photochemical production rates does not capture the underlying processes controlling the known variability in either CO_2 or CO AQY spectra. Integrated water column photochemical rates calculated with a single pooled CO AQY spectrum only track photon absorption rates over the year and show a much smaller production range. By partitioning the study region into two distinct AQY domains based on changes in the surface water $a_g(\lambda)$, estimated rates no longer entirely track with CDOM absorption of solar radiation and show more of the variability expected in a river-dominated coastal system (Figure 2.7).

Although estimates made using two CO AQY spectra appear to give temporal changes more representative of the dynamic nature of the Northern Gulf of Mexico, they

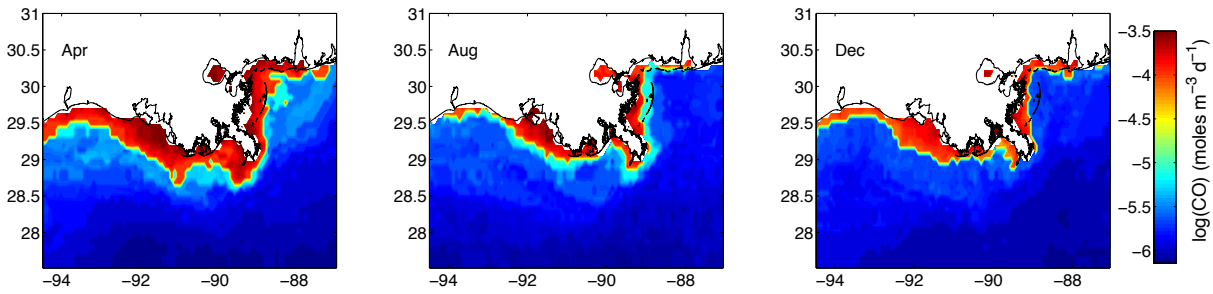

Figure 2.7. Modeled CO photoproduction rates (moles m^{-3} d^{-1}) using two AQY spectra for CO, determined for the top meter (April, August, and December climatologies are shown to demonstrate the varying influence of the river system).

are still heavily dependent on the selection of these two AQY spectra and the $a_g(320)$ transition point chosen to distinguish between inshore/coastal waters and clear waters offshore. Current open ocean estimates are in general agreement that the global CO photoproduction rate is about 40 to 50 Tg C yr^{-1} (Fichot and Miller, 2010; Stubbins et al., 2006; Zafiriou et al., 2003). If we exclude the surface area of the shelf seas and assume they represent 7.5% of the global ocean surface area (Wollast, 2003), this amounts to an areal photoproduction rate of 27.4 – 34.2 μmole m^{-2} d^{-1} for the open ocean. While at the lower end of our large range of production values, it is surprisingly larger than our average CO photoproduction rate for the Northern Gulf of Mexico (12.3 μmole m^{-2} d^{-1}). This is perhaps due to the fact that the open ocean AQY spectra determined here are lower than those previously reported (Stubbins et al., 2006; Zafirou et al., 2003; Ziolkowski and Miller, 2007). The pooled offshore AQY spectrum (Equation 2.13) is ~10 times lower than these published quantum yields at 290 nm and 2.5 – 4 times lower than these quantum yields at 350 nm. Even our study's pooled AQY spectrum, determined from all experimental data, is 2 – 5 times lower than other published open ocean AQY spectra at 290 nm but agrees well at 350 nm. Despite the body of work on CO AQY spectra in virtually all marine water types, the discrepancies here again stress that the variability in these spectra is poorly constrained when examined on large spatial and temporal scales.

Some issues may derive from characterizing the CDOM values for oligotrophic waters. Because all CO AQY determinations rely on precise and accurate CDOM spectra, the use of long pathlength methods (50 – 200 cm) may eliminate some systematic errors in open ocean CO AQY spectra. In addition, the $a_g(320)$ transition

point used here is based on a statistical fitting exercise with a limited number of samples from the clearest waters of the Gulf and thus may not be the best way to model the CDOM continuum from inshore and offshore waters. Considering our offshore CDOM absorption coefficients, the $a_g(320)$ transition point of 1.3 m^{-1} is at the high end of our CDOM measurements for these samples (Table 2.2). Combining this $a_g(320)$ transition point with a low blue water AQY spectrum could mean that our CO estimates are somewhat conservative. Depending on the influence of the river system, the inshore/coastal AQY is applied to only 6 to 15% of our study area using an $a_g(320)$ transition point of 1.3 m^{-1}.

3.5 Role of Photochemistry in the Carbon Cycle of the Northern Gulf of Mexico

The inability to determine CO_2 AQY spectra directly for clear offshore waters severely compromises the calculation of CO_2 photochemical flux from optical properties using the methods put forward by Fichot and Miller (2010) and modified for use with our Northern Gulf of Mexico study site. As a means to circumvent these analytical problems, CO_2:CO photoproduction ratios provide a tool for determining CO_2 photochemical rates in blue waters from the direct determinations for CO AQY spectra. Regrettably, considering the extreme range of this ratio reported in the literature and determined in our coastal samples, this approach continues to provide only a poor constraint on the process. Nonetheless, CO_2:CO ratios remain one of the few mechanisms whereby estimates of the total photo-oxidation of DOC to CO_2 and CO can obtained.

Here we determined depth resolved CO photoproduction rates for our study region using the methods outlined in Section 2.7 (Fichot and Miller, 2010) and 2 CO AQY spectra (Equations 13 and 14) determined for the Northern Gulf of Mexico

partitioned using the $a_g(320) = 1.3\ m^{-1}$ transition point. CO_2 photoproduction rates (P_{CO2}) were then estimated by multiplying P_{CO} (Table 2.3) by our median CO_2:CO ratio of 24.4. To highlight the differences between production rates calculated in this manner, CO_2 photoproduction rates were also calculated for this region using the pooled CO_2 AQY spectrum (Table A3). Because CO_2 photoproduction measured under longer wavelength cutoff filters (i.e. the 425 and 480 nm filters) is at, or below the detection limit for our methods, the CO_2 AQY spectra determined here are viewed as unreliable at visible wavelengths and extrapolation of the exponential AQY curve was viewed to be inappropriate. Consequently, CO_2 photoproduction estimates were limited to a range of 290 to 400 nm instead of the 290 to 490 nm range used for CO estimates (Equations 12).

CO_2 photoproduction estimates made for the study area using the CO_2:CO ratio and our 2 CO AQY spectra are lower and have a much larger range with greater month-to-month variability than those made using a single average CO_2 AQY spectrum. The "2 CO AQY Ratio" method gave CO_2 production ranging from 86.7 to 3690 μmole m^{-2} d^{-1}, with monthly averages from 146 to 431 μmole m^{-2} d^{-1}. Estimates made using a single average CO_2 AQY spectrum, from pooled CO_2 experimental data as described in Section 3.1.3, range from 436 to 1500 μmole m^{-2} d^{-1}, with monthly averages ranging from 441 to 1100 μmole m^{-2} d^{-1}. The yearly average CO_2 production estimate made with an average CO_2 AQY (811 μmole m^{-2} d^{-1}) is very similar to the average CO_2 photochemical flux estimate made by Reader and Miller (2012) for inshore waters along the Georgia Coast (824 μmole m^{-2} d^{-1}). This is not surprising since the only direct CO_2 AQY spectra determined for our study area were also from inshore and coastal samples.

On the other hand, Belanger et al. (2006) estimated CO_2 photoproduction rates between 242 and 508 μmole m^{-2} d^{-1} at the summer solstice in the Mackenzie estuary and shelf and in the Amundsen Gulf. This result is in better agreement with our average monthly estimate (300 μmole m^{-2} d^{-1}) obtained with the "2 CO AQY Ratio" method. A great deal of caution should be taken in interpreting this comparison since the average CO_2:CO photoproduction ratios determined in this study are poorly constrained and consequently estimates for regional CO_2 photoproduction rate remain ill-defined. It is possible that the lower photochemical CO_2 flux estimates determined by Belanger et al. (2006) are at least partly explained by their long (i.e. 24 – 46 hour) irradiations and reports that initial CO_2 photoproduction rates are faster than those measured after lengthy irradiation, thus giving a nonlinear accumulation of CO_2 that may result in underestimates for CO_2 photoefficiency (Miller and Zepp, 1995; White et al., 2008).

Currently, the greatest uncertainties lie within our estimates of CO_2 photoproduction rates for offshore water, which contribute about half of our estimated CO_2 signal annually in our study area. For example, our inshore waters were generally more photoefficient for CO than offshore waters, with pooled AQY spectra being about an order of magnitude higher for inshore waters. This translates directly to CO_2 production with the ratio method. However, Johannessen and Miller (2001) found the opposite trend for CO_2 where offshore waters were more photoefficient for CO_2 than inshore waters, thereby providing further support that CO_2 photoefficiency may not link directly to that for CO. Higher CDOM-normalized DIC photoproduction rates from samples with a marine algal CDOM source than those with a riverine CDOM source have also been reported (Johannessen et al., 2007). However, considering the analytical

difficulty in successfully measuring DIC photoproduction in offshore samples, further support for any trend is lacking. To further examine how calculation methods might help constrain CO_2 photoproduction estimates, we compared calculations on CO photoproduction rates using only the offshore CO AQY spectrum (Equation 2.13), only the inshore CO AQY spectrum (Equation 2.14), and the "2 CO AQY Ratio" method all multiplied by the median CO_2:CO ratio. In addition we compared these results to those obtained with the pooled CO_2 AQY spectrum (Figure A7). Using yearly averages, the two extreme CO AQY spectra (Equations 13 and 14) constrain CO_2 estimates to within about an order of magnitude (i.e. ~ 160 and 1600 μmole m^{-2} d^{-1}). This may suggest that the "2 CO AQY Ratio" estimate of a yearly CO_2 photoproduction average of 300 μmole m^{-2} d^{-1} may be at the lower end of possible values. This of course depends on whether offshore photoefficiencies for CO_2 follow a similar pattern as those for CO, and until more mechanistic work on these two photoproducts becomes available, this assumption is still questionable.

Recent compilations of over 375,000 pCO_2 measurements in the Gulf of Mexico indicate that, on a whole, the Gulf is a sink for CO_2, with an annual flux of -0.19 mole C m^{-2} yr^{-1} (Robbins et al., 2014). For comparison to our study region, the Northern Gulf of Mexico was a -0.44 mole C m^{-2} yr^{-1} sink over a 1.47 x 10^{11} m^2 area, taking up 7.76 x 10^{11} g C yr^{-1} on average (Robbins et al., 2014). Our study region, defined as in Fichot and Benner (2014), covered ~ 6.21 x 10^{10} m^2, making our average CO_2 photoproduction rates on the order of 8.17 x 10^{10} g C yr^{-1} using the "2 CO AQY ratio" method versus 2.20 x 10^{11} g C yr^{-1} for estimates made using an average CO_2 AQY spectrum. While poorly

defined, these estimates indicate that direct CO_2 photochemistry could offset the air-sea flux of CO_2 by about 7.6 to 28% depending on which method above is chosen.

Considering the results from the "2 CO AQY ratio" approach, which provides the more conservative CO and CO_2 flux estimates, photochemistry would be capable of remineralizing at least 8.5 x 10^{10} g C yr^{-1} as CO_2 plus CO in this region. Based on published estimates of the average terrigenous DOC remineralization in this region (0.68 Tg C yr^{-1}, Fichot and Benner, 2014), our calculations indicate that direct photochemistry could, on average, contribute ~12.5% to this DOC loss, an estimate close to the Fichot and Benner (2014) value of 6 – 8%, made from broadband, (≥ 48 hr) irradiations measuring DOC photochemical loss. This agreement is encouraging, but may be somewhat fortuitous. Our approach incorporates observed photoefficiency differences between inshore and offshore waters for CO and assumes these translate to CO_2 photoefficiencies using a simple, yet admittedly ill-defined CO_2:CO ratio. Fichot and Benner (2014) used inshore and coastal waters for their broadband irradiations, assuming there is no difference in DOC photochemical loss between these waters and those offshore. In addition, long irradiations used in this study may lead to underestimates of overall DOC loss rates since evidence suggests that photoproduction rates for DIC and other photochemical products tend to decrease with prolonged irradiation time (Kieber et al., 2014; Miller and Zepp, 1995; White et al., 2008), which could also explain the lower DIC photoproduction rates reported for the Mackenzie Estuary derived from irradiations of up to 46 hours (Belanger et al., 2006). In both our study and that of Fichot and Benner (2014), the estimates for the contribution of direct photochemistry to the remineralization of terrigenous DOC should be considered conservative.

4. Conclusions

We can say with some certainty that for this river dominated marine system, and likely for others, at least two groups of CO AQY spectra are needed for comprehensive models that include both inshore and offshore waters. Of these two spectra types, offshore CO AQY are not as well constrained as inshore CO AQY spectra, likely due to lower production numbers measured during experiments and larger uncertainty in CDOM spectra. Nonetheless, regional estimates made using two CO AQY spectra together with ocean color data and an optical transition point of $a_g(320) = 1.3\ m^{-1}$ allow a better view of annual photochemical variability in the Mississippi/Atchafalaya River system than does a single pooled AQY spectrum alone. As expected, modeled estimates of photochemical CO fluxes over our defined study area were highest during periods of maximum discharge from these rivers (Shen et al., 2012).

By examining an extensive spatio-temporal data set for CO photoefficiency in the Northern Gulf of Mexico, we have demonstrated that reported correlations between CO photoproduction rates or efficiency and CDOM absorption coefficients (Stubbins et al., 2011) or with $SUVA_{254}$ (Zhang et al., 2006) are not universally applicable. In fact, application of these empirical relationships based on limited data is not recommended for large-scale regional or global estimates of marine CO photoproduction rates. While recent studies are still generating CO data for a few samples (most recently n = 5 - 9, Hong et al., 2014; Ren et al., 2014), caution should be taken in interpreting any observed correlations between CO AQY spectra and various optical properties (namely $SUVA_{254}$ and $a_g(\lambda)$) with such a small sample size.

Even with our new and more extensive CO_2 photochemical efficency data, estimates for its photoproduction in both coastal and blue water areas remain poorly defined for this region. Without accessible methods to determine direct CO_2 AQY spectral measurements in oligotrophic waters, as is the case for CO, two less precise, but common methods can be used to constrain CO_2 photochemistry using regional optical models in the Northern Gulf of Mexico. By either assuming that coastal CO_2 AQY spectra can be applied to offshore waters or by using a more well constrained 2 CO AQY spectral model for inshore and offshore waters with the assumption that a poorly constrained CO_2:CO ratio is appropriate to infer CO_2 photoefficiencies throughout the study region, photochemical production of CO_2 can be calculated from ocean color. Using these approaches, ~12% of the terrestrial DOC remineralized on the shelf (Fichot and Benner, 2014) is estimated to be loss via photochemical oxidation to CO_2.

A recent method involving pool isotope exchange (W. Wang et al., 2009) that replaces background $DI^{12}C$ with $DI^{13}C$, has shown promise in providing lower detection limits for photoproduced $DI^{12}C$ but use of this method for determining CO_2 AQY spectra is missing. Based on data for both CO and CO_2 photoproduction in coastal and inshore samples that demonstrate an exponential increase in photoefficiency with decreasing wavelengths, the use of an average CO_2:CO ratio seems to be an attractive and easy alternative to complicated isotope methods to estimate CO_2 photochemistry from that for CO. As observed here and elsewhere, however, CO_2:CO photoproduction ratios determined from CO_2 photochemical experiments using acidified pretreated samples show a very large range, from ~2 to > 70. Consequently, current evidence seems to suggest that CO photoproduction rates are not suitable proxies to further constrain CO_2

photoproduction rates and perhaps inferring CO_2 photochemical efficiency in particular, from CO photochemistry should be discontinued.

Acknowledgements

This work was supported by NSF grant OCE-0850677. The authors would like to thank Fang Cao, Cedric Fichot, Heather Reader and the crews of the *R/V cape Hatteras* and the *R/V Sharp* for their assistance with sample collection and Dr. Steve Lohrenz and Dr. Wei-Jun Cai as collaborators in the GulfCarbon cruises, supported by NSF grants 0752254 to Lohrenz and 0752110 to Cai.

References

Anesio, A.M., Graneli, W., 2003. Increased photoreactivity of DOC by acidification : Implications for the carbon cycle in humic lakes. Limnol. Oceanogr. 48, 735–744.

Bélanger, S., Xie, H., Krotkov, N., Larouche, P., Vincent, W.F., Babin, M., 2006. Photomineralization of terrigenous dissolved organic matter in Arctic coastal waters from 1979 to 2003: Interannual variability and implications of climate change. Global Biogeochem. Cycles 20. doi:10.1029/2006GB002708

Bertilsson, S., Tranvik, L.J., 2000. Photochemical transformation of dissolved organic matter in lakes. Limnol. Oceanogr. 45, 753–762. doi:10.4319/lo.2000.45.4.0753

Bianchi, T.S., Filley, T., Dria, K., Hatcher, P.G., 2004. Temporal variability in sources of dissolved organic carbon in the lower Mississippi river. Geochim. Cosmochim. Acta. 68, 959–967. doi:10.1016/j.gca.2003.07.011

Bowers, D.G., Brett, H.L., 2008. The relationship between CDOM and salinity in estuaries: An analytical and graphical solution. J. Mar. Syst. 73, 1–7. doi:10.1016/j.jmarsys.2007.07.001

Bryne, R.H., Kester, D.K., 1976. Solubility of hydrous ferric oxide and iron speciation in seawater. Mar. Chem. 4, 255–274.

Cao, F., Fichot, C.G., Hooker, S.B., Miller, W.L., 2014. Improved algorithms for accurate retrieval of UV/visible diffuse attenuation coefficients in optically complex, inshore waters. Remote Sens. Environ. 144, 11–27. doi:10.1016/j.rse.2014.01.003

Chen, R.F., Gardner, G.B., 2004. High-resolution measurements of chromophoric dissolved organic matter in the Mississippi and Atchafalaya River plume regions. Mar. Chem. 89, 103–125. doi:10.1016/j.marchem.2004.02.026

Fichot, C.G., Benner, R., 2011. A novel method to estimate DOC concentrations from CDOM absorption coefficients in coastal waters. Geophys. Res. Lett. 38. doi:10.1029/2010GL046152

Fichot, C.G., Benner, R., 2012. The spectral slope coefficient of chromophoric dissolved organic matter ($S_{275\text{-}295}$) as a tracer of terrigenous dissolved organic carbon in river-influenced ocean margins. Limnol. Oceanogr. 57, 1453–1466. doi:10.4319/lo.2012.57.5.1453

Fichot, C.G., Benner, R., 2014. The fate of terrigenous dissolved organic carbon in a river-influenced ocean margin. Global Biogeochem. Cycles. 28, 300–318. doi:10.1002/2013GB004670.Received

Fichot, C.G., Miller, W.L., 2010. An approach to quantify depth-resolved marine photochemical fluxes using remote sensing: Application to carbon monoxide (CO) photoproduction. Remote Sens. Environ. 114, 1363–1377. doi:10.1016/j.rse.2010.01.019

Fichot, C.G., Sathyendranath, S., Miller, W.L., 2008. SeaUV and SeaUV_C: Algorithms for the retrieval of UV/Visible diffuse attenuation coefficients from ocean color. Remote Sens. Environ. 112, 1584–1602. doi:10.1016/j.rse.2007.08.009

Gao, H., Zepp, R.G., 1998. Factors Influencing Photoreactions of Dissolved Organic Matter in a Coastal River of the Southeastern United States. Environ. Sci. Technol. 32, 2940–2946. doi:10.1021/es9803660

Gennings, C., Molot, L.A., Dillon, P.J., 2001. Enhanced photochemical loss of organic carbon in acidic waters. Biogeochemistry 52, 339–354.

Grebel, J.E., Pignatello, J.J., Song, W., Cooper, W.J., Mitch, W.A., 2009. Impact of halides on the photobleaching of dissolved organic matter. Mar. Chem. 115, 134–144.

Helms, J.R., Stubbins, A., Ritchie, J.D., Minor, E.C., Kieber, D.J., Mopper, K., 2008. Absorption spectral slopes and slope ratios as indicators of molecular weight, source, and photobleaching of chromophoric dissolved organic matter. Limnol. Oceanogr. 53, 955–969. doi:10.4319/lo.2008.53.3.0955

Hoge, F.E., Vodacek, A., Blough, N.V., 1993. Inherent optical properties of the ocean : Retrieval of the absorption coefficient of chromophoric dissolved organic matter from fluorescence measurements. Limnol. Oceanogr. 38, 7032–7038.

Hong, J., Xie, H., Guo, L., Song, G., 2014. Carbon monoxide photoproduction: implications for photoreactivity of arctic permafrost-derived soil dissolved organic matter. Environ. Sci. Technol. 48, 9113–9121. doi:10.1021/es502057n

Hu, C., Muller-karger, F.E., Zepp, R.G., 2002. Absorbance, absorption coefficient, and apparent quantum yield: A comment on common ambiguity in the use of these optical concepts. Limnol. Oceanogr. 47, 1261–1267.

Johannessen, S.C., 2000. A photochemical sink for dissolved organic carbon in the ocean. Ph.D. Thesis, Dalhousie University. Halifax, Nova Scotia.

Johannessen, S.C., Miller, W.L., 2001. Quantum yield for the photochemical production of dissolved inorganic carbon in seawater. Mar. Chem. 76, 271–283. doi:10.1016/S0304-4203(01)00067-6

Johannessen, S.C., Miller, W.L., Cullen, J.J., 2003. Calculation of UV attenuation and colored dissolved organic matter absorption spectra from measurements of ocean color. J. Geophys. Res. 108, C9, 3301. doi: 10.1029/2000JC000514

Johannessen, S.C., Peña, M.A., Quenneville, M.L., 2007. Photochemical production of carbon dioxide during a coastal phytoplankton bloom. Estuar. Coast. Shelf Sci. 73, 236–242. doi:10.1016/j.ecss.2007.01.006

Kieber, D.J., Miller, G.W., Neale, P.J., Mopper, K., 2014. Wavelength and temperature-dependent apparent quantum yields for photochemical formation of hydrogen peroxide in seawater. Environ. Sci.: Processes Impacts. 16, 777–791.

Kieber, R.J., Zhou, X., Mopper, K., 1990. Formation of carbonyl compounds from UV-induced photodegradation of humic substances in natural waters: Fate of riverine carbon in the sea. Limnol. Oceanogr. 35, 1503–1515.

Miller, W.L., Moran, M.A., 1997. Interaction of photochemical and microbial processes in the degradation of refractory dissolved organic matter from a coastal marine environment. Limnol. Oceanogr. 42, 1317–1324. doi:10.4319/lo.1997.42.6.1317

Miller, W.L., Zepp, R.G., 1995. Photochemical production of dissolved inorganic carbon from terrestrial organic matter: Significance to the oceanic organic carbon cycle. Geophys. Res. Lett. 22, 417–420. doi:10.1029/94GL03344

Moran, M.A., Sheldon, W.M., Zepp, R.G., 2000. Carbon loss and optical property changes during long-term photochemical and biological degradation of estuarine dissolved organic matter. Limnol. Oceanogr. 45, 1254–1264.

Moran, M.A., Zepp, R.G., 1997. Role of photoreactions in the formation of biologically compounds from dissolved organic matter. Limnol. Oceanogr. 42, 1307–1316.

Mopper, K., Kieber, D.J., 2002. Photochemistry and the Cycling of Carbon, Sulfur, Nitrogen and Phosphorus, in: Hansell, D.A., Carlson, C.A. (Eds.), Biogeochemistry of Marine Dissolved Organic Matter. Academic Press, San Diego, pp. 455–507.

Nelson, N.B., Siegel, D.A., Carlson, C.A., Swan, C., Smethie, W.M., Khatiwala, S., 2007. Hydrography of chromophoric dissolved organic matter in the North Atlantic. Deep Sea Res. Part I Oceanogr. Res. Pap. 54, 710–731. doi:10.1016/j.dsr.2007.02.006

Pos, W.H., Riemer, D.D., Zika, R.G., 1998. Carbonyl sulfide (OCS) and carbon monoxide (CO) in natural waters: evidence of a coupled production pathway. Mar. Chem. 62, 89–101.

Reader, H.E., Miller, W.L., 2011. Effect of estimation of ultraviolet absorption spectra of chromophoric dissolved organic matter on the uncertainty of photochemical production estimates. J. Geophys. Res., 116, C08002. doi:10.1029/2010JC006823

Reader, H.E., Miller, W.L., 2012. Variability of carbon monoxide and carbon dioxide apparent quantum yield spectra in three coastal estuaries of the South Atlantic Bight. Biogeosciences 9, 4279–4294. doi:10.5194/bg-9-4279-2012

Ren, C., Yang, G., Lu, X., 2014. Autumn photoproduction of carbon monoxide in Jiaozhou Bay, China. J. Ocean Univ. China. 13, 428–436. doi:10.1007/s11802-014-2225-1

Robbins, L.L., R. Wanninkhof, L. Barbero, X. Hu, S. Mitra, S. Yvon-Lewis, W-J. Cai, W.-J. Huang, T. Ryerson, 2014. Air-Sea Exchange. In: Benway, H.M., Coble, P.G. (Eds.), 2014. Report of the U.S. Gulf of Mexico Carbon Cycle Synthesis Workshop, March 27-28, 2013, Ocean Carbon and Biogeochemistry Program and North American Carbon Program, pp. 17–23.

Ruggaber, A., Dlugi, R., Nakajima, T., 1994. Modeling Radiation Quantities and Photolysis Frequencies in the Troposphere. J. Atmos. Chem. 18, 171–210.

Shen, Y., Fichot, C.G., Benner, R., 2012. Floodplain influence on dissolved organic matter composition and export from the Mississippi-Atchafalaya River system to the Gulf of Mexico. Limnol. Oceanogr. 57, 1149–1160. doi:10.4319/lo.2012.57.4.1149

Siegel, D.A., Maritorena, S., Nelson, N.B., Hansell, D.A., Lorenzi-Kayser, M., 2002. Global distribution and dynamics of colored dissolved and detrital organic materials. J. Geophys. Res. 107, 3228. doi:10.1029/2001JC000965

Spencer, R.G.M., Stubbins, A., Hernes, P.J., Baker, A., Mopper, K., Aufdenkampe, A.K., Dyda, R.Y., Mwamba, V.L., Mangangu, A.M., Wabakanghanzi, J.N., Six, J., 2009. Photochemical degradation of dissolved organic matter and dissolved lignin phenols from the Congo River. J. Geophys. Res. 114, G03010. doi:10.1029/2009JG000968

Stubbins, a., Law, C.S., Uher, G., Upstill-Goddard, R.C., 2011. Carbon monoxide apparent quantum yields and photoproduction in the Tyne estuary. Biogeosciences 8, 703–713. doi:10.5194/bg-8-703-2011

Stubbins, A., Hubbard, V., Uher, G., Law, C.S., Upstill-Goddard, R.C., Aiken, G.R., Mopper, K., 2008. Relating carbon monoxide photoproduction to dissolved organic matter functionality. Environ. Sci. Technol. 42, 3271–3276.

Stubbins, A., Uher, G., Law, C.S., Mopper, K., Robinson, C., Upstill-Goddard, R.C., 2006. Open-ocean carbon monoxide photoproduction. Deep Sea Res. Part II Top. Stud. Oceanogr. 53, 1695–1705. doi:10.1016/j.dsr2.2006.05.011

Swan, C.M., Nelson, N.B., Siegel, D.A., Kostadinov, T.S., 2012. The effect of surface irradiance on the absorption spectrum of chromophoric dissolved organic matter in the global ocean. Deep. Res. Part I-Oceanographic Res. Pap. 63, 52–64. doi:10.1016/j.dsr.2012.01.008

Swan, C.M., Siegel, D.A., Nelson, N.B., Carlson, C.A., Nasir, E., 2009. Biogeochemical and hydrographic controls on chromophoric dissolved organic matter distribution in the Pacific Ocean. Deep. Res. Part I Oceanogr. Res. Pap. 56, 2175–2192. doi:10.1016/j.dsr.2009.09.002

Twardowski, M.S., Boss, E., Sullivan, J.M., Donaghay, P.L., 2004. Modeling the spectral shape of absorption by chromophoric dissolved organic matter. Mar. Chem. 89, 69–88. doi:10.1016/j.marchem.2004.02.008

Valentine, R.L., Zepp, R., 1993. Formation of Carbon Monoxide from the Photodegradation of Terrestrial Dissolved Organic Carbon in Natural Waters. Environ. Sci. Technol. 27, 409–412.

Wang, W., Johnson, C.G., Takeda, K., Zafiriou, O.C., 2009. Measuring the photochemical production of carbon dioxide from marine dissolved organic matter by pool isotope exchange. Environ. Sci. Technol. 43, 8604–8609. doi:10.1021/es901543e

Wang, X.-C., Chen, R.F., Gardner, G.B., 2004. Sources and transport of dissolved and particulate organic carbon in the Mississippi River estuary and adjacent coastal waters of the northern Gulf of Mexico. Mar. Chem. 89, 241–256. doi:10.1016/j.marchem.2004.02.014

Weishaar, J.L., Aiken, G.R., Bergamaschi, B A., Fram, M.S., Fujii, R., Mopper, K., 2003. Evaluation of specific ultraviolet absorbance as an indicator of the chemical composition and reactivity of dissolved organic carbon. Environ. Sci. Technol. 37, 4702–4708.

White, E.M., Kieber, D.J., Mopper, K., 2008. Determination of photochemically produced carbon dioxide in seawater. Limnol. Oceanogr. Methods. 6, 441–453. doi:10.4319/lom.2008.6.441

White, E.M., Kieber, D.J., Sherrard, J., Miller, W.L., Mopper, K., 2010. Carbon dioxide and carbon monoxide photoproduction quantum yields in the Delaware Estuary. Mar. Chem. 118, 11–21. doi:10.1016/j.marchem.2009.10.001

Wiesenburg, D.A., Guinasso, N.L., 1979. Equilibrium solubilities of methane, carbon monoxide, and hydrogen in water and sea water. J. Chem. Eng. Data. 24, 356–360. doi:10.1021/je60083a006

Wollast, R., 2003. Continental Margins — Review of Geochemical Settings In: Wefer, G., Billett, D., Hebbeln, D., Jørgensen, B., Schlüter, M., van Weering, T.E. (Eds.), Ocean Margin Systems SE - 2. Springer, Berlin Heidelberg, pp. 15–31. doi:10.1007/978-3-662-05127-6_2

Wu, F.C., Mills, R.B., Cai, Y.R., Evans, R.D., Dillon, P.J., 2005. Photodegradation-induced changes in dissolved organic matter in acidic waters. Canadian Journal of Fisheries and Aquatic Sciences. 62, 1019–1027. doi:10.1139/F05-009

Xie, H., Andrews, S.S., Martin, W.R., Miller, J., Ziolkowski, L., Taylor, C.D., Zafiriou, O.C., 2002. Validated methods for sampling and headspace analysis of carbon monoxide in seawater. Mar. Chem. 77, 93–108. doi:10.1016/S0304-4203(01)00065-2

Xie, H., Bélanger, S., Demers, S., Vincent, W.F., Papakyriakou, T.N., 2009. Photobiogeochemical cycling of carbon monoxide in the southeastern Beaufort Sea in spring and autumn. Limnol. Oceanogr. 54, 234–249. doi:10.4319/lo.2009.54.1.0234

Zafiriou, O.C., Andrews, S.S., Wang, W., 2003. Concordant estimates of oceanic carbon monoxide source and sink processes in the Pacific yield a balanced global "blue-water" CO budget. Global Biogeochem. Cycles. 17. doi:10.1029/2001GB001638

Zafiriou, O.C., Xie, H., Nelson, N.B., Najjar, R.G., Wang, W., 2008. Diel carbon monoxide cycling in the upper Sargasso Sea near Bermuda at the onset of spring and in midsummer. Limnol. Oceanogr. 53, 835–850. doi:10.4319/lo.2008.53.2.0835

Zhang, Y., Xie, H., 2012. The sources and sinks of carbon monoxide in the St. Lawrence estuarine system. Deep Sea Res. Part II Top. Stud. Oceanogr. 81–84, 114–123. doi:10.1016/j.dsr2.2011.09.003

Zhang, Y., Xie, H., Chen, G., 2006. Factors affecting the efficiency of carbon monoxide photoproduction in the St. Lawrence estuarine system (Canada). Environ. Sci. Technol. 40, 7771–7777. doi:10.1021/es0615268

Ziolkowski, L.A., Miller, W.L., 2007. Variability of the apparent quantum efficiency of CO photoproduction in the Gulf of Maine and Northwest Atlantic. Mar. Chem. 105, 258–270. doi:10.1016/j.marchem.2007.02.004

Zuo, Y., Jones, R.D., 1995. Formation of carbon monoxide by photolysis of dissolved marine organic material and its significance in the carbon cycling of the oceans. Naturwissenschaften. 82, 472–474.

CHAPTER 3

BLENDING REMOTE SENSING DATA PRODUCTS TO ESTIMATE PHOTOCHEMICAL PRODUCTION OF HYDROGEN PEROXIDE AND SUPEROXIDE IN THE SURFACE OCEAN[1]

---

[1]L.C. Powers and W.L. Miller, Blending remote sensing data products to estimate photochemical production of hydrogen peroxide and superoxide in the surface ocean, *Environ. Sci.: Processes Impacts*, 2014 DOI: 10.1039/c3em00617d. Reproduced by permission of The Royal Society of Chemistry.

Abstract

Hydrogen peroxide (H_2O_2) and its precursor, superoxide (O_2^-), are well-studied photochemical products that are pivotal in regulating redox transformations of trace metals and organic matter in the surface ocean. In attempts to understand the magnitude of both H_2O_2 and O_2^- photoproduction on a global scale, we implemented a model to calculate photochemical fluxes of these products from remotely sensed ocean color and modeled solar irradiances. We generated monthly climatologies for open ocean H_2O_2 photoproduction rates using an average apparent quantum yield (AQY) spectrum determined from laboratory irradiations of oligotrophic water collected in the Gulf of Alaska. Because the formation of H_2O_2 depends on secondary thermal reactions involving O_2^-, we also implemented a temperature correction for the H_2O_2 AQY using remotely sensed sea surface temperature and an Arrhenius relationship for H_2O_2 photoproduction. Daily photoproduction rates of H_2O_2 ranged from <1 to over 100 nM d^{-1}, amounting to ~30 μM yr^{-1} in highly productive regions. When production rates were calculated without the temperature correction, maximum daily rates were underestimated by 15 – 25%, highlighting the importance of including the temperature modification for H_2O_2 in these models. By making assumptions about the relationship between H_2O_2 and O_2^- photoproduction rates and O_2^- decay kinetics, we present a method for calculating midday O_2^- steady-state concentrations ($[O_2^-]_{ss}$) in the open ocean. Estimated $[O_2^-]_{ss}$ ranged from 0.1 – 5 nM assuming bimolecular dismutation was the only sink for O_2^-, but were reduced to 0.1 – 290 pM when catalytic pathways were included. While the approach presented here provides the first global scale estimates of marine $[O_2^-]_{ss}$ from remote sensing, the potential of this model to quantify O_2^- photoproduction rates and $[O_2^-$

$]_{ss}$ will not be fully realized until the mechanisms controlling O_2^- photoproduction and decay are better understood.

1. Introduction

In the marine environment, photochemical reactions in surface waters lead to a number of oxidized products. The absorption of solar radiation by the chromophoric fraction of dissolved organic matter (CDOM) initiates reactions with molecular oxygen that lead to the formation of an array of reactive oxygen species (ROS), including superoxide (O_2^-), hydroxyl radical ($^{\cdot}OH$), singlet oxygen (O_2^1), and hydrogen peroxide (H_2O_2) (review by Burns et al., 2012). Of these, O_2^- is especially interesting in that it acts as both an oxidant and a reductant, as well serving as the precursor for H_2O_2, the longest lived ROS in the photic zone (Kieber et al., 2003, references therein). Together, O_2^- and H_2O_2 (and $^{\cdot}OH$ derived from them) are involved in degradation of organic pollutants and indirect photobleaching of CDOM (Chen et al., 2009; Scully et al., 2003; White et al., 2003), creation of exogenous oxidative stress in aquatic organisms (Baltar et al., 2013; Clark et al., 2008; Kieber et al., 2003; Morris et al., 2011; Zepp et al., 2003), and alteration of redox cycling of trace metals like Fe, Cu and Mn (Kieber et al., 2013; Moffett and Zika, 1987; Rose and Waite, 2006; Voelker and Sulzberger, 1996; Wuttig et al., 2013). Consequently, quantitative information on the production, sinks, and concentrations of O_2^- and H_2O_2 in the open ocean is fundamental to fully understanding their role in global biogeochemical cycles.

The formation of these reactive species in surface seawater begins with the absorbance of ultraviolet radiation (UVR; 280-400 nm) that elevates ground state CDOM to an excited state (CDOM*). Zhang et al. (2012) suggest that CDOM* most likely

generates reactive intermediates via intramolecular charge transfer that subsequently reduce molecular oxygen to superoxide (O_2^- or its conjugate acid HO_2). O_2^- then decays through disproportionation to produce H_2O_2 via the following reactions (O'Sullivan et al., 2005):

$$HO_2 + O_2^- \rightarrow HO_2^- + O_2 + OH^- \qquad (k_1 = 9.7 \times 10^7\ M^{-1}s^{-1}) \qquad (3.1)$$

$$HO_2 + HO_2 \rightarrow H_2O_2 + O_2 \qquad (k_2 = 8.3 \times 10^5\ M^{-1}s^{-1}) \qquad (3.2)$$

$$H^+ + O_2^- \longleftrightarrow HO_2 \qquad (K_a = 1.6 \times 10^{-5}\ M^{-1}) \qquad (3.3)$$

where k_1 and k_2 are rate constants determined in pure water at 25°C and K_a is the superoxide acidity constant (Bielski et al., 1985). Zafiriou (1990) reported similar superoxide dismutation kinetics in seawater, determining a pKa of 4.60 ± 0.15, defining the overall second order rate law for O_2^- decay by dismutation as

$$\frac{d[O_2^-]}{dt} = k_{dis}[O_2^-][HO_2] \approx 2k_D[O_2^-]^2 \qquad (3.4)$$

where k_D for seawater = (5 ± 1) x $10^{12}[H^+]$, confirming a direct dependence on pH for O_2^- kinetics that has been verified by subsequent work (Heller and Croot, 2010a).

Laboratory studies have shown that UV-B radiation (280 to 320 nm) is the most efficient spectral region for production of H_2O_2 in marine systems, reflected in global distributions of H_2O_2 photoproduction rates (Andrews et al., 2000; Kieber et al., 2014; O'Sullivan et al., 2005; Yocis et al., 2000). These rates typically decrease with increasing latitude, in part due to decreasing UVR flux but also due to temperature differences between polar and equatorial waters. Because the rate limiting step for the photochemical formation of H_2O_2 is a thermal process (Equations 3.1, 3.2 and 3.4), the efficiency for H_2O_2 photoproduction typically increases by a factor of 2 for every 10°C increase in water temperature (Kieber et al., 2014). Szymczak and Waite (1988) demonstrated that

total H_2O_2 production under full spectral solar irradiation follows an Arrhenius rate law and calculated an activation energy (E_a) for the reaction of 37.4 kJ mol^{-1}. Instead of determining an E_a from full spectrum irradiations, Miller (2000) demonstrated that wavelength-dependent activation energies could also be calculated from Arrhenius plots for H_2O_2 photoproduction. This data can therefore be used to quantify the change in H_2O_2 production efficiency due to temperature.

Comparing work done on H_2O_2 and O_2^-, H_2O_2 photoproduction has been studied most extensively, not only due to its biogeochemical reactivity, but also due to its greater concentration and stability relative to other ROS (O'Sullivan et al., 2005). Additionally, the instability of O_2^- in aqueous solutions makes analytical standards difficult to maintain, even when metal chelators are added and alkaline pH is used to slow O_2^- loss rates (Heller and Croot, 2010b). Consequently, there are currently no spectral photochemical efficiency data for the formation of O_2^- in surface ocean waters, but as the primary photochemical precursor for H_2O_2 formation in sunlit waters, it should be possible to infer O_2^- chemistry from H_2O_2 data.

Superoxide, and in turn H_2O_2 photoproduction rates, are controlled by the rate of photon absorption ($Q_a(\lambda,z)$; mol(photons) m^{-3} s^{-1}) at a given wavelength (λ; m) and depth (z; m) together with the efficiency of the reaction sequence; in other words, the probability that absorption of solar radiation will lead to O_2^- or H_2O_2 formation. $Q_a(\lambda,z)$ is a function of CDOM "concentration" (defined with a spectral absorption coefficient, $a_{g,}m^{-1}$), the solar spectral scalar irradiance ($E_0(\lambda,0^-)$; mol (photons) m^{-2} s^{-1} nm^{-1}), and its attenuation in the water column ($K_d(\lambda)$; m^{-1}). This is quantified as

$$Q_a(\lambda,z) = E_0(\lambda,0^-)e^{-K_d(\lambda)z}a_g(\lambda,z) \quad (3.5)$$

For marine systems, the reaction efficiency is typically quantified spectrally as the apparent quantum yield (AQY; $\phi(\lambda)$), defined as the ratio of the number of moles product produced to the number of moles of photons absorbed by CDOM in the sample.

Once $Q_a(\lambda,z)$ is defined, and assuming active photochemical production is confined to the 290 – 490nm wavelength range, *in situ* photochemical H_2O_2 production rates (P_{H2O2}; mol(H_2O_2) m^{-3} s^{-1}) in sunlit waters can be modeled as follows,

$$P_{H_2O_2} = \int_{290}^{490} Q_a(\lambda,z)\phi(\lambda,z)\,d\lambda \qquad (3.6)$$

This general approach is appropriate for any scale for which the optical and photochemical variables can be defined and has been used to describe results ranging from laboratory irradiations in quartz containers (Reader and Miller, 2012) to global ocean calculations (Fichot and Miller, 2010) from satellite data. This later development is critical for new examination of the importance of photochemical reactions over large spatio-temporal scales.

It is well known that the oceans are exhibiting increased temperatures (Ishii et al., 2006), salinity changes (Boyer et al., 2005), reductions in pH and changes in the calcium carbonate saturation point (Steinacher et al., 2009). All of these affect marine redox kinetics. In order to assess the effects of widespread oceanic shifts on O_2^- and H_2O_2 cycling, we have employed the methods of Fichot and Miller (2010) to examine the photochemical formation of these ROS from satellite data on a global scale. To define the variables discussed above ($E_d(\lambda,z)$, $K_d(\lambda)$, $a_g(\lambda,z)$ and $\phi(\lambda,z)$), this study combines remotely sensed ocean color and sea surface temperature data with modeled solar irradiances and laboratory derived H_2O_2 AQY spectra corrected for temperature to calculate global H_2O_2 production rates in the surface ocean. New data for O_2^- kinetics

from open ocean samples are then used to infer superoxide dynamics underlying the H_2O_2 photoproduction rates, providing insight into the global trends in the turnover rates of these two reactive oxygen species in a warmer and more acidic future ocean.

2. Methods

2.1 Sample Treatment

Surface seawater samples, taken within the top meter, used for photochemical experiments in this study were collected from two locations: the Northern Gulf of Mexico onboard the R/V *Pelican* in May 2012 and in the Gulf of Alaska onboard the R/V *Melville* in August 2013. Samples were 0.2 μm gravity-filtered (Whatman; Polycap-36&75AS) directly from standard Niskin bottles into 1 L acid-cleaned (2 M HCl), ashed borosilicate glass bottles (Kimax; Gulf of Mexico) or 2 L acid-cleaned, Milli-Q (Millipore, >18 MΩ) rinsed polycarbonate bottles (Nalgene; Gulf of Alaska). Sample locations and properties relevant for photochemistry are listed in Table 3.1. Samples for H_2O_2 quantum yield determinations used in this study were stored at 4 °C in the dark for up to 3 months prior to use. CDOM absorption spectra are reported to exhibit no significant changes when stored in this manner for up to 12 months (Johannessen and Miller, 2001; Swan et al., 2012) and photochemical properties were assumed unchanged. Gulf of Alaska samples for shipboard superoxide irradiations were typically partitioned directly into acid-cleaned, Milli-Q rinsed, 600 mL jacketed beakers (Ace Glass) maintained at 20 °C with a recirculating water bath for photochemical experiments, either within hours of collection or stored on the ship at 4 °C until use, typically 1-2 days. While all equipment in contact with seawater samples was acid-cleaned as described

Table 3.1. Sample characteristics and $\phi(\lambda)$ fitting parameters (m values with 95% confidence intervals) for laboratory H_2O_2 $\phi(\lambda)$ determined at 20 °C for seawater samples from the Gulf of Mexico and the Gulf of Alaska (A). The r^2 is for the correlation between measured H_2O_2 production and that calculated from the $\phi(\lambda)$ for all quartz cells in a given exposure. Sample characteristics and k_{pseudo} (s^{-1} with 95% confidence intervals) determined from non-linear curve fitting of shipboard superoxide decay curves (B).

(A)

Station	Latitude (N)	Longitude (W)	S (PSU)	$a_g(320)$ (m^{-1})	m_1	m_2	r^2
GoM1	28.97	89.11	26.5	2.82	7.23 ± 1.15	0.025 ± 0.017	0.91
GoM2	28.90	89.44	n.d.	6.64	6.88 ± 0.54	0.019 ± 0.007	0.98
GoM3	28.70	89.50	n.d.	3.57	8.87 ± 0.51	0.020 ± 0.008	0.98
GoM4	27.92	90.37	36.4	0.090	7.12 ± 1.41	0.025 ± 0.022	0.75
GoA1	53.00	152.00	34.5	0.279	8.23 ± 0.48	0.024 ± 0.011	0.96
GoA2	50.00	145.00	32.4	0.162	7.90 ± 1.02	0.027 ± 0.025	0.84
GoA Pooled	-	-	-	-	8.201 ± 0.47	0.0238 ± 0.011	0.92

(B)

Station	Latitude (N)	Longitude (W)	S (PSU)	$a_g(320)$ (m^{-1})	pH_{NBS}	k_{pseudo} (x 10^{-3} s^{-1})	r^2
GoA2	50.00	145.00	32.4	0.162	8.08	4.59 ± 0.08	0.96
GoA3	49.28	134.67	32.4	0.138	8.07	2.02 ± 0.03	0.91
GoA4	54.60	141.41	32.5	0.222	8.05	1.95 ± 0.02	0.94
GoA5	56.47	141.24	32.4	0.428	8.17	1.71 ± 0.04	0.89

above and gloves were used in handling samples, neither the R/V *Pelican* nor the R/V *Melville* was equipped with special trace metal processing facilities and consequently, limited trace metal contamination could be present.

2.2 Optical Measurements

Three separate systems were employed for solution absorbance measurements. A Perkin Elmer Lamda 40 dual beam spectrophotometer was used for H_2O_2 standard determinations and CDOM samples. For superoxide standard determinations, an Ocean Optics Inc. system composed of a DT-MINI-2-GS light source linked to a USB2000-UV-VIS Miniature Fiber Optic Spectrometer with Premium grade Si fiber optic assemblies allowed real-time absorbance measurements in a 1 cm cell. For oligotrophic seawater used in H_2O_2 AQY calculations and superoxide irradiations, the USB2000 was replaced with a MAYA2000-Pro UV-VIS spectrometer (Ocean Optics) and connected to a LWCC-2100 Type II, 1-meter liquid waveguide capillary flow cell (World Precision Instruments) to check CDOM measurements on the same samples made using the Lambda 40. The LWCC was filled via a peristaltic pump positioned to pull from glass sample bottles through Teflon tubing. CDOM and H_2O_2 baselines were zeroed against Milli-Q water and pre-irradiated acetone/ethanol for superoxide standards as described below.

2.3 Laboratory Determinations of ROS

2.3.1 Hydrogen Peroxide Analysis

H_2O_2 was measured using a FeLume chemiluminescence (CL) system (Waterville Analytical) and modifications to the methods of King et al. (2007). Briefly, H_2O_2 in samples will chemiluminesce at alkaline pH when mixed in a flow injection analytical

system with 2 μM 10-methyl-0-(*p*-formylphenyl)-acridinium carboxylate trifluoromethanesulfonate (AE; provided by Dr. James J. Kiddle, Western Michigan University). A syringe was used to flush (≥1 mL) and fill a 195 μL Teflon sample loop (VICI 10-port valve) that was subsequently moved with carrier to mix with the AE reagent and then transported to a spiral flow cell located in front of a photomultiplier tube (PMT) where it is mixed with 0.1 M carbonate buffer to initiate CL (Hamamatsu HC135 PMT, 900 V, 400 ms integration). This system requires 50 seconds for each H_2O_2 measurement and a limit of detection of 350 pM for open ocean seawater is reported by King et al. (2007). Instead of adding an acid wash loop to the injection valve to prevent interference of precipitated $MgOH_2$ at high pH (King et al., 2007), we decreased the carbonate buffer pH to 10.4 and used 0.2 M HCl as the carrier, which also helped decrease background CL. A 2 mM H_2O_2 stock solution was prepared from 30% H_2O_2 (J.T. Baker) and checked weekly using its absorbance at 240 nm and a molar absorptivity for H_2O_2 of 38.1 M^{-1} cm^{-1} (Miller and Kester, 1988). Standards were prepared in aged seawater checked for low H_2O_2 against the same seawater with added catalase (20 μL of 100 units L^{-1} in 20 mL seawater: C100 Sigma-Aldrich). Under these conditions, the H_2O_2 detection limit, defined as three times the standard deviation of the blank, was 2.2 nM.

2.3.2 Superoxide Analysis

Superoxide was also measured using the FeLume system employing the chemiluminescent reaction between O_2^- and a methyl Cypridina luciferin analogue (2-methyl-6-(4-methoxyphenyl)-3,7-dihydroimidazo[1,2-a]pyrazin-3(7*H*)-one; MCLA; TCI America), following the methods of Rose et al. (2008) and Garg et al. (2011). In this

case, no sample loop was used and both the seawater sample and chemiluminescent reagent were continuously delivered directly to the flow cell with a peristaltic pump (Rainin, 15 RPM). The PMT was operated at 1200V with an 800 ms integration time. The chemiluminescent reagent contained 2.45 μM MCLA in 0.5 M sodium acetate/50 μM diethylenetriaminepentaacetic acid (DTPA) solution, adjusted to pH 6 with concentrated HCl. The conjugate base of MCLA ($MCLA^-$; pKa = 7.64 ± 0.03) also reacts with molecular oxygen to chemiluminesce (Fujimori et al., 1993), giving an increased background signal due to the $MCLA^-/O_2$ reaction at basic pH. While acidic pH increases the reaction rate for MCLA with O_2^- (Akutsu et al., 1995), it also increases the rate of uncatalyzed superoxide dismutation by about an order of magnitude for every unit decrease in pH. To prevent changes in signal due to changes in reaction temperature (Heller and Croot, 2010b), all seawater samples were brought to room temperature before each experiment. The enzyme superoxide dismutase (SOD; 200 U L^{-1} based on the manufacturer's assay; S5395-15KU Sigma) was added at the end of irradiation experiments (see Section 2.4.2) to observe the subsequent signal reduction to near pre-irradiation background levels. A stock solution of ~1.5 x 10^6 U L^{-1} SOD was prepared in Milli-Q and stored at 4 °C in the dark when not in use.

2.3.3 Superoxide System Calibration and Standards

Because of its instability in aqueous solutions, all methods that produce superoxide standards in μM concentrations are subject to their own analytical issues (Heller and Croot, 2010b). To calibrate the MCLA reaction in the FeLume system for each freshly prepared MCLA reagent, superoxide standards were generated via UV photolysis of acetone in an ethanol solution following modifications to the methods of

McDowell et al. (1983) and Ong (2007). A solution of 41 mM acetone, 6 M ethanol, 30 μM DTPA in 0.1 M borate buffer (pH = 12.5) was irradiated in a 1 cm quartz cell with a Hg lamp (Pen-Ray) for ≤30 seconds. The concentration of superoxide was monitored in real time using the absorbance at 240 nm and a O_2^- extinction coefficient (ε) of 2183 M^{-1} cm^{-1} corrected for the absorbance of H_2O_2 at 240 nm as described by Bielski (1978) as follows

$$\varepsilon_{O2\text{- CORRECTED}} = \varepsilon_{O2-} - 0.5\varepsilon_{H2O2}\ M^{-1}\ cm^{-1} = 2183 \text{ at pH } 12.5 \qquad (3.7)$$

It has been noted that DTPA breaks down in UV light and increases absorbance that can interfere with O_2^- determination (Heller and Croot, 2010b), but given the very short irradiation time required to generate O_2^- in our standard method, it is not likely that DTPA photolysis contributed significantly to the absorbance reading. When the superoxide reached about 100 μM, an aliquot was withdrawn and spiked into seawater samples containing 30 μM DTPA to eliminate metal catalyzed O_2^- decay (Hansard et al., 2010; Heller and Croot, 2010a). Concentrations for O_2^- standards ranged from 5 - 50 nM ($[O_2^-]_0$) and were monitored by the FeLume for ~10 minutes. In un-amended, filtered seawater, O_2^- decay can be described with the following equation

$$\frac{-\mathrm{d}[O_2^-]}{\mathrm{dt}} = 2k_D[O_2^-]^2 + \sum k_M[M]_X[O_2^-] + k_{pseudo}[O_2^-] \qquad (3.8)$$

where k_D is the is the pH and temperature dependent dismutation rate constant (derived from Equation 3.4), k_M is the rate constant for the reaction of superoxide with metal species (M_x), and k_{pseudo} is the rate constant for the reaction of O_2^- with other sinks (Goldstone and Voelker, 2000). If all pseudo-first order decay terms are summed, or metal sink terms are eliminated with the chelator DTPA, then Equation 3.8 reduces to

$$\frac{-\mathrm{d}[O_2^-]}{\mathrm{dt}} = 2k_D[O_2^-]^2 + k_{pseudo}[O_2^-] \quad (3.9)$$

Integrating Equation 3.9 and assuming that the FeLume signal (*S*, corrected for background chemiluminescence) is directly proportional to O_2^- concentration ($S = C\,[O_2^-]$) (Heller and Croot, 2011, 2010a, 2010c), *S* is modeled as a function of time (*t*) with the following equation (Garg et al., 2011; Heller and Croot, 2010a)

$$S = \frac{k_{pseudo}S_0}{k_{pseudo}e^{k_{pseudo}t} + k_D[O_2^-]_0(e^{k_{pseudo}t} - 1)} \quad (3.10)$$

where S_0 is the FeLume signal at time zero and $[O_2^-]_0$ is the spiked superoxide concentration. FeLume data was fit to Equation 3.10 with a non-linear regression of *S* vs. *t* using the curve fitting toolbox in MATLAB ®. The second order dismutation rate constant, k_D, was calculated for each seawater sample using Equation 3.4 (Zafiriou, 1990) and pH values determined using a Ross Ultra, glass combination pH electrotrode (Thermo Scientific) calibrated with NBS standard buffers. Although calibrating seawater pH with Tris buffers of a similar composition to seawater (i.e. of a similar ionic strength) is recommended (Marion et al., 2011), primary standards were used here for direct compatibility with the procedures of Zafiriou (1990). The pseudo-first order rate constant for catalyzed O_2^- decay (k_{pseudo}) and S_0 at the time of the spike were used as fitting parameters. The model fit observed O_2^- decay ($r^2 > 0.94$ for all decay curves, n = 9) giving a k_{pseudo} of 15 ± 2 x 10^{-3} s^{-1}, in good agreement with the k_{pseudo} of 6.6 x 10^{-3} s^{-1} for superoxide decay in non-irradiated solutions containing 1 mg L^{-1} Suwannee River fulvic acid (SRFA) (Garg et al., 2011) and the k_{org} of 9.3 – 15.6 x 10^{-3} s^{-1} determined in tropical Atlantic water from 10 m (Heller and Croot, 2010c). A linear regression of S_0 vs $[O_2^-]_0$ gave a *C* value of 3.05 x 10^4 counts nM^{-1} ($r^2 = 0.90$, n = 9) which was used in

subsequent O_2^- concentration determinations.

2.4 Photochemical Irradiations

2.4.1 Apparent Quantum Yield Experiments for H_2O_2

Photochemical experiments for H_2O_2 $\phi(\lambda)$ determinations were preformed using a Suntest CPS solar simulator equipped with a 1.5 kW xenon lamp (Atlas), as detailed in Johannessen and Miller (2001). Each seawater sample was brought to room temperature and partitioned into 15 gas-tight 10 cm cylindrical quartz spectrophotometric cells, filled and sealed with no headspace using caps fitted with Teflon faced, butyl rubber septa. The absorbance in each cell was measured from 250 – 800 nm both prior to and post irradiation and Milli-Q water was used as the absorbance blank. Raw absorbance spectra were corrected for scattering, the difference in refractive index between salt water and the pure water blank, and instrument drift by fitting individual spectra to the equation:

$$A = Fe^{-S\lambda} + O \tag{3.11}$$

over the 680 – 800 nm range for CDOM measured in 10 cm spectrophotometer cells and over the 700-750 nm range for CDOM measured in 1 m pathlength LWCC (D'Sa et al., 1999) using the MATLAB® nonlinear curve fitting routine *nlinfit*, where *A* (unitless) is absorbance, *F* is a fitting coefficient, *S* is the spectral slope coefficient, and *O* is the offset (Reader and Miller, 2011). The offset was subtracted from the absorbance spectra, and any differences in absorbance spectra measured using the LWCC and the Lambda 40 were attributed to differences in the baseline offset. Because salt solutions have a higher refractive index than the freshwater on which instruments are blanked, seawater should show an apparent negative absorbance at certain wavelengths, an effect that can be exacerbated in the long pathlength LWCC (D'Sa et al., 1999; Miller et al., 2002; Nelson

et al., 2007). This refractive index effect can be corrected by preparing blanks with a similar refractive index to the samples (Miller et al., 2002) or by employing an empirical salinity correction (Nelson et al., 2007). Our absorbance spectra determined using both instruments were comparable in the UV (<350 nm) to the extent that no significant alterations to our final apparent quantum yield calculation could be detected given the overall uncertainty of the multispectral AQY method. Corrected absorbance spectra were converted to Napierian absorption coefficient ($a_g(\lambda)$ (m^{-1})) with the equation:

$$a_g(\lambda) = \frac{\ln(10)A}{L} \quad (3.12)$$

over the 280 – 700 nm range, where L (m) is the pathlength of the spectrophotometric cell. Irradiations typically lasted 3 to 12 hours, and CDOM absorption spectra measured before and after irradiation were averaged for each cell for calculation but did not change significantly.

Spectrophotometric cells were placed vertically in a black water-cooled aluminum irradiation block below the solar simulator, which maintained the cells at 20 °C and allowed no transfer of light between cells. Each cell was aligned under a variety of evenly spaced Schott long-band-pass cutoff filters (280, 295, 305, 320, 380, 425, and 480 nm). Since the irradiation block holds 15 cells, the setup included duplicate cutoff filters and a dark. The spectral downwelling irradiance entering each cell, $E_0(\lambda)$ (mol(photons) m^{-2} s^{-1} nm^{-1}), was quantified at 1 nm intervals with a UV-Vis portable spectroradiometer (OL756, Optronic Laboratories) fitted with a quartz fiber optic cable and integrating sphere, previously calibrated with a NIST standard lamp (OL 83A & OL220 lamp, Optronic Laboratories). Photons absorption rate by CDOM, $Q_a(\lambda)$ (mol(photons) s^{-1} nm^{-1}), in each sample was calculated following the recommendations of Hu et al. (2002),

correcting for self-shading via the equation:

$$Q_a(\lambda) = E_0(\lambda)S(1 - e^{-a_g(\lambda)L})t \quad (3.13)$$

where S (m^2) is the surface area of the irradiated cell and t (s) is irradiation time.

The H_2O_2 production rate is equal to the product of the H_2O_2 $\phi(\lambda)$ and $Q_a(\lambda)$:

$$\frac{d[H_2O_2]}{dt} = \phi(\lambda)Q_a(\lambda) \quad (3.14)$$

allowing for the determination of $\phi(\lambda)$. The spectral quantum yield for each sample is modeled from the H_2O_2 production rate and $Q_a(\lambda)$ with the following equation:

$$\phi(\lambda) = e^{-(m_1 + m_2(\lambda - 290))} \quad (3.15)$$

The fitting parameters (m values above) were again determined using the MATLAB ® nonlinear curve fitting routine, *nlinfit* (Table 3.1A).

2.4.2 Photochemical Superoxide Kinetic Experiments

All photochemical superoxide experiments were carried out on fresh 0.2 μm filtered surface seawater collected in the Gulf of Alaska aboard the R/V *Mellville*. Samples were irradiated under the solar simulator in acid-cleaned and Milli-Q rinsed 600 mL jacketed beakers (Ace Glass) covered with quartz glass. Two crossed glass rods and a Teflon stir bar ensured turbulent mixing and all samples were maintained at 20 °C with a recirculating water bath. O_2^- concentrations were monitored with MCLA chemiluminescence both during and post irradiation to observe O_2^- steady-state concentrations ($[O_2^-]_{ss}$) and decay kinetics respectively. Typically, samples were irradiated about 30 minutes, to ensure $[O_2^-]_{ss}$ had been reached. Post irradiation, FeLume signal, and thus O_2^- decay, were again described by Equations 3.9 and 3.10, effectively combining metal sinks and all other first order sinks into the k_{pseudo} term.

2.5 Model for Photochemical Rate Estimates from Satellite Data

Our general methods for estimating the photochemical production rate of H_2O_2 in the surface ocean from remotely sensed satellite data very closely follow the approach of Fichot and Miller (2010) for global estimates for CO photoproduction. For full details regarding application, assumptions, and error analysis for retrieval of UV attenuation data from SeaWiFS imagery using the original Sea*UV* algorithms and implementation of this optical data for photochemical calculations on global scales, the reader is referred to the original publications (Fichot and Miller, 2010; Fichot et al., 2008). We implemented the "practical" model (section 2.1.2, Equation (4), Fichot and Miller, 2010) with the published assumptions that the 290-490 nm spectral range captures photochemical activity, that upwelling scalar irradiance can be ignored, and that the attenuation of downwelling scalar irradiance can be described by $K_d(\lambda)$. This approach was used to determine total H_2O_2 photoproduction rates (P_{H2O2}; mol(H_2O_2) m^{-3} d^{-1}) with the equation:

$$P_{H_2O_2} \approx \int_{290}^{490} E_{0d}(\lambda,0^-)e^{-K_d(\lambda,z)}a_g(\lambda,z)\phi(\lambda,z)d\lambda \qquad (3.16)$$

Knowledge of $\phi(\lambda)$, $a_g(\lambda)$, and the *in situ* light field obtained from the downwelling scalar irradiance just below the surface ($E_{0d}(\lambda,0^-)$) and the average $K_d(\lambda)$ for the depth range in question, allows the photochemical production rate to be calculated for any depth (z; m) or depth interval (Equation 3.16).

2.5.1 Retrieving Optical Parameters for Global Photochemical Model

Fichot et al. (2008) published a set of algorithms (Sea*UV*/SeaUV_C) for retrieving $K_d(\lambda)$ from SeaWiFS normalized water-leaving radiance ($nLw(\lambda)$) with an estimated overall accuracy of ±15-20% based on comparison to Hydrolight-modeled and *in situ* $K_d(\lambda)$ measurements. Fichot and Miller (2010) subsequently used the Sea*UV* model

retrievals of $K_d(\lambda)$ with $a_g(\lambda)$ data to estimate global, depth-resolved photochemical fluxes of CO as a demonstration of the model's application. Briefly, our implementation of this approach is outlined as follows.

The Sea*UV* algorithms were used to retrieve $K_d(\lambda)$ at 320, 340, 380, 412, 443 and 490 nm from the last 7 years of SeaWiFS monthly data (2003 –2010) and binned to create monthly average climatologies for the global ocean with a spatial resolution of 40 x 40 *cos*(latitude) and a grid size of 500 x 1000 pixels. Spectrally resolved $K_d(\lambda)$ (320 – 490 nm) was determined with a cubic interpolation and extended into the UVB (290 – 320) with a spectral slope coefficient determined between $K_d(320)$ and $K_d(340)$. Full $a_g(\lambda)$ spectra were calculated assuming a $a_g(320)/K_d(320)$ ratio of 0.68 and a spectral slope coefficient, S_{ag}, of 0.0194 (Fichot and Miller, 2010) with the following equation:

$$a_g(\lambda) = a_g(320)e^{(-S_{a_g}(\lambda-320))} \quad (3.17)$$

To supply $E_{0d}(\lambda, 0^-)$ for the photochemical model, we started with modeled global clear-sky downwelling irradiance reaching the earth's surface from 280 to 700 nm at 1 nm intervals using the System for Transfer of Atmospheric Radiation (STAR; Ruggaber et al., 1994). Model inputs included monthly average total ozone concentrations from the Total Ozone Mapping Spectrometer (TOMS) and oceanic values for aerosol, humidity, etc. as described in Fichot and Miller (2010) and a cloud correction for solar irradiance at the sea surface was obtained using monthly averaged TOMS UV reflectivities from 1996 to 2003. The final product from this model is a 7-year climatology for cloud-corrected, daily-integrated, downwelling scalar irradiance, $E_{0d}^{Day}(\lambda,0^-)$, at the sea surface for the 15th of each month. By combining STAR-modeled $E_{0d}^{Day}(\lambda,0^-)$ with $K_d(\lambda)$ retrieved with Sea*UV* and $a_g(\lambda)$ estimates, and assuming the these

optical properties do not vary over the temporal and spatial scales of the calculation, we mapped monthly climatologies for average daily photon absorption rates and used them in subsequent photochemical calculations (e.g. Equation 3.16).

2.5.2 Retrieving Temperature for Global Photochemical Model

There is clear evidence that a significant portion of observed natural variability in H_2O_2 photoproduction is temperature dependent (Kieber et al., 2014). This is expected given the secondary thermal reactions (Equations 3.1 – 3.4) that control H_2O_2 formation following primary photochemical CDOM reactions with oxygen. Activation energies (E_a), determined by Kieber et al. (2014) using an Arrhenius plot are similar between 295 and 370 nm, giving an average value of 21.8 kJ mol^{-1}. Therefore, to better implement our global photochemical production model, H_2O_2 spectral $\phi(\lambda)$ values determined at 20°C (Section 2.4.1) were corrected for temperature-dependence with the equation:

$$\ln \frac{\phi_{\lambda,T}}{\phi_{\lambda,298}} = \frac{21.8}{R}\left(\frac{1}{298} - \frac{1}{T}\right) \qquad (3.18)$$

where $\phi_{\lambda,T}$ is the wavelength-temperature-dependent AQY, $\phi_{\lambda,298}$ is the AQY at 298 K, R is the universal gas constant (8.3145 x 10^{-3} kJ K^{-1} mol^{-1}), and T is temperature (K) (Kieber et al., 2014). For more accurate global mapping of photochemical H_2O_2 production, Level 3 global monthly-binned daytime SST data from MODIS Aqua, with a spatial resolution of 4.63 km, were averaged from 2003 to 2010 to create monthly climatologies for the global ocean and fit to a grid size of 500 x 1000 pixels to match the modeled solar irradiances and the outputs from the Sea*UV* model ($K_d(\lambda)$ and $a_g(\lambda)$). The matched T value retrieved at each pixel was then used in Equation 3.18 to modify the entire H_2O_2 $\phi(\lambda)$ spectra for use in H_2O_2 photoproduction rates (Equation 3.16). Daytime

SST products are susceptible to contamination from reflected sunlight but are still considered accurate to ± 0.4 °C (Brown and Minnett, 1999). Limitations inherent in using an average activation energy are discussed in Section 3.2 below.

3. Results and Discussion

3.1 H_2O_2 Apparent Quantum Yield Spectra

Given that the optical components of the practical model (Equation 3.16) are derived from Sea*UV* and STAR as described in the preceding sections, this leaves our selection of H_2O_2 AQY ($\phi(\lambda)$) as a critical, yet somewhat subjective choice that contributes significant control over photoproduction estimates. Here we have based our selection on an evaluation of our laboratory irradiation results performed on both clear, oceanic and dark, coastal surface samples (Table 3.1A) in comparison with reported spectral AQY for H_2O_2 available in the literature.

Our laboratory determined H_2O_2 AQY spectra decreased by about an order of magnitude over UV wavelengths, ranging from 1.41 – 10.0 x 10^{-4} at 290 nm to 0.15 – 1.34 x 10^{-4} at 400 nm (Table 3.1A, Figure 3.1). These are in reasonable agreement with AQY data determined for the Antarctic at 0 °C (7.4 x 10^{-4} at 290 nm to 0.1 x 10^{-4} at 400 nm; Yocis et al., 2000), for marine (coastal and open ocean) stations at 25 °C (3.56 – 10.4 x 10^{-4} at 290 nm to 0.17 – 0.97 x 10^{-4} at 400 nm; Kieber et al., 2014), and coastal sites at 30 °C (4.7 x 10^{-4} at 290 nm; O'Sullivan et al., 2005). Yocis et al. (2000) and Kieber et al. (2014) compared apparent quantum yield data for H_2O_2 photoproduction from a variety of freshwater and marine samples and found that the $\phi(\lambda)$ was quite similar for all regions studied. Yocis et al. (2000) additionally determined H_2O_2 quantum yield spectra at 20°C in Antarctic samples, which increased the $\phi(\lambda)$ for H_2O_2 by about a factor of 3 (22 x 10^{-4}

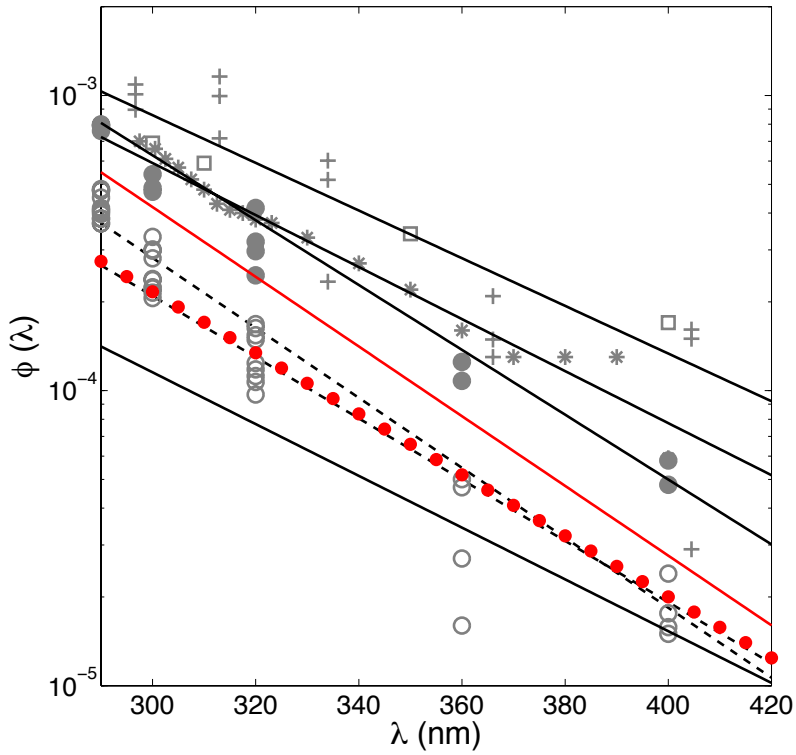

Figure 3.1. Apparent quantum yield spectra ($\phi(\lambda)$) for H_2O_2 photoproduction at 20 °C for our Gulf of Mexico (solid line) and the Gulf of Alaska (dashed line) experiments (this study). The red dotted line is the pooled AQY spectrum for both Gulf of Alaska stations. Select AQY data from other studies are also shown: Kieber et al. (2014) average seawater AQY spectrum adjusted to 20 °C (solid red line), Miller (2000) Antarctic at 15 °C (open circle), Miller (2000) Station ALOHA at 15 °C (closed circle), Cooper et al. (1988) VH Pond, Florida (*), Moore et al. (1993) Orinoco River outflow (+) and Andrews et al. (2000) 1:5 Shark River water (open squares).

at 290 nm) over the same samples at 0 °C. These AQY spectra are comparable to H_2O_2 quantum yield data determined in VH Pond and Newman's Lake, FL (6.6 and 15 x 10^{-4} at 300 nm; Cooper et al., 1988), in the Orinoco River outflow (8.95 – 13.6 x 10^{-4} at 300 nm; Moore et al., 1993), and in 1:5 diluted Shark River water (6.9 x 10^{-4} at 300 nm; Andrews et al., 2000). The AQY spectra we determined for our clearest open ocean samples (GOM4, GOA1, and GOA2, Table 3.1A) in this study, however, are generally lower than those determined in freshwater systems (Figure 3.1). O'Sullivan et al. (2005) observed a similar result, reporting H_2O_2 quantum yield values at the lower range of those determined for the Orinoco River outflow by Moore et al. (1993). In fact, the AQY spectra determined in our open ocean water samples agree best with those determined for the oligotrophic Antarctic (Miller 2000; Yocis et al., 2000) and for Station ALOHA (Miller 2000), suggesting that there may be differences in the efficiency for H_2O_2 photoproduction between terrigenous and marine CDOM sources (Figure 3.1).

Some progress has been made in understanding the mechanisms involved in the photoproduction of H_2O_2 from CDOM. O'Sullivan et al. (2005) observed a linear correlation between H_2O_2 production and CDOM photobleaching and Dalrymple et al. (2010) found a strong correlation between the H_2O_2 AQY and the E2/E3 ratio (CDOM absorbance at 254 nm divided by that at 365 nm), a property correlated to DOM molecular weight (Helms et al., 2008). Through a detailed mechanistic investigation of photochemical H_2O_2 production from humic substances and CDOM, Zhang et al. (2012) concluded that charge transfer states, aromatic ketones and aldehydes, $^1O_2$, and excited triplet states of quinones do not contribute significantly to H_2O_2 production. More work

is needed to determine whether these relationships hold true in samples primarily containing marine DOM. In marine samples, and in the open ocean in particular, H_2O_2 AQY spectra are generally very similar and their variability is controlled mainly by differences in temperature (Kieber et al., 2014; Szymczak and Waite, 1988).

To best reflect the oligotrophic waters that dominate the global ocean, we determined a pooled quantum yield spectrum, calculated by fitting Equation 3.15 to all H_2O_2 production data (n = 26) measured for irradiation experiments done in the Gulf of Alaska (Samples GOA1 and GOA2), resulting in the following equation

$$\phi(\lambda)_{\text{pooled}} = e^{-(8.201+0.0238(\lambda-290))} \quad (3.19)$$

This result was used as input for subsequent global photochemical calculations (Equation 3.16). Although GOM4 is also an open ocean sample, data from this irradiation were excluded from the pooled AQY fit because of its poor agreement between measured H_2O_2 production and that predicted from its individual AQY spectrum ($r^2 = 0.75$). The pooled quantum yield values determined here are about 2 times lower than the Kieber et al. (2014) average AQY value at 290 nm (adjusted to 20°C as described in Section 2.5.2; Figure 3.1) and 1.4 times lower than the average AQY value at 400 nm, determined for a variety of marine waters (coastal through open ocean). Because the H_2O_2 quantum yield spectrum used in our model is at the lower end of published AQY spectra (Figure 3.1), we consider our estimates of P_{H2O2} determined in Section 3.2 below to be minimum rates for the open ocean.

3.2 Global Photochemical H_2O_2 Flux Estimates

With the additional temperature modification for the pooled H_2O_2 AQY spectrum, global distributions of surface ocean P_{H2O2} were calculated for each month at a

depth of 1 m and were converted to nM d^{-1} from mol(H_2O_2) m^{-3} d^{-1} to compare to literature values (Table 3.2). Open ocean production rates ranged from <1 to over 100 nM d^{-1}, with a yearly global average of ~45 nM d^{-1}. Spatial and temporal variability in P_{H2O2} is shown in Figure 3.2B using the months of January, April, July, and October as examples. Considering the potential errors associated with retrieving seawater optical properties from satellite data, Fichot and Miller (2010) demonstrated that the Sea*UV* algorithm (Fichot et al., 2008) provides a relatively good approximation of UV-visible photon absorption rates in the open ocean. However, as noted in Fichot and Miller (2010), the use of a single quantum yield spectrum does not have the capacity to capture the underlying processes controlling the known variability in AQY spectra (Figure 3.1), limiting the complete understanding of the magnitude and distributions of H_2O_2 photoproduction rates in surface seawater. Therefore, spatial and temporal distributions of calculated photoproduction rates only track with sea surface temperature and solar irradiation absorption rates.

Perhaps surprisingly, H_2O_2 photoproduction rates determined from our global 7-year climatologies are in reasonable agreement with discrete H_2O_2 production measurements. In a free floating drifter study, Kieber et al. (2014) measured gross P_{H2O2} of 72 nM d^{-1} for an oligotrophic station in the northwest Atlantic in the summer. To compare, P_{H2O2} was 63 nM d^{-1} at 40N 70W on our July map. Yocis et al. (2000) measured gross P_{H2O2} rates of 2.5 – 3.5 nM h^{-1} in Antarctic waters in the summer. Assuming a 12 h deployment, these rates are on the order of 25 – 37 nM d^{-1}, similar to the 32.5 nM d^{-1} estimated at 55S 55W on our December map. Figure 3.3 shows daily H_2O_2 photoproduction rates averaged for the year are highest in equatorial regions and lowest

Table 3.2. Average, maximum and minimum H_2O_2 production rates (nM d^{-1}) for the global ocean at 1 m depth for each month.

	Jan	Feb	Mar	Apr	May	Jun	Jul	Aug	Sep	Oct	Nov	Dec
Avg	48.7	47.1	44.6	42.3	43.2	42.9	42.4	41.6	43.5	46.6	48.3	48.5
Max	96.0	92.3	93.9	93.2	99.6	102.1	105.6	100.6	100.6	97.1	98.8	99.2
Min	0.06	0.06	0.06	0.12	0.05	0.09	0.11	0	0.06	0.05	0.03	0.08

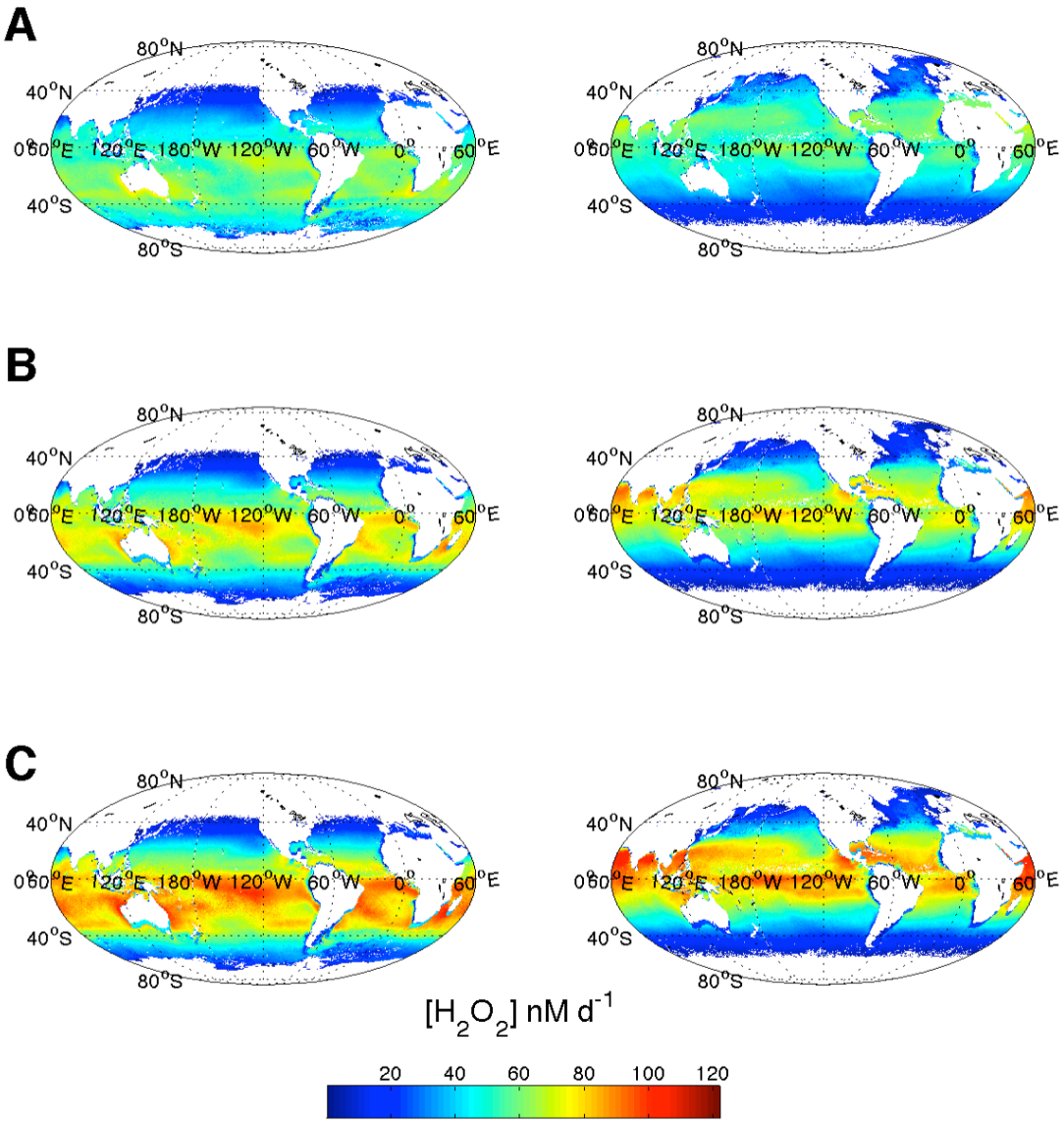

Figure 3.2. H_2O_2 photoproduction rates (nM d^{-1}) at 1 m depth for January (left) and April (right). Areas in white are where SeaWiFS ocean color is not available. 3 different quantum yields for H_2O_2 were used to create these climatologies: **(A)** The single pooled AQY spectrum not modified for temperature variation, **(B)** the AQY spectrum adjusted for temperature using current MODIS SST climatologies and **(C)** the AQY spectrum was adjusted for temperature with SST 5 °C higher than current MODIS climatologies.

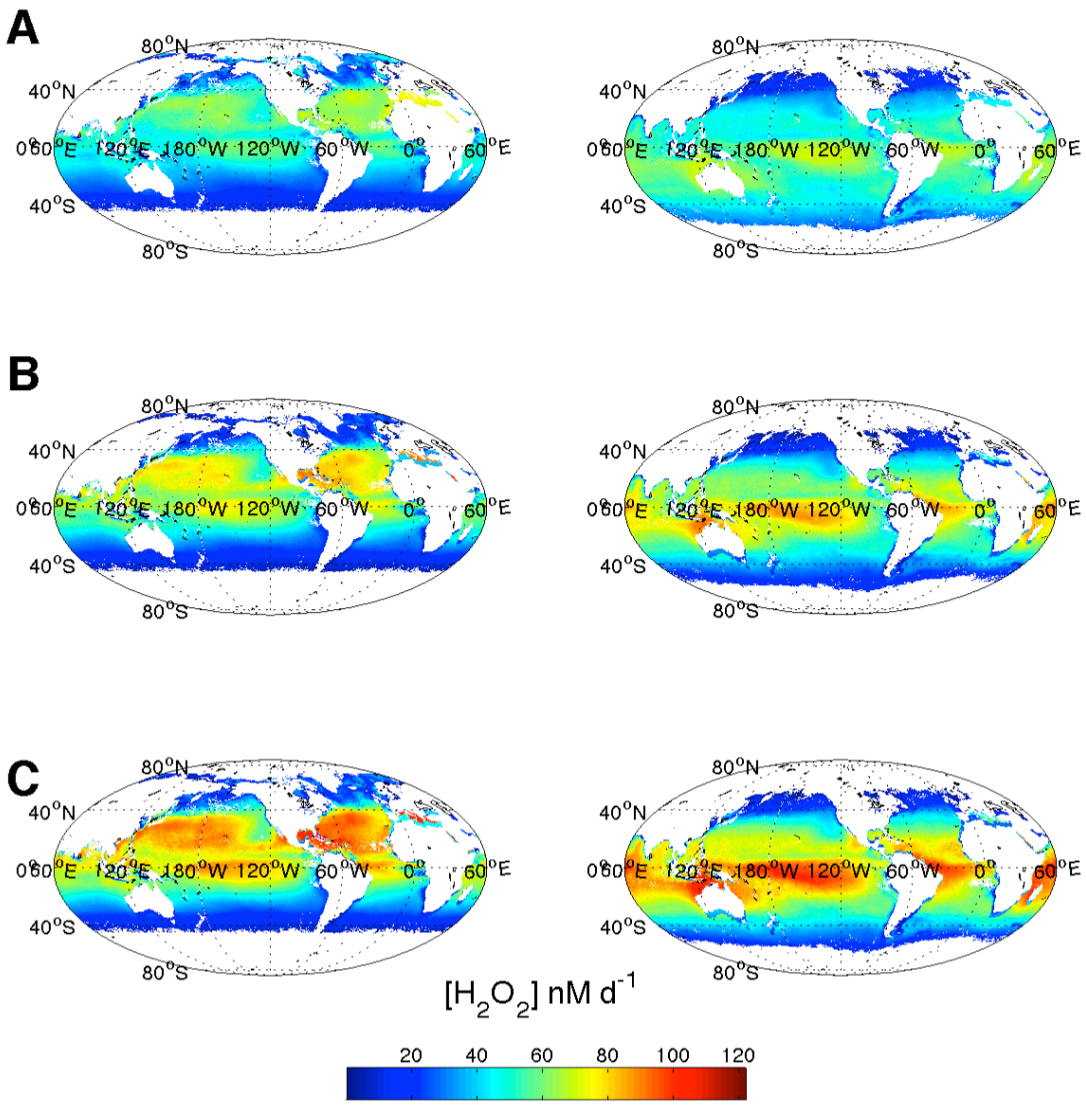

Figure 3.2 (continued). H_2O_2 photoproduction rates (nM d^{-1}) at 1 m depth for July (left) and October (right). All other as presented above.

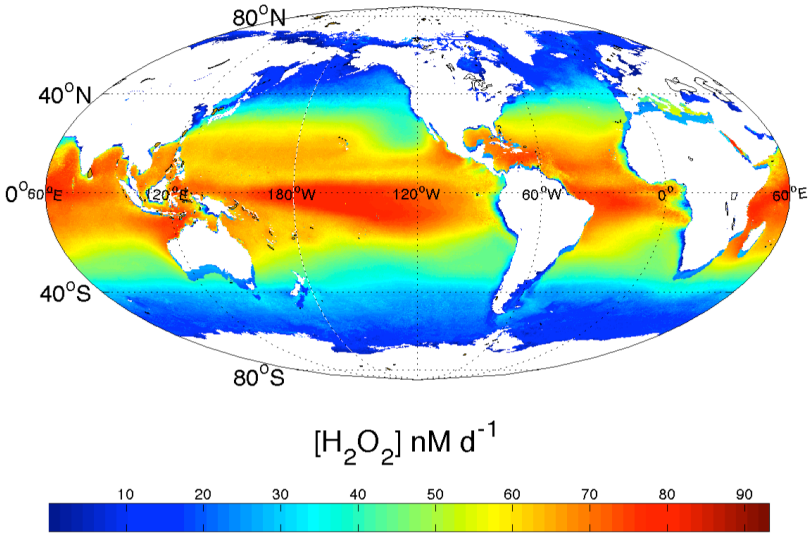

Figure 3.3. H_2O_2 photoproduction rates (nM d^{-1}) at 1 m for the entire year, calculated by averaging monthly climatologies created using temperature-modified AQY spectra. Areas in white are where SeaWiFS ocean color is not available.

at the poles (range: 0.07 - 93.2; average: 40.4; median; 39.5 nM d^{-1}). When summed over the entire year, this amounts to an average of about 8 μM yr^{-1} and near 30 μM yr^{-1} in productive regions. The reader is reminded however, that these data are calculated from 7-year average global climatologies and the comparisons made here are meant to show the applicability of our model, and by no means represent an attempt at validation with measured *in situ* H_2O_2 photoproduction rates.

Although the use of a single AQY spectrum has known limitations, it does allow for a direct assessment of the temperature dependence on photochemical H_2O_2 production rates. If the pooled H_2O_2 AQY spectrum (Equation 3.19) is not adjusted for temperature (Figure 3.2A), production rates are underestimated in equatorial regions and overestimated in polar regions when compared to production rates calculated with temperature modified AQY spectra (Equation 3.18, Figure 3.2B), thereby underestimating average global monthly photoproduction rates by ~3 – 9%. The difference is even more striking in monthly maximum production rates, which are underestimated by ~15 – 25% when not accounting for the temperature dependence on the H_2O_2 AQY spectrum. Estimates of P_{H2O2} determined at 40N 70W in July drop from 63 nM d^{-1} to 59 nM d^{-1} and at 55S 55W in December increase from 32.5 nM d^{-1} to 49.1 nM d^{-1}, creating greater deviations from *in situ* rates discussed above (Kieber et al., 2014; Yocis et al., 2000).

While the studies cited in Section 3.1 above have improved our understanding of mechanisms involved in H_2O_2 production from the photoexcitation of CDOM, the fact that H_2O_2 production is a result of a thermal reaction is greatly ignored. Kieber et al. (2014) represents the first attempt at simultaneously understanding the temperature and

wavelength dependence of H_2O_2 photochemistry. The E_a determined by Kieber et al. (2014) ranges from 8.3 to 52.7 kJ mol^{-1}, with the largest difference in E_a between 290 and 400 nm (average E_a values increased from 16.6 to 31.9 kJ mol^{-1}). Further investigation into the apparent variability in E_a with excitation wavelength will improve estimates of H_2O_2 photoproduction rates, which is pressing when considering rising sea surface temperatures in the ocean. Results from Kieber et al. (2014) demonstrated that a 10 °C increase in seawater increased H_2O_2 AQY spectra by a factor of about 1.8 on average. In order to predict the effect of a warmer future ocean, we applied a uniform 5 °C increase to our monthly SST climatologies. When these "future" SST maps were used to modify the pooled H_2O_2 AQY spectrum, H_2O_2 photoproduction rates increased by 16% on average (Figure 3.2C). This does not necessarily mean that *in situ* H_2O_2 will change in the same regard, especially if the rates of H_2O_2 decay increase as well in a warmer ocean. Steigenberger and Croot (2008) found a negative correlation between H_2O_2 concentration and SST, attributing the effect to higher enzymatic sink strength for H_2O_2 at higher temperatures. In a future scenario where P_{H2O2} increases by 16%, biological decay will most certainly increase as well. Although it is unclear how biology will respond to an increased P_{H2O2}, it is clear that organisms will have to adjust the metabolic energy required to counter the increased rate of H_2O_2 photoproduction.

3.3 Global Superoxide Steady-State Estimates

While AQY spectra determined here and implemented in our model are for H_2O_2, in reality, thermal reactions involving superoxide control its formation. Although it is vitally important to quantify superoxide distributions and photoproduction rates on a global scale in order to understand its role in biogeochemical cycles, determining O_2^-

photoproduction rates from that for H_2O_2 is not a simple task. Presently, the extension of our photochemical H_2O_2 production model to include estimates of global O_2^- photoproduction rates and $[O_2^-]_{ss}$ in the surface ocean remains highly speculative, primarily due to incomplete understanding of the mechanisms regulating O_2^- formation and decay. The following sections, therefore, outline the approach taken and justifications for the choices we made to best estimate spatial and seasonal distributions of superoxide dynamics in the open ocean.

3.3.1 Global Photochemical Superoxide Steady-State Estimates assuming Dismutation as the Dominant Sink

At steady-state, superoxide production and loss terms must balance. As a simplified first approach, we estimated open ocean $[O_2^-]_{ss}$ assuming bimolecular dismutation is the only sink for O_2^-. There is evidence that H_2O_2 production in natural waters can be explained primarily by O_2^- dismutation (Garg et al., 2011; Micinski et al., 1993). Therefore, in making this assumption, Equation 3.9 reduces to:

$$\frac{-\mathrm{d}[O_2^-]}{\mathrm{dt}} = 2k_D[O_2^-]^2 \tag{3.20}$$

The stociometry of superoxide dismutation (Equation 3.1 or 3.2) predicts $0.5H_2O_2$ per O_2^-, implying that

$$P_{O_2^-} = 2P_{H_2O_2} \tag{3.21}$$

and $[O_2^-]_{ss}$ can be estimated on a global scale with Equation 3.22 below

$$[O_2^-]_{ss} = \left(\frac{P_{O_2^-}}{2k_D}\right)^{0.5} = \left(\frac{P_{H_2O_2}}{k_D}\right)^{0.5} \tag{3.22}$$

Since superoxide exists as either HO_2 or O_2^-, the overall dismutation rate constant (k_D)

was calculated at an average oceanic pH of 8.2 from the rate constants for reactions 1 and 2 (Bielski et al., 1985) and the K_a for HO_2 (4.6 ± 0.15 in seawater; Zafiriou, 1990). Therefore, the overall dismutation rate constant for superoxide decay can be expressed as:

$$k_D = \frac{k_2[H^+]^2 + k_1 K_a [H^+]}{(K_a + [H^+])^2} \quad (3.23)$$

Rate constants calculated using this method are in good agreement with those calculated by Zafiriou (1990) for superoxide dismutation in seawater. Second order O_2^- decay is highly pH dependent and a decrease of just 0.4 pH units, from 8.2 to 7.8, increases k_D from 2.43 to 6.11 x 10^4 M^{-1} s^{-1}. We also adjusted k_D for changes in temperature assuming that the average E_a determined by Kieber et al. (2014) for H_2O_2 AQY spectra could also be applied to k_D (Equation 3.18).

Using temperature and pH modified k_D in conjunction with our global models of P_{H2O2} only allows for calculation of daily-integrated $[O_2^-]_{ss}$ values. These integrated values are misleading however because $[O_2^-]_{ss}$ changes dramatically with the intensity of the sun throughout the day. It is therefore more appropriate to calculate steady-state concentrations at a certain time of day. We chose to examine midday $[O_2^-]_{ss}$ because superoxide concentrations should be highest at solar noon. We modeled daily-integrated H_2O_2 photoproduction as a sine curve with the equation:

$$P_{H_2O_2}(\text{daily-integrated}) = A \int_0^{t_{end}} \sin(2\pi f t)\,dt \quad (3.24)$$

where $A = P_{H2O2}(\text{at midday}) = \pi P_{H2O2}(\text{daily-integrated})/(2t_{end})$, $f = 1/(2t_{end})$, t is the time of day and t_{end} is the length of day. For our global climatologies, t_{end} was calculated as a function of latitude for the 15th of each month. Solving for midday H_2O_2 and O_2^-

production rates yields the following modification to Equation 3.22:

$$[O_2^-]_{ss}(\text{midday}) = \left(\frac{\pi P_{H_2O_2}(\text{daily-integrated})}{2 t_{end} k_D} \right)^{0.5} \quad (3.25)$$

Global distributions of midday $[O_2^-]_{ss}$ were modeled for the 15th of each month using a SST-modified k_D at a pH of 8.2, showing October as an example in Figure 3.4. In general, $[O_2^-]_{ss}$ values are highest in equatorial regions and lowest in the poles ranging from ~0.1 – 5 nM, with a yearly average of about 2.6 nM. In order to examine changes in $[O_2^-]_{ss}$ in a future ocean that is not only warmer but also more acidic, midday $[O_2^-]_{ss}$ concentrations were recalculated with an increased SST and a decreased pH. k_D and $\phi(\lambda)$ were again modified with Equation 3.18, but increasing SST by 5 °C did not change the $[O_2^-]_{ss}$ determined with our model because, having no other direct data to consider, we assumed both the rates of superoxide photoproduction *and* it's loss can be adjusted using the same activation energy. However, when the pH was decreased the resulting $[O_2^-]_{ss}$ concentrations at pH 7.8 were ~55% lower than those calculated at pH 8.2 (Figure 3.4).

3.3.2 Investigating Superoxide Decay via Pathways other than Dismutation

The steady-state O_2^- concentrations modeled by assuming that dismutation is the dominant sink are higher than those reported for the surface equatorial Pacific (~220 pM; Rose et al., 2008b) and the Gulf of Alaska (~ 550 pM; Hansard et al., 2010) even though neither fully reflect the photochemical source, having been removed from UV light prior to measurements. Other estimates that use dismutation alone have also overestimated $[O_2^-]_{ss}$ by about 7 – 8 nM (Voelker and Sedlak, 1995; Zafiriou, 1990). This most likely results from ignoring additional sinks of superoxide. To this point, some observations have successfully modeled superoxide decay via a

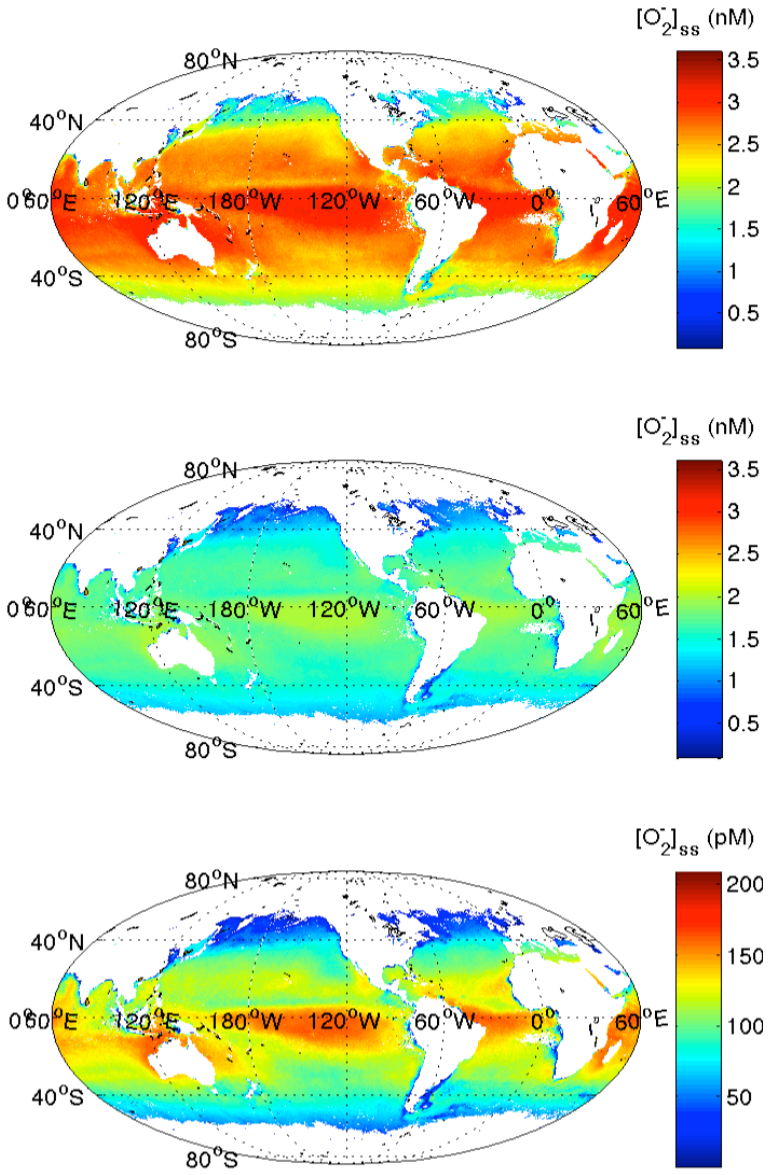

Figure 3.4. $[O_2^-]_{ss}$ (nM or pM) determined at 1 m for October: (Top) with O_2^- assumed to decay solely through dismutation at pH = 8.2, (Middle) with O_2^- assumed to decay solely through dismutation at pH = 7.8, (Bottom) with additional sinks added to dismutation at pH = 8.2 in order to more completely describe O_2^- decay.

pseudo-first order rate law, and not the second order fit required by dismutation (Heller and Croot, 2010a; Shaked et al., 2010). To determine the best approach for our calculations, we irradiated surface seawater in the Gulf of Alaska until a $[O_2^-]_{ss}$ was measured, shut off the lamp, and measured the subsequent O_2^- signal post-irradiation. The resulting O_2^- decay was modeled according to Equation 3.10, as described in Section 2.3.3. The pseudo-first order rate constants determined from our irradiation experiments ranged from 1.7 to 4.6 x 10^{-3} s^{-1} (Table 3.1B), in good agreement with pseudo-first order rate constants for O_2^- decay determined in the Equatorial Pacific in the presence of DTPA ($<10^{-4}$ to 9.7 x 10^{-3} s^{-1}; Rose et al., 2008) and the Southern Ocean (6 ± 1 x 10^{-3} s^{-1}; Heller and Croot, 2010a). These results are consistent with the probability that a large portion of O_2^- in oligotrophic waters decays via pathways other than dismutation.

Given the fact that O_2^- can act as both an oxidant and a reductant, the potential decay mechanisms in seawater are complex. Figure 3.5 presents a compilation of generic superoxide decay pathways, showing the modeling approach of describing the non-dismutation pathways using a single rate constant, k_{pseudo}. If catalytic O_2^- decay is irreversible, then the amount of H_2O_2 generated per O_2^- should be between 0 and 1, and in fact the ratio has been calculated in coastal seawater to be around 0.6 – 0.75 H_2O_2 per O_2^- (Petasne and Zika, 1987). On the other hand, a catalytic redox cycle, (i.e. the dashed lines connecting paths (2) and (3) in Figure 3.5), would produce 0.5 H_2O_2 per O_2^- consumed, and maintain the 2:1 stoichiometric ratio between P_{O2-} and P_{H2O2} typical of dismutation. This catalytic cycling is consistent with results reported for coastal seawater (Goldstone

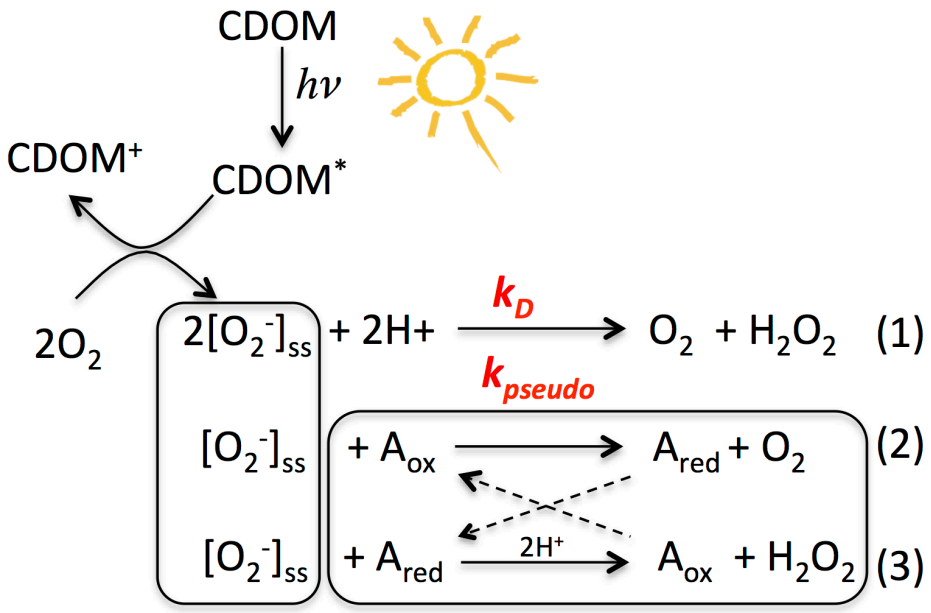

Figure 3.5. Possible mechanistic pathways for H_2O_2 production by O_2^-. A_{ox} and A_{red} are oxidized and reduced forms respectively of an unidentified reactant, A. Dashed lines represent the possible catalytic cycling of a single redox catalyst participating in both the oxidation and reduction of O_2^-.

and Voelker, 2000) and 1 mg L^{-1} SRFA solutions (Garg et al., 2011), but it is unclear whether or not this is a valid assumption for the open ocean. Recently, Wuttig et al. (2013b) found H_2O_2 production rates that were about half the O_2^- production rates generated by a thermal superoxide source (Heller and Croot, 2010b) in open ocean seawater. However, considering other possible reactions that occur between superoxide and excited state CDOM *in situ*, it has not been determined whether this ratio is true of H_2O_2 produced photochemically. Furthermore, Micinski et al. (1993) suggested that O_2^- dismutation accounts for nearly all photochemical H_2O_2 production based on measured O_2^- production rates in the eastern Caribbean. However, there was large variability in P_{O2-} (0.1 – 6 nM min^{-1} spring; 0.2 – 8 nM min^{-1} fall) and P_{H2O2} measured during the same field campaigns (0.39 ± 0.19 nM min^{-1} spring, 2.23 ± 1.5 nM min^{-1} fall) (Micinski et al., 1993) suggesting that for the open ocean, it is possible that the stoichiometric relationship between P_{H2O2} and P_{O2-} may not simply be described using a factor of two.

For this reason, we compared H_2O_2 produced in irradiated filtered seawater with and without additions of the enzyme superoxide dismutase (SOD) to help clarify existing pathways in our open ocean model. Since SOD catalyzes O_2^- disproportionation at a rate $>10^9$ M^{-1} s^{-1} (Cudd and Fridovich, 1982), when present, essentially all superoxide proceeds through the dismutation path (1) to H_2O_2. Following the recommendations of Garg et al. (2011), SOD at 200 U L^{-1} was added to open ocean surface seawater samples from the Gulf of Alaska (GoA1&2 Table 3.1). These samples were irradiated side by side in the solar simulator in 600 mL jacketed beakers at 20 °C with quartz lids for up to 3 hours. For these samples, H_2O_2 photoproduction in the presence of SOD was indistinguishable from that produced in its absence (Figure 3.6). Shaked et al. (2010)

also observed that SOD had no effect on H_2O_2 photoproduction in the Gulf of Aqaba. Additionally, based on O_2^- steady-state measurements during irradiation experiments and modeled pseudo-first order O_2^- decay constants in the dark, Shaked et al. (2010) also calculated P_{O2^-} ranging from 3 – 25 pM s^{-1} and P_{H2O2} ranging from 4 – 10 pM s^{-1}. Their results suggest that the P_{O2^-}:P_{H2O2} of 2:1 is a reasonable estimate in seawater, but the authors note that a 1:1 ratio cannot be ruled out.

A direct approach to establishing this stoichiometric relationship is to monitor both P_{H2O2} and P_{O2^-} at the same time in the same sample. Rusak et al. (2011) have done this during irradiations of unfiltered water collected east of New Zealand, reporting P_{H2O2} and P_{O2^-} to be 28 pM min^{-1} and 76 pM min^{-1}, respectively, giving a P_{O2^-}:P_{H2O2} of 2.7:1 possibly due to H_2O_2 loss in unfiltered water. However, during 20 minute irradiations of filtered seawater, Rusak et al. (2011) also saw P_{O2^-} decrease while P_{H2O2} increased, an ambiguous result that points out the current poorly constrained relationship between P_{H2O2} and P_{O2}. Based on our laboratory results and with limited research into the ratio of P_{H2O2} to P_{O2^-}, it seems that in clear, open ocean surface waters, an oxidative pathway (2) for O_2^- is negligible , and depending on the relative strengths of reductive catalysis (3) and dismutation (1), the P_{O2^-}:P_{H2O2} is somewhere between 1 and 2. It is also apparent that until significantly more information on the photo-efficiency of O_2^- production becomes available, estimates of P_{O2^-} based on hydrogen peroxide production will remain ill-defined.

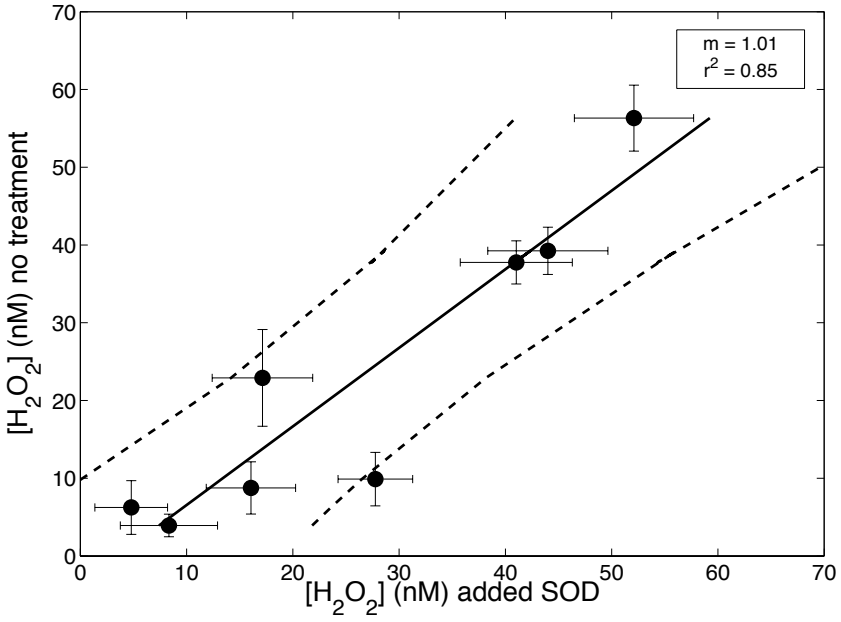

Figure 3.6. $[H_2O_2]$ (nM) produced during short (<3 h) irradiations of low CDOM seawater plotted against $[H_2O_2]$ produced in the presence of 200 U L^{-1} SOD. The solid line represents the linear regression between $[H_2O_2]$ produced during both treatments (m = 1.01, r^2 = 0.85) and the dashed lines are the 95% confidence interval.

3.3.3 Global Photochemical Superoxide Steady-State Estimates Including Additional Sinks for Superoxide

In addition to our work in the Gulf of Alaska, there are only a few studies on superoxide decay kinetics in the open ocean (Hansard et al., 2010; Heller and Croot, 2010a, 2010c; Rose et al., 2008). In these studies, DTPA was used to examine decay kinetics in seawater (Heller and Croot, 2010a, 2010c; Rose et al., 2008) but all use different chelator concentrations and pre-equilibration times, making the selection of a literature value for use in superoxide decay models in the open ocean difficult. Because bimolecular dismutation kinetics for superoxide are well defined as a function of temperature and pH (Bielski et al., 1985; Zafiriou 1990) we included the additional term for combined catalytic decay, k_{pseudo} (Equation 3.9), in our model to improve estimates of $[O_2^-]_{ss}$ in the surface ocean. For our open ocean model, we chose an average k_{pseudo} value of $2.6 \pm 1.4 \times 10^{-3}$ s^{-1}, determined from irradiation experiments done at sea on freshly collected surface seawater from the Gulf of Alaska as described in Section 2.4.2 (Table 3.1B). Using this average value for k_{pseudo} is an oversimplification of the complexity inherent in O_2^- dynamics in the open ocean because it does not include metal rate constants and therefore the effects of seawater pH and ionic strength on metal oxidation are lost. However, until we better understand the specific mechanisms involved in a variety of oceanic environments and can make reasonable estimates of trace metals, it remains a defendable choice for this initial attempt to model $[O_2^-]_{ss}$ in the surface ocean from space.

Because a little bit of mystery remains in defining a universal relationship between P_{H2O2} and P_{O2-}, our subsequent estimates are still made assuming that superoxide

photoproduction rates are twice that of hydrogen peroxide photoproduction rates. Superoxide decay can be modeled by solving Equation 3.9, and $[O_2^-]_{ss}$ can be estimated at midday as

$$[O_2^-]_{ss}(\text{midday}) = \frac{-k_{\text{pseudo}} + \left[k_{\text{pseudo}}^2 + \left(8\pi k_D P_{H_2O_2}(\text{daily-integrated})/t_{\text{end}}\right)\right]^{0.5}}{4k_D} \quad (28)$$

Further, even though the temperature dependence of k_{pseudo} is not known, for our steady-state estimates, we assumed the same temperature correction to k_{pseudo} that we applied to k_D and $\phi(\lambda)$ (Equation 3.18). Additionally, because the effect of pH on k_{pseudo} was not determined here, we could not adjust k_{pseudo} for a change in pH. Despite these limitations, this model attempts to involve all the known superoxide decay kinetics for a more realistic estimate of $[O_2^-]_{ss}$, and results in concentrations reduced by a factor of about 20 (Figure 3.4). In addition to over an order of magnitude drop in concentration, $[O_2^-]_{ss}$ becomes less variable when compared to both modeled month-to-month average values and maximum midday concentrations. This implies that globally, k_{pseudo} is the dominant sink term for O_2. To check this line of reasoning, we recalculated $[O_2^-]_{ss}$ at midday using k_D climatologies determined at pH 7.8. Instead of reducing $[O_2^-]_{ss}$ by 55%, the inclusion of k_{pseudo} reduced $[O_2^-]_{ss}$ by only ~0.5%. These observations again stress that uncatalyzed dismutation is not the major pathway for superoxide in the open ocean.

3.4 Considerations for Future Remote Sensing Estimates Relating H_2O_2 & O_2^-

Presently, using our modeled P_{H2O2} to estimate $[O_2^-]_{ss}$ in the surface ocean is speculative due to insufficient knowledge of the specific mechanisms and kinetic pathways that regulate O_2^- formation and decay. However, this modeling exercise has identified several necessary assumptions and correction terms that will be required to

more accurately estimate superoxide dynamics from data on H_2O_2. One key issue when addressing global ROS distributions is the assumption that P_{O2^-} is twice that of P_{H2O2}, and this needs to be verified for oligotrophic water systems. While measuring P_{H2O2} and P_{O2^-} simultaneously is useful, current reports are for only a few locations and do not reflect the diversity that exists in a variety of marine waters. The best way to model P_{O2^-} in seawater would involve direct measurements of the AQY spectra for O_2^- in representative water types. Until we understand and constrain the photo-efficiency for O_2^- production, we cannot accurately predict P_{O2^-} on a global scale.

As confirmed here and elsewhere, bimolecular dismutation is not the major sink for superoxide in the open ocean (Hansard et al., 2010; Heller and Croot, 2010a; Rose et al., 2008). Therefore, the multiple first-order pathways for superoxide decay need to be accurately incorporated into the overall kinetic model. A compilation of O_2^- data from open ocean environments and a standardization of sample treatments for use in models will help immensely in this regard. For example, pseudo-first order decay rate constants have been determined in a variety of marine waters by adding known quantities of a superoxide standard to seawater (either as KO_2 or a photochemical standard) and monitoring the subsequent chemiluminescence signal (Heller and Croot, 2010c; Rusak et al., 2011). In these studies, however, spiked superoxide ranged from about 50 to 100 nM, well higher than *in situ* concentrations. While some studies suggest that this is not a problem (Heller and Croot, 2010b), with elevated O_2^- levels, and given the typically low nM reactant concentrations involved in open ocean ROS reactions, it is possible that measured decay rates may be altered. Perhaps indicating a dependence of decay pathway distribution on initial O_2^-, the k_{pseudo} values we determined for 25 – 42 nM spikes of the

photochemical standard into Gulf of Alaska samples were about 4 – 10 times higher than k_{pseudo} values determined post-irradiation, typically starting at $[O_2^-]_{ss} \approx 2$ nM (unpublished data). Therefore, it may be difficult to equate pseudo-first order decay kinetics determined from superoxide spikes to those appropriate for naturally occurring conditions. Unfortunately, there have only been a few shipboard studies measuring the decay of O_2^- concentrations that are representative of the open ocean (Hansard et al., 2010; Rusak et al., 2011). Without conclusive data on superoxide decay kinetics at ambient superoxide concentrations, it has been hard to figure out the best decay terms for use in $[O_2^-]_{ss}$ estimates based on remotely derived estimates of P_{H2O2}.

When attempting to understand the overall magnitude of superoxide decay as it relates to hydrogen peroxide formation, it is also essential to know the specific sink terms that control O_2^- decay. The observed pseudo-first order decay rate constants determined here represent the sum of all first order reaction rates. To accurately describe O_2^- decay in the open ocean, we now understand that not only is the magnitude of k_{pseudo} likely to change according to what drives O_2^- decay in different marine environments, but the stoichiometry of H_2O_2 production could change as well. Researchers have made a great deal of progress in recognizing the reactivity of superoxide with metals and organic matter. However, the rates for specific sink terms that control superoxide in seawater remain elusive. Heller and Croot (2010a) spiked ~50 nM of O_2^- standard into unamended seawater, as well as samples with added Cu, Fe or DTPA. Shaked et al. (2010) performed a very similar experiment with sub- to low-nM concentrations of O_2^-. By observing O_2^- decay in all of these treatments, both groups found Cu to be a major sink for O_2^- in both the Southern Ocean and the Gulf of Aqaba. Recently, Wuttig et al. (2013)

performed a similar experiment in the eastern tropical North Atlantic, but also included additions of Mn to seawater, finding that Mn and organics were the primary sinks for O_2^- in that region. Further mechanistic studies like this will increase our confidence when predicting O_2^- chemistry from modeled or observed photochemical H_2O_2 production.

4. Conclusions

Algorithms that derive *in situ* UV optical properties from remote sensing products are attractive in that they allow expanded spatial and temporal coverage when evaluating the role of photochemical reactions in the global ocean. To that end, we have expanded the methods of Fichot and Miller (2010) for estimating photochemical rates from ocean color data to include MODIS SST data, and have presented what we feel is a more accurate calculation of H_2O_2 photoproduction rates in the surface ocean. By blending maps for UV optics and temperature, an improvement over the previous use of a single AQY spectrum for the entire global ocean has been achieved. In the case of H_2O_2, the known temperature dependence for peroxide photochemical efficiency, as defined with published activation energies (Kieber et al., 2014; Miller 2000), can provide not only an improvement in estimated H_2O_2 photoproduction rates as shown here, but also a general approach for addressing any photochemical rate that has a definable temperature dependence. As is the case for all marine photochemical models using a photochemical efficiency approach, the accuracy with which peroxide production estimates can be made from optical data is primarily constrained by limited availability of H_2O_2 AQY spectral data and the ability to match observed variations in the surface ocean with proper AQY spectra. Improved confidence in this model to calculate global distributions of H_2O_2, O_2^-,

or any other photochemical product, will require well-defined, improved knowledge of the mechanisms regulating the system of interest.

To push our model approach towards estimation of surface ocean H_2O_2 *concentrations*, additional H_2O_2 sources, like rain and biological production, together with both abiotic (i.e. chemical reactions and mixing) and biological H_2O_2 sinks must be accurately described and incorporated. On the source side, oceanic microwave-based precipitation maps are available (Alder et al., 2012; Kucera et al., 2013), but the changing relation between rain rate and peroxide concentration over the ocean is not well constrained. Both production and consumption rates due to organisms depend on biological variability with additional sinks arising from chemical reactants (ex. Fe, Cu, organic antioxidants, etc.; Mostofa et al., 2013a,b). The detailed data required to modify and inform peroxide concentration models, especially in open ocean systems, are not currently fully retrievable from remote sensing and, the quantitative approaches to embed the temperature dependence for each are yet to be determined. With new comprehensive data on rates and mechanism, a concentration model for H_2O_2 in the surface ocean based on remotely sensed data may be attainable.

The method presented here to estimate O_2^- concentrations from H_2O_2 photoproduction rates is considerably more challenging than simply altering the H_2O_2 AQY spectra as a function of temperature. It actually represents a more general attempt to use remote sensing data together with direct knowledge of chemical reaction mechanisms to modify biogeochemical estimates related to photochemistry. We believe this is a promising direction for future work based on more than simple correlations. Our calculations rely heavily on the relationship between H_2O_2 and O_2^- photoproduction rates

and the O_2^- decay kinetics in the open ocean. At present, much about the processes that control the fate of O_2^- are not completely understood. After new work quantifies the photo-efficiency for O_2^- production and better defines the magnitude and partitioning of various sinks for superoxide, our estimates of superoxide steady-state values will be much better constrained. Because pseudo-first order O_2^- decay is almost certainly affected by both temperature and pH (in the same way as bimolecular dismutation), new data on the effects of these variables on O_2^- decay reactions should put things a bit more in focus. With this fundamental chemical information and clever use of multiple data products generated from remotely sensed data (S, pH, mixed layer depth, precipitation, etc.), it should be possible to quantify O_2^- concentrations with more accuracy on a global scale under current and future oceanic conditions. Although well beyond the scope of the present study, as more data on oceanic redox cycling becomes available, this approach can be used to make reasonable global estimates for the lifetimes of various important redox active elements like Fe, Cu and Mn, using their chemical reaction rates with ROS in the surface ocean.

Acknowledgements

This work was supported by NSF grant OCE-1234388 and NASA grant NNX07AD85G awarded to Dr. William L. Miller. The authors would like to thank Lydia Babcock-Adams, Jade Enright and the captain and crew of *R/V Pelican* and *R/V Melville* for sampling assistance and Dr. Wayne S. Gardner for the invitation to participate on the *R/V Pelican* cruise, supported by NOAA-CSCOR grant number NA07NOS4780225. We thank NASA for providing SeaWiFS, TOMS, and MODIS data and the American Meteorological Society for graduate student support for L.C.P. to attend the 2013 Duce Symposium at the 93rd AMS Annual Meeting, which led directly to the development of this paper.

References

Alder, R.F., Gu, G., Huffman, G.J., 2012. Estimating climatological bias errors for the global precipitation climatology project (GPCP). J. Appl. Meteor. Climatol. 51, 84–99. doi: 10.1175/JAMC-D-11-052.1

Akutsu, K., Nakajima, H., Katoh, T., 1995. Chemiluminescence of Cipridina luciferin analogues. Part 2. Kinetic studies on the reaction of 2-methyl-6-phenylimidazo pyrazin-3 (7H)-one (CLA) with. J. Chem. Soc., Perkin Trans. 2, 1699–1706.

Andrews, S.S., Caron, S., Zafiriou, O.C., 2000. Photochemical oxygen consumption in marine waters: A major sink for colored dissolved organic matter? Limnol. Oceanogr. 45, 267–277. doi:10.4319/lo.2000.45.2.0267

Baltar, F., Reinthaler, T., Herndl, G.J., Pinhassi, J., 2013. Major effect of hydrogen peroxide on bacterioplankton metabolism in the Northeast Atlantic. PLoS One. 8, e61051. doi:10.1371/journal.pone.0061051

Bielski, B.H.J., 1978. Reevaluation of the spectral and kinetic properties of HO_2 and O_2^- free radicals. Photochem. Photobiol. 28, 645–649.

Bielski, B.H.J., Cabelli, D.E., Arudi, R.L., Ross, A.B., 1985. Reactivity of HO_2/O_2^- radicals in aqueous solution. J. hys. Chem. Ref. Data. 14(4), 1041–1100.

Boyer, T.P., Levitus, S., Antonov, J.I., Locarnini, R.A., Garcia, H.E., 2005. Linear trends in salinity for the World Ocean, 1955–1998. Geophys. Res. Lett. 32, L01604. doi:10.1029/2004GL021791

Brown, O.B., Minnett, P.J., 1999. *MODIS infrared sea surface temperature algorithm, algorithm theoretical basis document*, Version 2.0, htpp://modis.gsfc.nasa.gov/data/atbd/atbd_mod25.pdf

Burns, J.M., Cooper, W.J., Ferry, J.L., King, D.W., DiMento, B.P., McNeill, K., Miller, C.J., Miller, W.L., Peake, B.M., Rusak, S.A., Rose, A.L., Waite, T.D., 2012. Methods for reactive oxygen species (ROS) detection in aqueous environments. Aquat. Sci. 74, 683–734. doi:10.1007/s00027-012-0251-x

Chen, Y., Hu, C., Hu, X., Qu, J., 2009. Indirect Photodegradation of Amine Drugs in Aqueous Solution under Simulated Sunlight. Environ. Sci. Technol. 43, 2760–2765. doi:10.1021/es803325j

Clark, C.D., De Bruyn, W.J., Jakubowski, S.D., Grant, S.B., 2008. Hydrogen peroxide production in marine bathing waters: Implications for fecal indicator bacteria mortality. Mar. Pollut. Bull. 56, 397–401. doi:10.1016/j.marpolbul.2007.10.017

Cooper, W.J., Zlka, R., Petasne, R.G., Plane, J.M.C., 1988. Photochemical Formation of H_2O_2 in Natural Waters Exposed to Sunlight. Environ. Sci. Technol. 22, 1156–1160.

Cudd, A., Fridovich, I., 1982. Electrostatic interactions in the reaction mechanism of bovine erythrocycte superoxide dismutase. J. Biol. Chem. 257(19), 11443–11447.

D'Sa, E.J., Steward, R.G., Vodacek, A., Blough, N. V., Phinney, D., 1999. Determining optical absorption of colored dissolved organic matter in seawater with a liquid capillary waveguide. Limnol. Oceanogr. 44, 1142–1148. doi:10.4319/lo.1999.44.4.1142

Dalrymple, R.M., Carfagno, A.K., Sharpless, C.M., 2010. Correlations between dissolved organic matter optical properties and quantum yields of singlet oxygen and hydrogen peroxide. Environ. Sci. Technol. 44, 5824–5829. doi:10.1021/es101005u

Fichot, C.G., Miller, W.L., 2010. An approach to quantify depth-resolved marine photochemical fluxes using remote sensing: Application to carbon monoxide (CO) photoproduction. Remote Sens. Environ. 114, 1363–1377. doi:10.1016/j.rse.2010.01.019

Fichot, C.G., Sathyendranath, S., Miller, W.L., 2008. Sea*UV* and SeaUV_C: Algorithms for the retrieval of UV/Visible diffuse attenuation coefficients from ocean color. Remote Sens. Environ. 112, 1584–1602. doi:10.1016/j.rse.2007.08.009

Fujimori, K., Nakajima, S.H., Akutsu, K., Mitani, M., Sawadab, H., Nakayamab, M., 1993. Chemiluminescence of cypridina luciferin analogues. Part 1. Effect of pH on rates of spontaneous autoxidation of CLA in aqueous buffer solutions. J. Chem. Soc., Perkin Trans. 2 2405–2409.

Garg, S., Rose, A.L., Waite, T.D., 2011. Photochemical production of superoxide and hydrogen peroxide from natural organic matter. Geochim. Cosmochim. Acta. 75, 4310–4320. doi:10.1016/j.gca.2011.05.014

Goldstone, J., Voelker, B., 2000. Chemistry of superoxide radical in seawater: CDOM associated sink of superoxide in coastal waters. Environ. Sci. Technol. 34, 1043–1048.

Hansard, P.S., Vermilyea, A.W., Voelker, B.M., 2010. Measurements of superoxide radical concentration and decay kinetics in the Gulf of Alaska. Deep Sea Res. Part I Oceanogr. Res. Pap. 57, 1111–1119. doi:10.1016/j.dsr.2010.05.007

Heller, M.I., Croot, P.L., 2010a. Superoxide decay kinetics in the southern ocean. Environ. Sci. Technol. 44, 191–196. doi:10.1021/es901766r

Heller, M.I., Croot, P.L., 2010b. Application of a superoxide (O_2^-) thermal source (SOTS-1) for the determination and calibration of O_2^- fluxes in seawater. Anal. Chim. Acta. 667, 1–13. doi:10.1016/j.aca.2010.03.054

Heller, M.I., Croot, P.L., 2010c. Kinetics of superoxide reactions with dissolved organic matter in tropical Atlantic surface waters near Cape Verde (TENATSO). J. Geophys. Res. 115, C12038. doi:10.1029/2009JC006021

Heller, M.I., Croot, P.L., 2011. Superoxide decay as a probe for speciation changes during dust dissolution in Tropical Atlantic surface waters near Cape Verde. Mar. Chem. 126, 37–55. doi:10.1016/j.marchem.2011.03.006

Helms, J.R., Stubbins, A., Ritchie, J.D., Minor, E.C., Kieber, D.J., Mopper, K., 2008. Absorption spectral slopes and slope ratios as indicators of molecular weight, source, and photobleaching of chromophoric dissolved organic matter. Limnol. Oceanogr. 53, 955–969. doi:10.4319/lo.2008.53.3.0955

Hu, C., Muller-karger, F.E., Zepp, R.G., 2002. Absorbance, absorption coefficient, and apparent quantum yield: A comment on common ambiguity in the use of these optical concepts. Limnol. Oceanogr. 47, 1261–1267.

Ishii, M., Kimoto, M., Sakamoto, K., Iwasaki, S.-I., 2006. Steric Sea Level Changes Estimated from Historical Ocean Subsurface Temperature and Salinity Analyses. J. Oceanogr. 62, 155–170.

Johannessen, S.C., Miller, W.L., 2001. Quantum yield for the photochemical production of dissolved inorganic carbon in seawater. Mar. Chem. 76, 271–283. doi:10.1016/S0304-4203(01)00067-6

Kieber, D.J., Miller, G.W., Neale, P.J., Mopper, K., 2014. Wavelength and temperature-dependent apparent quantum yields for photochemical formation of hydrogen peroxide in seawater. Environ. Sci. Process. Impacts 16, 777–791. doi:10.1039/c4em00036f

Kieber, D.J., Peake, B.M., Scully, N.M. 2002. Reactive oxygen species in aquatic ecosystems. In: Helbling, E.V., Zagarese, H., (Eds.), UV Effects in Aquatic Organisms. Royal Chemistry Society, Cambridge, UK, pp. 251–288.

King, D.W., Cooper, W.J., Rusak, S.A., Peake, B.M., Kiddle, J.J., O'Sullivan, D.W., Melamed, M.L., Morgan, C.R., Theberge, S.M., 2007. Flow injection analysis of H2O2 in natural waters using acridinium ester chemiluminescence: method development and optimization using a kinetic model. Anal. Chem. 79, 4169–4176. doi:10.1021/ac062228w

Kucera, P.A., Ebert, E.E., Turk, F.J., Levizzani, V., Kirschbaum, D., Tapiador, F.J., Loew, A., Borsche, M., 2013. Precipitation from space: advancing earth system science. Bull. Am. Meteorol. Soc. 94, 365–375.

Marion, G.M., Millero, F.J., Camões, M.F., Spitzer, P., Feistel, R., Chen, C.-T.A., 2011. pH of seawater. Mar. Chem. 126, 89–96. doi:10.1016/j.marchem.2011.04.002

McDowell, M.S., Bakač, Espenson, JH., 1983. A convenient route to superoxide ion in aqueous solution. Inorg. Chem. 22, 847–848.

Micinski, E., Ball, L., Zafiriou, O., 1993. Photochemical Oxygen Activation : Superoxide Radical Detection and Production Rates in the Eastern Caribbean. J. Geophys. Res. 98, 2299–2306.

Miller, G.W., 2000. Wavelength and temperature-dependent apparent quantum yields for phorochemical formation of hydrogen peroxide in seawater, in College of Environmental Science and Forestry, State University of New York, Syracuse, NY.

Miller, R.L., Belz, M., Castillo, C. Del, Trzaska, R., 2002. Determining CDOM absorption spectra in diverse coastal environments using a multiple pathlength, liquid core waveguide system. Cont. Shelf Res. 22, 1301–1310. doi:10.1016/S0278-4343(02)00009-2

Miller, W.L., Kester, D.R., 1988. Hydrogen Peroxide Measurement in Seawater by (p-Hydroxyphenyl)acetic Acid Dimerization. Anal. Chem. 60, 2711–2715.

Moffett, J.W., Zika, R.G., 1987. Reaction kinetics of hydrogen peroxide with copper and iron in seawater. Environ. Sci. Technol. 21, 804–810. doi:10.1021/es00162a012

Moore, C., Farmer, C., Zika, R., 1993. Influence of the Orinoco River on Hydrogen Peroxide Distribution and Production in the Eastern Caribbean. J. Geophys. Res. 98, 2289–2298.

Morris, J.J., Johnson, Z.I., Szul, M.J., Keller, M., Zinser, E.R., 2011. Dependence of the cyanobacterium Prochlorococcus on hydrogen peroxide scavenging microbes for growth at the ocean's surface. PLoS One 6. e16805. doi:10.1371/journal.pone.0016805

Mostofa, K.M., Liu, C.Q., Sakugawa, H., Vione, D., Minakata, D., Wu, F., 2013a. Photoinduced and microbial generation of hydrogen peroxide and organic peroxides in natural waters. In: Photobiogeochemistry of Organic Matter. Springer, Berlin, Heidelberg, pp. 139–207.

Mostofa, K.M., Liu, C.Q., Gao, K., Li, S., Vione, D., Mottaleb, M.A., 2013b. Impacts of global warming on biogeochemical cycles in natur waters. In: Photobiogeochemistry of Organic Matter. Springer, Berlin, Heidelberg, pp. 851–915.

Nelson, N.B., Siegel, D.A., Carlson, C.A., Swan, C., Smethie, W.M., Khatiwala, S., 2007. Hydrography of chromophoric dissolved organic matter in the North Atlantic. Deep Sea Res. Part I Oceanogr. Res. Pap. 54, 710–731. doi:10.1016/j.dsr.2007.02.006

Ong, T.-C., 2007. Detailed mechanistic and optimization of the photochemical production method of superoxide, in Department of Chemistry, Colby College, Waterville, ME.

O'Sullivan, D.W., Neale, P.J., Coffin, R.B., Boyd, T.J., Osburn, C.L., 2005. Photochemical production of hydrogen peroxide and methylhydroperoxide in coastal waters. Mar. Chem. 97, 14–33. doi:10.1016/j.marchem.2005.04.003

Petasne, R.G., Zika, R.G., 1987. Fate of superoxide in coastal seawater. Nature. 325, 516–618.

Reader, H.E., Miller, W.L., 2011. Effect of estimations of ultraviolet absorption spectra of chromophoric dissolved organic matter on the uncertainty of photochemical production calculations. J. Geophys. Res. 116, C08002. doi:10.1029/2010JC006823

Reader, H.E., Miller, W.L., 2012. Variability of carbon monoxide and carbon dioxide apparent quantum yield spectra in three coastal estuaries of the South Atlantic Bight. Biogeosciences. 9, 4279–4294. doi:10.5194/bg-9-4279-2012

Rose, A.L., Moffett, J.W., Waite, T.D., 2008a. Determination of Superoxide in Seawater Using Using 2-Methyl-6-(4-methoxyphenyl)-3,7-dihydroimidazo[1,2-a]pyrazin-3(7H)-one chemiluminescence. Anal. Chem. 80, 1215–1227.

Rose, A.L., Waite, T.D., 2006. Role of superoxide in the photochemical reduction of iron in seawater. Geochim. Cosmochim. Acta. 70, 3869–3882. doi:10.1016/j.gca.2006.06.008

Rose, A.L., Webb, E.A., Waite, T.D., Moffett, J.W., 2008b. Measurement and implications of nonphotochemically generated superoxide in the equatorial Pacific Ocean. Environ. Sci. Technol. 42, 2387–2393.

Ruggaber, A., Dlugi, R., Nakajima, T., 1994. Modeling Radiation Quantities and Photolysis Frequencies in the Troposphere. J. Atmos. Chem. 18, 171–210.

Rusak, S.A., Peake, B.M., Richard, L.E., Nodder, S.D., Cooper, W.J., 2011. Distributions of hydrogen peroxide and superoxide in seawater east of New Zealand. Mar. Chem. 127, 155–169. doi:10.1016/j.marchem.2011.08.005

Scully, N.M., Cooper, W.J., Tranvik, L.J., 2003. Photochemical effects on microbial activity in natural waters: the interaction of reactive oxygen species and dissolved

organic matter. FEMS Microbiol. Ecol. 46, 353–357. doi:10.1016/S0168-6496(03)00198-3

Shaked, Y., Harris, R., Klein-Kedem, N., 2010. Hydrogen peroxide photocycling in the Gulf of Aqaba, Red Sea. Environ. Sci. Technol. 44, 3238–3244.

Steigenberger, S., Croot, P.L., 2008. Identifying the processes controlling the distribution of H_2O_2 in surface waters along a meridional transect in the eastern Atlantic. Geophys. Res. Lett. 35, L03616. doi:10.1029/2007GL032555

Steinacher, M., Joos, F., Frolicher, T.L., Plattner, G.-K., Doney, S.C., 2009. Imminent ocean acidification in the Arctic projected with the NCAR global coupled carbon cycle-climate model. Geophys. Res. Lett. 6, 515–533.

Swan, C.M., Nelson, N.B., Siegel, D. a, Kostadinov, T.S., 2012. The effect of surface irradiance on the absorption spectrum of chromophoric dissolved organic matter in the global ocean. Deep. Res. Part I-Oceanographic Res. Pap. 63, 52–64. doi:10.1016/j.dsr.2012.01.008

Szymczak, R., Waite, T., 1988. Generation and decay of hydrogen peroxide in estuarine waters. Aust. J. Mar. Freshw. Res. 39, 289–299. doi:10.1071/MF9880289

Voelker, B.M., Sedlak, D.L., 1995. Iron reduction by photoproduced superoxide in seawater. Mar. Chem. 50, 93–102.

Voelker, B.M., Sulzberger, B., 1996. Effects of Fulvic Acid on Fe(II) Oxidation by Hydrogen Peroxide. Environ. Sci. Technol. 30, 1106–1114. doi:10.1021/es9502132

White, E.M., Vaughan, P.P., Zepp, R.G., 2003. Role of the photo-Fenton reaction in the production of hydroxyl radicals and photobleaching of colored dissolved organic matter in a coastal river of the southeastern United States. Aquat. Sci. - Res. Across Boundaries. 65, 402–414. doi:10.1007/s00027-003-0675-4

Wuttig, K., Heller, M.I., Croot, P.L., 2013a. Pathways of superoxide (O_2^-) decay in the Eastern Tropical North Atlantic. Environ. Sci. Technol. 47, 10249–10256. doi:10.1021/es401658t

Wuttig, K., Heller, M.I., Croot, P.L., 2013b. Reactivity of inorganic Mn and Mn desferrioxamine B with O2, O_2^-, and H_2O_2 in seawater. Environ. Sci. Technol. 47, 10257–10265. doi:10.1021/es4016603

Yocis, B.H., Kieber, D.J., Mopper, K., 2000. Photochemical production of hydrogen peroxide in Antarctic Waters. Deep Sea Res. Part I Oceanogr. Res. Pap. 47, 1077–1099. doi:10.1016/S0967-0637(99)00095-3

Zafiriou, O.C., 1990. Chemistry of superoxide ion-radical (O_2^-) in seawater. I . pK^*a_{sw} (HOO) and uncatalyzed dismutation kinetics studied by pulse radiolysis. Mar. Chem. 30, 31–43.

Zepp, R.G., Callaghan, T.V., Erickson III, D.J., 2003. Interactive effects of ozone depletion and climate change on biogeochemical cycles. Photochem. Photobiol. Sci. 2, 51–61. doi:10.1039/b211154n

Zhang, Y., Del Vecchio, R., Blough, N.V., 2012. Investigating the mechanism of hydrogen peroxide photoproduction by humic substances. Environ. Sci. Technol. 46, 11836–11843. doi:10.1021/es3029582

CHAPTER 4

PROBING THE PHOTOCHEMICAL REACTIVITY OF DEEP OCEAN REFRACTORY CARBON (DORC): LESSONS FROM HYDROGEN PEROXIDE AND SUPEROXIDE KINETICS[1]

---

[1]L.C. Powers, Babcock-Adams, L.C, Enright, J.K., and W.L. Miller. Submitted to *Marine Chemistry*, 10/31/14.

Abstract

The marine dissolved organic carbon (DOC) pool is a vast reservoir of reduced carbon, containing about the same mass of carbon stored in the atmosphere as CO_2. Most marine DOC is thought to be biologically recalcitrant with one removal pathway proposed as photochemical reactions when refractory DOC circulates through sunlit surface waters (Mopper et al., 1991). Here, we reevaluate the photoreactivity of refractory DOC by investigating the photochemical production of two reactive oxygen species (ROS), hydrogen peroxide (H_2O_2) and superoxide (O_2^-), using controlled irradiations at sea and in the laboratory. The deep ocean DOC pool in the North Pacific is almost entirely refractory and in particular, waters are not formed locally and are therefore the most of all aged marine waters. The photoproduction of these two ROS were primarily compared between bottom and surface water samples collected in the Gulf of Alaska. For irradiated samples, initial superoxide steady-state concentrations ($[O_2^-]_{ss}$) and first-order decay constants (k_{pseudo}) were similar between surface and deep waters, ranging from ~1 – 4 nM and 4 – 12 x 10^{-3} s^{-1}, respectively. Initial photoproduction rates were comparable between surface and deep waters, ranging from 6 – 48 pM s^{-1} for O_2^- and from 1 – 8.3 nM h^{-1} for H_2O_2, indicating that a large portion of photoproduced O_2^- does not lead to H_2O_2 formation. Results indicate that in this environment, dismutation is not the dominant sink for O_2^- and the stoichiometry of H_2O_2 formation from O_2^- is not 1:2 as expected from dismutation. Continued irradiation for up to 48 hours showed photoproduced H_2O_2 to be much lower in deep samples compared to surface samples with accumulation slowing or stopping in deep samples despite both measurable $[O_2^-]_{ss}$ and photon absorbance by colored dissolved organic matter (CDOM). These results are

consistent with a loss of source material (i.e. CDOM) for O_2^- photoproduction and a shift to a predominantly oxidative pathway for O_2^- decay. Low photoproduction rates, loss of continued accumulation with extended radiation, and an apparent loss of O_2^- source material argues that the deep refractory DOC pool is less photochemically reactive than previously suggested.

1. Introduction

The marine dissolved organic carbon (DOC) pool contains 662 ± 32 Pg C (Hansell et al., 2009) and is therefore one of Earth's largest active carbon reservoirs, similar in size to the carbon stored as CO_2 in the atmosphere. Marine DOC has been classified based on qualitative assessments of its reactivity, ranging from labile DOC that is turned over on time scales of minutes to days to refractory DOC that survives from years to millennia (Carlson, 2002; Kirchman et al., 1993). Refractory DOC is largely biologically unavailable, with a mean radiocarbon age of 4000 – 6000 years (Bauer et al., 1992; Williams and Druffel, 1987), and comprises the majority of the oceanic carbon pool (~642 Pg C; Hansell, 2013). Currently, a quantitative assessment of refractory DOC turnover has been hampered by the fact that neither its sources nor sinks are completely understood (Hansell, 2013). Since refractory DOC cycles on timescales of millennia, a better understanding of the processes responsible for changes in this pool may provide insight into its role in past and future climates (Sexton et al., 2011). For instance, ventilation and oxidation of DOC from the ocean's interior has been implicated in rapid hyperthermal warming events during the Palaeogene period (Sexton et al., 2011).

Refractory DOC is ubiquitous in the ocean, with deep ocean (>1000 m) refractory carbon (DORC) representing ~70% of the entire DOC pool (Hansell et al., 2009).

Carbon dynamics in the deep sea remain largely unstudied due to the large spatial and temporal scales required to comprehensively sample deep ocean basins. As more bulk DOC concentration data has become available, however, models of DOC concentration gradients and radiocarbon ages have been used to indirectly estimate an average refractory DOC removal rate of ~0.003 μmol C kg^{-1} yr^{-1} in the deep ocean (Hansell et al., 2009; Hansell et al., 2012). Further analysis suggests that refractory DOC may be conserved during circulation but that unknown local sinks exist in both the deep far North Pacific and mid depth subtropical South Pacific (Hansell and Carlson 2013). On the other hand, one identified sink for refractory DOC appears to be via UV photooxidation as it circulates through the surface ocean (Mopper et al., 1991; Stubbins et al., 2012). Based on increased photoproduction rates for select low molecular weight carbonyl compounds in short (<5 h) irradiations of deep Atlantic water relative to surface samples, Mopper et al. (1991) estimated a residence time for photolabile biorefactory DOC of ~2100 years, well below its measured average age. This inconsistency and the lack of follow-up investigations on the strength of this photochemical sink for refractory DOC argue that further evaluation is warranted.

While direct links between radical photoproducts and the carbon cycle have not been fully addressed, the formation of reactive oxygen species (ROS) is ubiquitous in irradiated marine waters and should be a useful proxy for DOC photoreactivity. Accordingly, Mopper and Zhou (1990) used increased photoproduction of hydroxyl radicals (•OH) in deep Sargasso Sea samples relative to surface samples from the same location to argue for increased photoreactivity of deep ocean DOC. Hydrogen peroxide (H_2O_2) and its precursor, superoxide (O_2^-), are long-lived photoproducts of CDOM

relative to other ROS (e.g. $^{\bullet}OH$ and $^1O_2$) and their study has the benefit of sensitive (sub-nanomolar) chemiluminescent detection methods (King et al., 2007; Rose et al., 2008a). Based on a detailed mechanistic investigation involving borohydrate reduction and triplet state quenchers, Zhang et al. (2012) suggest that the formation of O_2^- arises from electron transfer from excited state CDOM to form oxygen reducing intermediates ($CDOM^{+/-}$) that then react with O_2 to generate O_2^-. Traditionally, H_2O_2 formation has been described by O_2^- disproportionation via the following reactions (O'Sullivan et al., 2005):

$$HO_2 + O_2^- \rightarrow HO_2^- + O_2 + OH^- \qquad (k_1 = 9.7 \times 10^7\ M^{-1}s^{-1}) \qquad (4.1)$$

$$HO_2 + HO_2 \rightarrow H_2O_2 + O_2 \qquad (k_2 = 8.3 \times 10^5\ M^{-1}s^{-1}) \qquad (4.2)$$

$$H^+ + O_2^- \longleftrightarrow HO_2 \qquad (K_a = 1.6 \times 10^{-5}\ M^{-1}) \qquad (4.3)$$

where HO_2 is the conjugate acid of O_2^-, k_1 and k_2 are rate constants determined in pure water at 25°C and K_a is the superoxide acidity constant (Bielski et al., 1985). Zafiriou (1990) reported similar superoxide dismutation kinetics in seawater, determining a pK_a of 4.60 ± 0.15, and defining the overall second order rate law for O_2^- decay via dismutation as

$$\frac{d[O_2^-]}{dt} = k_{dis}[O_2^-][HO_2] \approx 2k_D[O_2^-]^2 \qquad (4.4)$$

where k_D for seawater = (5 ± 1) x $10^{12}[H^+]$, thus confirming a direct dependence on pH for O_2^- kinetics similar to that described for pure water (Bielski et al., 1985).

In addition to H_2O_2 formation via O_2^- dismutation, metals (e.g. Fe, Cu, and Mn) and CDOM also efficiently react with O_2^- in natural waters (Goldstone and Voelker, 2000; Heller and Croot, 2010a, 2010b; Wuttig et al., 2013). Because O_2^- can act as both an oxidant and a reductant, its decay pathways are far more complex than can be

described by dismutation alone (Voelker and Sedlak, 1995; Zafiriou, 1990). Reactions of CDOM and/or metals (A) with O_2^- could produce either H_2O_2 or O_2 via the equations

$$A_{ox} + O_2^- \rightarrow A_{red} + O_2 \quad (4.5)$$

$$A_{red} + O_2^- \xrightarrow{2H^+} A_{ox} + H_2O_2 \quad (4.6)$$

where A_{ox} is an oxidant and A_{red} is a reductant. If the catalytic O_2^- decay described above is irreversible, then the amount of H_2O_2 generated per O_2^- should be between 0 and 1. On the other hand, if catalytic redox cycling is occurring between A_{ox} and A_{red}, then the same stoichiometry typical of dismutation ($0.5H_2O_2$ per O_2^-) should be maintained. These possible pathways create confusion in determining which pathway (or neither) is dominant in superoxide decay. Studies using additions of superoxide dismutase (SOD), an enzyme that ensures O_2^- decay through dismutation, have been done to ascertain the proportion of O_2^- decay leading to H_2O_2. For irradiated samples collected in the Gulf of Aqaba (Shaked et al., 2010), as well as surface water from the Gulf of Alaska (Powers and Miller, 2014), H_2O_2 photoproduction in the presence of SOD was indistinguishable from that produced in its absence, leading to estimates of $0.5H_2O_2$ molecules formed per O_2^-. However, other evidence suggests that the oxidative pathway (Equation 4.5) may dominate O_2^- decay based on direct superoxide steady state ($[O_2^-]_{ss}$) and H_2O_2 measurements ($0.37H_2O_2$ per O_2^- albeit for unfiltered samples; Rusak et al., 2011). Even though these studies suggest that the fate of superoxide in seawater is complex and likely specific to season and oceanic region, examining open ocean O_2^- and H_2O_2 photochemical production together should be a better indicator of general photoreactivity than the photoproduction of small organic carbon molecules, which may require more specific reactions and starting material.

A number of studies using chemiluminescent methods have attempted to rectify the issues stated above by investigating the dominant superoxide decay pathways in seawater (Heller and Croot, 2010a, 2010b; Voelker et al., 2000; Wuttig et al., 2013). An interesting observation resulting from these recent superoxide studies is evidence for a widespread particle associated, biological source of superoxide (Diaz et al., 2013; Hansard et al., 2010; Rose et al., 2008b). While some studies attribute O_2^- signals to a predominately biological source, most of the open ocean $[O_2^-]_{ss}$ measurements have been made well after samples are removed from UV radiation and do not fully reflect the photochemical source (Hansard et al., 2010; Rose et al., 2008b). Despite the recognition that DOM photolysis in natural waters will produce O_2^- at significant rates (Micinski et al., 1993; Petasne and Zika, 1987; Zafiriou et al., 1990) direct O_2^- photoproduction rates in marine environments are rare. Additionally, early seawater superoxide studies using the NO probe by Micinski et al. (1993) and Zafiriou et al. (1990) may underestimate photoproduction rates by 30 – 40% (Blough and Zepp, 1995). Therefore, further investigation of abiotic O_2^- production in seawater via photochemical reactions is warranted.

With this in mind, we have made direct measurements of both H_2O_2 and O_2^- concentrations during controlled laboratory and shipboard irradiations of deep ocean water (containing essentially only DORC), mesopelagic water, and surface samples (DORC plus semi-labile fractions of DOC). The focus of this paper is twofold; to assess the reactivity of DORC using the dynamics and relationships of photochemically generated H_2O_2 and O_2^- and to provide a better evaluation of direct O_2^- photoproduction rates in open ocean seawater.

2. Methods

2.1 Sample Collection and Handling

Surface seawater samples (~5m), abyssal seawater samples (deepest cast depth, ~3500-5000m), and mesopelagic samples (~1000m), were collected in the Gulf of Alaska onboard the R/V *Melville* in August 2013 (Figure 4.1) and *in situ* hydrographic (depth, T, S) and chemical (nitrate, nitrite, ammonia, silicate, phosphate, oxygen) distribution data sets were collected for each cast and submitted to the U.S. Biological and Chemical Oceanography Data Management Office by the chief scienctist (D. Hansell, University of Miami; http://www.bco-dmo.org/dataset/527102). Samples used for photochemical experiments were 0.2 μm gravity-filtered (Whatman; Polycap-36&75AS) directly from standard Niskin bottles into 2 L acid-cleaned (overnight in 2 M HCl), Milli-Q (Millipore; >18 MΩ) rinsed polycarbonate bottles (Nalgene). Samples for shipboard hydrogen peroxide and superoxide irradiation experiments were typically partitioned directly into acid-cleaned, Milli-Q rinsed, 10 cm quartz spectrophotometric cells (Spectrocell; H_2O_2 measurements only) or into 0.6 or 1.0 L jacketed beakers (Ace Glass) with quartz lids, either within hours of collection or stored (typically 1 – 2 days) on the ship at 4 °C until use. All samples were maintained at ~20 °C with a recirculating water bath during irradiation. While all equipment in contact with seawater samples was acid cleaned as described above and nitrile gloves were used in handling samples, the R/V *Melville* was not equipped with special trace metal processing facilities and consequently, limited trace metal contamination could be present. Post cruise, remaining samples were shipped cold back to the laboratory and stored at 4 °C until use. CDOM absorption

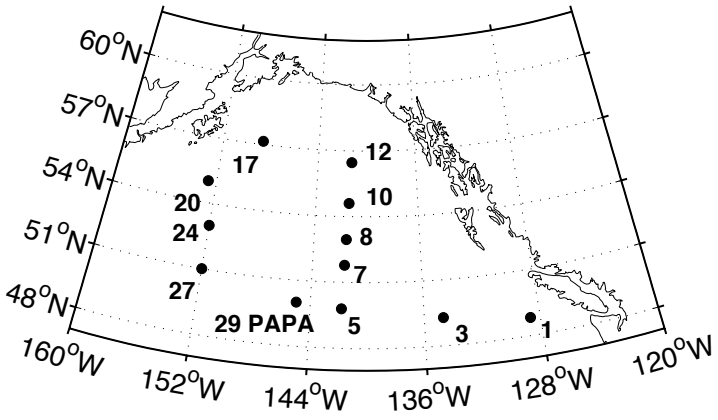

Figure 4.1. Stations sampled between August 5, 2013 and August 22, 2013 in the Gulf of Alaska.

spectra exhibit no significant changes when stored in this manner for up to 12 months (Johannessen and Miller, 2001; Swan et al., 2012) and photochemical properties are often assumed unchanged. Shipboard results are directly compared to post cruise laboratory irradiations to assess any potential effects from sample storage.

2.2 Determinations of Photoproducts

2.2.1 Hydrogen Peroxide Analysis

H_2O_2 was measured using a FeLume chemiluminescence (CL) system (Waterville Analytical) and modifications to the methods of King et al. (2007). Briefly, samples were mixed with 2 μM 10-methyl-9-(p-formylphenyl)-acridinium carboxylate trifluoromethanesulfonate (AE; provided by Dr. James J. Kiddle, Western Michigan University), which reacts with H_2O_2 to chemiluminesce at alkaline pH in this flow injection analysis system. A syringe was used to flush (≥1 mL) and fill a 195 μL Teflon sample loop (VICI 10-port valve) that was subsequently mixed with the AE reagent using a peristaltic pump (Rainin) and the sample/carrier – AE mix was transported to a spiral flow cell located in front of a photomultiplier tube (PMT; Hamamatsu HC135 PMT, 900 V, 400 ms integration) where it mixed with 0.1 M carbonate buffer to initiate CL. Decreased carbonate buffer pH (10.4) with 0.2 M HCl as the carrier prevented interference by precipitated $MgOH_2$ and helped decrease background CL. A ~2 mM H_2O_2 stock solution was prepared from 30% H_2O_2 (J.T. Baker) and checked both prior and post cruise using its absorbance (molar absorptivity of 38.1 $M^{-1} cm^{-1}$ at 240 nm; Miller and Kester, 1988) on a benchtop spectrophotometer (Perkin Elmer Lambda 40) with Milli-Q as the absorbance blank. Standards were prepared in seawater samples matching those used in irradiations and were checked for low or undetectable H_2O_2

starting values against the same seawater with added catalase (20 μL of 100 units L^{-1} in 20 mL seawater; C100 Sigma-Aldrich). Under these conditions, the H_2O_2 detection limit, defined as three times the standard deviation of the blank, was 2.2 nM.

2.2.2 Superoxide Analysis

Superoxide was also measured using the FeLume system employing the chemiluminescent reaction between O_2^- and a methyl *Cypridina* luciferin analogue (2-methyl-6-(4-methoxyphenyl)-3,7-dihydroimidazo[1,2-a]pyrazin-3(7*H*)-one; MCLA; TCI America), following the methods of Rose et al. (2008) and Garg et al. (2011). In this case, no sample loop was used and both the seawater sample and chemiluminescent (CL) reagent were continuously pumped directly to the flow cell where CL signal was measured (PMT 1200V, 800 ms integration time). The CL reagent contained 2.45 μM MCLA in 50 mM sodium acetate/50 μM diethylenetriaminepentaacetic acid (DTPA) solution, adjusted to pH 6 with concentrated HCl. A pH of 6 was selected because the chemiluminescent reaction of the conjugate base of MCLA ($MCLA^-$; pKa = 7.64 ± 0.03) with molecular oxygen increases background signal at basic pH (Fujimori et al., 1993) and the rate of uncatalyzed superoxide dismutation increases at acidic pH (Equations 4.1 and 4.2). To prevent changes in signal due to changes in reaction temperature (Heller and Croot, 2010c), all solutions were equilibrated to room temperature prior to each experiment. Occasionally the enzyme superoxide dismutase (SOD; 200 U L^{-1} from manufacturer's assay; S5395-15KU Sigma) was added at the end of irradiation experiments to observe the subsequent signal reduction to near pre-irradiation background levels. A stock solution of ~1.5 x 10^6 U L^{-1} SOD was prepared in Milli-Q and stored at 4 °C in the dark when not in use. With SOD in solution, we observed no

photochemical production when re-irradiating the sample, ensuring that changes in FeLume signal during non SOD irradiations were due to photochemically generated O_2^-. Because SOD can interfere with MCLA autooxidation (i.e. the $MCLA^-$ CL reaction with oxygen; Fujimori et al., 1993; Hansard et al. 2010), and lower the FeLume signal below the baseline, pre-irradiation baselines were always subtracted from O_2^- photoproduction data.

2.2.3 Superoxide System Calibration and Standards

The instability of superoxide in aqueous solutions creates analytical issues for all methods that produce superoxide standards in μM concentrations (Heller and Croot, 2010c). To calibrate the MCLA-O_2^- reaction in the FeLume system for each freshly prepared MCLA reagent, superoxide standards were generated via the UV photolysis of acetone in an ethanol solution following modifications to the methods of McDowell et al. (1983) and the recommendations of Ong (2007). A solution of 41 mM acetone, 6 M ethanol, 30 μM DTPA in 0.1 M borate buffer (pH = 12.5) was irradiated in a "superoxide generator" (Waterville Analytical) in a 1 cm quartz cell with a Hg lamp (Pen-Ray) for ≤30 seconds. The concentration of superoxide was monitored in real time using the absorbance at 240 nm, blanked with the absorbance of the solution at 400 nm (Ong 2007), and a O_2^- extinction coefficient (ε) of 2183 M^{-1} cm^{-1} corrected for the absorbance of H_2O_2 at 240 nm as described by Bielski (1978) as follows

$$\varepsilon_{O2\text{-}\,CORRECTED} = \varepsilon_{O2\text{-}} - 0.5\varepsilon_{H2O2}\ M^{-1}\ cm^{-1} = 2183 \text{ at pH } 12.5 \qquad (4.7)$$

Absorbance measurements of these superoxide standards were made using a USB2000-UV-VIS Miniature Fiber Optic Spectrometer (Ocean Optics) linked to a DT-MINI-2-GS light source (Ocean Optics) with Premium grade Si fiber optics. Un-irradiated

acetone/ethanol solution was used as the absorbance blank. It has been noted that DTPA breaks down in UV light causing absorbance increases that can interfere with O_2^- determination (Heller and Croot, 2010c), but given the very short irradiation time required to generate O_2^- in our standard method, it is not likely that DTPA photolysis contributed significantly to the absorbance reading. For this reason, however, seawater irradiations under the solar simulator and coincident superoxide data reported here never contain DTPA. When the superoxide reached about 100 μM, an aliquot was withdrawn and spiked into filtered seawater samples containing 30 μM DTPA to eliminate metal catalyzed O_2^- decay (Heller and Croot, 2010a; Hansard et al., 2010). Concentrations after these spikes for O_2^- standards ranged from 5 - 50 nM ($[O_2^-]_0$) and were monitored by the FeLume for ~10 minutes. O_2^- decay was described with the following equation

$$\frac{-\mathrm{d}[O_2^-]}{\mathrm{dt}} = 2k_D[O_2^-]^2 + \sum k_M[M]_X[O_2^-] + k_{pseudo}[O_2^-] \quad (4.8)$$

where k_D is the pH dependent dismutation rate constant, k_M is the rate constant for the reaction of superoxide with metal species (M_x), and k_{pseudo} is the rate constant for the reaction of O_2^- with other sinks like CDOM (Goldstone and Voelker, 2000). If all pseudo-first order decay terms are summed, or metal sink terms are eliminated with the chelator DTPA, as is the case with our standards, then Equation 4.8 reduces to

$$\frac{-\mathrm{d}[O_2^-]}{\mathrm{dt}} = 2k_D[O_2^-]^2 + k_{pseudo}[O_2^-] \quad (4.9)$$

We assumed that the FeLume signal (S, corrected for background chemiluminescence) is directly proportional to O_2^- concentration ($S = C\,[O_2^-]$) based on previous work (Heller and Croot 2011, 2010a, 2010b), and modeled S as a function of time (t) with the following equation (Garg et al., 2011; Heller and Croot, 2010a)

$$S = \frac{k_{\text{pseudo}} S_0}{k_{\text{pseudo}} e^{k_{\text{pseudo}} t} + k_D [O_2^-]_0 (e^{k_{\text{pseudo}} t} - 1)} \quad (4.10)$$

where S_0 is the FeLume signal at time zero and $[O_2^-]_0$ is the spiked superoxide concentration. FeLume data was fit to Equation 4.10 with a non-linear regression of signal (S) over time (t) using the curve fitting routine *nlinfit* in MATLAB®. The second order dismutation rate constant, k_D, was calculated for each seawater sample using Equation 4.4 (Zafiriou, 1990) and pH values determined with a Ross Ultra, glass combination pH electrotrode (Thermo Scientific) calibrated with NBS standard buffers. Although calibrating seawater pH with Tris buffers of a composition and ionic strength similar to seawater is recommended (Marion et al., 2011), here we chose NBS buffers for direct compatibility with k_D values determined in seawater by Zafiriou (1990). For each set of standards, a linear regression of S_0 vs $[O_2^-]_0$ gave C values ranging from 1.53 to 3.62×10^4 counts nM^{-1} ($r^2 > 0.90$ for all standard curves, n = 8) which were used in subsequent O_2^- concentration determinations.

2.3 Photochemical Irradiations

All irradiations were preformed using two identical Suntest CPS solar simulators equipped with a 1.5 kW xenon lamp (Atlas) fitted with a window glass to simulate sunlight reaching the earth's surface (~305 nm and above, Figure 4.2). Two separate sample exposure configurations were used for photochemical experiments. The first was used solely for photochemical H_2O_2 determinations to provide a highly quantifiable light field. The second was used for simultaneous determinations of photoproduced H_2O_2 and O_2^- in jacketed beakers. Both systems are described in detail below.

2.3.1 Experiments for Determination of H_2O_2 Photoproduction Rates and Efficiencies

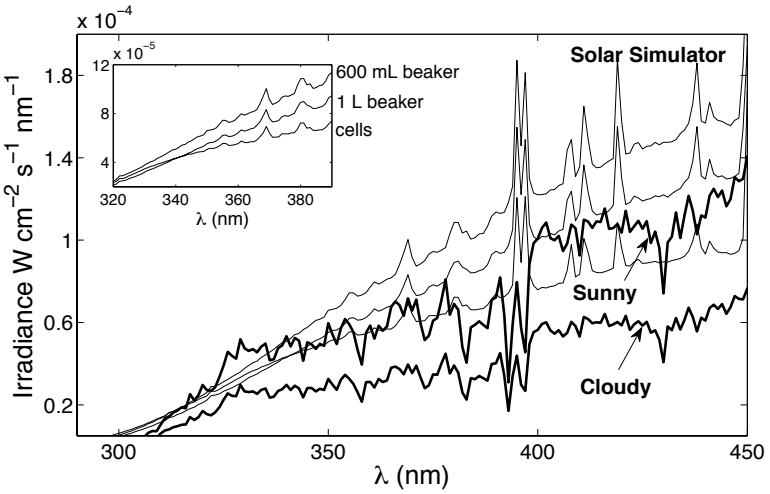

Figure 4.2. Measured irradiance (W cm^{-2} s^{-1} nm^{-1}) under the solar simulator entering the various experimental setups used in this study (thin black lines) compared to measured irradiance on a sunny day (Station 6, 50.75N 141.73 W, August 8, 2013 at 2:45 PM, PST) and on a cloudy day (Station 8, 52.95 N 141.55 W, August 9, 2013, 2:30 PM, PST) collected on the ship (bold black lines). The inset graph shows the irradiance for all solar simulator setups from highest to lowest: 600 mL jacketed beakers on a stir plate, 1 L jacket beakers on the benchtop, and the average irradiance for spectrophotometric cells in the water cooled aluminum block).

For these exposures, each seawater sample was brought to room temperature and distributed into 15 matched 10 cm cylindrical quartz spectrophotometric cells, filled with no headspace and sealed using gas-tight caps fitted with Teflon faced, butyl rubber septa. Cells were placed vertically below the solar simulator into a black, water-cooled, aluminum irradiation block fitted with a half inch grey PVC lid with 1.6 cm apertures directly above the cell windows to eliminate residual off-axis photons. The block maintained the samples at 20 °C and allowed no transfer of light between cells during irradiation. Wavelength dependent experiments were also performed on surface and deep seawater samples by aligning the block, and therefore each cell, under a variety of evenly spaced Schott long-band-pass cutoff filters (305, 320, 335, 345, 380, 425, and 480 nm). We measured no significant H_2O_2 photoproduction under the 425 and 480 nm cutoff filters. Similar studies suggest that less than 15% of total H_2O_2 photoproduction is caused by wavelengths above 400 nm (Kieber et al., 2014). Dark cells were kept in the water bath until the end of the irradiation. For broadband irradiations, the long band-pass cutoff filters were removed, allowing for the irradiation of 15 cells simultaneously (typically sampling in triplicate for each time point). The spectral downwelling irradiance entering each cell, $E_0(\lambda)$ (mol(photons) m^{-2} s^{-1} nm^{-1}), was quantified at 1 nm intervals with a UV-Vis portable spectroradiometer (OL756; Optronic Laboratories) fitted with a quartz fiber optic cable and 2 inch diameter integrating sphere. Solar irradiance was also measured throughout the cruise, replacing the 2 inch integrating sphere with a 6 inch diameter integrating sphere with a quartz dome window (OLIS-670; Optronic Laboratories). The OL756 was calibrated for both collection spheres with a NIST standard lamp (OL752-10 irradiance standard; Optronic Laboratories) pre and post cruise. Measured irradiance

entering each cell very closely matches mid day irradiance measured throughout the cruise (typical scans shown in Figure 4.2).

The sample absorbance in each sample cell was measured from 250 – 800 nm both prior to, during and post irradiation with a MAYA2000-Pro UV-VIS spectrometer (Ocean Optics) connected to a 1 meter liquid waveguide capillary flow cell (LWCC-2100 Type II; World Precision Instruments). The LWCC was filled via a peristaltic pump positioned to pull the sample through Teflon tubing. Because Milli-Q water was used as the absorbance blank, the Perkin Elmer Lamda 40 dual beam spectrophotometer was used to check UV CDOM absorbance measurements in 10 cm spectrophotometric cells post cruise on the same samples made during the cruise using the LWCC. Raw absorbance spectra were corrected for possible scattering, refractive index differences between salt water and the pure water blank, and instrument drift by fitting individual spectra to the equation:

$$A = Fe^{-S\lambda} + O \tag{4.11}$$

using the MATLAB® nonlinear curve fitting routine *nlinfit*, where A (unitless) is absorbance, F is a fitting coefficient, S is the spectral slope coefficient, and O is the offset (Reader and Miller, 2011). Data was fit over the 680 – 800 nm range for 10 cm spectrophotometer cells and over the 700 – 750 nm range for the 1 m pathlength LWCC (D'Sa et al., 1999). The offset (O) was subtracted from the absorbance spectra, and any differences in absorbance spectra measured using the LWCC and the Lambda 40, while generally small below 350 nm, were attributed to differences in the baseline offset. Because salt solutions have a higher refractive index than the freshwater on which both instruments are blanked, seawater should show an apparent negative absorbance at

certain wavelengths, an effect that can be exacerbated in the long pathlength LWCC (D'Sa et al., 1999; Miller et al., 2002; Nelson et al., 2007). This refractive index effect can be corrected by preparing blanks with a similar refractive index to the samples (Miller et al., 2002) or by employing an empirical salinity correction (Nelson et al., 2007). We rarely observed this negative offset and absorbance spectra from both instruments were comparable in the UV (<350 nm), indicating that CDOM absorption measurements made using pure water blanks in the LWCC are robust. Absorbance data was primarily used to correct H_2O_2 photoproduction data for CDOM fading and to normalize photoproduction rates for comparison among samples.

Corrected *A* spectra were converted to Napierian absorption coefficient ($a_g(\lambda)$; m^{-1}) with the equation:

$$a_g(\lambda) = \frac{\ln(10)A}{L} \tag{4.12}$$

over the 280 – 700 nm range, where *L* (m) is the pathlength. Sample irradiations in spectrophotometric cells typically lasted 3 to 12 hours but up to 24 or 48 hours for some samples. Percent CDOM loss was monitored at each wavelength from 290 – 390 nm and averaged to correct time series data. Additionally, the photon absorption rate by CDOM, $Q_a(\lambda)$ (mole photons s^{-1} nm^{-1}), in each cell was calculated following the recommendations of Hu et al. (2002) for optically thin solutions (i.e. $a_g(\lambda) \times L << 1$):

$$Q_a(\lambda) = E_0(\lambda) \times S \times a_g(\lambda) \times L \tag{4.13}$$

where *S* (m^2) is the surface area of the irradiated cell and *t* (s) is irradiation time. For short irradiation times in spectrophotometric cells, the $Q_a(\lambda)$ was integrated from 290 – 400

nm, allowing the calculation of a pseudo apparent quantum yield (ϕ_{pseudo}; moles H_2O_2 per moles photons absorbed):

$$\phi_{pseudo} = (d[H_2O_2]/dt) \Big/ \int_{290}^{400} Q_a(\lambda) d\lambda \quad (4.14)$$

where $d[H_2O_2]/dt$ is the H_2O_2 photoproduction rate.

2.3.2 Photochemical H_2O_2 and Superoxide Kinetic Experiments

For the photochemical superoxide experiments and paired O_2^-/H_2O_2 experiments described here the samples were irradiated under the solar simulator in acid-cleaned and Milli-Q rinsed 600 mL or 1 L jacketed beakers (Ace Glass) covered with quartz glass. Spectral irradiance entering the beakers was higher than that entering the spectrophotometric cells (Figure 4.2) when measured as described in Section 2.3.1. O_2^- concentrations were monitored with MCLA chemiluminescence both during and post irradiation in 600 mL jacketed beakers to observe O_2^- steady state concentrations ($[O_2^-]_{ss}$) and decay kinetics respectively. For determinations of initial steady state values, samples were irradiated up to 15 minutes to establish a stable $[O_2^-]_{ss}$. Samples were well mixed with a Teflon stir bar for these short irradiations and maintained at 20 °C with a recirculating water bath. Post irradiation, the FeLume signal, and thus O_2^- decay, was again monitored and fit using Equations 4.9 and 4.10 for the first 60 seconds of decay, effectively combining metal sinks and all other first order sinks into the k_{pseudo} term. $[O_2^-]_0$ was replaced in Equation 4.10 with $C \times S_0$ and S_0 and k_{psuedo} were again used as fitting parameters for nonlinear decay fitting (Section 2.2.3). Assuming that at steady state O_2^- production equals its decay, O_2^- photoproduction rates (P_{O2^-}) were described using modeled $[O_2^-]_0$, determined by multiplying modeled S_0 by the $[O_2^-]$ to signal ratio ($C \times S_0$)

for $[O_2^-]_{ss}$, to account for the time (~10 sec) out of the light required for the sample to reach the detector, and k_{pseudo} using the following equation

$$P_{O2^-} = 2k_D[O_2^-]_{ss}^2 + k_{pseudo}[O_2^-]_{ss} \quad (4.15)$$

During long term (>20 hour) exposures, $[O_2^-]_{ss}$ was monitored in 600 mL beakers throughout the experiment to assess any changes in steady state with continued irradiation. H_2O_2 concentrations were also periodically measured during these long term experiments to assess the stoichiometry between O_2^- and H_2O_2 production in these oligotrophic seawater samples. Additional long term irradiations were performed in 1 L beakers with H_2O_2 measurements at 24 and 48 hours. We assumed that H_2O_2 is uniform in these optically thin (i.e. $a_g(\lambda) \times L << 1$) samples at the time points sampled and did not stir the 1 L beakers. Although photochemical degradation of H_2O_2 has been reported (Moffett and Zafiriou, 1993), it was estimated to be only 5% of the photoproduction rate and therefore were neglected when evaluating H_2O_2 results in our experiments.

3. Results and Discussion

3.1 General Trends in Initial H_2O_2 and O_2^- Photoproduction Rates

3.1.1 Initial H_2O_2 Photoproduction Rates and CDOM Normalized Rates

Initial photoproduction rates for H_2O_2 were determined over 6 hours during shipboard irradiations or over 7 – 9 hours during laboratory irradiations post cruise (Table 4.1) with a linear regression of photoproduced $[H_2O_2]$ (nM) versus irradiation time (h). During the cruise, overall initial rates were determined by pooling all production data for a given depth and again fitting a linear regression to $[H_2O_2]$ vs. time. These rates were slightly slower for bottom samples (2.36 ± 0.66 nM h^{-1}; range 1.19 – 4.90 nM h^{-1}) and less variable than surface samples (4.89 ± 1.00 nM h^{-1}; range 1.07 – 7.13 nM h^{-1}).

Table 4.1. Sample information for those used to determine initial H_2O_2 photoproduction rates (P_{HOOH}; nM h^{-1}) for 6 hour shipboard irradiations in spectrophotometric cells (Cells) and for 7 – 9 hour irradiations done in 600 mL jacketed beakers post cruise (Beaker).

Station	Lat (N)	Long (W)	Depth (m)	$a_g(325)$ (m^{-1})	[DOC] µmol kg^{-1}	[NO3-] µmol kg^{-1}	Irradiation system	P_{HOOH} (nM h^{-1})	r^2	$P_{HOOH}/a_g(325)$ (nM m h^{-1})
8	52.95	141.55	Bottom (3852.4)	0.182	36.96	37.09	Cells	4.90 ± 0.68	0.98	26.89 ± 3.72
			Surface (nd)	0.209	62.07	17.51	Cells	3.62 ± 1.37	0.87	17.27 ± 6.56
17	57.15	148.71	Bottom (5146.2)	0.141	37.52	35.89	Cells	2.01 ± 0.66	0.65	14.19 ± 4.69
			50:50 mix	0.238	53.98	20.50	Cells	4.09 ± 1.09	0.78	17.16 ± 4.59
			Surface (4.8)	0.335	70.43	5.10	Cells	7.13 ± 1.31	0.94	21.31 ± 3.90
24	53	152	Bottom (4541.1)	0.159	37.52	36.19	Cells	1.42 ± 0.71	0.58	8.96 ± 4.45
			50:50 mix	0.203	51.39	22.22	Cells	0.88 ± 0.26	0.86	4.36 ± 1.27
			Surface (5.3)	0.247	65.27	8.25	Cells	4.00 ± 0.05	0.99	16.24 ± 0.18
29 (PAPA)	50	145	Bottom (4075.1)	0.141	38.3	36.39	Cells	1.19 ± 0.36	0.79	8.43 ± 2.52
			Surface (nd)	0.199	55.93	13.82	Cells	1.07 ± 0.68	0.71	5.40 ± 3.44
7	51.78	141.64	Bottom (3850.7)	0.16	37.82	37.89	Beaker	3.66 ± 1.58	0.84	22.97 ± 9.93
			Surface (5.3)	0.131	62.44	10.61	Beaker	1.66 ± 0.08	0.99	12.64 ± 0.57

8	52.95	141.55	1000 m (1005.4)	0.195	40.3	45.51	Beaker	2.68 ± 1.36	0.8	13.79 ± 6.99
20	55	152.66	Bottom (4274.1)	0.154	37.12	36.56	Beaker	4.98 ± 1.72	0.89	32.34 ± 11.18
			Surface (3.9)	0.389	67.31	38.88	Beaker	8.27 ± 0.50	0.99	21.26 ± 1.27
			1000 m (1011.9)	0.19	40.46	2.83	Beaker	4.41 ± 2.92	0.7	21.24 ± 14.04
27	51	152	Bottom (5078.9)	0.141	38.39	37.11	Beaker	4.62 ± 0.23	0.99	32.72 ± 1.64
			Surface (3.9)	0.24	63.33	45.47	Beaker	5.59 ± 2.21	0.76	23.34 ± 9.23
			1000 m (1011.1)	0.2	41.22	10.24	Beaker	4.71 ± 2.92	0.72	23.55 ± 10.28

Surface water photoproduction rates were similar to those measured by Yuan and Shiller (2001) on a 0.4 μm filtered oligotrophic sample (5.4 nM h^{-1}) from the south central Atlantic during a midday shipboard irradiation, and to those measured by Yocis et al. (2000) on 0.2 μm filtered samples collected from the oligotrophic Antarctic (2.1 to 9.4 nM h^{-1}). Otherwise, most other open ocean hydrogen peroxide photoproduction rate data available are actually *net* production rates as they were measured either *in situ* (Avery et al., 2005; Obernosterer et al., 2001) or on unfiltered samples (Yuan and Shiller, 2005) and include sinks together with the photochemical source for H_2O_2.

Once normalized to $a_g(325)$ (m^{-1}), initial shipboard photoproduction rates were less variable in surface waters as compared to bottom water samples. Interestingly, CDOM normalized rates for deep and surface samples match within error (14.7 ± 3.79 and 17.6 ± 2.51 nM m h^{-1}, respectively). Similarly, ϕ_{pseudo} values were similar for deep (43.1 – 156 μmole H_2O_2 per mole photons absorbed) and surface samples (30.0 – 122 μmole H_2O_2 per mole photons absorbed), indicating that differences in rates are due to higher CDOM absorption coefficients in surface samples and not a difference in their efficiency for H_2O_2 photochemical production. Previous studies have also indicated that the apparent quantum yield spectra for H_2O_2, which describes the efficiency of H_2O_2 photoproduction, are similar in the open ocean and differences in H_2O_2 photoproduction may be primarily controlled by differences in temperature (Kieber et al., 2014; Yocis et al., 2000) since the reactions described in Equations 4.1, 4.2, 4.5 and 4.6 are all thermal.

Additional evidence for comparable initial rates between bottom and surface waters were obtained post cruise for 7 – 9 hour laboratory irradiations (Table 4.1) in 600 mL jacketed beakers and paired H_2O_2/O_2^- measurements. H_2O_2 photoproduction rates

were essentially indistinguishable between bottom water samples (4.34 ± 0.55 nM h^{-1}, range 3.66 – 4.98 nM h^{-1}) and the more variable surface water samples (4.99 ± 1.70 nM h^{-1}, range 1.66 – 8.27 nM h^{-1}). Rates determined in beakers in the laboratory are in the same range, but slightly higher than those measured in spectrophotometric cells, likely due to the 37.5% higher measured photon flux (integrated from 290 – 400 nm) entering these jacketed beakers than entering spectrophotometric cells (Figure 4.2), and probably not related to storage effects. When normalized to $a_g(325)$, H_2O_2 photoproduction rates were somewhat higher for bottom water (29.1 ± 5.12 nM m h^{-1}), but not significantly different from that for surface water (19.9 ± 5.05 nM m h^{-1}).

Other than having DOC concentrations ~20 – 30 μM higher in surface water than in bottom water (Table 4.1), a primary compositional difference between these samples is in the concentration of NO_3^-. Surface water NO_3^- concentrations are typically low (0.03 – 10.6 μmol kg^{-1}) when compared to bottom water concentrations (35.9 – 39.6 μmol kg^{-1}). Nitrate photolysis can lead to significant production of the highly reactive hydroxyl radical ($^{\bullet}OH$) in seawater (Zafiriou, 1974; Zepp et al., 1987) and nitrate and nitrite were reported to account for 15 – 20% of $^{\bullet}OH$ photoproduction rate in deep (>700 m) waters collected in the Sargasso Sea (Mopper and Zhou, 1990). However, once in the surface, DORC will be exposed to sunlight without such high NO_3^- concentrations found at depth.

To evaluate the significance of higher NO_3^- on ROS rates in irradiated bottom water, we preformed additional irradiations with 50:50 mixed samples (bottom:surface; 1 L each of water filtered into 2 L polycarbonate bottles, as described in Section 2.1) while at sea and with 1000 m samples (containing the highest NO_3^- concentrations, 38.9 – 45.5 μmol kg^{-1}) back in the laboratory. For spectrophotometric cell irradiations containing

mixed samples, initial H_2O_2 production data was pooled and a linear accumulation (i.e. P_{HOOH}) was calculated as 3.19 ± 1.22 nM h^{-1}, in good agreement with both bottom and surface water. Similarly, rates determined from irradiations of water collected at ~1000 m in jacketed beakers were 3.98 ± 1.16 nM h^{-1}, the same as bottom and surface water rates within error. Normalizing initial H_2O_2 production rates to $a_g(325)$ removed variability from CDOM, isolating differences from other sources. Examining the $P_{HOOH}/a_g(325)$ rates in Table 4.1 shows no consistent trend to argue a significant role of nitrate in H_2O_2 photoproduction, with samples having significantly different nitrate concentrations showing similar $P_{HOOH}/a_g(325)$ rates (e.g. stations 20 & 27). Studies have shown that bleaching of CDOM and formation of DOM photoproducts by $^{\bullet}OH$ is slow for solutions containing SRFA and SRHA (Goldstone et al., 2002; Grebel et al., 2009) and unimportant as pH was increased from 7 to 9 in a freshwater stream (75 – 100% non $^{\bullet}OH$ mechanisms for DOM loss, Molot et al., 2005). These results are consistent with limited influence of $^{\bullet}OH$ production by nitrate photochemistry on observed initial H_2O_2 photoproduction rates in surface and bottom water experiments.

3.1.2. Initial Superoxide Photoproduction, Steady States and Decay

3.1.2.1. Initial Net Superoxide Accumulation Rates

Surface, deep, 50:50 surface/deep mixtures, and 1000 m samples were irradiated up to 30 minutes in 600 mL jacketed beakers to investigate initial rates and steady state concentrations for superoxide photoproduction under simulated sunlight (Table 4.2). The initial net accumulation rate was determined for the first 15 – 60 seconds of irradiation with a linear regression of FeLume Signal versus time (r^2 = 0.96 – >0.99) converted to O_2^- concentrations. Like those for H_2O_2, these initial *net* production rates were again quite

Table 4.2. Initial $[O_2^-]$ net accumulation rate ($d[O_2^-]/dt$; pM s^{-1}) and $[O_2^-]_{ss}$ (nM) measured during short (< 30 min) irradiations of seawater in jacketed beakers and that modeled from Equation 10, correcting for the time required (~10 sec) for the sample to reach the flow cell. $d[O_2^-]/dt$ was determined from a linear regression of FeLume signal vs. t for the first 15 – 60 seconds of irradiation and k_{pseudo} (s^{-1}) was determined from a nonlinear regression of FeLume signal vs. t to Equation 10, as described in Section 2.2.3. Modeled O_2^- photoproduction rates (P_{O2-}; pM s^{-1}) were determined using Equation 15 with k_D determined for seawater according to Zafiriou (1990), modeled $[O_2^-]_{ss}$ and k_{pseudo}.

Station	Lat (N)	Long (W)	Depth (m)	$a_g(325)$ (m^{-1})	[DOC] (μmol kg)	$[NO_3^-]$ (μmol kg)	Initial P_{O2-} (pM s^{-1})	$[O_2^-]_{ss}$ (nM)	Modeled $[O_2^-]_{ss}$ (nM)	k_{pseudo} (10^{-3} s^{-1})	P_{O2-} (pM s^{-1})
1	48.42	128.68	2539.8	0.184	37.15	39.64	6.73 ± 1.02	1.24 ± 0.19	1.44 ± 0.23	6.18 ± 0.86	9.10 ± 1.89
			50:50 mix	0.223	51.02	19.84	7.28 ± 1.10	1.91 ± 0.29	2.16 ± 0.33	7.72 ± 0.77	17.1 ± 3.07
3	49.28	134.67	3680.5	0.154	38.12	37.50	7.16 ± 1.09	1.04 ± 0.16	1.13 ± 0.19	8.86 ± 1.58	10.2 ± 2.43
			1010.4	0.189	40.62	44.99	n.d.	1.23 ± 0.19	1.34 ± 0.21	6.21 ± 0.78	8.51 ± 1.65
			4.2	0.12	64.49	6.85	9.75 ± 1.51	1.61 ± 0.24	1.84 ± 0.28	7.12 ± 0.51	13.4 ± 2.21
10	54.6	141.41	3720.2	0.208	38.63	40.51	13.8 ± 2.11	1.37 ± 0.21	1.45 ± 0.22	4.02 ± 0.62	6.06 ± 1.28
			50:50 mix	0.201	51.72	24.74	2.33 ± 0.36	4.21 ± 0.64	3.88 ± 0.72	12.1 ± 2.92	48.4 ± 14.3
			4.2	0.194	64.81	8.97	9.81 ± 1.48	3.73 ± 0.56	3.81 ± 0.59	3.97 ± 0.40	16.5 ± 2.78
12	56.47	141.24	3630.4	0.154	n.d.	37.96	22.9 ± 3.48	4.34 ± 0.67	4.66 ± 0.72	5.75 ± 0.87	29.0 ± 5.83
			2.9	0.387	n.d.	0.23	10.8 ± 1.63	3.25 ± 0.49	3.41 ± 0.52	2.84 ± 0.58	10.8 ± 2.48
29	50	145	4075.1	0.141	38.3	36.39	16.2 ± 2.45	2.49 ± 0.38	2.72 ± 0.47	5.01 ± 1.41	14.1 ± 5.90
			49.8	0.199	55.93	13.82	7.98 ± 1.20	2.66 ± 0.40	2.70 ± 0.42	5.37 ± 0.75	15.2 ± 3.01

similar between bottom (13.4 ± 8.38 pM s^{-1}, range 6.73 – 22.9 pM s^{-1}) and surface waters (9.58 ± 3.16 pM s^{-1}, range 7.98 – 10.8 pM s^{-1}). When normalized to $a_g(325)$, initial net accumulation rates remained similar between bottom water (60.5 ± 45.4 pM m s^{-1}, range 36.4 – 124 pM m s^{-1}) and surface water (51.9 ± 17.1 pM m s^{-1}, range 43.2 – 58.6 pM m s^{-1}). These rates are comparable to initial O_2^- formation rates of 3 – 25 pM s^{-1} measured over 4 to 10 seconds of sun exposure in surface samples from the Gulf of Aqaba (Shaked et al., 2010). To our knowledge, the only other O_2^- photoproduction rates reported for the open ocean using chemiluminescent methods were made over 20 minutes of irradiation under simulated sunlight showing O_2^- concentrations increasing ~1.3 pM s^{-1} for an unfiltered seawater sample and decreasing by about ~ 0.006 pM s^{-1} in a filtered sample (Rusak et al., 2011). Because the first time point was taken beyond 3 minutes, these are in actuality, measurements of a series of O_2^- steady state values during the irradiation and not production rates.

Furthermore, even when determined within 60 seconds using filtered samples, initial O_2^- accumulation rates are representative of the *net* photoproduction rate since decay processes are occurring as O_2^- increases to steady state levels with continued irradiation. In fact, O_2^- photoproduction rates measured with a ^{15}NO trap, presumably excluding O_2^- decay mechanisms, in the Eastern Caribbean were more variable and much higher, on the order of 1.83 to 94.8 pM s^{-1} sun^{-1} in the spring and 3.5 to 131 pM s^{-1} sun^{-1} in the fall (Micinski et al., 1993). As noted previously, the NO probe/isotopic mass spectrometry method employed by Micinski et al. (1993) may underestimate photoproduction rates by 30 – 40% (Blough and Zepp, 1995). For comparison, superoxide photoproduction rates inferred from H_2O_2 photoproduction rates determined

during exposures to natural sunlight of coastal seawater with added SOD were on the order of 78 – 160 pM s^{-1} (Petasne and Zika, 1987). Otherwise, direct measurements of O_2^- photoproduction rates in marine waters are surprisingly lacking, possibly due to the difficulty in quantifying low O_2^- concentrations and its short lifetime in seawater.

The observation here that bottom water rates were more variable than those for surface water, a trend not observed for H_2O_2 photoproduction rates, could be a function of the smaller time scale over which they were calculated (seconds versus hours for O_2^- and H_2O_2, respectively). To check precision in these rates, repeat irradiations were performed on several samples. Initial net accumulation rates for O_2^- varied between 4 and about 35% between the first and second irradiation, but varied by 88% within one sample. As noted by Shaked et al. (2010) and observed here, these net O_2^- photoproduction rates are subjective and depend on the interval (15 – 60 s here) over which they are determined.

3.1.2.2 Superoxide Steady States, Decay Kinetics, and Determination of Photoproduction Rates

An alternative approach to these net photoproduction rate determinations is to estimate O_2^- photoproduction using measured or modeled $[O_2^-]_{ss}$ and a modeled superoxide decay constant following Equation 4.15. Modeled $[O_2^-]_{ss}$ were higher than measured $[O_2^-]_{ss}$ for all but one sample, ranging from 1.2 – 16% higher for modeled concentrations. During these short irradiations under simulated sunlight, $[O_2^-]_{ss}$ in deep samples (2.10 ± 1.60 nM measured and 2.28 ± 1.74 nM modeled) was slightly lower but not significantly different from that in surface samples (2.82 ± 1.27 nM measured and 2.94 ± 1.27 nM modeled). Assuming CDOM photoexcitation is the predominant pathway for superoxide generation under these conditions, higher CDOM absorption coefficients

in surface samples could explain this difference. Repeat irradiations were again used to check precision and measured steady-state concentrations were between 2 and 16% of their original values, a large improvement over the variability seen when comparing initial accumulation rates.

These steady state concentrations measured during our irradiation experiments are ~4 to >30 times higher than those measured in the field (Hansard et al., 2010; Rose et al., 2008b; Shaked et al., 2010). This likely reflects our higher and constant photon flux under simulated sunlight relative to natural sunlight with variable cloud cover (Figure 4.2). In an unfiltered sample under natural sunlight, Shaked et al. (2010) measured a $[O_2^-]_{ss}$ of ~140 pM in water from the Gulf of Aqaba. Otherwise, we are not aware of any $[O_2^-]_{ss}$ data in the literature that adequately reflects the photochemical source for superoxide. Rose et al. (2008b) reported $[O_2^-]_{ss}$ values of 37 – 66 pM from water collected in the Equatorial Pacific. However, these samples were added to bottles containing DTPA, supposedly to slow O_2^- decay, and then analyzed about an hour after collection. In a diel study during the same field campaign, surface $[O_2^-]_{ss}$ reached 64 pM measured directly after filtration. Even so, the sample was collected through polypropylene tubing, likely shielding the sample from UV light and lowering the measured $[O_2^-]_{ss}$. Hansard et al. (2010) measured superoxide concentrations in surface waters of the Gulf of Alaska ranging from 140 – 540 pM but, as the authors note, the 2 – 3 minute transit time required for the sample to reach the flow cell and react with MCLA greatly underestimates the contribution of photochemical O_2^- production. Based on these reports, and because the irradiance spectra measured under our solar simulator is comparable to natural sunlight in our study region (Figure 4.2), the O_2^- steady states measured during our experiments

should be representative of a maximum midday $[O_2^-]_{ss}$ in the open ocean waters of the Gulf of Alaska.

For each irradiation, once the steady state was measured, the solar simulator was turned off and O_2^- decay was monitored for at least 10 minutes. Pseudo-first order rate constants were determined as described in Section 2.2.3 over the first ~60 seconds of decay (Table 4.2). Modeled decay over the first 60 seconds generally matched that determined for the entire decay curve, but in some cases was faster during this initial phase of decay (data not shown). Heller and Croot (2010b) also observed faster initial decay followed by slower decay for superoxide reacting with CDOM. This effect was explained by either a back reaction producing superoxide or the presence of two CDOM pools with high and low reactivity for superoxide. These observations were made by monitoring the decay of O_2^- spikes and not from photogenerated O_2^-, which could potentially react with new photogenerated CDOM transients (Zhang et al., 2012). The pseudo-first order rate constants (k_{pseudo}) determined over the initial period of decay in our study ranged from 2.84 – 12.1 x 10^{-3} s^{-1} and again, were not significantly different in bottom waters (6.00 ± 3.39 x 10^{-3} s^{-1}) compared to surface waters (4.82 ± 2.17 x 10^{-3} s^{-1}). Decay was also monitored after repeated irradiations of the same sample, and k_{pseudo} determined after the second irradiation varied from ~5 to 30%, typically becoming somewhat faster, possibly indicating long-lived photoproducts that increase the overall reaction rate with O_2^-.

Pseudo-first order decay constants determined here are in excellent agreement with k_{pseudo} values previously reported that have used additional precautions to collect trace metal clean samples in the Gulf of Alaska (2 – 16 x 10^{-3} s^{-1}; Hansard et al., 2010),

providing support that metal contamination was not a significant issue in our experiments. Otherwise, k_{pseudo} values determined here are at the lower end of k_{pseudo} values determined from superoxide additions in the Eastern Pacific (18.9 – 27.6 x 10^{-3} s^{-1}; Rusak et al., 2011), the Southern Ocean (4 – 74 x 10^{-3} s^{-1}; Heller and Croot, 2010a), and DTPA amended seawater from the equatorial Atlantic, which solely reflects the CDOM sink (9 – 34 x 10^{-3} s^{-1}, Heller and Croot, 2010b). In these studies, however, spiked superoxide concentrations ranged from about 50 to 100 nM, well higher than *in situ* concentrations. While some studies suggest that this is not a problem (Heller and Croot, 2010c), with elevated O_2^- levels, and given the typically low nM reactant concentrations involved in open ocean ROS reactions, it is possible that measured decay rates may be altered. Interestingly, the k_{pseudo} values we determined for 7 – 42 nM spikes of the photochemical standard spiked into DTPA amended samples, as required for FeLume calibration (Section 2.2.3), were about 15 – 35 x 10^{-3} s^{-1}, in good agreement with the k_{pseudo} values determined from ~100 nM O_2^- spikes in DTPA amended seawater (Heller and Croot, 2010b). This provides additional evidence for a possible dependence of decay pathway distribution on initial O_2^- concentration. Post-irradiation k_{pseudo} determinations typically started at $[O_2^-]_{ss}$ of ~1 – 4 nM (Table 4.2), and as previously noted, it may be difficult to equate pseudo-first order decay kinetics determined from superoxide spikes to those appropriate for naturally occurring conditions (Rusak et al., 2011). Unfortunately, there have only been a few shipboard studies measuring the decay of O_2^- over concentration ranges that are representative of those found in the open ocean (e.g. Hansard et al., 2010; Shaked et al., 2010).

Assuming superoxide production is equal to its decay at steady state, O_2^- photoproduction rates (P_{O2^-}) were calculated via Equation 4.15, using both modeled $[O_2^-]_{ss}$ together with k_{pseudo} values determined post irradiation. Modeled $[O_2^-]_{ss}$ was chosen over measured $[O_2^-]_{ss}$ as more representative of the steady state concentrations present during irradiation prior to the 10 second lag time required to pump the sample from the irradiation container to the FeLume detector. As expected, calculated P_{O2^-} was generally higher than the initial net accumulation rate, showing surprisingly large variations (–56 to 1980%) from the initial net accumulation rates. Calculated P_{O2^-} ranged from 6.06 – 48.4 pM s^{-1} in all samples (Table 4.2) and was comparable to the rates discussed above. Like net accumulation rates, photoproduction rates for bottom water were more variable (13.8 ± 12.7 pM s^{-1}) but quite similar to those for surface water (14.0 ± 5.83 pM s^{-1}). When normalized to $a_g(325)$, the average P_{O2^-} was slightly lower and unconstrained for bottom water samples (62.5 ± 69.0 pM m s^{-1}) but not significantly different from surface water (75.9 ± 31.6 pM m s^{-1}).

3.1.3 Oxidative and Reductive Sinks for O_2^-

Perhaps the most striking finding from our short irradiation experiments discussed above is that the initial photoproduction rates of both O_2^- and H_2O_2 are similar between surface and bottom water samples. Studies investigating O_2^- and H_2O_2 in coastal seawater (Petasne and Zika, 1987) and in solutions containing SRFA (Garg et al., 2011) suggest that a large portion of photoproduced O_2^- in seawater does not lead to H_2O_2. The stoichiometry of dismutation (Equations 1 and 2) predicts $0.5H_2O_2$ produced per O_2^-, implying that the photoproduction rate of superoxide should be twice that for hydrogen peroxide. Because O_2^- photoformation data is limited and apparent quantum yield data for

O_2^- is unavailable, currently the only option is to infer O_2^- photoefficiency from that for H_2O_2. Therefore most studies assume this relationship holds when inferring O_2^- information from H_2O_2 observations (Heller and Croot, 2010a; Powers and Miller, 2014). However, most studies investigating O_2^- decay mechanisms have found that O_2^- decay typically follows first order kinetics, and not the second order fit required of dismutation (Heller and Croot, 2010a, 2010b; Rose et al., 2008b; Shaked et al., 2010). Therefore, the relationship between H_2O_2 and O_2^- can only be defined as being between 0 and 1, and can still be ~0.5 even if dismutation is not the dominant O_2^- sink depending on whether oxidative (Equation 4.5) or reductive (Equation 4.6) sinks are dominant.

To examine the portion of photoproduced O_2^- leading to H_2O_2, we compared initial H_2O_2 photoproduction rates to those calculated for O_2^- via Equation 4.15. Because short term shipboard irradiations for H_2O_2 and O_2^- were preformed in two separate irradiation systems, we scaled P_{O2^-} by the average measured difference (0.723) in integrated irradiance (290 – 400 nm) entering spectrophotometric cells versus that entering jacketed beakers (Figure 4.2). For shipboard experiments, initial H_2O_2 and O_2^- photoproduction rates were determined in bottom and surface water only for Station 29. Initial H_2O_2 rates (P_{HOOH}) were at the lower end of those measured during the cruise (Table 4.1) and consequently the ratio between H_2O_2 photoproduction and O_2^- photoproduction (determined as P_{O2^-} as discussed above) was 0.0306 ± 0.0152 for the deep sample and 0.0269 ± 0.0180 in the surface sample, and albeit poorly constrained, well below the 0.5 ratio predicted from O_2^- dismutation. Because we could find no evidence to support such a low (<5%) amount of O_2^- leading to H_2O_2, we pooled and compared photoproduction rates for deep and surface samples normalized to $a_g(325)$ in

an attempt to best compare the overall relationship between P_{O2^-} and P_{HOOH} for all shipboard data. Due to the variability in P_{O2^-} determined in deep water, the H_2O_2:O_2^- photoproduction ratio (P_{HOOH}:P_{O2^-}) was not well defined (0.090 ± 0.102). On the other hand, the ratio for $a_g(325)$ normalized surface water samples was better constrained (0.318 ± 0.140). Because variability of both $[O_2^-]_{ss}$ and k_{pseudo} factors into the calculation of P_{O2^-}, we also determined the ratio between initial H_2O_2 photoproduction rates and the initial net accumulation rate for O_2^-, again normalized to CDOM absorption. In this case, the H_2O_2:O_2^- production ratio was 0.093 ± 0.074 and 0.129 ± 0.046 for bottom and surface water respectively. While the true relationship between these photoproducts remains unresolved, these results suggest that a large portion of O_2^- decay does not lead to H_2O_2 production.

The possibility remains that at least part of the variability in P_{HOOH}:P_{O2^-} for deep samples was due to comparison of irradiations done in different containers with different light fields. Post cruise, to eliminate this variation, we performed additional laboratory irradiations in jacketed beakers and monitored both O_2^- steady states and H_2O_2 accumulation in the same 600 mL container for surface, bottom and ~1000m water samples (Tables 1 and 2). Even for these paired laboratory irradiations, ratios were variable, largely due to poor fits for k_{pseudo}. Ratios determined for surface and 1000 m water were generally lower than those for bottom water. P_{HOOH}:P_{O2^-} ranged from 0.10 – 0.45 in surface water samples and from 0.13 – 0.46 in 1000 m water samples while ratios for bottom water samples ranged from 0.37 – 0.67. Ratios were also calculated using initial superoxide accumulation rates that are generally lower than calculated P_{O2^-}, and accordingly these ratios were lower. Using this method, ratios overlapped for all water

types but were better constrained for bottom (0.13 – 0.27) and 1000 m samples (0.089 – 0.18) when compared to surface water (0.089 – 0.37).

Assuming metal contamination was minimal, and since trace metal distributions in this region are low (i.e. dissolved Fe concentrations <0.2 nM in surface waters and ~0.6 nM at depth at Ocean Station PAPA, September 1997, Nishioka et al., 2001), the dominant sink for O_2^- in our samples is thought to be dissolved organic matter. Goldstone and Voelker (2000) found that CDOM and humic substances were a significant sink for superoxide in coastal seawater and they observed a strong correlation between k_{pseudo} (s^{-1}) determined in samples with added DTPA (k_{org}) and $a_g(300)$ (m^{-1}) ($r^2 = 0.73$). The authors suggested that portions of CDOM are active in the redox cycling of O_2^- based on their observation that the stoichiometry between H_2O_2 and O_2^- was ~0.4, albeit determined after μM O_2^- additions. Studies investigating the CDOM sink for O_2^- in the open ocean report variable results, and no statistically significant correlations were observed between k_{org} (s^{-1}) and CDOM absorption coefficients in the tropical North Atlantic (Heller and Croot, 2010b; Wuttig et al., 2013). Similarly, we observed little ($r^2 = 0.18$) to no correlation between $a_g(325)$ and k_{pseudo} or $[O_2^-]_{ss}$, respectively (Figure 4.3). Heller and Croot (2010b) observed increases in k_{org} with increases in the proportion of seawater mixed with pure water at constant DTPA concentrations, indicating that organics were responsible for the observed first-order superoxide decay kinetics. The authors then suggest that reactions with quinone functionalities most likely control observed k_{org}, a mechanism also suggested for k_{org} in coastal waters (Goldstone and Voelker, 2000).

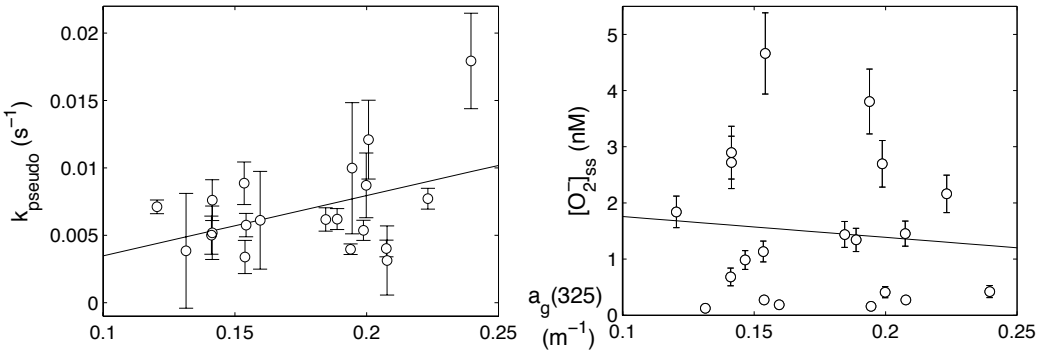

Figure 4.3. Relationships between $a_g(325)$ (nm) and k_{pseudo} (s^{-1}) (left) and modeled $[O_2^-]_{ss}$ (nM) (right). A weak but positive correlation exists between k_{pseudo} and $a_g(325)$ ($r^2 = 0.18$) and no correlation exists between $[O_2^-]_{ss}$ and $a_g(325)$ ($r^2 = 0.009$).

While redox cycling of CDOM may be occurring here, our results indicate that more O_2^-decays via an oxidative pathway (Equation 4.5) than a reductive pathway to produce H_2O_2 (Equation 4.6). Because the photoproduction of O_2^- leads to CDOM photooxidation, thus suggesting that H_2O_2 is a convenient proxy for CDOM e^- loss (Sharpless and Blough, 2014), it is not surprising that an oxidative sink (Equation 4.5) could be more important in our experiments, even during these short irradiations. More work is needed in marine systems to better understand redox cycling with CDOM from both autochotonous and allochotonous sources.

3.2 Trends in H_2O_2 Accumulation and O_2^- Steady States with Continued Irradiation

The photoproduction rates of these two ROS are very low compared to rates from high CDOM coastal waters (Petasne and Zika, 1987). This alone might argue against photochemistry as a significant removal mechanism for the low DOC and CDOM abyssal waters containing DORC. Using short irradiations (4 – 5 hrs), $^{\bullet}OH$ photoproduction rates were ~6 times higher in deep samples (Mopper and Zhou, 1990) and carbonyl photoproduction rates were higher for deep samples than for surface samples (Mopper et al., 1991) in the Sargasso Sea. Our initial photoproduction rates for H_2O_2 and O_2^- were similar in the surface and bottom waters studied here. This result does not argue for an increased photochemical activity for at least some part of the DORC pool. Because it is possible that initial photochemical rates may not be sustained over times more consistent with oceanic circulation in surface waters, we performed long term irradiations, up to 48 hours, to further investigate DORC photoreactivity beyond initial exposure.

3.2.1 Long Term H_2O_2 Photoproduction Rates

Figure 4.4. shows typical shipboard results for bottom, surface and 50:50 mixed samples using water collected at Station 17 in both irradiation systems (spectrophotometric cells and jacketed beakers). Despite the similarity in initial rates between these three samples, H_2O_2 stops accumulating in the bottom water sample with continued irradiation. This was not observed in the surface or mixed sample, perhaps due to differences in initial CDOM absorption coefficients at this station ($a_g(325)$ listed in Table 4.1). These exposure experiments were repeated both shipboard and post cruise for water from several stations. H_2O_2 concentrations over time for 48 hr shipboard irradiations in 1 L jacketed beakers are shown in Fig 5. H_2O_2 accumulation was always lower in deep samples when compared to surface samples. By correcting H_2O_2 accumulation using the average % CDOM absorption fading over the 290 – 390 nm range, the nonlinear nature of these results could be partly explained (e.g. St. 24 and 29, Figure 4.5). After 48 hours of irradiation bottom water samples (Figure 4.4 and 4.5) faded between 24 – 47%. In comparison, the average fading in surface water samples was only 6 – 33%, suggesting that surface waters may have been "prefaded" yet capable of producing much higher concentrations H_2O_2 photochemically. Even when corrected for fading, H_2O_2 either slows down (St. 24 and 29) or stops accumulating entirely in deep samples (St. 8 and 17). In fact, for the longer irradiations shown in Figure 4.4 and 4.5, photoproduced H_2O_2 in bottom water did not exceed about ~40 nM and sometimes did not increase in concentration beyond 9 hours of irradiation (Figure 4.4 and 4.5).

Because H_2O_2 photoproduction in surface samples was not exhausted in the same manner, these results beg the question as to whether or not H_2O_2 photoproduction stopped

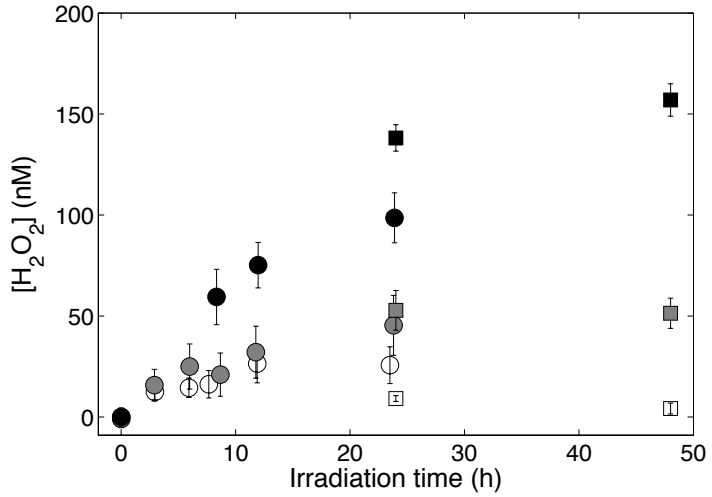

Figure 4.4. Photoproduced H_2O_2 (nM) for water collected at Station 17: surface (black symbols), deep (white symbols), and 50:50 mix of surface and deep water (gray symbols) for shorter irradiations in spectrophotometric cells (circles) and longer irradiations in jacketed beakers (squares). Circles are averages of 3 cells, squares are single samples taken from the jacketed beaker, multiplied by a correction factor, 0.8727, for the difference in integrated irradiance (290 – 400 nm) reaching the surface of the cell vs. that reaching the surface of the 1 L jacketed beaker.

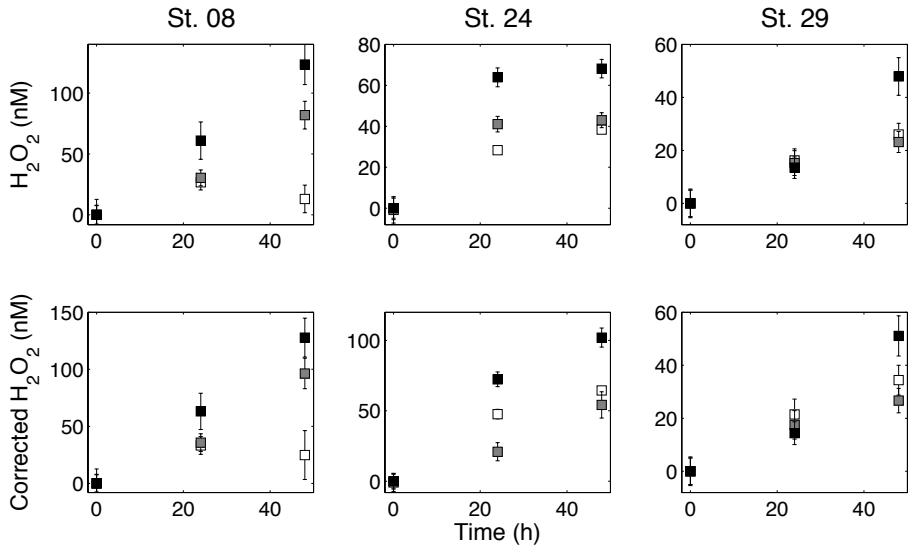

Figure 4.5. Photoproduced H_2O_2 in 1L jacketed beakers for long term irradiation (top) and that corrected for average % CDOM fading from 290 – 390 nm (bottom).

in deep samples or H_2O_2 simply reached a steady state, with H_2O_2 still being photoproduced but a sink having developed to remove it at an increased rate. As CDOM fades, the diminished photon absorption rates will lower the photoproduction of H_2O_2, however we observed the photoproduction of H_2O_2 stopping well before even 50% of the CDOM was lost in these deep samples. Photodecomposition of H_2O_2 has been reported for samples collected from a "river to oligotrophic ocean" transect in the Eastern Caribbean (Moffet and Zafiriou, 1993), but similar to the photoproduction rates at oligotrophic stations, photodecomposition rates were low (less than 5% of production rates). These results were from short (2 hour) irradiations and it is not known whether photodecomposition rates change with continued irradiation. *In situ* estimates suggest that H_2O_2 photodecomposition could be over 50% of the photoproduction rate when photoproduction rates are low (Yocis et al., 2000) so direct photodecomposition, or perhaps loss due to a photochemically generated product cannot be ruled out. Unfortunately, we cannot find any published studies monitoring the photochemical production of H_2O_2 beyond that required for determination of initial rates.

3.2.2 Paired H_2O_2 and O_2^- Dynamics with Continued Irradiation

To better interpret H_2O_2 results, especially the extreme drop off in photoproduction rates during continued irradiation of bottom waters, we performed two shipboard beaker experiments monitoring superoxide steady state and hydrogen peroxide concentrations together in bottom water samples throughout 20 – 30 hour exposures under the solar simulator (Figure 4.6). For these experiments, the sample was split and irradiated in two 600 mL jacketed beakers side by side. Throughout the experiment, one beaker was continually sampled and the other was left untouched until the end of the

experiment to check for significant effects from changing light field due to lowering the sample volume while sampling. Superoxide and hydrogen peroxide values measured at the end of the experiment were the same, within error, between both beakers. Over the course of the irradiation, measured $[O_2^-]_{ss}$ continually decreased. For the irradiation of bottom water collected from Station 5 (Figure 4.6A), we were unable to correct $[O_2^-]_{ss}$ for the time taken for the sample to travel to the FeLume because we did not monitor superoxide decay throughout the experiment. At the end of this irradiation experiment, however, we measured superoxide decay in the same way as was done for experiments measuring initial $[O_2^-]_{ss}$ and decay (Section 3.1.2). As before, we can assume that measured $[O_2^-]_{ss}$ throughout the experiment is slightly lower that that under the solar simulator due to a small loss of O_2^- during transfer to the FeLume. At the end of the first irradiation (Figure 4.6A), k_{pseudo}, determined as described above (Section 2.2.2 Equation 4.10), was 13.4 ± 2.16 x 10^{-3} s^{-1}, in the range of k_{pseudo} values determined after short irradiations for bottom waters (Table 4.2) but on the higher end of calculated k_{pseudo} values.

To examine whether or not O_2^- decay kinetics changed throughout the long irradiation, we repeated the experiment with bottom water from station 12, turning the solar simulator off after each $[O_2^-]_{ss}$ determination to measure O_2^- decay (Figure 4.6B and C). During the first 8 hours of irradiation, k_{pseudo} values were 5.76 ± 0.87, 5.59 ± 0.43, and 5.80 ± 0.59 x 10^{-3} s^{-1} at 1.7 hr, 4 hr and 7.2 hrs of irradiation, essentially unchanged. For the remainder of the irradiation calculated k_{pseudo} values increased to 9.04 ± 1.55, 8.59 ± 0.25, and 9.47 ± 1.41 x 10^{-3-} s^{-1} at 9.5hr, 11.5hr, and 18.7 hrs of irradiation (decay after 4 – 11.5 hours shown in Figure 4.6C). Despite this apparent shift in decay kinetics, calculated

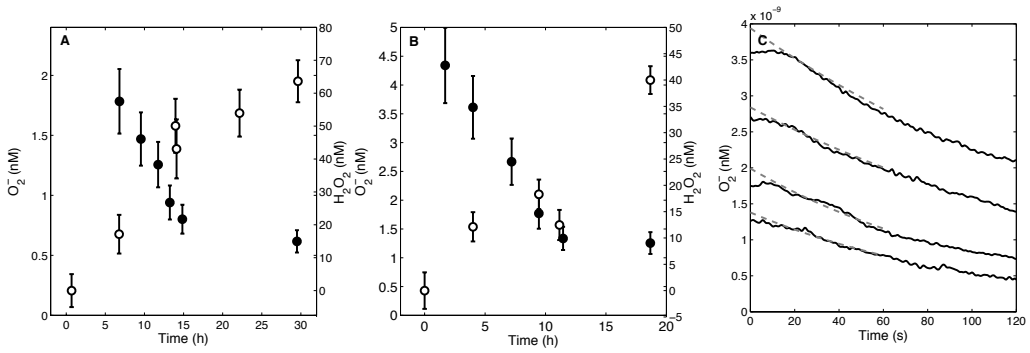

Figure 4.6. Paired shipboard irradiations of deep seawater collected at Station 05 (A) and Station 12 (B) monitoring photoproduced H_2O_2 (nM; white circles) and $[O_2^-]_{ss}$ (nM; black circles). After each time point during the irradiation of Station 12 deep seawater, the irradiation was stopped to monitor O_2^- decay (C) were black line are the decay data and dashed lines are that modeled according to Equation 4.10.

P_{O2^-} decreased with continued irradiation from 29.0 ± 5.83 pM s^{-1} for the first hour to 13.2 ± 2.85 pM s^{-1} at 18.7 hours.

The observation that $[O_2^-]_{ss}$ decreases with continued irradiation argues for a consumption of source, most simply explained by CDOM photobleaching. However, in both of these experiments, there was still a measurable superoxide steady state even after H_2O_2 had stopped accumulating, meaning that CDOM was still capable of superoxide photoproduction. These results provide the strongest evidence that a large portion of photoproduced O_2^- decays through an oxidative pathway, and perhaps, in the DORC samples, decay mechanisms shift to an almost entirely oxidative pathway over long irradiations. Zhang et al. (2012) observed H_2O_2 photoproduction under anaerobic conditions, which they attributed to the introduction of O_2 during H_2O_2 analysis and long-lived reactive reducing intermediates formed during the irradiation. They suggest that photoproduced reductants formed when CDOM is exposed to solar radiation will reduce O_2 to O_2^- as expected, but they are also likely capable of reducing O_2^- to H_2O_2 (Equation 4.6). Towards the end of our long irradiation experiments, O_2^- concentrations are low (~60 – 100 pM) and perhaps cannot compete for these reductants with the $>10^6$ times higher concentrations of molecular oxygen present in seawater equilibrated with the atmosphere, as is the case for our exposures.

While comparative studies in oligotrophic seawater are missing, our results and those reported elsewhere (Garg et al. 2011; Petasne and Zika, 1987) suggest that a large portion of superoxide decays via an oxidative pathway (Equation 4.5) even under short exposures. Garg et al. (2011) concluded that a large portion of O_2^- decays via an oxidative pathway based on experiments measuring the photoproduction of H_2O_2 and O_2^- from

irradiations of SRFA, explaining O_2^- oxidation via unknown organic radicals produced during irradiation. Petasne and Zika (1987) estimated that only 30% of superoxide photoproduction leads to H_2O_2 formation from irradiations of coastal seawater. A recent study by Sharpless et al. (2014), using standard aquatic fulvic acids and a soil humic acid, demonstrated that while photooxidation lowered DOM electron donating capacity, it had little effect on electron accepting capacity, even after 59 hours of irradiation. They also reported that the efficiency for H_2O_2 photoproduction (i.e. the apparent quantum yield) decreased over time with continued irradiation, noting that their results do not support photochemical oxidation of electron donor groups to electron acceptor groups because the destruction of donor groups did not accompany an increase in acceptor groups. Although the experimental source material contained in our low CDOM waters collected in the \Gulf of Alaska are most certainly different from those using commercially available fulvic and humic acids, results from Sharpless et al. (2014) may help explain our observation that H_2O_2 photoproduction slows tremendously or stops in deep ocean samples. Other than the results presented here, information is not available on the potential changes in the oxidative and reductive sinks for O_2^- and subsequent production stoichiometry for H_2O_2 in marine waters during long irradiations. These are needed to fully evaluate the photochemical reactivity of marine DORC over time scales relevant to surface circulation and global cycles.

Post cruise, we performed additional $[O_2^-]_{ss}$ simultaneous irradiations on stored surface (top 5 m), 1000 m, and deep samples (Figure 4.7) to determine if observed long term $[O_2^-]_{ss}$ decreases in the DORC (bottom water) samples were unique in our samples. As discussed before, initial H_2O_2 photoproduction rates were similar for samples at all

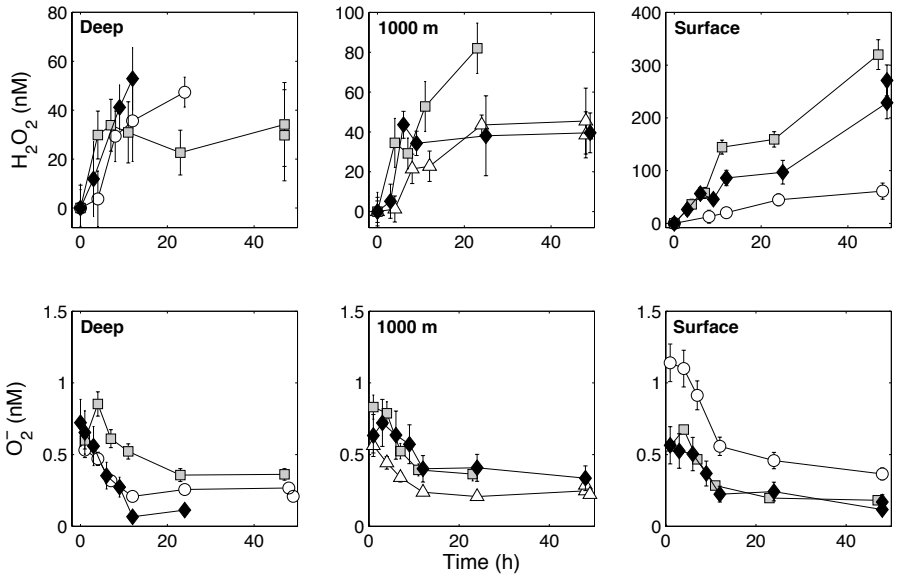

Figure 4.7. Irradiations for simultaneous monitoring of H_2O_2 photoproduction rates and O_2^- steady-states (bottom) for Station 07 (white circles), Station 8 (white triangles), Station 20 (gray squares) and Station 27 (black diamonds).

depths (Section 3.1.1) and similarly, H_2O_2 photoproduction between bottom and 1000 m water were comparible over the course of the long irradiation (Figure 4.7), never exceeding ~50 nM in bottom water irradiations and ~80 nM in 1000 m water irradiations. At these two depths, in all but one 1000 m sample (Station 20), H_2O_2 concentrations did not increase beyond 12 hours of irradiation. Surface water H_2O_2 photoproduction rates, however, were much more variable, with H_2O_2 ranging from ~60 nM (Station 07) to >300 nM (Station 20) after 48 hours of irradiation.

For these extremes in surface water production, we corrected both H_2O_2 and $[O_2^-]_{ss}$ concentrations using the average %CDOM fading between 290 – 390 nm (Figure 4.8). Once corrected, H_2O_2 photoproduction rates were similar for all depths at Station 7, but remained much higher for surface water compared to bottom or 1000 m water at Station 20. Interestingly, for both stations, corrected $[O_2^-]_{ss}$ values were similar for bottom and 1000 m water and once corrected for fading, were about the same both at the first experimental time point and after 48 hours of irradiation, perhaps reflecting similar efficiencies and/or decay pathways. On the other hand, $[O_2^-]_{ss}$ in surface water samples continued to decrease despite the correction, and were lowest when H_2O_2 photoproduction rates were highest (Station 20). This could indicate a greater change in photoproduction efficiency and/or decay pathway with long exposures than seen in the deeper samples. Additionally, the low corrected $[O_2^-]_{ss}$ values seen at 48hrs with continued H_2O_2 production would argue for a change in formation stoichiometry.

Even after correcting H_2O_2 data for fading, only ~75 nM or less was generated after 48 hours of irradiation, implying that even if the initial rates were maintained for 48 hours and no fading occurred, for the DORC samples at least, there is both a loss of

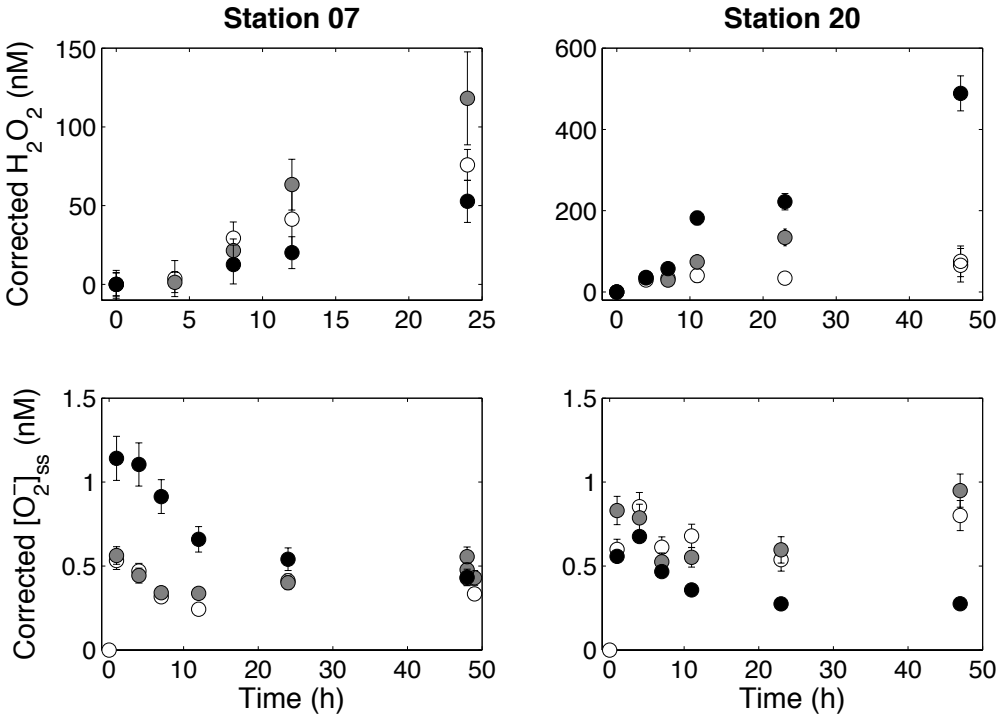

Figure 4.8. Photoproduced H_2O_2 (top) and $[O_2^-]_{ss}$ (bottom) in 600 mL jacketed beakers for long term irradiations corrected for average % CDOM fading from 290 – 390 nm (bottom).

source for O_2^- (CDOM) and a shift to primarily oxidative sinks for O_2^-. While surface water samples were more variable, perhaps suggesting a less uniform source for CDOM or differing exposure histories at our sampling stations, H_2O_2 photoproduction was sometimes quite large, reaching >300 nM after 48 hours of irradiation. Even though $[O_2^-]_{ss}$ decreased during surface water irradiations, this did not prevent nearly linear accumulation of H_2O_2, providing evidence that reduced intermediates, perhaps generated from CDOM (Zhang et al., 2012), may be more prevalent in surface water CDOM than in that for bottom waters.

4. Conclusions

In an effort to probe the photochemical reactivity of deep ocean refractory DOC, we have provided the first simultaneously measured rates of both H_2O_2 and O_2^- photoproduction in the surface and deep waters of the subarctic North Pacific on samples analyzed at sea and back in the laboratory, thus adding to the very limited number of direct measurements of O_2^- photochemical production in natural samples. Our initial production rates for both O_2^- (<10 min) and H_2O_2 (<6 hrs) were comparable between surface and deep waters. However, with continued irradiation up to 48 hours, photoproduced H_2O_2 was generally much lower in deep samples compared to surface samples and its accumulation in deep samples either stopped or slowed despite both measurable CDOM absorption coefficients and superoxide steady state values. Because the accumulation of H_2O_2 appears to be exhausted in these deep samples, our data suggest that the photoreactive CDOM there is a very small component of the already low DOC

pool (<40 μM), in the most aged waters of the North Pacific. Swan et al. (2009) also found that CDOM and DOC do not correlate in their large survey of Pacific waters, indicating that the processes controlling CDOM and DOC distributions are not related. A strong linear relationship between CDOM absorption coefficients and AOU has been reported in the interior of the Pacific Ocean (Swan et al., 2009; Yamashita and Tanoue, 2009), indicating that new CDOM accumulates via biological oxidation and this appears to be semilabile and photolabile (Helms et al., 2013).

In addition to the work of Mopper et al. (1991), dissolved black carbon collected in the deep waters (3000 m) of the North Atlantic was found to be very photoreactive, decreasing by 95% in a 28 day irradiation (Stubbins et al., 2012). The high molecular weight fraction of dissolved black carbon has a radiocarbon age of ~18,000 years (Ziolkowski and Druffel, 2010), and has led to its recent classification as an ultrarefractory component of marine DOC, containing about 12 Pg C (Hansell, 2013), a small part of the entire refractory DOC pool (~642 Pg C for refractory and ultra refractory together; Hansell, 2013). Additional evidence that dissolved black carbon should not be classified as refractory is that stable compounds in marine DOM tend to have higher H/C and O/C ratios and lower aromatic content than that of dissolved black carbon (Lechtenfeld et al., 2014). Therefore, the photochemical production rates of ROS observed here in bottom water samples collected in the Gulf of Alaska are likely due to the photooxidation of new CDOM generated at depth and/or dissolved black carbon and probably not from bulk refractory DOC.

While one goal of this study was to probe the photoreactivity of deep ocean DOC, it also contributes significant new understanding of the processes controlling the

photoproduction and decay of superoxide in marine environments. We calculated O_2^- photoproduction rates for surface waters in the Gulf of Alaska ranging from 10.8 – 16.5 pM s^{-1}, well above those estimated for biological O_2^- production in this region (< 0.3 – ~5.5 pM s^{-1}; Hansard et al., 2010) and in the Equatorial Pacific (~0.3 – 1.2 pM s^{-1}; Rose et al., 2008b). Because the biological source for superoxide in the ocean has received recent attention (Diaz et al., 2013), we believe that any study that adds to the scarce information regarding the photochemical production of this ROS, which is most likely the largest source of O_2^- in sunlit waters, is well justified and the subject warrants further attention.

Because oceanic H_2O_2 distributions and photoproduction rates have been so widely studied, the photoproduction rates of O_2^- have often been inferred from those for H_2O_2. However, of all the identified ROS formed from CDOM photochemistry in natural waters (i.e. O_2^-, H_2O_2, $^{\bullet}OH$ and $^1O_2$), O_2^- is the only one for which direct apparent quantum yield spectra have not been reported. Our results indicate that in the open ocean, a large fraction of photoproduced O_2^- does not lead to H_2O_2, meaning that the relationship between these two ROS may not simply be a simple factor of two (Equation 4.4). Our shipboard experiments alone indicate that for surface waters, the photoproduction rate of O_2^- ranges between 1.76 and 4.53 times greater than that for H_2O_2. Until O_2^- apparent yield spectra become available, applying this relationship to H_2O_2 apparent quantum yield spectra to obtain estimates of O_2^- photoproduction rates in marine waters will be poorly constrained and very likely inaccurate.

Acknowledgements

This work was supported by NSF grant OCE-1234388 awarded to Dr. William L. Miller. The authors would like to thank Dr. Dennis Hansell for use of DOC and nitrate data and Dr. Whitney King for use of a new FeLume system. We would also like to thank Dr. Patricia Medeiros for sampling assistance on board, Dr. Lisa Miller and Marie Robert for sampling and shipping samples for preliminary experiments, collected along Line P, and the captain and crew of the *R/V Melville* for sampling assistance in the Gulf of Alaska.

References

Avery, G.B., Cooper, W.J., Kieber, R.J., Willey, J.D., 2005. Hydrogen peroxide at the Bermuda Atlantic Time Series Station: Temporal variability of seawater hydrogen peroxide. Mar. Chem. 97, 236–244. doi:10.1016/j.marchem.2005.03.006

Bauer, J.E., Williams, P.M., Druffel, E.R.M., 1992. ^{14}C activity of dissolved organic carbon fractions in the north-central Pacific and Sargasso Sea. Nature. 357, 667–670.

Bielski, B.H.J., 1978. Reevaluation of the spectral and kinetic properties of HO_2 and O_2^- free radicals. Photochem. Photobiol. 28, 645–649.

Bielski, B.H.J., Cabelli, D.E., Arudi, R.L., Ross, A.B., 1985. Reactivity of HO_2/O_2^- radicals in aqueous solution. J. Phys. Chem. Ref. Data. 14(4), 1041–1100.

Blough, N.V., Zepp, R.G., 1995. Reactive oxygen species in natural waters. In: Active oxygen in chemistry. Springer, Netherlands, pp. 280–333.

Carlson, C.A., 2002. Production and removal processes. In: Hansell, D.A., Carlson, C.A. (Eds.), Biogeochemistry of Marine Dissolved Organic Matter. Academic, San Diego, pp. 91–151.

D'Sa, E.J., Steward, R.G., Vodacek, A., Blough, N. V., Phinney, D., 1999. Determining optical absorption of colored dissolved organic matter in seawater with a liquid capillary waveguide. Limnol. Oceanogr. 44, 1142–1148. doi:10.4319/lo.1999.44.4.1142

Diaz, J.M., Hansel, C.M., Voelker, B.M., Mendes, C.M., Andeer, P.F., Zhang, T., 2013. Widespread production of extracellular superoxide by heterotrophic bacteria. Science. 340, 1223–1226. doi:10.1126/science.1237331

Fujimori, K., Nakajima, S.H., Akutsu, K., Mitani, M., Sawadab, H., Nakayamab, M., 1993. Chemiluminescence of cypridina luciferin analogues. Part 1. Effect of pH on rates of spontaneous autoxidation of CLA in aqueous buffer solutions. J. Chem. Soc., Perkin Trans. 2, 2405–2409.

Garg, S., Rose, A.L., Waite, T.D., 2011. Photochemical production of superoxide and hydrogen peroxide from natural organic matter. Geochim. Cosmochim. Acta. 75, 4310–4320. doi:10.1016/j.gca.2011.05.014

Goldstone, J., Voelker, B., 2000. Chemistry of superoxide radical in seawater: CDOM associated sink of superoxide in coastal waters. Environ. Sci. Technol. 34, 1043–1048.

Goldstone, J. V, Pullin, M.J., Bertilsson, S., Voelker, B.M., 2002. Reactions of hydroxyl radical with humic substances: bleaching, mineralization, and production of bioavailable carbon substrates. Environ. Sci. Technol. 36, 364–372.

Grebel, J.E., Pignatello, J.J., Song, W., Cooper, W.J., Mitch, W.A., 2009. Impact of halides on the photobleaching of dissolved organic matter. Mar. Chem. 115, 134–144. doi:10.1016/j.marchem.2009.07.009

Hansard, P.S., Vermilyea, A.W., Voelker, B.M., 2010. Measurements of superoxide radical concentration and decay kinetics in the Gulf of Alaska. Deep Sea Res. Part I Oceanogr. Res. Pap. 57, 1111–1119. doi:10.1016/j.dsr.2010.05.007

Hansell, D.A., 2013. Recalcitrant dissolved organic carbon fractions. Ann. Rev. Mar. Sci. 5, 421–45. doi:10.1146/annurev-marine-120710-100757

Hansell, D.A., Carlson, C.A., Repeta, D.J., Schlitzer, R., 2009. Dissolved Organic Matter in the Ocean: A Controversy Stimulates New Insights. Oceanography. 22, 202–211. doi:doi.org/10.5670/oceanog.2009.109

Hansell, D.A., Carlson, C.A., Schlitzer, R., 2012. Net removal of major marine dissolved organic carbon fractions in the subsurface ocean. Global Biogeochem. Cycles 26. doi:10.1029/2011GB004069

Heller, M.I., Croot, P.L., 2010a. Superoxide decay kinetics in the southern ocean. Environ. Sci. Technol. 44, 191–196. doi:10.1021/es901766r

Heller, M.I., Croot, P.L., 2010b. Kinetics of superoxide reactions with dissolved organic matter in tropical Atlantic surface waters near Cape Verde (TENATSO). J. Geophys. Res. 115, C12038. doi:10.1029/2009JC006021

Heller, M.I., Croot, P.L., 2010c. Application of a superoxide (O_2^-) thermal source (SOTS-1) for the determination and calibration of O_2^- fluxes in seawater. Anal. Chim. Acta. 667, 1–13. doi:10.1016/j.aca.2010.03.054

Helms, J.R., Stubbins, A., Perdue, E.M., Green, N.W., Chen, H., Mopper, K., 2013. Photochemical bleaching of oceanic dissolved organic matter and its effect on absorption spectral slope and fluorescence. Mar. Chem. 155, 81–91. doi:10.1016/j.marchem.2013.05.015

Hu, C., Muller-karger, F.E., Zepp, R.G., 2002. Absorbance, absorption coefficient, and apparent quantum yield: A comment on common ambiguity in the use of these optical concepts. Limnol. Oceanogr. 47, 1261–1267.

Johannessen, S.C., Miller, W.L., 2001. Quantum yield for the photochemical production of dissolved inorganic carbon in seawater. Mar. Chem. 76, 271–283. doi:10.1016/S0304-4203(01)00067-6

Kieber, D.J., Miller, G.W., Neale, P.J., Mopper, K., 2014. Wavelength and temperature-dependent apparent quantum yields for photochemical formation of hydrogen peroxide in seawater. Environ. Sci. Process. Impacts 16, 777–791. doi:10.1039/c4em00036f

King, D.W., Cooper, W.J., Rusak, S.A., Peake, B.M., Kiddle, J.J., O'Sullivan, D.W., Melamed, M.L., Morgan, C.R., Theberge, S.M., 2007. Flow injection analysis of H_2O_2 in natural waters using acridinium ester chemiluminescence: method development and optimization using a kinetic model. Anal. Chem. 79, 4169–4176. doi:10.1021/ac062228w

Kirchman, D.L., Lancelot, C., Fasham, M., Legendre, L., Radach, G., Scott, M., 1993. Dissolved organic matter in biogeochemical models of the ocean. In: Evans, G.T., Fasham, M.J.R. (Eds.), Towards a Model of Ocean Biogeochemical Processes. Springer, Berlin, pp. 209–225.

Lechtenfeld, O.J., Kattner, G., Flerus, R., McCallister, S.L., Schmitt-Kopplin, P., Koch, B.P., 2014. Molecular transformation and degradation of refractory dissolved organic matter in the Atlantic and Southern Ocean. Geochim. Cosmochim. Acta. 126, 321–337. doi:10.1016/j.gca.2013.11.009

Marion, G.M., Millero, F.J., Camões, M.F., Spitzer, P., Feistel, R., Chen, C.-T.A., 2011. pH of seawater. Mar. Chem. 126, 89–96. doi:10.1016/j.marchem.2011.04.002

McDowell, M.S., Bakač, Espenson, JH., 1983. A convenient route to superoxide ion in aqueous solution. Inorg. Chem. 22, 847–848.

Micinski, E., Ball, L., Zafiriou, O., 1993. Photochemical Oxygen Activation: Superoxide Radical Detection and Production Rates in the Eastern Caribbean. J. Geophys. Res. 98, 2299–2306.

Miller, R.L., Belz, M., Castillo, C. Del, Trzaska, R., 2002. Determining CDOM absorption spectra in diverse coastal environments using a multiple pathlength, liquid core waveguide system. Cont. Shelf Res. 22, 1301–1310. doi:10.1016/S0278-4343(02)00009-2

Miller, W.L., Kester, D.K. 1988. Hydrogen Peroxide Measurement in Seawter by (p-Hydroxyphenyl)acetic Acid Dimerization. Anal. Chem. 60, 2711–2715.

Moffett, J.W., Zafiriou, O.C., 1993. The Photochemical Decomposition of Hydrogen Peroxide in Surface Waters of the Eastern Caribbean and Orinoco River. J. Geophys. Res. 98, 2307–2313.

Molot, L.A., Hudson, J.J., Dillon, P.J., Miller, S.A., 2005. Effect of pH on photo-oxidation of dissolved organic carbon by hydroxyl radicals in a coloured, softwater stream. Aquat. Sci. 67, 189–195. doi:10.1007/s00027-005-0754-9

Mopper, K., Zhou, X., 1990. Hydroxyl radical photoproduction in the sea and its potential impact on marine processes. Science. 250, 661–664.

Mopper, K., Zhou, X., Kieber, R.J., Kieber, D.J., Sikorski, R.J., Jones, R.D., 1991. Photochemical degradation of dissolved organic carbon and its impact on the oceanic carbon cycle. Nature. 353, 60–62. doi:10.1038/353060a0

Nelson, N.B., Siegel, D.A., Carlson, C.A., Swan, C., Smethie, W.M., Khatiwala, S., 2007. Hydrography of chromophoric dissolved organic matter in the North Atlantic. Deep Sea Res. Part I Oceanogr. Res. Pap. 54, 710–731. doi:10.1016/j.dsr.2007.02.006

Nishioka, J., Takeda, S., Wong, C.., Johnson, W.., 2001. Size-fractionated iron concentrations in the northeast Pacific Ocean: distribution of soluble and small colloidal iron. Mar. Chem. 74, 157–179. doi:10.1016/S0304-4203(01)00013-5

Ong, T.-C., 2007. Detailed mechanistic and optimization of the photochemical production method of superoxide. In: Department of Chemistry, Colby College, Waterville, ME.

O'Sullivan, D.W., Neale, P.J., Coffin, R.B., Boyd, T.J., Osburn, C.L., 2005. Photochemical production of hydrogen peroxide and methylhydroperoxide in coastal waters. Mar. Chem. 97, 14–33. doi:10.1016/j.marchem.2005.04.003

Obernosterer, I., Ruardij, P., Herndl, G.J., 2001. Spatial and diurnal dynamics of dissolved organic matter (DOM) fluorescence and H_2O_2 and the photochemical oxygen demand of surface water DOM across the subtropical Atlantic Ocean. Limnol. Oceanogr. 46, 632–643. doi:10.4319/lo.2001.46.3.0632

Petasne, R.G., Zika, R.G., 1987. Fate of superoxide in coastal seawater. Nature. 325, 516–618.

Powers, L.C., Miller, W.L., 2014. Blending remote sensing data products to estimate photochemical production of hydrogen peroxide and superoxide in the surface ocean. Environ. Sci. Process. Impacts 16, 792–806. doi:10.1039/c3em00617d

Reader, H.E., Miller, W.L., 2011. Effect of estimations of ultraviolet absorption spectra of chromophoric dissolved organic matter on the uncertainty of photochemical production calculations. J. Geophys. Res. 116, C08002. doi:10.1029/2010JC006823

Rose, A.L., Moffett, J.W., Waite, T.D., 2008a. Determination of superoxide in seawater using 2-Methyl-6-(4-methoxyphenyl)-3,7-dihydroimidazo[1,2-a]pyrazin-3(7H)-one chemiluminescence. Anal. Chem. 80, 1215–1227.

Rose, A.L., Webb, E.A., Waite, T.D., Moffett, J.W., 2008b. Measurement and implications of nonphotochemically generated superoxide in the equatorial Pacific Ocean. Environ. Sci. Technol. 42, 2387–23893.

Rusak, S.A., Peake, B.M., Richard, L.E., Nodder, S.D., Cooper, W.J., 2011. Distributions of hydrogen peroxide and superoxide in seawater east of New Zealand. Mar. Chem. 127, 155–169. doi:10.1016/j.marchem.2011.08.005

Sexton, P.F., Norris, R.D., Wilson, P.A, Pälike, H., Westerhold, T., Röhl, U., Bolton, C.T., Gibbs, S., 2011. Eocene global warming events driven by ventilation of oceanic dissolved organic carbon. Nature 471, 349–352. doi:10.1038/nature09826

Shaked, Y., Harris, R., Klein-Kedem, N., 2010. Hydrogen peroxide photocycling in the Gulf of Aqaba, Red Sea. Environ. Sci. Technol. 44, 3238–3244.

Sharpless, C.M., Aeschbacher, M., Page, S.E., Wenk, J., Sander, M., McNeill, K., 2014. Photooxidation-induced changes in optical, electrochemical, and photochemical properties of humic substances. Environ. Sci. Technol. 48, 2688–96. doi:10.1021/es403925g

Sharpless, C.M., Blough, N.V., 2014. The importance of charge-transfer interactions in determining chromophoric dissolved organic matter (CDOM) optical and photochemical properties. Environ. Sci. Process. Impacts. 16, 654–671. doi:10.1039/c3em00573a

Stubbins, A., Niggemann, J., Dittmar, T., 2012. Photo-lability of deep ocean dissolved black carbon. Biogeosciences 9, 1661–1670. doi:10.5194/bg-9-1661-2012

Swan, C.M., Nelson, N.B., Siegel, D. a, Kostadinov, T.S., 2012. The effect of surface irradiance on the absorption spectrum of chromophoric dissolved organic matter in the global ocean. Deep. Res. Part I-Oceanographic Res. Pap. 63, 52–64. doi:10.1016/j.dsr.2012.01.008

Swan, C.M., Siegel, D.A., Nelson, N.B., Carlson, C.A., Nasir, E., 2009. Biogeochemical and hydrographic controls on chromophoric dissolved organic matter distribution in the Pacific Ocean. Deep. Res. Part I Oceanogr. Res. Pap. 56, 2175–2192. doi:10.1016/j.dsr.2009.09.002

Voelker, B.M., Sedlak, D.L., 1995. Iron reduction by photoproduced superoxide in seawater. Mar. Chem. 50, 93–102.

Voelker, B.M., Sedlak, D.L., Zafiriou, O.C., 2000. Chemistry of Superoxide Radical in Seawater: Reactions with Organic Cu Complexes. Environ. Sci. Technol. 34, 1036–1042. doi:10.1021/es990545x

Williams, P.M., Druffel, E.R.M., 1987. Radiocarbon in dissolved organic matter in the central North Pacific Ocean. Nature. 330, 246–248.

Wuttig, K., Heller, M.I., Croot, P.L., 2013. Pathways of superoxide (O_2^-) decay in the Eastern Tropical North Atlantic. Environ. Sci. Technol. 47, 10249–10256. doi:10.1021/es401658t

Yamashita, Y., Tanoue, E., 2009. Basin scale distribution of chromophoric dissolved organic matter in the Pacific Ocean. Limnol. Oceanogr. 54, 598–609. doi:10.4319/lo.2009.54.2.0598

Yocis, B.H., Kieber, D.J., Mopper, K., 2000. Photochemical production of hydrogen peroxide in Antarctic Waters. Deep Sea Res. Part I Oceanogr. Res. Pap. 47, 1077–1099. doi:10.1016/S0967-0637(99)00095-3

Yuan, J., Shiller, A.M., 2005. Distribution of hydrogen peroxide in the northwest Pacific Ocean. Geochemistry, Geophys. Geosystems 6. doi:10.1029/2004GC000908

Zafiriou, O.C., 1974. Sources and reactions of OH and daughter radicals in seawater. J. Geophys. Res. 79, 4491–4497. doi:10.1029/JC079i030p04491

Zafiriou, O.C., 1990. Chemistry of superoxide ion-radical (O_2^-) in seawater. I . pK*a_{sw} (HOO) and uncatalyzed dismutation kinetics studied by pulse radiolysis. Mar. Chem. 30, 31–43.

Zafiriou, O.C., Blough, N.V., Micinski, E., Dister, B., Kieber, D., Moffet, J. 1990. Molecular probe systems for reactive transients in natural waters. Mar. Chem. 30, 45–70.

Zepp, R.G., Hoigne, J., Bader, H., 1987. Nitrate-induced photooxidation of trace organic chemicals in water. Environ. Sci. Technol. 21, 443–450.

Zhang, Y., Del Vecchio, R., Blough, N.V., 2012. Investigating the mechanism of hydrogen peroxide photoproduction by humic substances. Environ. Sci. Technol. 46, 11836–11843. doi:10.1021/es3029582

Ziolkowski, L.A., Druffel, E.R.M., 2010. Aged black carbon identified in marine dissolved organic carbon. Geophys. Res. Lett. 37. doi:10.1029/2010GL043963

CHAPTER 5

H_2O_2 PHOTOPRODUCTION IN MARINE WATERS: A SIMPLE PROXY FOR ESTIMATING DIRECT CO_2 PHOTOCHEMICAL FLUXES FROM RIVERINE IMPACTED TO OLIGOTROPHIC WATERS[1]

[1]L.C. Powers and W.L. Miller. To be submitted to *Geophysical Research Letters*.

Abstract

CO_2 is the largest identified carbon product of dissolved organic matter (DOM) photochemistry in natural waters, but its analysis has been hampered in marine waters due to high background DIC concentrations and the lack of sensitive gas phase detection methods. Hence, a quantitative description of its photochemical production efficiency (i.e. apparent quantum yield (AQY) spectra), especially for the open ocean, remains poorly constrained. Here we present evidence that the photoproduction of H_2O_2, with sub-nanomolar detection limits, appears to be a simple proxy for CO_2 photoproduction with an average CO_2:H_2O_2 ratio of 6.89 ± 1.64 determined in a variety of marine waters ranging from dark waters collected in a tidal creek to those collected offshore near the Gulf Stream. Even when corrected for photobleaching, photoproduction rates for both H_2O_2 and CO_2 were nonlinear beyond 12 hours of irradiation, indicating that production efficiency for both products decreases with prolonged exposure. Because a necessary assumption in calculating AQY spectra with one time point is that the photoproduction rate remains linear, any AQY spectra for CO_2 or H_2O_2 determined from long irradiations should be interpreted with caution. However, H_2O_2 is a thermal product of superoxide (O_2^-) decay, and measurements of O_2^- photoproduction and dark decay made here indicate that O_2^- may be the best proxy for photochemical DOM oxidation to CO_2. Results here, combined with the short irradiations times needed to determine O_2^- production rates (~2 minutes) compared to the time required for measurable CO_2 production (~6 hours), suggest that O_2^- photoproduction rates (3300 nM hr^{-1} at our tidal creek station) may provide the best estimates of initial CO_2 photoproduction rates (2800 nM hr^{-1} at the same station), or at least its maximum rate in the marine environment.

1. Introduction

The photodegradation of dissolved organic matter (DOM) plays a direct role in oceanic carbon cycling as it is a significant process in the oxidation of organic carbon to carbon dioxide (CO_2), carbon monoxide (CO), and a number of low molecular weight organic molecules (Miller and Zepp, 1995; Mopper and Kieber, 2002). For twenty years, CO_2 has been recognized as the largest carbon product of aquatic DOM photochemistry, and its photoproduction could play a direct role in air-sea CO_2 fluxes. Additionally, photochemistry indirectly affects CO_2 fluxes because a large portion of photoreactive DOM is biologically refractory (Mopper and Kieber 2000, refs therein), and a number of the resulting photoproducts are readily available for microbial assimilation (Miller and Moran, 1997; Mopper and Kieber 2002). In attempts to quantify the photoproduction of these biologically labile products (BLPs) by using oxygen consumption as a proxy for community carbon use, Reader and Miller (2014) observed a microbial response from -21% to +155% relative to dark controls. They observed that the formation of these BLPs was highly dependent on photon dose, as a competition between the formation and destruction of BLPs occurs during irradiation. Due to the complexity and difficulty in quantifying photochemical BLP formation, the impact of indirect photochemistry on carbon cycling remains poorly constrained.

Perhaps due to analytical challenges associated with investigating BLP photochemistry and its indirect impact on marine photochemistry, direct formation of oxidized carbon products has been studied as a relatively well understood part of DOC photo-oxidation and is often quantified as the spectral apparent quantum yield (AQY; $\phi(\lambda)$), defined as the ratio of the number of moles product produced to the number of

moles photons absorbed by the sample. However, while the direct photochemical oxidation of colored DOM (CDOM) most efficiently produces CO_2 (Miller & Zepp, 1995; Miller & Moran, 1997; White et al., 2010), analysis of this photoproduct is hampered by the fact that most methods require CO_2 measurement in gas phase, and current IR methods are not particularly sensitive (±1 μatm, Wang et al., 2005). Therefore, all studies have measured photoproduced CO_2 as DIC (the sum of dissolved CO_2, HCO_3^-, and CO_3^{2-}). This approach is analytically challenging in freshwaters with high concentrations of carbonate and in marine waters with even higher DIC concentrations (~2 mM) present in seawater. To detect low concentrations of DIC formed over the course of a typical irradiation experiment (i.e. low μM levels), sample pretreatment is required to remove background DIC from the system and requires irradiation times ~2 times longer than for other photoproducts (e.g. CO and H_2O_2). These CO_2-free seawater samples are therefore susceptible to contamination from atmospheric CO_2 and microbial respiration, making measurements from clear, open ocean samples with low photon absorption requiring longer irradiation times exceedingly difficult.

Because the use of a simple proxy for CO_2 photoproduction is a convenient method for overcoming these difficulties, Miller and Zepp (1995) first reported simultaneous measurements of CO_2 and CO photoproduction rates, reporting a CO_2:CO ratio between 15 and 20. Perhaps because the photoefficiency for both photoproducts (i.e. the AQY spectrum) tends to follow an exponential shape and CO photoproduction rates are readily accessible in almost all marine waters (e.g. via methods of Xie et al., 2002), the use of a simple CO_2:CO ratio for this purpose is attractive. Unfortunately, subsequent publication of CO_2:CO photoproduction ratios from different locations and time of year

have expanded the range, now spanning from ~2 to >65 (Johannessen 2000; Miller & Zepp 1995; Powers and Miller, 2014a; Reader and Miller, 2012; White et al., 2010). They also may vary with sample pretreatment, as required for CO_2 measurements (Powers and Miller, 2014a) and are generally not correlated to CDOM absorbance or salinity (Powers and Miller 2014a; Reader and Miller 2012). These results suggest that the mechanisms involved in CO_2 and CO photochemistry are likely different, involving both direct and (primarily) indirect photosensitized reactions (Gao and Zepp, 1998; Pos et al., 1998; Xie et al., 2004). It has been reported that initial CO_2 photoproduction rates are faster than long term CO_2 photoproduction rates measured after prolonged exposure (Miller and Zepp, 1995), which has not been observed for the photoproduction of CO (Valentine and Zepp, 1993). This could add to the variability seen in these CO_2:CO ratios, providing further evidence that photoproduced CO is not a suitable proxy for photoproduced CO_2.

Alternatively, Sharpless and Blough (2014) suggest that the suspected precursor for H_2O_2, a photoreduced transient $CDOM^{+\bullet/-\bullet}$, may be important in DOM photo-oxidation and therefore in the formation of CO_2. H_2O_2 photochemical efficiencies have been correlated to CDOM photobleaching (O'Sullivan et al., 2005), an important process in CDOM photo-oxidation, thus indicating that H_2O_2 may be a more suitable proxy for CO_2 photochemical production in marine waters. Here, we investigated this possible relationship with broadband irradiations and simultaneous measurements of photoproduced CO_2 and H_2O_2 for 6 samples collected in the South Atlantic Bight off the coast of Georgia, USA, ranging from inshore/coastal waters to clear waters collected near the Gulf Stream. Experiments include irradiations up to 48 hours to check the earlier

observation of nonlinear DIC photoproduction during long irradiations (e.g. >8 hour, Miller and Zepp, 1995) and AQY spectra determination for H_2O_2 and CO_2 in our the darkest sample to further quantify the potential use of H_2O_2 photoproduction as a useful proxy for DOC photo-oxidation to CO_2 in irradiated seawater.

2. Methods

Preliminary experiments performed to check for linearity in CO_2 photoproduction during long irradiations up to 48 hours on samples collected in the Northern Gulf of Mexico in November 2009 are listed in Table 5.1 and described in detail in Powers and Miller (2014a). These experiments were done in the polychromatic irradiation system used for AQY experiments, described below, with the key difference being that bandpass cutoff filters, as required for polychromatic AQY irradiations, were removed and a window glass filter was added to the solar simulator that provided full spectral irradiance to enter each sample. Additional samples were collected by hand dockside from Dean Creek, a tidal creek on Sapelo Island, GA, December 13, 2013 and onboard the R/V *Savannah* in the South Atlantic Bight between May 15 – 18, 2014 using standard Niskin bottles mounted on a CTD-Rosette (Table 5.1). Upon collection, 2 – 8 liters of water were 0.2 μm filtered (precleaned Whatman Polycap 75 AS nylon membrane) into 2 L acid-cleaned (2 M HCl, J.T. Baker), Milli-Q rinsed (18 MΩ, Millipore) polycarbonate bottles (Nalgene). Samples were stored at 4 °C until used in experimental irradiations, up to 6 months.

For paired CO_2/H_2O_2 irradiation experiments, samples were partitioned into spectrophotometric cells and sealed with no headspace using caps lined with Teflon faced, butyl rubber septa. As required to obtain CO_2 photoproduction data with DIC

Table 5.1. Station locations in the Gulf of Mexico (GoM) and South Atlantic Bight (SAB), salinity, and $a_g(320)$ (m^{-1}) at the beginning and end of experiments for all samples used in broadband irradiations. Production rates for CO_2 and H_2O_2 normalized to the average $a_g(320)$ over various rate intervals are compared, as well as the ratio between photoproduced CO_2:$H2O_2$ measured at each time point.

Station	Lat. (N)	Long. (W)	Salinity	$a_g(320)$ (m^{-1})		Interval	CO_2 Prod. Rate	H_2O_2 Prod. Rate	Irradiation	DIC:HOOH°
				Initial	Final*	(h)	(nM m hr^{-1})^	(nM m hr^{-1})^	time (h)	
Atchafalaya River GoM[a]	29.38	91.37	6.10	24.5	17.5	0 - 5.4	85 ± 37			
						5.4 - 13.5	64 ± 1.2			
						13.5 - 22.6	35 ± 27			
						22.6 - 45.2	41 ± 13			
Inshore GoM[a]	29.13	90.59	25.80	5.44	3.44	0 - 6	43 ± 10			
						6 - 10.5	24 ± 41			
						10.3 - 21.3	15 ± 1			
						21.3 - 48.4	32 ± 12			
Dean Creek SAB	31.397	81.281	5.00	8.78	3.14	0 - 6	292 ± 16	149 ± 18	6.00	7.48 ± 1.62
						6 - 11.7	216 ± 23	149 ± 62	11.7	7.32 ± 0.98
						11.7 - 23.2	113 ± 34	21 ± 6	23.2	7.12 ± 1.54
						23.2 - 47.9	35 ± 6	17 ± 3	47.9	6.09 ± 0.47
SS2 SAB	31.039	81.241	34.05	2.54	1.26	0 - 10.6	64 ± 57	40 ± 12	10.6	6.42 ± 1.81
						10.6 - 24.3	128 ± 83	35 ± 4	24.3	3.93 ± 1.13
						24.3 - 35.4	85 ± 4	23 ± 1	35.4	4.01 ± 0.88
G7 SAB	31.519	80.670	34.94	1.92	1.05	0 - 11	76 ± 20	12 ± 6	11.0	6.21 ± 4.46
						11 - 24.7	113 ± 38	22 ± 3	24.7	5.45 ± 1.93
						24.7 - 48.9	28 ± 53	0.2 ± 1.0	48.9	6.52 ± 1.90
C5 SAB	31.297	80.927	34.51	2.07	1.54	0 - 11	55 ± 10	7 ± 1	11.0	7.34 ± 5.62
C14 SAB	31.238	71.718	36.27	0.476	0.319	0 - 11	96 ± 59	11 ± 7	11.0	8.98 ± 5.56
						11 - 25.7	107 ± 49	13 ± 1	25.7	8.67 ± 0.80
						25.7 - 49.1	67 ± 19	6 ± 1	49.1	9.37 ± 1.22

C15 SAB	31.230	79.587	36.25	0.475	0.354	0 - 38.4	49 ± 12	5 ± 0.1	38.4	8.53 ± 5.85
									Average	6.89 ± 1.64
									Median	7.12
									Range	3.93 - 9.37

[a]Irradiation dose was approximately % lower in the system used for Gulf of Mexico samples than that for the South Atlantic Bight samples

*Final $a_g(320)$ measured at the end of the experiment, typically after ≥40 hours of irradiation

°CO_2:H_2O_2 value is the average of duplicate cells at each time point

[^]Production rates were normalized to the average $a_g(320)$ for each rate interval and are determined for duplicate samples

analyzers in air-equilibrated seawater containing mM concentrations of DIC, samples were pretreated to remove the carbonate system. In a clean glass kettle, samples were acidified to a pH between 2 and 3, bubbled overnight with hydrated, CO_2-free air using an air tank (Air Ultra Zero, CO_2 <1 ppm, Airgas) fitted with a soda lime (indicating, ACS grade, Alfa Aesar) column, and returned to their original pH with crystalline sodium borate (ACS grade, Fisher) as in Johannessen and Miller (2001). All irradiations were performed using a Suntest CPS solar simulator fitted with a 1.5 kW xenon lamp (Atlas). Because contamination, potentially from CO_2 in room air diffusing across or around the septa, was found for some dark control cells in our preliminary experiments with Northern Gulf of Mexico samples, broadband irradiations for the 2013 samples were done by placing cells upright under pure water in 600 mL jacketed beakers (Ace Glass) attached to a circulating water bath maintained at 15 °C, and fitted with quartz glass lids. For apparent quantum yield experiments, sample cells were irradiated in a water cooled aluminum block, also maintained at 15 °C, allowing for no transfer of light between cells, under a variety of Schott long bandpass cutoff filters as described in Powers and Miller (2014a). Paired irradiations for both H_2O_2 and its precursor, superoxide (O_2^-), were performed for the darkest sample (Dean Creek) by filling a clean 600 mL jacketed beaker with filtered sample, stirred with a Teflon stir bar and covered with a quartz lid.

Photoproducts quantified in this study were CO_2, measured as DIC using a Shimadzu TOC-V run in DIC mode, and H_2O_2 and O_2^-, both measured using a FeLume chemiluminescence system (Waterville Analytical) and/or a GLOCEL-2 serpentine flow cell (Global FIA) following the methods of King et al. (2007) and Rose et al. (2008), respectively. Calibration methods for these photoproducts are described in Powers and

Miller (2014b) and Powers et al. (2014). Sample CDOM absorbance spectra were measured in 10 cm cells using a benchtop spectrophotometer (Perkin Elmer, Lambda 40) and converted to CDOM absorption coefficients ($a_g(\lambda)$; m^{-1}) as in Reader and Miller (2011). For AQY calculations, the photon absorption rate ($Q_a(\lambda)$; mole photons s^{-1}) for each sample was determined with $a_g(\lambda)$ and measured irradiance entering each cell in the aluminum block on 1 nm intervals determined using an OL756 spectroradiometer (Optronics laboratories) following the methods of Hu et al. (2002) to correct for self-shading in dark samples. In this multispectral irradiation system, for each product (either CO_2 or H_2O_2), the production rate measured in each cell is equal to the product of the AQY spectrum ($\phi(\lambda)$) and the photon absorption rate, $Q_a(\lambda)$, which allows for the determination of $\phi(\lambda)$ as the only unmeasured variable. The spectral AQY for each sample was therefore modeled from either the CO_2 or H_2O_2 photoproduction rate and $Q_a(\lambda)$ for all light treatments with the following exponential equation

$$\phi(\lambda) = e^{-(m_1+m_2(\lambda-290))} \quad (5.1)$$

and a statistical curve fitting method to solve for the parameters m_1 and m_2, detailed in Johannessen and Miller (2001).

3. Results and Discussion

3.1 Broadband Irradiations

Results of preliminary experiments to check for reciprocity in CO_2 photoproduction for a river sample and an inshore sample, collected in the Northern Gulf of Mexico, are shown in Figure 5.1. For both samples, initial rates were faster than those measured after prolonged exposure, even when concentrations were corrected for CDOM photochemical fading (averaged % CDOM loss over 290 – 400 nm wavelength range).

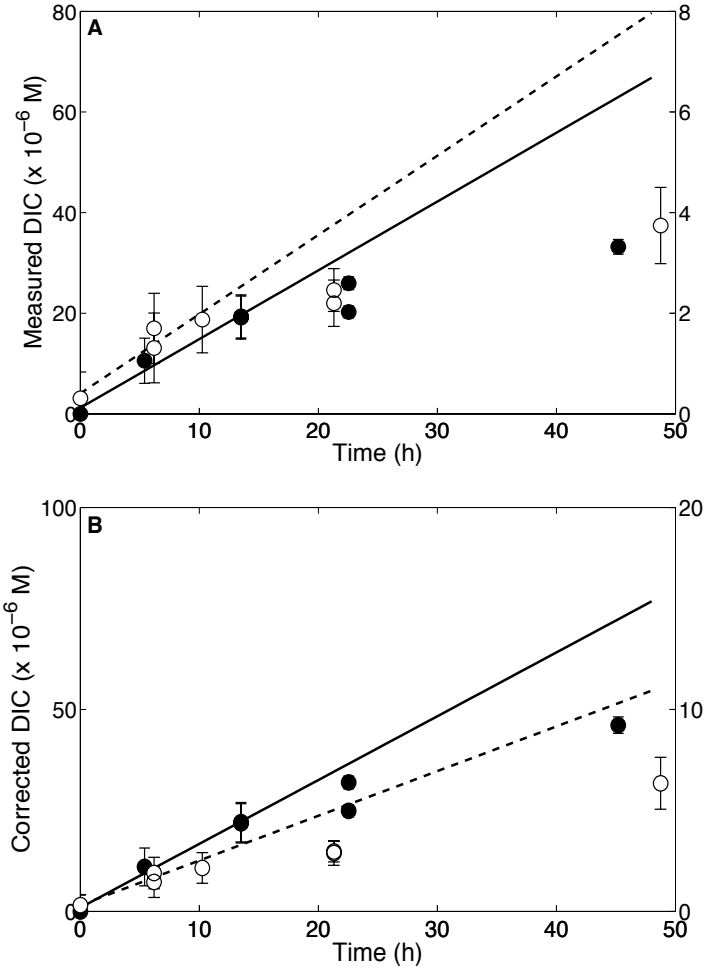

Figure 5.1. Measured photoproduced CO_2 (A) from the Atchafalaya River sample (black circles, right axis) and a coastal Gulf of Mexico sample (white circles, left axis) together with data corrected for average %CDOM loss from 290 – 400 nm (B). Solid and dashed lines are fits for initial rates determined for the first ~6 hours of irradiation for the riverine and coastal sample, respectively.

Although nonlinearity in CO_2 photoproduction in natural waters has been reported previously (Miller and Zepp, 1995; White et al., 2008), it is often not been considered in studies using CO_2 photoproduction rates measured with a single measurement taken after ~48 hours of irradiation to infer AQY data (e.g. Bélanger et al., 2006; Fichot and Benner, 2014). Albeit from a small sample size, photoproduction rates determined over the entire irradiation period (~48 hours) for corrected CO_2 data (Figure 5.1B) were 39% lower in the river sample and 49% lower in the inshore sample than those determined over the first 6 – 12 hours of irradiation. A fundamental assumption in AQY calculations using a single production time point is that the production rate of the product of interest is a linear function of photon exposure (Miller, 1998). These results suggest that spectral AQY values for CO_2 decrease with continued irradiation, which has also been observed for both the CDOM photobleaching and O_2 loss AQY at 310 nm (Andrews et al., 2000) as well as H_2O_2 AQY data at various wavelengths (Andrews et al., 2000; Kieber et al., 2014). This makes comparisons of CO_2 AQY spectra between studies using various irradiation times, ranging from 4 to >40 hours, difficult if not impossible. Unfortunately, for waters with low CDOM absorption spectra, especially in the open ocean, accurately measuring CO_2 photoproduction is exceedingly difficult given low production rates and the long exposure time required for measurable photoproduction (Powers and Miller, 2014a).

Previously, photochemically produced CO has been used as a proxy for CO_2 photoproduction, but the ratio between these two photoproducts remains unconstrained (Miller and Zepp, 1995; White et al., 2010; Reader and Miller 2012; Powers and Miller, 2014a) and has not been correlated to $a_g(\lambda)$ or salinity. Intriguingly, photoproduced H_2O_2

may be a better proxy for CO_2 based on evidence that the two photoproducts may have the same precursor (Sharpless and Blough, 2014) and both are correlated with CDOM photo-oxidation (Andrews et al., 2000). To our knowledge, simultaneously measured rates of these two photoproducts in the same sample have never been reported for natural waters. However, the magnitude of reported H_2O_2 AQY spectra determined for freshwater and coastal marine samples ranges from about $5 – 15 \times 10^{-4}$ at 300 nm (Andrews et al., 2000; Cooper et al., 1988; Kieber et al., 2014; Moore et al., 1993) while that for CO_2 ranges from about $5 – 30 \times 10^{-4}$ at 300 nm (Johannessen and Miller, 2001; Koehler et al., 2014; Reader and Miller, 2012), having the highest AQY values reported for any measurable photoproduct in natural samples. In addition, Gao and Zepp (1998) reported similar rates for CO_2 photoproduction (2.2×10^{-5} M hr^{-1}) and O_2 photochemical loss (2.4×10^{-5} M hr^{-1}) in Satilla River samples and noted that most of the O_2 loss likely goes to H_2O_2. On the other hand, Andrews et al. (2000) reported that H_2O_2 was only about 45% of O_2 uptake from irradiations of diluted Shark River water, but that both had similar photon dose dependencies. Obviously direct determinations of H_2O_2 and CO_2 photoproduction rates together in marine samples ranging from dark inshore (Dean Creek sample) to oligotrophic waters (Gulf Stream samples, Stations C14 and C15) will address these issues.

Samples collected in the South Atlantic Bight were irradiated in 10 cm cylindrical spectrophotometer cells submerged under water in jacketed beakers up to 48 hours (Table 5.1). Although this set up does not allow for an easily quantifiable light field within the cell, irradiance measured at the top of the beaker was equivalent to about 6 days of exposure at 30 °N in mid May. The purpose of these experiments was twofold: to

further check for linearity in CO_2 and H_2O_2 photoproduction, because nonlinearity has been reported for both photoproducts (Kieber et al., 2014; Miller and Zepp, 1995), and to determine the ratio between photoproduced CO_2 and H_2O_2. Even when normalized to CDOM, using the average $a_g(320)$ (m^{-1}) between values measured at each time point, initial rates were faster than those measured after prolonged exposure (Table 5.1 and Figure 5.2). Similar to the results from waters collected in the Northern Gulf of Mexico, nonlinearity was most striking for rates in the darkest sample (Dean Creek, Figure 5.3A&B), perhaps due to having the largest and most accurately determined production numbers. Again, even when corrected for an average % CDOM fading, both H_2O_2 and CO_2 photoproduction were nonlinear in both the darkest and clearest samples. Previous studies have reported nonlinearity in H_2O_2 photoproduction for much shorter (<2 h) irradiation times (Andrews et al., 2000; Kieber et al., 2014) but longer irradiations were required here in order to accurately measure photoproduced CO_2. Therefore it is possible that the initial rates observed here for 6 – 12 hours of irradiation are underestimates of the true initial rate even though some of the clear samples (e.g. Station C14) appear to maintain linearity up to 24 hours of irradiation (Figure 5.2). In our experiments, it appears that linearity for photoproduction of both CO_2 and H_2O_2 can be estimated for ~12 hours of irradiation by correcting for the loss of CDOM with a measured average %fading value. However, beyond this point, fading corrections fall short of explaining the loss of production.

At each time point, two cells were removed from the beakers for duplicate time point measurements. Although cells were intended to be vertical during experiments, some cells certainly received quite different photon doses if they became tilted in the

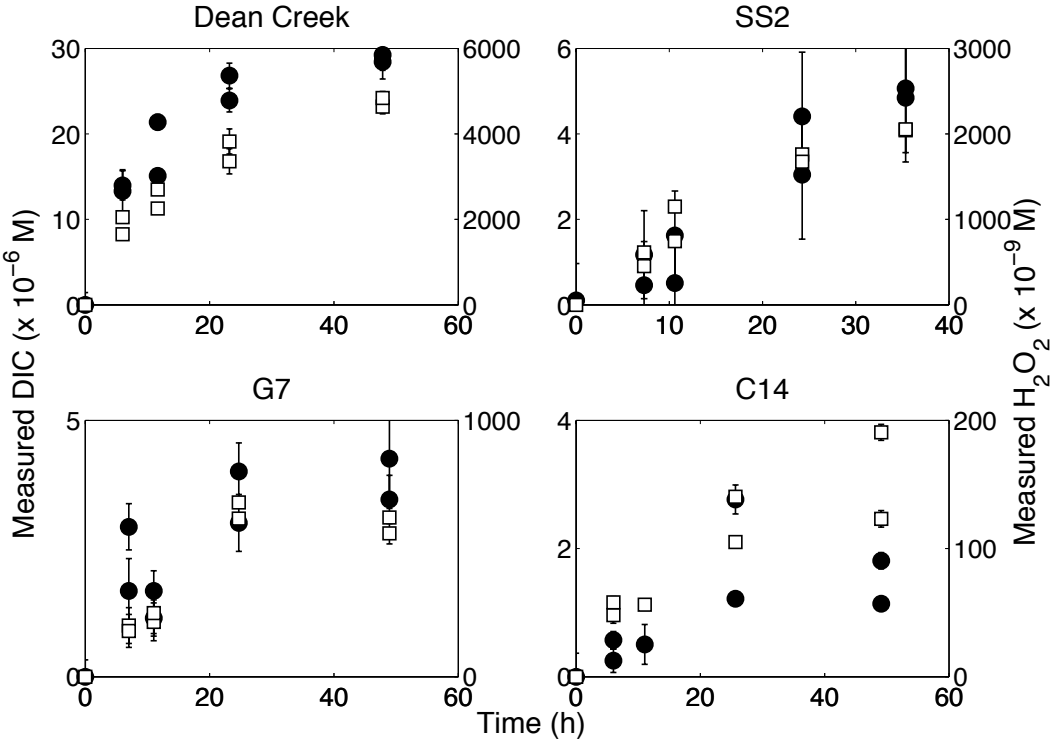

Figure 5.2. Measured photoproduced CO_2 as DIC (μM) (left axes) and H_2O_2 (nM) (right axes) in marine waters from the Georgia coast, representing dark inshore water (Dean Creek), coastal water (SS2 and G7), and offshore water (C14).

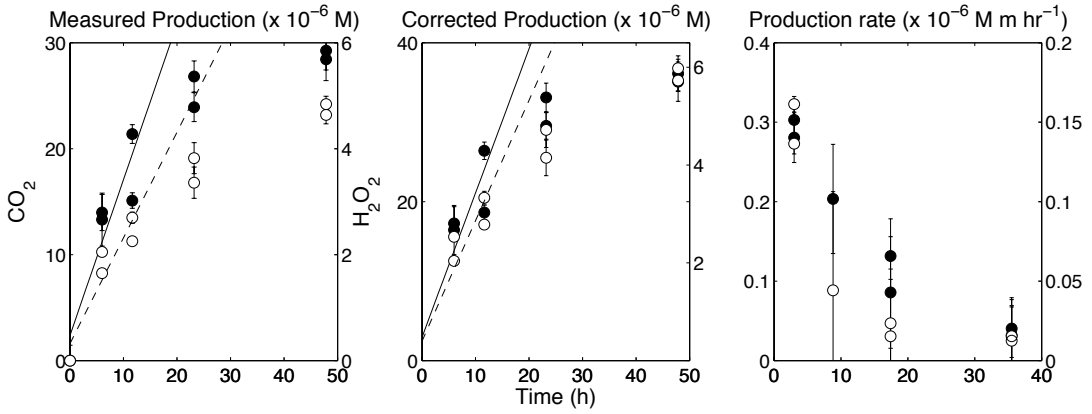

Figure 5.3. Photoproduced CO_2 (black circles, left axes) and H_2O_2 (white circles, right axes) during 48-hour irradiations of the Dean Creek sample (left) and that corrected for average %CDOM loss between 290 – 400 nm (middle). Solid and dashed lines represent initial photoproduction rates, determined over the first 12 hours of irradiation, for CO_2 and H_2O_2 respectively. Photoproduction rates (μM m hr^{-1}) for both products were determined between each time point and normalized with the average $a_g(320)$ between each time point (right).

beaker. This is well illustrated by the observed large differences in CO_2 and H_2O_2 at certain time points (Figure 5.2). However, regardless of light field differences, for all experiments the ratio between photoproduced CO_2:H_2O_2 remained nearly constant for each duplicate measurement and throughout the course of the irradiation (Table 5.1). For all experiments and all time points, CO_2:H_2O_2 averaged 6.89 ± 1.64 (range 3.93 – 9.37), and was far better constrained than any ratios reported for photoproduced CO_2:CO (Miller and Zepp, 1995; Powers and Miller, 2014a; Reader and Miller, 2012; White et al., 2010). Although ratios determined here are from a limited number of samples, the similarity between photoproduced CO_2:H_2O_2 for the darkest sample (Dean Creek: average ~7.0) and the clearest samples (C14/C15: average ~8.9) suggests that this ratio may be useful for a variety of marine waters. While more studies are needed to determine whether this ratio remains robust, it does provide promise for estimating offshore CO_2 photoproduction rates, which are currently not directly measured, ill-defined, and currently inaccessible for clear waters. This is not the case for H_2O_2, which can be measured directly with chemiluminescent methods at sub-nanomolar concentrations (King et al., 2007).

3.2 Multispectral Irradiations

Apparent quantum yield spectra were determined for both H_2O_2 and CO_2 for the Dean Creek sample (Figure 5.4A), using the polychromatic irradiation system described previously (Ziolkowski and Miller, 2007). As expected, the CO_2 AQY spectrum had the highest magnitude at all wavelengths. Production ratios for CO_2:H_2O_2 in this system under the UVB cutoff filters ranged from 3.5 – 5.3, in the range of ratios determined in broadband experiments, but somewhat lower than those determined for this particular

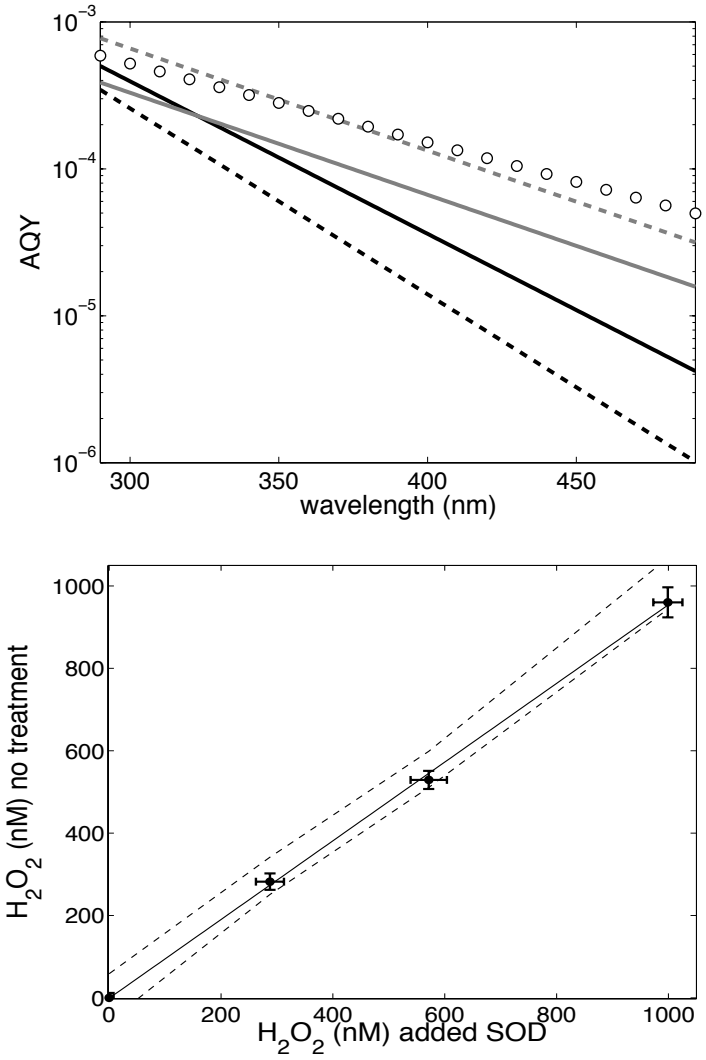

Figure 5.4. All apparent quantum yield spectra (AQY) (top) determined for the Dean Creek sample in this study (Equation 1). Solid and dashed black lines are the H_2O_2 AQY spectra for unamended and pretreated (acidified and rebuffered) samples, respectively. The solid gray line is the H_2O_2 AQY spectrum determined with added SOD, maximizing O_2^- decay to H_2O_2. The dashed gray line is an estimated O_2^- AQY, calculated by doubling the SOD H_2O_2 AQY, the stoichiometry required by O_2^- dismutation. The circles are the CO_2 AQY spectrum determined for the pretreated sample. H_2O_2 photoproduction measured in samples irradiated side by side in 600 mL jacketed beakers, with and without 200 kU L^{-1} SOD (bottom). Solid and dashed lines are the fit and 95% confidence interval between H_2O_2 produced with and without added SOD (slope = 0.955 ± 0.018, r^2 >0.99).

sample (6.1 – 7.5). Although we did our best to rebuffer the sample to its original pH after acidification and sparging, pH values were close but never exactly the same (±0.05 – 0.1 pH units), which may have caused this difference. More work is needed to ascertain how this ratio may change with varying pH, temperature and other variables since H_2O_2 production is both pH and temperature dependent (e.g. Equation 5.1).

Because pretreatment with acidification, sparging with CO_2-free air, and rebuffering is currently required to remove background DIC before determination of CO_2 photoproduction rates and because all ratios discussed above were measured on pretreated samples, an AQY spectrum for H_2O_2 was also determined for Dean Creek with no treatment beyond 0.2 μm filtration. The r^2 values between measured H_2O_2 and that predicted from the AQY spectrum were >0.97 for both of these samples, indicating that the individual AQY spectrum does an excellent job of modeling observed H_2O_2 photoproduction. The AQY spectrum for H_2O_2 was lower for the pretreated sample when compared to the unamended one, varying from about 1.5 times larger for the unamended sample at 300 nm to about 2.4 times larger at 400 nm. It has been noted that this pretreatment process may alter photochemical reactions (White et al., 2008), especially with complexed metals like iron and copper, because these metals are more soluble at low pH and may be slow to re-equilibrate once the sample is rebuffered (Powers and Miller, 2014a). Higher photoproduction rates for CO_2 have been reported in the presence of free iron than when it is chelated with unreactive ligands (Bertilsson and Tranvik, 2000; Gao and Zepp, 1998). On the other hand, the standard deviations and 95% confidence intervals for AQY fitting parameters (m_1 and m_2 values, Equation 5.1) overlap for unamended and pretreated H_2O_2 AQY spectra (Table 5.2). Therefore, within error, the

Table 5.2. Summary of Dean Creek experiments to quantify AQY spectra for H_2O_2 and CO_2. AQY fitting parameters are given ± the 95% confidence interval (m_1 and m_2 values, Equation 1) along with the r^2 between measured H_2O_2 and that predicted from the AQY spectrum. Measured and modeled $[O_2^-]_{ss}$ (nM) and calculated decay constants, k_{obs} (s^{-1}) (all ± 1 standard deviation) are also listed for the repeat irradiations of the unamended sample.

Treatment	Experiment	Irradiation Time	m_1	m_2	r^2	k_{obs} ($\times 10^{-3}$ s^{-1})	$[O_2^-]_{ss}$ (nM) Measured	Modeled
Unamended	H_2O_2 AQY	3 h	7.60 ± 0.45	0.024 ± 0.009	0.97			
	$[O_2^-]_{ss}$	3 min				13.9 ± 2.4	34.7 ± 5.4	44.3 ± 7.8
	$[O_2^-]_{ss}$	2 min				13.0 ± 1.8	33.1 ± 5.1	42.4 ± 7.1
Pretreated	H_2O_2 AQY	5.5 h	7.97 ± 0.29	0.029 ± 0.007	0.99			
	CO_2 AQY	5.5 h	7.44 ± 0.82	0.012 ± 0.012	0.92			
Added SOD	H_2O_2 AQY	3 h	7.86 ± 0.39	0.016 ± 0.006	0.98			

H_2O_2 AQY spectra for pretreated versus unamended samples may not be significantly different. To check if pretreatment significantly affects H_2O_2 photoproduction rates, we performed additional broadband irradiations using unamended samples. For the clearest samples (e.g. C14), initial production rates were essentially the same, but in one case, the initial rate was up to 40% lower in the pretreated sample (Station C5). This difference could also reflect a differing photon dose since this was not well controlled in the submerged cells. While repeat experiments are necessary to determine if pretreatment significantly alters the H_2O_2 AQY spectrum, little change to CO AQY spectra between pretreated and unamended samples has been reported previously (Powers and Miller, 2014a).

Additionally, we performed an AQY experiment for the 0.2 μm filtered Dean Creek sample with added superoxide dismutase (SOD; 200 U L^{-1} based on the manufacturer's assay, S5395-15KU, Sigma). SOD catalyzes superoxide disproportionation with a rate constant $>10^9$ M^{-1} s^{-1} (Cudd and Fridovich, 1982), likely ensuring that generated O_2^- decays through dismutation to H_2O_2. Superoxide dismutation is described by the following equation

$$2O_2^- + 2H^+ \rightarrow H_2O_2 + O_2 \qquad (5.2)$$

and predicts one mole of H_2O_2 will be produced for every two moles of O_2^- consumed, with a defined pH dependent second order decay constant for seawater ($k_D = (5 \pm 1) \times 10^{12}[H^+]$ M^{-1} s^{-1}; Zafiriou, 1990). However, in most coastal and open ocean studies (Goldstone and Voelker, 2000; Heller and Croot, 2010a, 2010b; Wuttig et al., 2013), dismutation is not the dominant fate of O_2^- because O_2^- readily reacts with trace metals,

CDOM, and other unidentified sinks. Because O_2^- can act as an oxidant and a reductant, decay can follow either of the pathways below:

$$A_{ox} + O_2^- \rightarrow A_{red} + O_2 \quad (5.3)$$

$$A_{red} + O_2^- \xrightarrow{2H^+} A_{ox} + H_2O_2 \quad (5.4)$$

where A_{ox} are oxidants and A_{red} are reductants. The H_2O_2 AQY curve with added SOD was slightly higher but not significantly different from that determined on the unamended sample (Figure 5.4), indicating that a stoichiometry typical of dismutation is present in the Dean Creek water, even if dismutation is not the dominant sink for O_2^-. In fact, a catalytic redox cycling in CDOM between A_{ox} and A_{red} has been suggested for coastal waters (Goldstone and Voelker, 2000) and solutions containing commercially available Suwannee River Fulvic Acid (SRFA; Garg et al., 2011), which would predict the same stoichiometry as dismutation. Because O_2^- photoproduction should be twice that of H_2O_2, especially in the presence of added SOD, and the fact that O_2^- AQY spectra have not been reported for natural waters, we also included a plot of the SOD H_2O_2 AQY spectrum multiplied by two to simulate an O_2^- AQY spectrum. Because the SOD AQY spectrum and the CO_2 AQY spectrum have similar slopes (m_2 values; Table 5.2), this simulated O_2^- AQY spectrum is almost an exact match to the CO_2 AQY spectrum. While further study is needed to check the reproducibility in this result, it does pose a very interesting idea that perhaps direct quantification of O_2^- photoproduction rates are the best proxies for CO_2 photoproduction rates in natural waters.

3.3 H_2O_2 and O_2^- as proxies for CO_2 photoproduction

Although H_2O_2 AQY spectra are reported here and elsewhere, H_2O_2 is a thermal product of O_2^- decay. In fact, the temperature dependence for H_2O_2 AQY spectra has

been reported, predicting an increase in H_2O_2 production efficiency by a factor of 1.8 per every 10 °C increase in temperature (Kieber et al., 2014). Because a similar temperature dependence has not been reported for CO_2, nor has it been expected based on the temperature insensitivity reported for CO (Zhang et al., 2006), the CO_2:H_2O_2 ratios reported here may change if determined from experiments at temperatures other than 15 °C. While more work is needed to ascertain whether the temperature effect changes CO_2:H_2O_2 ratios significantly, perhaps a more direct route to estimating CO_2 photoproduction rates is by directly measuring O_2^- photoproduction rates, as suggested by the similarity in the simulated O_2^- AQY spectrum and that for CO_2 (Figure 5.4A). Unfortunately, measurements of O_2^- photoproduction rates that adequately reflect the photochemical source are rare in natural waters owing to the difficulty in measuring this transient species in the field.

In this regard, we exposed the Dean Creek sample with broadband irradiation for up to two hours in clean quartz-covered 600 mL jacketed beakers to monitor H_2O_2 concentrations in the sample with and without added SOD. With added SOD, H_2O_2 photoproduction rates were slightly higher, generating a slope of 0.955 when H_2O_2 measured with and without SOD are plotted against one another, providing an estimate of 0.47 moles H_2O_2 produced per every mole O_2^- generated (Figure 5.4B). These results differ slightly from those of Petasne and Zika (1987) who reported that the ratios between H_2O_2 and O_2^- photoproduction rates were from 0.29 to 0.39 in similar irradiations of SOD amended coastal seawater. In another coastal water study, Goldstone and Voelker (2000) observed the 0.5 H_2O_2:O_2^- stoichiometry typical of dismutation, albeit from additions of μM concentrations of O_2^- that are not environmentally relevant.

Therefore, to directly address the relationship between these two photoproducts, and to further examine the relationship between O_2^- and CO_2 photoproduction, we monitored O_2^- photoproduction, its steady-state concentration ($[O_2^-]_{ss}$), and decay during short (<3 minute) irradiations of the unamended Dean Creek sample (Figure 5.5). After only ~20 seconds of irradiation, $[O_2^-]_{ss}$ was reached and monitored for 2 – 3 minutes. Subsequently, the solar simulator was turned off and superoxide decay monitored for an additional 3 – 4 minutes. Superoxide decay was modeled via the following equation

$$\frac{-\mathrm{d}[O_2^-]}{\mathrm{dt}} = 2k_D[O_2^-]^2 + k_{pseudo}[O_2^-] \qquad (5.5)$$

where k_{pseudo} (s^{-1}) describes first order decay terms, represented by Equations 5.3 and 5.4. The statistical curve fitting method described previously (Powers et al., 2014) was used to solve for both k_{pseudo} and the steady state concentration at t = 0 ($[O_2^-]_0$), which accounts for the ~10 second transit time from the solar simulator to when the sample reached the flow cell in front of the detector (modeled $[O_2^-]_{ss}$ in Table 5.2 and shown Figure 5.5). $[O_2^-]_{ss}$ values measured at the flow cell were about 34 nM, while those predicted from the model fit were about 43 nM, in good agreement with $[O_2^-]_{ss}$ measured during laboratory irradiations of solutions containing SRFA (Garg et al., 2011) but higher than those measured from similar irradiations of open ocean seawater (1 – 4 nM; Powers et al., 2014) and well above those measured in open ocean water exposed to natural sunlight (~150 pM; Shaked et al., 2010). Unfortunately, comparative measurements of O_2^- steady states in coastal water are surprisingly scarce. Pseudo first order decay constants averaged 13.5×10^{-3} s^{-1} for repeat irradiations, similar to those found post irradiation of SRFA solutions (6.6×10^{-3} s^{-1}; Garg et al., 2011) and within the larger range found from

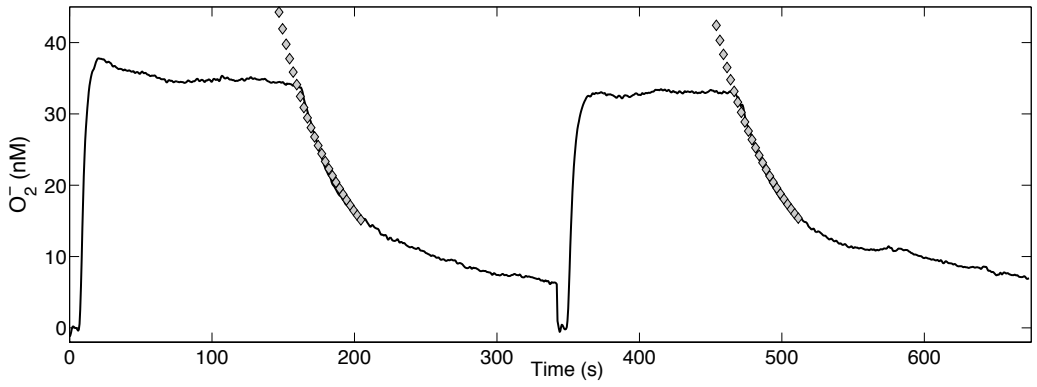

Figure 5.5. Measured O_2^- (nM) during repeat irradiations and decay experiments (black lines, calculated from continuous chemiluminecent signal). Gray diamonds are the O_2^- (nM) decay modeled using Equation 5 with k_{obs} (s^{-1}) and S_0 (counts) as fitting parameters.

exogenous additions of O_2^- to oligotrophic seawater ($2 – 74 \times 10^{-3}$ s^{-1}, Hansard et al., 2010; Heller and Croot, 2010a, 2010b; Rusak et al., 2011).

With measurements and models of $[O_2^-]_{ss}$, and decay kinetics, we can estimate the photochemical production rate of O_2^- by assuming that at steady state, O_2^- production equals its decay. Using modeled $[O_2^-]_{ss}$ to account for the 10 second delay in measurement, k_{pseduo} determined above, and k_D determined using the methods of Zafiriou (1990), we calculated O_2^- photoproduction rates on the order of 3300 nM hr^{-1} in these experiments. Using H_2O_2 photoproduction rates in the presence of SOD as a proxy for O_2^- production rates, Petasne and Zika (1987) also observed high O_2^- photoproduction rates of about 5040 nM hr^{-1} from irradiations of coastal seawater in a solar simulator. However, under natural sunlight, the O_2^- photoproduction rate for this sample was much lower (612 nM hr^{-1}; Petasne and Zika, 1987), suggesting that O_2^- photoproduction rates may be an order of magnitude lower under natural conditions. Direct O_2^- photoproduction rates measured with a ^{15}NO trap, presumably excluding O_2^- decay mechanisms, in the Eastern Caribbean from clearer waters were on the order of ~7 – 470 nM hr^{-1} sun^{-1} (Micinski et al., 1993). Because the NO probe method may underestimate photoproduction rates by 30 – 40% (Blough and Zepp, 1995) and direct measurements of superoxide photoproduction rates that correctly reflect its magnitude in marine waters are not available, further work is badly needed to quantify the AQY spectra for O_2^- for use in estimates of its photochemical flux in natural waters.

For the first 6 hours of irradiation, the in-cell CO_2 photoproduction rate for the Dean Creek sample in our broadband system, corrected for its average %CDOM fading, was 2800 nM hr^{-1}, only about 15% lower than the O_2^- photoproduction rate discussed

above, perhaps indicative of the potential use of photoproduced O_2^- as a proxy for photoproduced CO_2. Interestingly, the corrected in-cell H_2O_2 photoproduction rate measured over the same 6 hour interval was only 380 nM hr^{-1}, as shown by the CO_2:H_2O_2 ratio for this sample (Table 5.1). However, the 2:1 stoichiometry between O_2^- and H_2O_2 suggested by irradiations for H_2O_2 with and without added SOD, would predict a H_2O_2 photoproduction rate of 1650 nM hr^{-1}. Because the AQY experiments suggest that the photochemical efficiency for H_2O_2 production might be lower for pretreated samples, the discrepancy here may be in part due to the fact that the in-cell irradiation was for the sample pretreated to remove DIC, while that for the sample filled in jacketed beakers was left unamended. Additionally, the vertical cells may have received a lower photon dose. An alternative explanation for this observation could be due to nonlinearity in H_2O_2 photoproduction given that a lack of reciprocity is reported for H_2O_2 under irradiation times as short as 20 minutes (Kieber et al., 2014). In fact, the H_2O_2 photoproduction rate measured for 1.5 hours of irradiation in the jacketed beaker was 625 nM hr^{-1} without SOD and 665 nM hr^{-1} with SOD, almost twice that measured after 6 hours in the same experiment. Multiplying the SOD H_2O_2 rate by 2, as has been done previously to predict O_2^- photoproduction rates (Petasne and Zika, 1987), still underestimates the O_2^- photoproduction rate calculated here by about 60%. Because irradiations required to retrieve superoxide kinetics are very short (<3 minutes), the photoproduction rate calculated for O_2^- is most likely the best estimate of an initial rate for any species measured in this study. Therefore, the similarity between the AQY spectrum for CO_2 and twice that for H_2O_2 in the presence of SOD may suggest that the photochemical efficiency between O_2^- and CO_2 is similar, arguing that all AQY spectra reported

currently for long irradiations with high photon doses may not be indicative of initial rates. While more work is needed to understand the admittedly complex relationships between O_2^-, H_2O_2, and CO_2 photochemistry in natural waters, if initial rates are a requirement of AQY calculations, perhaps H_2O_2 and CO_2 AQY spectra reported here and previously (e.g. Johannessen and Miller, 2001; Kieber et al., 2014; O'Sullivan et al., 2005; Reader and Miller, 2012) are underestimates of the true photochemical efficiency for these products. If this is the case, photochemical oxidation of DOC to CO_2 could play a larger role in marine carbon cycling than is currently reported. Similarly, estimates of O_2^- photoproduction made from H_2O_2 measurements will underestimate its role in the redox chemistry of the surface ocean.

4. Conclusions

This study provides the first simultaneous measurements of photoproduction rates for H_2O_2 and CO_2 in a variety of marine samples. Rates for both photoproducts were always faster over the first 6 to 12 hours of irradiation when compared to those measured after prolonged exposure up to 24 and 48 hours, even when corrected for loss of photon absorbing material (i.e. CDOM photobleaching). These results stress that any production rates or AQY spectra reported for either CO_2 or H_2O_2 using measurements made at the end of long irradiations should be interpreted with caution, as the efficiency for both products decreases over time. The question remains as to whether long term or short term rates are more appropriate for regional and global scale estimates of the impact of photochemistry on carbon cycling, especially in terms of the loss of dissolved organic carbon (DOC) and its eventual oxidation to CO_2. Previous estimates of DOC oceanic half-life from short term irradiations include the questionable assumption that the entire

DOC pool is photochemically reactive (Mopper et al., 1991) and use first order kinetics to model the loss of DOC via photochemistry (Mopper et al., 1991; Miller and Zepp, 1995). Long term studies that follow the degradation of riverine and concentrated marine DOC have shown that almost all CDOM is removed while only ~40% of DOC is lost via photodegradation (Helms et al., 2013; Spencer et al., 2009), arguing that the entire DOC pool, in fact, is not available for direct photo-oxidation. Other evidence suggests that either multiple pools of photoreactive DOC (having fast and slow removal rates) are present as required for modeling purposes (Andrews et al., 2000; Moran et al., 2000) or reactions proceed by second order kinetics, consistent with secondary reactions and/or the superposition of multiple first order reactions proposed for the oxidation of DOC by Beaupré and Druffel (2012).

While these studies are certainly useful in assessing the potential fate of DOC in the marine environment, especially when attempting to understand the fate of terrestrial DOC that enters the ocean, whenever samples are simply collected and exposed to natural or simulated solar radiation in short exposures, the measurement is normally deemed an "initial" photoproduction rate. This is true even though surface samples have certainly experienced exposure to sunlight prior to collection. These "initial" rates do, however, reflect the photochemical production for any given water mass at time of collection. Additionally, except in specific cases such as fresh water lenses in areas of high river discharge, mixing in the marine mixed layer (days) is usually faster than photochemical fading of CDOM (weeks to months). As much as fading can be viewed as a proxy for the oxidation of photo-labile DOC, exposure of the mixed layer to sunlight will produce photochemical products at "initial" rates controlled by the photon absorption and reaction

efficiency. Consequently, it can be argued that AQY spectra based on initial rates should always be used for modeling photochemical reactions in marine waters.

In the variety of waters sampled here, the ratios for photoproduced CO_2:H_2O_2 fall within a narrow range, indicating that the use of H_2O_2 photoproduction rates as a proxy for CO_2 production in sunlit surface waters is far better constrained than using CO associated photoproduction rates (Powers and Miller, 2014a). This is especially useful for estimating CO_2 photochemical fluxes in coastal and offshore waters, where CO_2 AQY spectra remain scarce and are not well defined. Because H_2O_2 is a thermal product of O_2^- decay and thus sensitive to temperature and other intermediate reactions, perhaps the best proxy for CO_2 photochemistry is provided by O_2^-. Sensitive chemiluminescent methods are available to monitor O_2^- fluxes in both the field and controlled laboratory experiments (e.g. Rose et al., 2008), allowing instantaneous photoproduction rates for superoxide determined in less than ten minutes of irradiation. Constant rates are an assumption of almost all photochemical efficiency calculations (Miller, 1998) and a lack of reciprocity exists for both H_2O_2 and CO_2 photoproduction, even with short exposure times (Kieber et al., 2014). While further work is needed to investigate the relationships between the photochemical production of O_2^-, H_2O_2 and CO_2 in natural waters, perhaps calculation of initial O_2^- photoproduction rates from measured O_2^- steady state and dark decay data best represents the maximum potential for photochemical CDOM oxidation and DOC loss via CO_2 formation in the marine environment.

Acknowledgment

The authors would like to thank Bradley Tolar and Lydia Babcock-Adams for sample collection aboard the R/V *Savannah*.

References

Andrews, S.S., Caron, S., Zafiriou, O.C., 2000. Photochemical oxygen consumption in marine waters: A major sink for colored dissolved organic matter? Limnol. Oceanogr. 45, 267–277. doi:10.4319/lo.2000.45.2.0267

Beaupré, S.R., Druffel, E.R.M., 2012. Photochemical reactivity of ancient marine dissolved organic carbon. Geophys. Res. Lett. 39. doi:10.1029/2012GL052974

Bélanger, S., Xie, H., Krotkov, N., Larouche, P., Vincent, W.F., Babin, M., 2006. Photomineralization of terrigenous dissolved organic matter in Arctic coastal waters from 1979 to 2003: Interannual variability and implications of climate change. Global Biogeochem. Cycles 20. doi:10.1029/2006GB002708

Bertilsson, S., Tranvik, L.J., 2000. Photochemical transformation of dissolved organic matter in lakes. Limnol. Oceanogr. 45, 753–762. doi:10.4319/lo.2000.45.4.0753

Blough, N.V., Zepp, R.G., 1995. Reactive oxygen species in natural waters. In: Active oxygen in chemistry. Springer, Netherlands, 280–333.

Cooper, W.J., Zika, R., Petasne, R.G., Plane, J.M.C., 1988. Photochemical Formation of H_2O_2 in Natural Waters Exposed to Sunlight. Environ. Sci. Technol. 22, 1156–1160.

Cudd, A., Fridovich, I., 1982. Electrostatic interactions in the reaction mechanism of bovine erythrocyte superoxide dismutase. J. Biol. Chem. 257, 11443–11447.

Fichot, C.G., Benner, R., 2014. The fate of terrigenous dissolved organic carbon in a river-influenced ocean margin. Global Biogeochem. Cycles. 28, 300–318. doi:10.1002/2013GB004670.Received

Gao, H., Zepp, R.G., 1998. Factors Influencing Photoreactions of Dissolved Organic Matter in a Coastal River of the Southeastern United States. Environ. Sci. Technol. 32, 2940–2946. doi:10.1021/es9803660

Garg, S., Rose, A.L., Waite, T.D., 2011. Photochemical production of superoxide and hydrogen peroxide from natural organic matter. Geochim. Cosmochim. Acta. 75, 4310–4320. doi:10.1016/j.gca.2011.05.014

Goldstone, J., Voelker, B., 2000. Chemistry of superoxide radical in seawater: CDOM associated sink of superoxide in coastal waters. Environ. Sci. Technol. 34, 1043–1048.

Hansard, P.S., Vermilyea, A.W., Voelker, B.M., 2010. Measurements of superoxide radical concentration and decay kinetics in the Gulf of Alaska. Deep Sea Res. Part I Oceanogr. Res. Pap. 57, 1111–1119. doi:10.1016/j.dsr.2010.05.007

Heller, M.I., Croot, P.L., 2010a. Superoxide decay kinetics in the southern ocean. Environ. Sci. Technol. 44, 191–196. doi:10.1021/es901766r

Heller, M.I., Croot, P.L., 2010b. Kinetics of superoxide reactions with dissolved organic matter in tropical Atlantic surface waters near Cape Verde (TENATSO). J. Geophys. Res. 115, C12038. doi:10.1029/2009JC006021

Helms, J.R., Stubbins, A., Perdue, E.M., Green, N.W., Chen, H., Mopper, K., 2013. Photochemical bleaching of oceanic dissolved organic matter and its effect on absorption spectral slope and fluorescence. Mar. Chem. 155, 81–91. doi:10.1016/j.marchem.2013.05.015

Hu, C., Muller-karger, F.E., Zepp, R.G., 2002. Absorbance, absorption coefficient, and apparent quantum yield: A comment on common ambiguity in the use of these optical concepts. Limnol. Oceanogr. 47, 1261–1267.

Johannessen, S.C., 2000. A photochemical sink for dissolved organic carbon in the ocean, in Department of Oceanography, Dalhousie University, Halifax.

Johannessen, S.C., Miller, W.L., 2001. Quantum yield for the photochemical production of dissolved inorganic carbon in seawater. Mar. Chem. 76, 271–283. doi:10.1016/S0304-4203(01)00067-6

Kieber, D.J., Miller, G.W., Neale, P.J., Mopper, K., 2014. Wavelength and temperature-dependent apparent quantum yields for photochemical formation of hydrogen peroxide in seawater. Environ. Sci. Process. Impacts. 16, 777–791. doi:10.1039/c4em00036f

King, D.W., Cooper, W.J., Rusak, S.A., Peake, B.M., Kiddle, J.J., O'Sullivan, D.W., Melamed, M.L., Morgan, C.R., Theberge, S.M., 2007. Flow injection analysis of H2O2 in natural waters using acridinium ester chemiluminescence: method development and optimization using a kinetic model. Anal. Chem. 79, 4169–4176. doi:10.1021/ac062228w

Koehler, B., Landelius, T., Weyhenmeyer, G.A., Machida, N., Tranvik, L.J., 2014. Sunlight-induced carbon dioxide emissions from inland waters. Global Biogeochem. Cycles. 28, 696–711. doi:10.1002/2014GB004850.Received

Micinski, E., Ball, L., Zafiriou, O., 1993. Photochemical Oxygen Activation : Superoxide Radical Detection and Production Rates in the Eastern Caribbean. J. Geophys. Res. 98, 2299–2306.

Miller, W.L., 1998. Effects of UV radiation on aquatic humus: photochemical principles and experimental considerations. In: Aquatic Humic Substances. Springer, Berlin, Heidelberg, pp. 125–143.

Miller, W.L., Moran, M.A., 1997. Interaction of photochemical and microbial processes in the degradation of refractory dissolved organic matter from a coastal marine environment. Limnol. Oceanogr. 42, 1317–1324. doi:10.4319/lo.1997.42.6.1317

Miller, W.L., Zepp, R.G., 1995. Photochemical production of dissolved inorganic carbon from terrestrial organic matter: Significance to the oceanic organic carbon cycle. Geophys. Res. Lett. 22, 417–420. doi:10.1029/94GL03344

Moore, C., Farmer, C., Zika, R., 1993. Influence of the Orinoco River on Hydrogen Peroxide Distribution and Production in the Eastern Caribbean. J. Geophys. Res. 98, 2289–2298.

Mopper, K., Zhou, X., Kieber, R.J., Kieber, D.J., Sikorski, R.J., Jones, R.D., 1991. Photochemical degradation of dissolved organic carbon and its impact on the oceanic carbon cycle. Nature. 353, 60–62. doi:10.1038/353060a0

Mopper, K., Kieber, D.J., 2000. Marine photochemistry and its impact on carbon cycling. In: The Effects of UV Radiation in the Marine Environment. 10, 101–129.

Mopper, K., Kieber, D.J., 2002. Photochemistry and the Cycling of Carbon, Sulfur, Nitrogen and Phosphorus. In: Hansell, D.A., Carlson, C.A. (Eds.), Biogeochemistry of Marine Dissolved Organic Matter. Academic, San Diego. pp. 455–507.

Moran, M.A., Sheldon, W.M., Zepp, R.G., 2000. Carbon loss and optical property changes during long-term photochemical and biological degradation of estuarine dissolved organic matter 45, 1254–1264.

O'Sullivan, D.W., Neale, P.J., Coffin, R.B., Boyd, T.J., Osburn, C.L., 2005. Photochemical production of hydrogen peroxide and methylhydroperoxide in coastal waters. Mar. Chem. 97, 14–33. doi:10.1016/j.marchem.2005.04.003

Petasne, R.G., Zika, R.G., 1987. Fate of superoxide in coastal seawater. Nature. 325, 516–618.

Pos, W.H., Riemer, D.D., Zika, R.G., 1998. Carbonyl sulfide (OCS) and carbon monoxide (CO) in natural waters: evidence of a coupled production pathway. Mar. Chem. 62, 89–101.

Powers, L.C., Babcock-Adams, L.C., Enright, J.K., Miller, W.L., 2014. Phobing the photochemical reactivity of deep ocean refractory carbon (DORC): lessons from hydrogen peroxide and superoxide kinetics. *Submitted* to Mar. Chem.

Powers, L.C., Miller, W.L., 2014a. Photochemical production of CO and CO_2 in the northern Gulf of Mexico: estimates and challenges for quantifying the impact of photochemistry on carbon cycles. *Submitted* to Mar. Chem.

Powers, L.C., Miller, W.L., 2014b. Blending remote sensing data products to estimate photochemical production of hydrogen peroxide and superoxide in the surface ocean. Environ. Sci. Process. Impacts 16, 792–806. doi:10.1039/c3em00617d

Reader, H.E., Miller, W.L., 2011. Effect of estimations of ultraviolet absorption spectra of chromophoric dissolved organic matter on the uncertainty of photochemical production calculations. J. Geophys. Res. 116, C08002. doi:10.1029/2010JC006823

Reader, H.E., Miller, W.L., 2012. Variability of carbon monoxide and carbon dioxide apparent quantum yield spectra in three coastal estuaries of the South Atlantic Bight. Biogeosciences. 9, 4279–4294. doi:10.5194/bg-9-4279-2012

Reader, H.E., Miller, W.L., 2014. The efficiency and spectral photon dose dependence of photochemically induced changes to the bioavailability of dissolved organic carbon. Limnol. Oceanogr. 59, 182–194. doi:10.4319/lo.2014.59.1.0182

Rose, A.L., Moffett, J.W., Waite, T.D., 2008. Determination of Superoxide in Seawater Using 2-Methyl-6-(4-methoxyphenyl)-3,7-dihydroimidazo[1,2-a]pyrazin-3(7H)-one chemiluminescence. Anal. Chem. 80, 1215–1227.

Rusak, S.A., Peake, B.M., Richard, L.E., Nodder, S.D., Cooper, W.J., 2011. Distributions of hydrogen peroxide and superoxide in seawater east of New Zealand. Mar. Chem. 127, 155–169. doi:10.1016/j.marchem.2011.08.005

Shaked, Y., Harris, R., Klein-Kedem, N., 2010. Hydrogen peroxide photocycling in the Gulf of Aqaba, Red Sea. Environ. Sci. Technol. 44, 3238–3244.

Sharpless, C.M., Blough, N.V., 2014. The importance of charge-transfer interactions in determining chromophoric dissolved organic matter (CDOM) optical and photochemical properties. Environ. Sci. Process. Impacts. 16, 654–671. doi:10.1039/c3em00573a

Spencer, R.G.M., Stubbins, A., Hernes, P.J., Baker, A., Mopper, K., Aufdenkampe, A.K., Dyda, R.Y., Mwamba, V.L., Mangangu, A.M., Wabakanghanzi, J.N., Six, J., 2009. Photochemical degradation of dissolved organic matter and dissolved lignin phenols from the Congo River. J. Geophys. Res. 114, G03010. doi:10.1029/2009JG000968

Valentine, R.L., Zepp, R., 1993. Formation of Carbon Monoxide from the Photodegradation of Terrestrial Dissolved Organic Carbon in Natural Waters. Environ. Sci. Technol. 27, 409–412.

Wang, Z.A., Cai, W.-J., Wang, Y., Ji, H., 2005. The southeastern continental shelf of the United States as an atmospheric CO_2 source and an exporter of inorganic carbon to the ocean. Cont. Shelf Res. 25, 1917–1941. doi:10.1016/j.csr.2005.04.004

White, E.M., Kieber, D.J., Mopper, K., 2008. Determination of photochemically produced carbon dioxide in seawater. Limnol. Oceanogr. Methods. 6, 441–453. doi:10.4319/lom.2008.6.441

White, E.M., Kieber, D.J., Sherrard, J., Miller, W.L., Mopper, K., 2010. Carbon dioxide and carbon monoxide photoproduction quantum yields in the Delaware Estuary. Mar. Chem. 118, 11–21. doi:10.1016/j.marchem.2009.10.001

Wuttig, K., Heller, M.I., Croot, P.L., 2013. Pathways of superoxide (O_2^-) decay in the Eastern Tropical North Atlantic. Environ. Sci. Technol. 47, 10249–10256. doi:10.1021/es401658t

Xie, H., Andrews, S.S., Martin, W.R., Miller, J., Ziolkowski, L., Taylor, C.D., Zafiriou, O.C., 2002. Validated methods for sampling and headspace analysis of carbon monoxide in seawater. Mar. Chem. 77, 93–108. doi:10.1016/S0304-4203(01)00065-2

Zafiriou, O.C., 1990. Chemistry of superoxide ion-radical (O_2^-) in seawater. I . pK^*a_{sw} (HOO) and uncatalyzed dismutation kinetics studied by pulse radiolysis. Mar. Chem. 30, 31–43.

Zhang, Y., Xie, H., Chen, G., 2006. Factors affecting the efficiency of carbon monoxide photoproduction in the St. Lawrence estuarine system (Canada). Environ. Sci. Technol. 40, 7771–7777. doi:10.1021/es0615268

Ziolkowski, L.A., Miller, W.L., 2007. Variability of the apparent quantum efficiency of CO photoproduction in the Gulf of Maine and Northwest Atlantic. Mar. Chem. 105, 258–270. doi:10.1016/j.marchem.2007.02.004

CHAPTER 6

CONCLUSIONS AND FUTURE DIRECTIONS

The work in this dissertation utilizes photochemical models based on a photochemical efficiency approach and algorithms that derive *in situ* UV optical properties from remote sensing products. While this approach allows for expanded spatial and temporal coverage when evaluating the role of photochemical reactions from coastal zones to the global ocean, the accuracy with which photoproduction estimates can be made from optical data is primarily constrained by limited availability of AQY spectral data and the ability to match observed variations in the surface ocean with their proper AQY spectra. To that end, photochemical rate estimates like those made here rely heavily on the understanding and selection of the appropriate AQY spectrum for the reaction being studied. These remain largely elusive for many photochemical processes, and especially for the photoproduction of CO_2. Full confidence in these models to accurately calculate distributions of any photochemical product can only be possible once improved knowledge of the mechanisms regulating the system of interest are available.

In order to improve AQY estimates, we need more information for both the numerator and the denominator of the AQY equation (1.3). Until molecular level information becomes available that identify the specific absorbing compounds responsible for specific photoproducts, we remain limited by using overall solution absorption coefficients to determine the rate of photon absorption, the denominator, for

all products. Improving the numerator of the AQY equation is not trivial either. Chapter 2 provides good evidence that for the complex river dominated marine system in the northern Gulf of Mexico, and likely for others, at least two groups of CO AQY spectra are needed for comprehensive models that include both inshore and offshore waters. During the examination of such an extensive spatio-temporal data set for CO photoefficiency in the Northern Gulf of Mexico required for AQY determination, this study also revealed that reported correlations between CO photoproduction rates or efficiency and CDOM absorption coefficients or $SUVA_{254}$ are not universally applicable. In fact, these empirical relationships based on limited data should not be used for large-scale regional or global estimates of marine CO photoproduction rates. Even though CO is the most extensively studied photoproduct in marine systems, more mechanistic data on the reactions responsible for the large range in observed AQY spectra (Figure 2.2) is needed to overcome the fact that the selection of a few or a single CO AQY spectrum for modeling purposes is still quite subjective and insufficient to fully describe the system.

Throughout this dissertation, however, the two photoproducts that remain the most difficult to describe quantitatively are CO_2 (Chapter 2) and O_2^- (Chapters 3 and 4). Even with new CO_2 photochemical efficiency data for the Northern Gulf of Mexico, estimates for its photoproduction in both coastal and blue water areas remain poorly defined for this region because of the lack of accessible methods to determine direct CO_2 AQY spectral measurements in oligotrophic waters. This is particularly problematic since the photoproduction of CO_2 from DOC is the largest identifiable carbon product and its quantification is critical for full evaluation of photochemistry's role in oceanic carbon cycles. Assuming that coastal CO_2 AQY spectra can be applied to offshore waters

or the use of a poorly constrained CO_2:CO ratio to infer CO_2 photoefficiencies from that for CO does not provide a dependable estimate for the role of CO_2 photoproduction in coastal carbon cycling. New direct methods for measuring photoproduced CO_2 that do not require pretreatment are desperately needed to overcome these difficulties. Pool isotope exchange has been used as an alternative method for detecting photoproduced CO_2 (Wang et al., 2009), however it is quite involved, requiring the replacement of natural $DI^{12}C$ in seawater with $DI^{13}C$ at natural pH prior to irradiation. Photochemical CO_2 production is then measured as the difference in $^{12}CO_2/^{13}CO_2$ ratios before and after irradiation. While this method removes the need for sample acidification and rebuffering, it does alter the natural seawater matrix and makes assumptions about the fractionation of photoproduced CO_2. There remains a need to develop methodology that is sensitive enough to detect nM concentrations of photoproduced CO_2 above the background concentration of DIC.

One such possibility is the use of novel chemiluminescent techniques, which are inherently sensitive. There is evidence that not only does CO_2 affect 5-amino-2,3-dihydro-1,4-phthalazinedion (luminol) chemiluminescence (Lan and Mottola, 1996a; Xiao et al., 2002), it is also pivotal in ensuring that the chemiluminescence reaction takes place. Generally chemiluminescent techniques are rapid, relatively inexpensive, and provide extremely low detection limits. In the case of luminol-based chemiluminescence techniques, the species of interest promotes the oxidation of luminol to 3-aminophthalate so by modifying the analytical matrix, different species become more or less reactive with luminol, allowing for the determination of a wide range of trace chemicals (Xiao et al., 2002).

There is only a basic mechanistic understanding of luminol chemiluminescence so systems based on these reactions are highly empirical because the sensitivity in these systems depends on a number of factors, and reactions need to be optimized for pH, concentrations of reagents, flow rates, and potential interferences (Xiao et al., 2002). Xiao et al. (2002) were the first to attribute many of changes in luminol chemiluminescence to dissolved CO_2 either present in the sample or formed in the analytical system. The involvement of CO_2 in chemiluminescent reactions has been well documented. Bersis and Nikokavouras (1968) were the first to observe the ability of CO_2 to initiate chemiluminescence. They continuously measured the intensity of light during chemiluminescence reactions with changing pH, and observed a burst of light when CO_2(g) passed through the system. Years later, Lan and Mottola (1996a) observed the enhancement of luminol chemiluminescence with the addition of dissolved CO_2 to the system. They utilized the CO_2 effect in the determination of Co(II) in the 0.1 pM to 100 nM range and proposed a possible mechanism for signal enhancement via the formation of a carbonate radical. They, however, did not apply any kinetic or spectroscopic techniques to confirm this mechanism (Xiao et al. 2002). In luminol chemiluminescence systems, superoxide (O_2^-) is produced when the analyte of interest (usually a metal ion) is oxidized by oxygen. O_2^- then reacts with luminol to initiate the chemiluminescent reaction. Xiao et al. (2002) therefore proposed that a reaction between superoxide and CO_2, forming the peroxycarbonate radical, CO_4^-, initiates chemiluminescence more efficiently than O_2^- alone.

There have been two studies that have successfully employed the CO_2 effect on luminol chemiluminescence for CO_2 detection. Lan and Mottola (1996b) determined

CO_2(g) in air and human breath by the enhancement of luminol chemiluminescence. They determined CO_2 concentrations in one system over the range of 50 to 800 ppm (v/v) with a limit of detection of 1.5 ppm. Recently, Lai et al. (2012) utilized the chemiluminescence enhancement effect with a method for CO_2 detection. Their method is based on the CO_2 enhancement of the luminol-potassium permanganate ($KMnO_4$) signal. Using this system, they were able to detect dissolved CO_2 with a detection limit of 130 nM. By modifying this system for seawater, perhaps luminol chemiluminescence reactions can be used to detect photoproduced CO_2 over the course of an irradiation experiment.

While the determination of photoproduced CO_2 remains analytically challenging, especially in blue water, as highlighted in Chapters 3 and 4 of this dissertation, O_2^- AQY data simply do not exist for natural systems. While simple relationships between H_2O_2 and O_2^- photoproduction have often been assumed, the uncertainties in these assumptions, presented in Chapter 3, make estimations of O_2^- concentrations from H_2O_2 photoproduction rates considerably difficult. Although the method presented offers the first attempt to use remote sensing data together with direct knowledge of chemical reaction mechanisms to modify biogeochemical estimates related to photochemistry, these calculations rely heavily on the relationship between H_2O_2 and O_2^- photoproduction rates and the O_2^- decay kinetics in the open ocean. Presently, much about the processes that control the fate of O_2^- are not completely understood. New work is needed to directly quantify the photo-efficiency for O_2^- production and to better define the magnitude and partitioning of various sinks for superoxide. For example, O_2^-

disproportionation (Equations 1.6 and 1.7) is affected by both pH and temperature, so it is likely that pseudo-first order O_2^- decay is also impacted by these variables.

As more mechanistic and kinetic data become available, as well as data on the relationships between H_2O_2 and O_2^-, like those presented in Chapter 4, we will be able to better model the photochemical cycling of these reactive oxygen species in a variety of marine environments. While the purpose of Chapter 4 was to probe the photoreactivity of deep ocean DOC, it also contributes new understanding of the processes controlling the photoproduction and decay of superoxide in the open ocean. We calculated O_2^- photoproduction rates for surface waters in the Gulf of Alaska that are well above those estimated for biological O_2^- production in this region (Hansard et al., 2010). Because a widespread microbial source for superoxide in the ocean has received recent attention (Diaz et al., 2013), this result also stresses that the photochemical production of this ROS warrants further attention. O_2^- photoproduction is most likely a much larger source of O_2^- in sunlit waters and there is still very little information available that fully reflects its true magnitude. Because oceanic H_2O_2 distributions and photoproduction rates have been so widely studied, the photoproduction rates of O_2^- have often been inferred from H_2O_2 results. However, of all the identified ROS formed from CDOM photochemistry in natural waters (i.e. O_2^-, H_2O_2, $^{\bullet}OH$ and $^1O_2$), O_2^- is only one for which direct apparent quantum yield spectra have not been reported. Results in Chapter 4 indicate that in the open ocean a large fraction of photoproduced O_2^- does not lead to H_2O_2, meaning that the relationship between these two ROS may not simply be a factor of two. Our shipboard experiments alone indicate that for surface waters, the photoproduction rate of O_2^- ranges between 1.76 and 4.53 times greater than that for H_2O_2. Chapter 5 represents the first

attempt to address this issue, by reporting an O_2^- apparent yield spectrum determined from H_2O_2 AQY data in solutions containing the enzyme superoxide dismutase.

Chapter 5 presents an interesting study on the relationships between CO_2, H_2O_2 and O_2^- photoproduction. With the wide variety of waters sampled in Chapter 5 and the narrow range in ratios for photoproduced CO_2:H_2O_2, the use of H_2O_2 photoproduction rates as a proxy for that for CO_2 may be promising in regional and global photochemical flux estimates. While results suggest that O_2^- and CO_2 photoproduction may show the best relationship, the ratio between its dismutation product, H_2O_2 and CO_2 is far better constrained than the CO and CO_2 photoproduction relationships reported in Chapter 2. This may be especially useful for estimating CO_2 photochemical fluxes in coastal and offshore waters, where CO_2 AQY spectra remain under-reported and are not well defined. For example, Figure 6.1 shows the results of applying the CO_2:H_2O_2 ratio determined in Chapter 5 to the yearly average surface ocean H_2O_2 photoproduction rates calculated in Chapter 3. This method estimates a global averaged CO_2 photoproduction rate of 278 ± 149 nM d^{-1} over the year in the top meter, but can be as high as 642 nM d^{-1} in equatorial regions. Of course, the AQY spectrum used in this prediction is conservative (Chapter 3), meaning that this is very likely a low-end estimate. Because open ocean H_2O_2 AQY spectra determined in this study were measured after 12 hours of irradiation (Chapter 3), applying the CO_2:H_2O_2 ratio to these spectra will be hampered if a lack of reciprocity occurs earlier in the irradiation than when the AQY spectrum was determined. The AQY spectrum determined for a tidal creek in the South Atlantic Bight (Chapter 5) is about 1.8 times higher across the entire spectrum and H_2O_2 AQY spectra vary at least an order of magnitude in natural waters (Kieber et al., 2014; O'Sullivan et al., 2005), highlighting

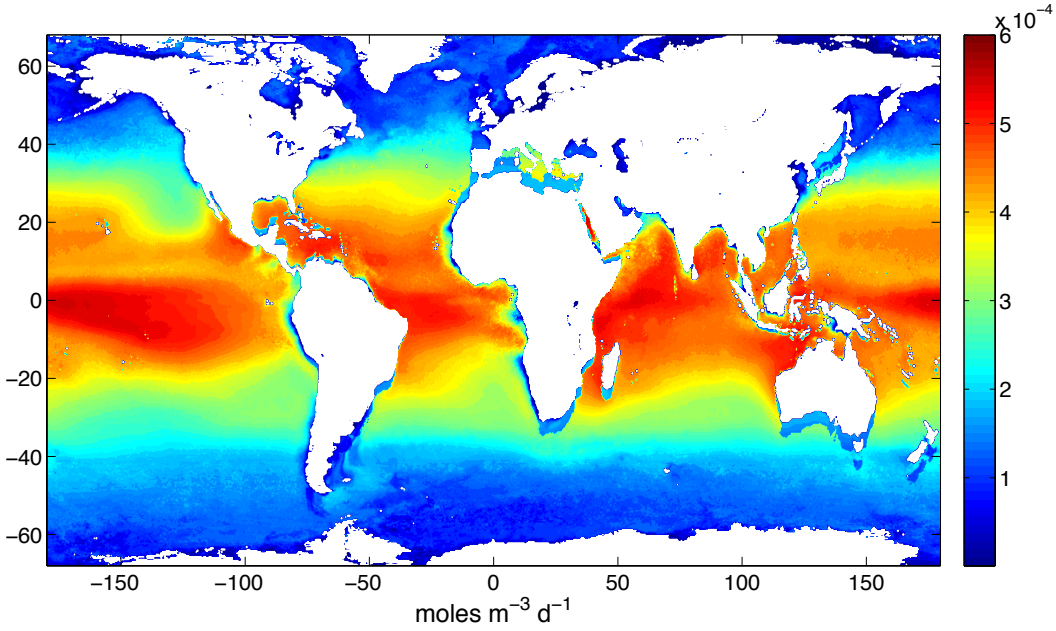

Figure 6.1. DIC photoproduction rates (moles m^{-3} d^{-1}) made by multiplying open ocean H_2O_2 photoproduction rates (moles m^{-1} d^{-1}) averaged over the year for the top meter (Chapter 3) and a CO_2:H_2O_2 ratio of 6.89 (Chapter 5).

that the AQY selection remains the most critical choice in these models. As another application of this new ratio method, we can reevaluate the results of Chapter 2 where CO_2 photoproduction estimates were inferred from those for CO. By using either the open ocean H_2O_2 AQY spectrum (Chapter 3) or the Dean Creek AQY spectrum (Chapter 5) and the new CO_2:H_2O_2 ratio, calculated CO_2 photoproduction rates average 246 or 441 Gg C yr^{-1}, respectively, well above the 85 Gg C yr^{-1} estimated in Chapter 2 for both CO_2 and CO combined. This could mean that direct photochemistry is capable of removing far more DOC, increasing from 12.5% of the 0.68 Tg C terrigenous DOC remineralized per year in the Northern Gulf of Mexico (Fichot and Benner, 2014) to potentially somewhere between 36 – 65% of that remineralization. A higher role of direct photochemistry is consistent with the findings of Miller and Moran (1997), who observed almost equal contributions of direct photochemical loss of DOC (as CO_2 and CO) and loss via microbial utilization of photoproduced labile products. In this study, only 4% of the DOC was lost due to microbial uptake in the absence of light. Of course, as more marine spectral photo-efficiency data for H_2O_2 become available, the overall value of this CO_2:H_2O_2 proxy may be fully realized.

Because sensitive chemiluminescent methods are available to monitor O_2^- fluxes in both the field and controlled laboratory experiments (Rose et al., 2008), instantaneous photoproduction rates for superoxide can be determined in less than two minutes of irradiation. Constant rates are an assumption of photochemical efficiency calculations (Miller, 1998) and a lack of reciprocity exists for both H_2O_2 and CO_2 photoproduction, even under short exposure times (Kieber et al., 2014). While further work is needed to investigate the relationships between the photochemical production of O_2^-, H_2O_2 and CO_2

in natural waters, perhaps calculation of initial O_2^- photoproduction rates from measured O_2^- steady state and dark decay data best represents the potential maximum rates for photochemical CDOM oxidation in the marine environment. Future work that teases out these relationships will likely impact our current understanding on the importance of photochemistry in the global ocean. This is especially true for the case of photoproduced CO_2, although it has been identified as the largest carbon based photoproduct for nearly 20 years, no reliable data on its magnitude in the global ocean exists.

References

Bersis, D. S., Nikokavouras, J., 1968. Discrimination of chemiluminescent mixtures: the chemiluminescencegram. Nature. 217, 451–452.

Diaz, J.M., Hansel, C.M., Voelker, B.M., Mendes, C.M., Andeer, P.F., Zhang, T., 2013. Widespread production of extracellular superoxide by heterotrophic bacteria. Science. 340, 1223–1226. doi:10.1126/science.1237331

Fichot, C.G., Benner, R., 2014. The fate of terrigenous dissolved organic carbon in a river-influenced ocean margin. Global Biogeochem. Cycles 28, 300–318. doi:10.1002/2013GB004670.Received

Hansard, P.S., Vermilyea, A.W., Voelker, B.M., 2010. Measurements of superoxide radical concentration and decay kinetics in the Gulf of Alaska. Deep Sea Res. Part I Oceanogr. Res. Pap. 57, 1111–1119. doi:10.1016/j.dsr.2010.05.007

Kieber, D.J., Miller, G.W., Neale, P.J., Mopper, K., 2014. Wavelength and temperature-dependent apparent quantum yields for photochemical formation of hydrogen peroxide in seawater. Environ. Sci. Process. Impacts. 16, 777–791. doi:10.1039/c4em00036f

Lai, C. –Y., Liang, B. –Q., Wang., X. –L., Zhu, J., Li., F., 2012. Determination of carbon dioxide by the enhancement of luminol-potassium permanganate chemiluminescence and its application for the biodegradation analysis of cellulose acetat-g-poly (*p*-dioxanone) copolymer. Anal. Lett. 45, 75–84.

Lan, Z.-H., Mottola, H.A., 1996a. Carbon Dioxide-enhance Luminol Chemiluminescence in the Absence of Added Oxidant. Analyst. 121, 211–218.

Lan, Z.-H., Mottola, H.A., 1996b. Determination of CO_2(g) by enhancement of luminol-cobalt(II) phthalocyanine chemiluminescence: Analysis of atmospheric air and human breath. Anal. Chim. Acta. 2670, 305–310.

Miller, W.L., 1998. Effects of UV radiation on aquatic humus: photochemical principles and experimental considerations. In: Aquatic Humic Substances. Springer, Berlin Heidelberg, pp. 125–143.

Miller, W.L., Moran, M.A., 1997. Interaction of photochemical and microbial processes in the degradation of refractory dissolved organic matter from a coastal marine environment. Limnol. Oceanogr. 42, 1317–1324. doi:10.4319/lo.1997.42.6.1317

Rose, A.L., Moffett, J.W., Waite, T.D., 2008. Determination of Superoxide in Seawater Using 2-Methyl-6-(4-methoxyphenyl)-3,7-dihydroimidazo[1,2-a]pyrazin-3(7H)-one chemiluminescence. Anal. Chem. 80, 1215–1227.

Wang, W., Johnson, C.G., Takeda, K., Zafiriou, O.C., 2009. Measuring the photochemical production of carbon dioxide from marine dissolved organic matter by pool isotope exchange. Environ. Sci. Technol. 43, 8604–8609. doi:10.1021/es901543e

Xiao, C., Palmer, D.A., Wesolowski, D.J., Lovitz, S.B., King, D.W., 2002. Carbon Dioxide Effects on Luminol and 1,10-Phenanthroline Chemiluminescence. Anal. Chem. 74, 2210–2216.

APPENDIX A

SUPPORTING INFORMATION FOR CHAPTER 2

Below are detailed tables and figures referenced in the Chapter 2. Details include locations and dates for all samples collected for CO photochemical experiments, fitting parameters (generally listed as *m*-values) for CO and CO_2 AQY spectra, relationships to CDOM optical properties, and various monthly estimates for CO and CO_2 photoproduction rates in our Northern Gulf of Mexico study region.

Table A1. AQY fitting parameters (m_1 and m_2, Equation 2.10), salinity (PSU), $a_g(320)$ (m^{-1}), and calculated vs. measured production r^2 for samples used in CO photochemical experiments. Stations in bold indicate repeated occupation for each of the 4 cruises (April 19 – May 1, 2009; July 18 – 30, 2009; October 28 – November 9, 2009; March 10 – 22, 2010).

Cruise	Station	Lat	Long	S	$a_g(320)$	m_1	m_2	r^2
April	**A1**	30.24	-88.04	13.9	14.44	8.82	0.026	0.94
April	A3	29.80	-88.02	30.7	1.33	8.85	0.030	0.96
April	**B1**	29.25	-89.76	24.8	4.03	10.28	0.029	0.95
April	B3	28.74	-89.76	23.4	3.42	8.88	0.030	0.86
April	B5	28.00	-89.77	36.3	0.15	10.33	0.036	0.95
April	**C0**	29.13	-90.59	28.1	4.19	9.81	0.041	0.91
April	**C2**	28.64	-90.36	28.6	2.21	7.36	0.056	0.92
April	D2	28.59	-91.02	30.1	1.98	8.28	0.040	0.96
April	D5	27.54	-91.03	37.5	0.22	9.97	0.059	0.96
April	**E0**	29.38	-91.37	0.2	13.36	7.87	0.044	0.96
April	**E1**	29.17	-91.56	26.1	3.62	8.91	0.030	0.94
April	E3	28.79	-91.69	31.3	1.61	9.06	0.030	0.97
April	**F1**	29.42	-92.43	29.0	2.61	8.51	0.038	0.93
April	F4	28.51	-92.35	36.1	0.64	9.14	0.064	0.97
April	G2	29.14	-93.00	34.2	0.90	11.31	0.032	0.96
April	**H1**	29.61	-93.81	25.1	4.64	8.85	0.032	0.95
April	**H2**	29.32	-93.67	32.6	1.34	9.20	0.030	0.93
April	H3	28.94	-93.67	35.9	0.30	9.77	0.061	0.93
April	**MR1**	29.03	-89.33	0.4	8.46	9.41	0.037	0.98
April	**MR2**	28.90	-89.43	31.0	6.88	8.43	0.031	0.95
July	**A1**	30.24	-88.04	30.3	2.93	7.53	0.066	0.93
July	A2	30.12	-88.04	34.2	1.31	9.84	0.020	0.95
July	A3	29.80	-88.03	33.6	0.88	10.26	0.054	0.95
July	**B1**	29.27	-89.76	15.1	5.50	8.97	0.044	0.86
July	B4	28.43	-89.77	28.6	1.42	11.67	0.023	0.93
July	**C0**	29.13	-90.59	20.6	3.74	9.99	0.040	0.95
July	**C2**	28.64	-90.36	32.6	0.84	9.45	0.069	0.88
July	C5	27.54	-90.36	30.9	0.79	11.19	0.029	0.97
July	D4	27.94	-91.03	32.4	0.63	11.47	0.031	0.89
July	**E0**	29.38	-91.37	0.4	10.40	9.17	0.045	0.97
July	**E1**	29.17	-91.56	9.0	9.26	8.06	0.076	0.94
July	E3	28.79	-91.69	32.4	0.86	12.41	0.011	0.92
July	**F1**	29.42	-92.43	30.8	2.13	8.81	0.038	0.94
July	F5	28.01	-92.36	36.6	0.06	9.65	0.046	0.73
July	G3	28.82	-93.01	32.8	0.63	10.33	0.054	0.81
July	**H1**	29.61	-93.81	35.6	1.09	8.66	0.041	0.87
July	**H2**	29.32	-93.67	35.7	0.45	11.25	0.024	0.45
July	**MR1**	29.03	-89.33	1.4	8.38	9.29	0.047	0.87
July	**MR2**	28.90	-89.43	17.6	5.35	8.17	0.040	0.89

July	MR3	28.70	-89.50	31.2	1.00	10.73	0.047	0.91
Oct	**A1**	30.24	-88.04	13.0	8.86	7.58	0.050	0.95
Oct	A2	30.12	-88.04	31.9	1.05	8.37	0.038	0.95
Oct	**B1**	29.27	-89.76	22.0	3.46	11.34	0.011	0.93
Oct	B2	28.96	-89.76	24.4	2.83	8.91	0.030	0.95
Oct	B3	28.74	-89.76	20.8	4.59	9.52	0.029	0.95
Oct	**C0**	29.13	-90.59	25.8	5.56	9.18	0.031	0.94
Oct	**C2**	28.64	-90.36	28.1	2.13	7.97	0.050	0.84
Oct	C4	27.93	-90.36	36.1	0.18	11.66	0.031	0.73
Oct	D2	28.59	-91.02	32.9	0.80	10.54	0.045	0.96
Oct	**E0**	29.38	-91.37	6.1	25.35	8.21	0.032	0.99
Oct	**E1**	29.17	-91.56	25.7	4.64	8.47	0.033	0.98
Oct	E2	29.03	-91.67	30.0	1.60	9.52	0.017	0.90
Oct	**F1**	29.42	-92.43	25.8	11.51	7.50	0.047	0.95
Oct	F5	28.01	-92.36	36.6	0.14	10.20	0.039	0.93
Oct	G1	29.44	-93.00	28.8	2.54	9.67	0.014	0.97
Oct	**H1**	29.61	-93.81	23.7	5.02	8.40	0.036	0.98
Oct	**H2**	29.32	-93.67	33.2	0.81	10.79	0.034	0.89
Oct	H3	28.94	-93.67	35.1	0.39	12.41	0.015	0.82
Oct	**MR1**	29.03	-89.33	0.2	12.63	8.58	0.062	0.98
Oct	**MR2**	28.90	-89.43	3.3	11.02	9.13	0.025	0.98
Oct	MR3	28.70	-89.50	27.2	2.42	8.19	0.048	0.95
March	**A1**	30.24	-88.04	23.0	3.97	7.12	0.075	0.77
March	A2	30.12	-88.04	32.2	1.26	10.35	0.027	0.75
March	**B1**	29.27	-89.76	20.8	3.29	10.67	0.018	0.93
March	B2	28.96	-89.76	28.6	1.71	8.48	0.039	0.96
March	B3	28.74	-89.76	25.2	2.25	8.65	0.032	0.91
March	**C0**	29.13	-90.59	22.2	4.05	8.37	0.050	0.95
March	C1	28.98	-90.36	27.8	1.75	8.94	0.026	0.96
March	**C2**	28.64	-90.36	27.7	1.95	8.86	0.030	0.92
March	D1	28.79	-91.01	21.3	4.54	8.83	0.040	0.90
March	D3	28.28	-91.03	31.9	1.15	9.62	0.063	0.93
March	**E0**	29.38	-91.37	0.1	13.54	8.34	0.035	0.96
March	E0.5	29.27	-91.46	9.4	9.10	8.74	0.026	0.97
March	**E1**	29.17	-91.56	21.0	5.01	7.88	0.046	0.98
March	E2	29.03	-91.67	26.6	2.56	8.98	0.029	0.94
March	**F1**	29.42	-92.43	29.1	2.16	8.70	0.033	0.96
March	G3	28.82	-93.01	30.7	1.05	8.24	0.039	0.93
March	**H1**	29.61	-93.81	24.4	5.71	8.79	0.027	0.97
March	**H2**	29.32	-93.67	23.1	3.99	7.98	0.042	0.91
March	**MR1**	29.03	-89.33	0.2	6.50	9.52	0.038	0.95
March	**MR2**	28.90	-89.43	5.9	5.50	8.49	0.029	0.99

Table A2. CO AQY fitting parameters (m_1 and m_2) for samples paired with CO_2 AQY experiments (listed in Table 1SI) with corresponding r^2 between measured production and that calculated from the AQY spectrum. CO AQYs were determined from both pretreated samples, as required for CO_2 experiments, and unamended (no pretreatment other than filtering) samples.

Cruise	Station	Pretreated CO fitting parameters			Unamended CO fitting parameters		
		m_1	m_2	r^2	m_1	m_2	r^2
April	E0	9.340	0.023	0.80	7.866	0.044	0.96
April	MR1	7.506	0.040	0.78	9.411	0.037	0.98
April	MR2	7.899	0.034	0.96	8.428	0.031	0.95
July	E0	7.850	0.031	0.95	9.173	0.045	0.97
July	MR1	8.243	0.039	0.97	9.286	0.047	0.87
July	MR2	8.010	0.042	0.87	8.172	0.040	0.89
July	MR3*	6.944	0.081	0.96	10.731	0.047	0.91
November	E0*	9.295	0.016	0.96	8.211	0.032	0.99
November	MR1*	7.664	0.029	0.98	8.582	0.062	0.98
November	MR3	7.850	0.041	0.93	8.192	0.048	0.95
November	F1	6.840	0.057	0.92	7.499	0.047	0.95
November	C0*	7.247	0.063	0.84	9.184	0.031	0.94
March	E0	8.911	0.027	0.98	8.336	0.035	0.96
March	MR1	7.889	0.043	0.93	9.517	0.039	0.95
March	MR2	7.488	0.043	0.96	8.494	0.029	0.99
March	E05*	3.371	0.16	0.71	8.744	0.026	0.97
March	B1	9.230	0.014	0.91	10.671	0.018	0.93
March	E1	7.461	0.034	0.74	7.885	0.046	0.98

*Samples excluded from CO_2:CO ratio determination

Table A3. Sample characteristics (location, salinity $a_g(320)$, and irradiations times), AQY fitting parameters (m_1 and m_2 fit to the exponential Equation 2.10 or k_1, k_2, and k_3, fit to the quasi-exponential Equation 2.11, described in section 2.6), and calculated vs. measured production r^2 for samples used in CO_2 photochemical experiments for both exponential (Equation 2.10) and quasi-exponential (Equation 2.11) AQY shapes. All samples are pretreated to remove background DIC. All paired DIC photoproduction and photon absorbance data were pooled to determine a pooled spectrum, listed at the bottom of the table.

Station	Salinity	Lat (deg N)	Long (deg W)	$a_g(320)$ (m^{-1})	Irradiation time (h)	m_1	m_2	r^2	k_1	k_2	k_3	r^2
E0	0.2	29.38	91.37	12.370	15.9	6.935	0.016	0.85	1.70×10^{-5}	366.71	-223.34	0.86
MR1	0.4	29.03	89.33	8.133	12.8	6.310	0.022	0.85	4.18×10^{-5}	197.37	-253.48	0.76
MR2	31.0	28.90	89.43	7.640	12.1	5.651	0.048	0.92	1.91×10^{-5}	202.59	-257.38	0.89
E0	0.4	29.38	91.37	10.322	5.5	5.802	0.037	0.64	1.26×10^{-5}	373.79	-225.81	0.55
MR1	1.4	29.03	89.33	8.088	15.4	5.320	0.051	0.85	1.57×10^{-5}	227.79	-254.15	0.82
MR2	17.6	28.90	89.43	5.517	14.7	6.255	0.008	0.91	2.65×10^{-4}	134.87	-255.26	0.90
MR3	31.2	28.70	89.50	1.436	13.0	5.928	0.011	0.88	9.93×10^{-8}	4857.1	158.45	0.86
E0	6.1	29.38	91.37	25.880	6.1	6.677	0.015	0.51	1.90×10^{-9}	4402.9	31.87	0.56
MR1	0.2	29.03	89.33	12.466	7.0	3.941	0.082	0.65	2.38×10^{-15}	9570.9	-100.04	0.45
MR3	27.2	28.70	89.50	2.791	8.0	6.563	0.007	0.52	1.99×10^{-4}	101.27	-269.73	0.61
F1	25.8	29.42	92.43	11.291	5.5	6.020	0.019	0.88	8.65×10^{-5}	143.32	-265.65	0.91
C0	25.8	29.13	90.59	5.563	6.0	4.228	0.060	0.84	5.98×10^{-5}	163.94	-263.90	0.87
E0	0.1	29.38	91.37	13.211	16.1	7.963	0.001	0.87	4.65×10^{-5}	4775.4	2138.3	0.75
MR1	0.2	29.03	89.33	6.545	15.1	6.006	0.011	0.93	9.12×10^{-6}	3045.3	338.06	0.62
MR2	5.9	28.90	89.43	5.014	22.4	5.967	0.026	0.81	1.16×10^{-4}	89.351	-271.11	0.83
E05	9.4	29.27	91.46	9.772	5.4	6.92	0.010	0.98	1.08×10^{-7}	4848.7	218.50	0.97
B1	20.8	29.25	89.76	3.228	11.0	7.097	0.008	0.79	1.38×10^{-8}	1.00×10^{-5}	600.44	0.78
E1	21.0	29.17	91.56	5.633	10.1	3.940	0.062	0.94	1.02×10^{-5}	414.52	-240.11	0.96
POOLED	-	-	-	-	-	7.254 ± 0.719	0.008 ± 0.008	.041				

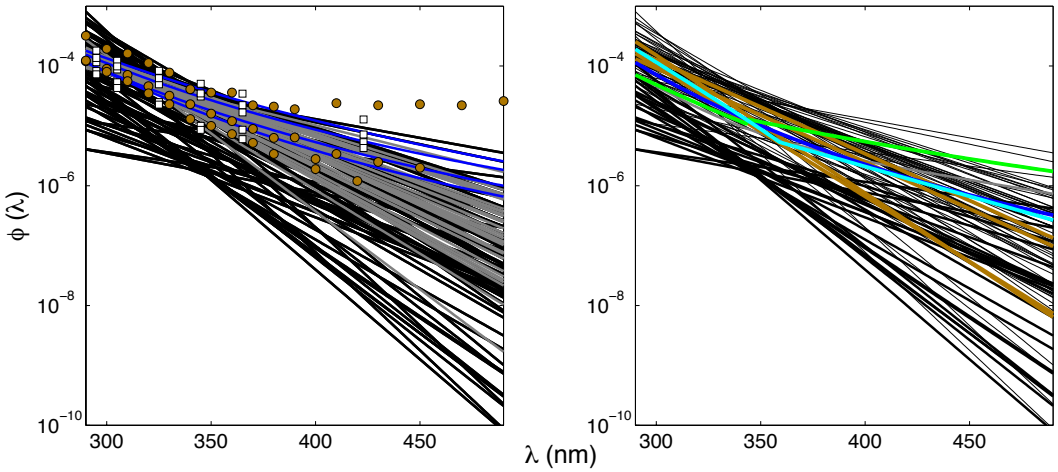

Figure A1. CO apparent quantum yield ($\phi(\lambda)$) spectra for our study (black lines) compared to literature values for other estuarine studies: gray lines - Reader and Miller (2012), blue lines - Zhang et al. (2006), gold circles - White et al. (2010), white squares – Stubbins et al. (2011) (left graph). CO apparent quantum yield ($\phi(\lambda)$) spectra for our study (black lines, offshore in bold) compared to literature values for open ocean studies: light blue line – Zafiriou et al. (2003), gold lines - Ziolkowski and Miller (2007), green line – Stubbins et al. (2006), blue line – Zhang et al. (2006) (right graph).

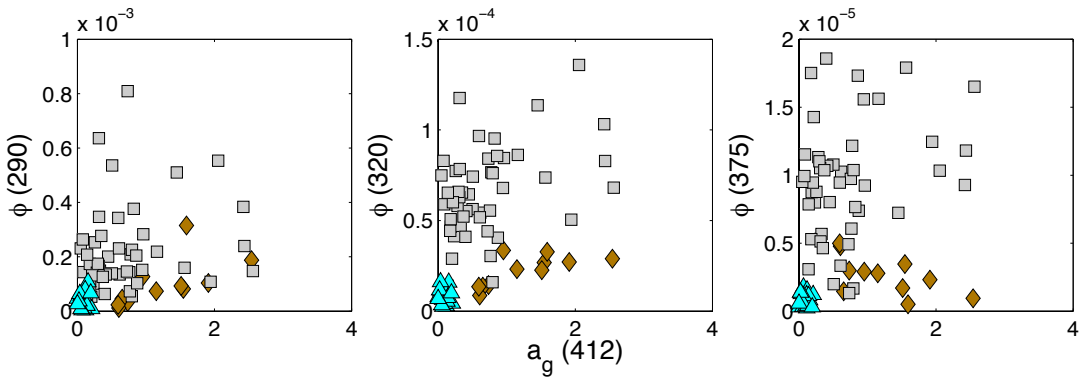

Figure A2. CO AQY values ($\phi(\lambda)$ at 290, 320, and 375 nm shown here) vs. $a_g(412)$ (m^{-1}). Blue triangles represent open ocean stations, gray squares represent inshore and coastal samples, and brown diamonds represent Mississippi River and stations nearby (see Fig. 3SI caption below for a detailed description of this partitioning). Although strong correlations were reported between CO AQY values and $a_g(412)$ by Stubbins et al. (2011), little to no correlations exist with between the $\phi(\lambda)$ for CO and $a_g(412)$ in our large data set.

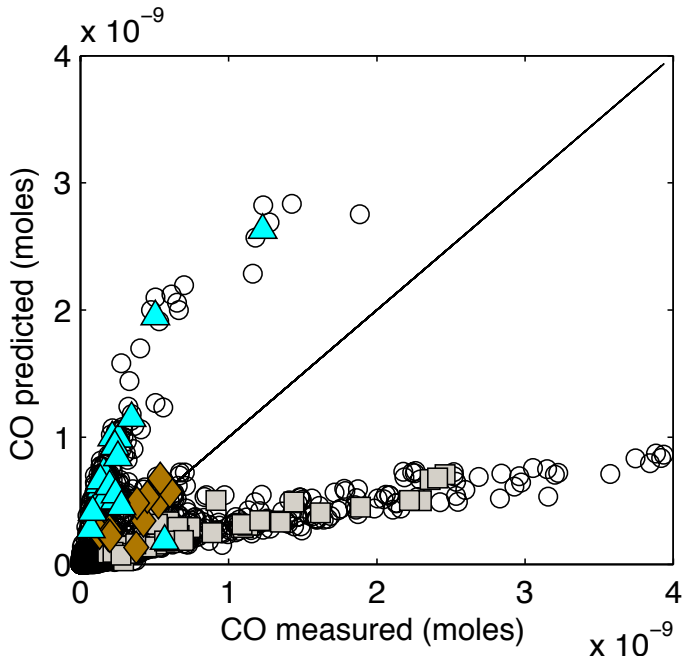

Figure A3. CO predicted (CO_{pred}) from a single pooled AQY (fitting parameters in Table 2SI below) determined from all experimental data vs. CO measured (CO_{meas}) in cell. Open circle represent all experimental data (n = 1134, for 81 experiments and each of the 14 cells with 7 different spectral λ-cutoff treatments, described in Section 2.2). Colored symbols are averages of data calculated and measured for the 305 nm cutoff filter. CO_{pred}/CO_{meas} for light blue triangles = 3.55 ± 0.99 and tend to be representative of samples collected offshore. CO_{pred}/CO_{meas} for brown diamonds = 1.12 ± 0.38 and are generally representative of inshore samples impacted by the Mississippi River. CO_{pred}/CO_{meas} for gray squares = 0.36 ± 0.13 and, representing the majority of our experiments, are generally representative of inshore and coastal waters, including those more impacted by the Atchafalaya River.

Table A4. AQY curve fitting parameters (m_1 and m_2) and their corresponding 95% confidence intervals for CO and absorbed photons data collected in each sampling season (n = 280 for all seasons but October/November when n = 294, overall fit shown in Fig. 3C) and for CO and absorbed photons data for the pooled for the entire data set (n = 1134, overall fit shown in Fig. 3B).

CRUISE	m_1	m_2	r^2
April 2009	10.138 ± 1.196	0.030 ± 0.021	0.20
July 2009	10.637 ± 1.229	0.029 ± 0.022	0.16
October 2009	10.567 ± 1.078	0.016 ± 0.014	0.19
March 2010	8.5452 ± 0.661	0.040 ± 0.015	0.51
POOLED	10.256 ± 0.584	0.024 ± 0.009	0.18

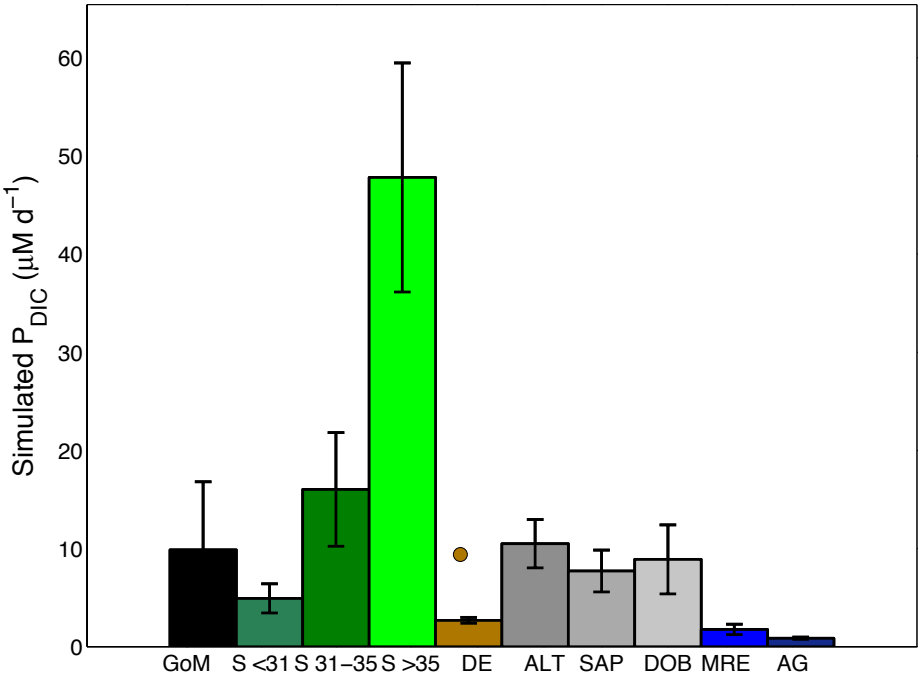

Figure A4. Simulated production (P_{DIC}, µM d^{-1}) determined with the $\phi(\lambda)$ spectra from our study (GoM, black bar) compared to those determined with $\phi(\lambda)$ spectra in the literature: green bars – inshore (S < 31), coastal (S 31 – 35) and offshore (S > 35) $\phi(\lambda)$ spectra from Johannessen and Miller, (2001), gold bar and dot - Delaware Estuary (DE) and River $\phi(\lambda)$ spectra, respectively, from White et al., (2010), gray bars - Altamaha Sound (ALT), Sapelo Sound (SAP), and Doboy Sound (DOB) $\phi(\lambda)$ spectra from Reader and Miller, (2012), blue bars- Mackenzie River Estuary (MRE) and Amundsen Gulf (AG) $\phi(\lambda)$ spectra from Belanger et al., (2006).

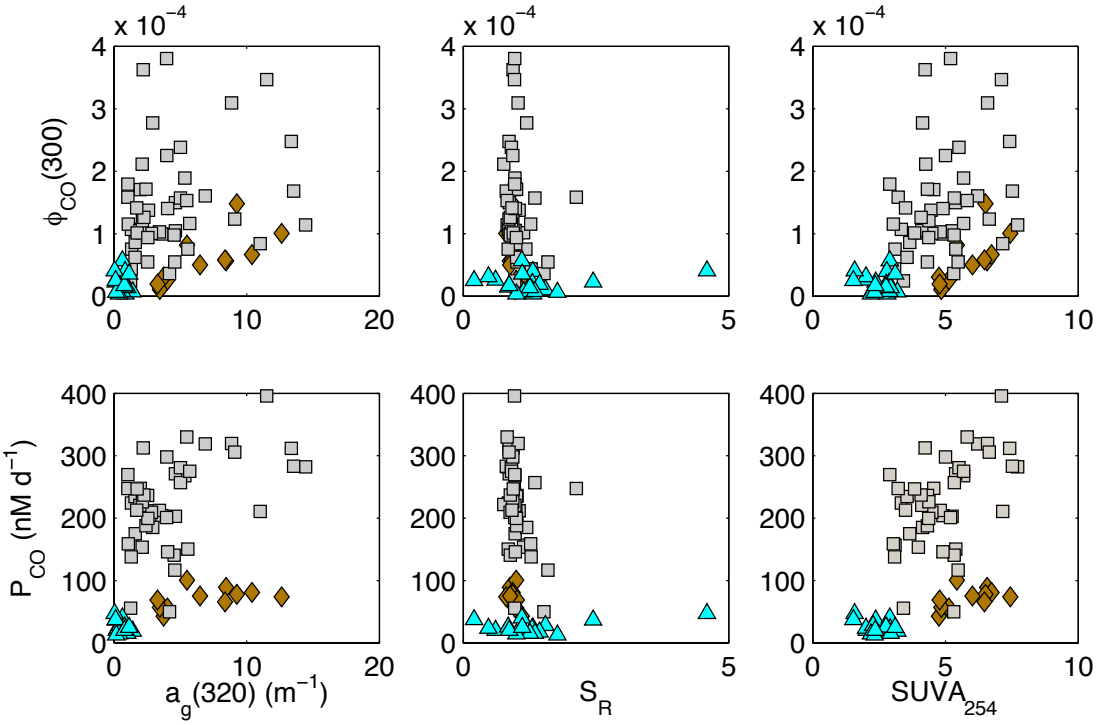

Figure A5. CO photoefficiency (as either the AQY at 300 nm, $\phi(300)$, top, or simulated production, P_{CO} (nM d^{-1}), bottom) vs. $a_g(320)$ (m^{-1}), the spectral slope ratio, S_R, and $SUVA_{254}$ (L mg^{-1} m^{-1}). This figure builds of Fig. 2SI and attempt to further investigate any possible relationships between CO photoefficiency and CDOM absorbance and its derived optical properties. Again, either weak or no correlations were observed. Symbols described in Figs. 2SI and 3SI above.

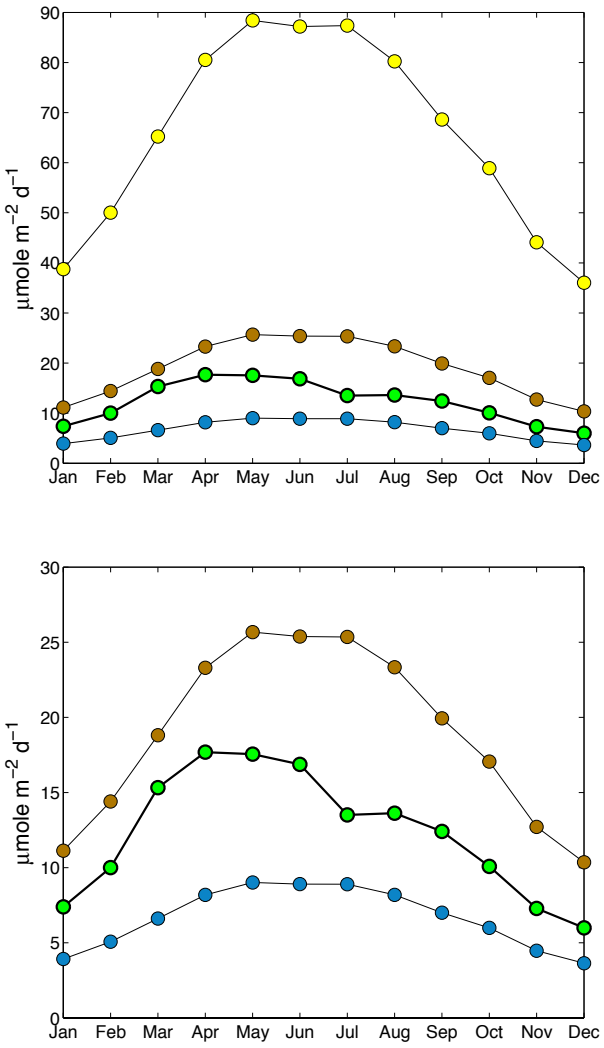

Figure A6. Monthly average CO photoproduction rates (µmole m^{-2} d^{-1}) determined for the sunlit layer for our Northern Gulf of Mexico study region using the methods of Fichot and Miller (2010) (described in Sections 2.7 and 3.4). Yellow circles and blue circles are monthly rates calculated using only the inshore (Equation 2.14) and offshore (Equation 2.13) CO AQY spectrum, respectively. Brown circles are monthly rates calculated using a pooled AQY spectrum for the entire dataset, with an experimental r^2 of 0.18 between measured and modeled production, thereby a poor selection in this regional estimate. Green circles are monthly average CO photoproduction rates determined using the "2 CO AQY" method and an $a_g(320)$ cutoff point of 1.3 m^{-1} for AQY (inshore vs. offshore selection). The figure to the right is zoomed in to show that the "2 CO AQY" method best captures month-to-month variability in CO AQY spectra (e.g. largest production values correspond with the max flow period, April – June, from the Mississippi and Atchafalaya Rivers) in this region as all methods using a single AQY only track with photon absorption rates.

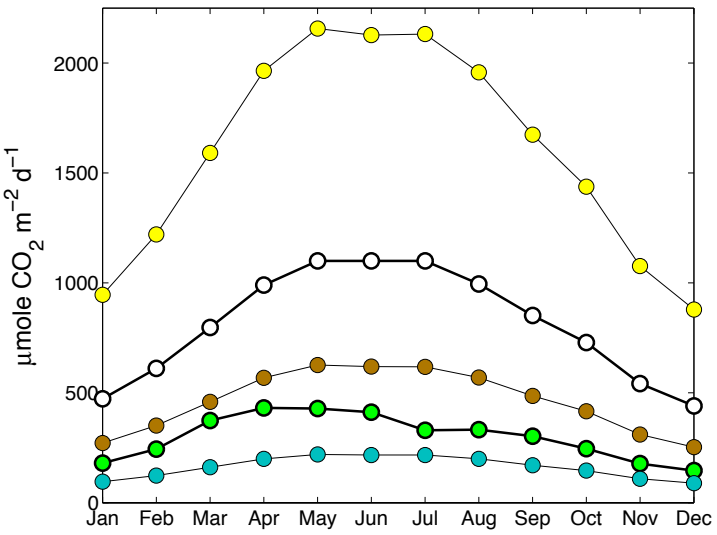

Figure A7. Monthly average CO_2 photoproduction rates determined for the sunlit layer as discussed above. Yellow circles and blue circles are monthly rates calculated using only the inshore (Equation 2.14) and offshore (Equation 2.13) CO AQY spectrum, respectively, multiplied by the median CO_2:CO ratio of 24.4. Brown circles are monthly rates calculated using a pooled AQY spectrum for the entire CO dataset, with an experimental r^2 of 0.18 between measured and modeled production, thereby a poor selection in this regional estimate, but again multiplied by 24.4. Green circles are monthly average CO photoproduction rates determined using the "2 CO AQY" method and an $a_g(320)$ cutoff point of 1.3 m^{-1} for AQY (inshore vs. offshore selection) and multiplied by 24.4. Open circles are determined using a pooled AQY spectrum for the entire CO_2 data set ($r^2 = 0.41$ between measured and modeled CO_2 photoproduction for laboratory experiments. Values for open circles are still much lower than those for yellow circles due to calculating photochemical rates (Equation 2.12) with integration to only 400 nm when using the pooled CO_2 AQY spectrum and to 490 nm when using any CO AQY spectrum.

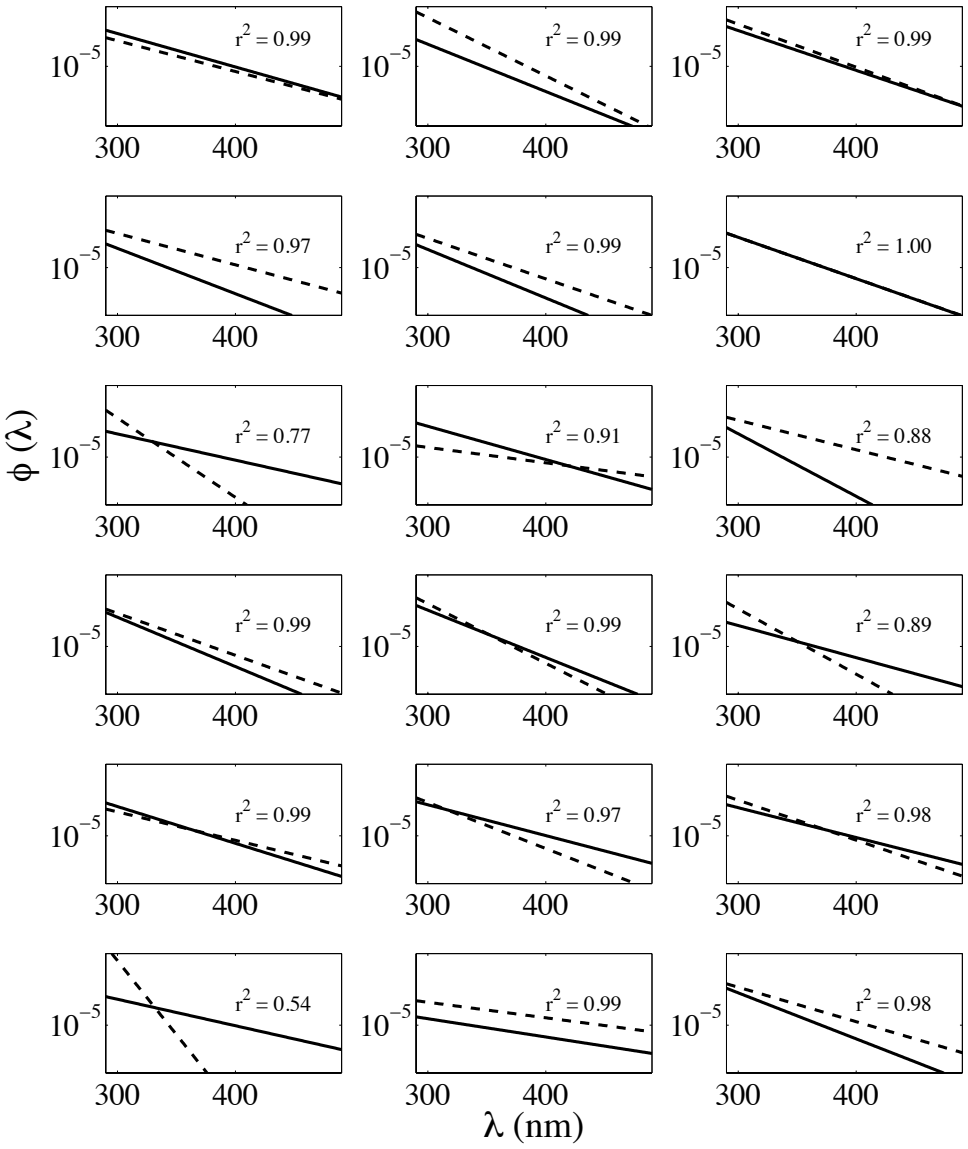

Figure A8. CO AQY spectra determined for samples pretreated to remove background DIC (dashed lines) and those left unamended beyond filtering (solid lines). The r^2 value is for a linear regression between both AQY spectra.

APPENDIX B

DETAILS FOR DETERMINING SUPEROXIDE CONCENTRATIONS AND DECAY KINETICS USING MCLA CHEMILUMINESCENCE

Photochemical Superoxide Standards

The O_2^- results presented in Chapters 3 – 5 rely heavily on the use of a photochemical standard for FeLume calibration and O_2^- detection both during and after sample irradiations under simulated sunlight. The method was first presented by McDowell et al. (1983) and has been mechanistically optimized by Ong (2007). The photochemical standard for O_2^- via ketone (e.g. acetone or benzophenone) photolysis in an alcohol (e.g. ethanol or 2-propanol) solution has been recently scrutinized (i.e. Heller and Croot, 2010), perhaps to justify the use of KO_2 for O_2^- standards, which for many years was thought to introduce metal contamination. The fact of the matter is that any method for O_2^- standards in seawater suffers from its instability in aqueous solutions. Standards have to be maintained at a high pH to slow O_2^- loss via dismutation (Reactions 4.1 and 4.2) and initial concentrations have to be calculated based on measured decay rates. Heller and Croot (2010) discount the photochemical standard because the absorbance spectrum of acetone and benzophenone overlap with that of O_2^- and their belief that the reaction with benzophenone produces acetone. On the other hand, Rose et al. (2011) provide a very nice argument as to why the photochemical method for O_2^- standards works well for applications in natural waters. In our system, the n-π* triplet state of acetone reacts with ethanol and produces O_2^- via the following reactions (McDowell et al., 1983):

$$(CH_3)_2CO \xrightarrow{h\nu} (CH_3)_2{}^{\bullet}C\text{-}{}^{\bullet}O^3 \quad \text{(B1)}$$

$$(CH_3)_2{}^{\bullet}C\text{-}{}^{\bullet}O^3 + (CH_3)CH_2OH \rightarrow 2\,{}^{\bullet}C(CH_3)OH \quad \text{(B2)}$$

$$O_2 + {}^{\bullet}C(CH_3)OH \rightarrow {}^{\bullet}OOC(CH_3)OH \quad \text{(B3)}$$

$${}^{\bullet}OOC(CH_3)OH + OH^- \rightarrow (CH_3)_2CO + H_2O + O_2^- \quad \text{(B4)}$$

Therefore, Rose et al. (2011) note that while the reaction involves the oxidation of an alcohol to a ketone (e.g. ethanol to acetaldehyde), the molar abosorptivity at 240 nm of acetaldehyde is 1.5 M^{-1} cm^{-1} whereas that for O_2^- is 2345 M^{-1} cm^{-1}, meaning that any acetaldehyde formed is insignificant in the absorbance reading (Rose et al., 2011). Furthermore, the absorbance due to acetone in solution is subtracted in the absorbance blank because it acts as a catalyst in the reaction and is regenerated when reacting with O_2 to form O_2^-.

Another aspect of the photochemical standard criticized by Heller and Croot (2010) is the use of DTPA in the photolysis solution. Although DTPA at neutral pH can break down when exposed UV light and sunlight (Metsärinne et al., 2004), Rose et al. (2011) demonstrate that ~70% of uncomplexed 100 μM DTPA and ~80% of 10 μM Fe(III)-complexed 100 μM DTPA breaks down in our standardization system over 10 minutes (i.e. irradiations with a Pen-ray Hg lamp). This corresponds to rate constants of 0.12 ± 0.01 min^{-1} and 0.17 ± 0.02 min^{-1} for unchelated and chelated DTPA, respectively (Rose et al., 2011). Given these rate constants and the <30 seconds that are required to produce sufficient O_2^- (~100 μM) for standardization in seawater samples (Figure B1), ample DTPA (91 – 94% of the 30 μM added originally) should remain in the photolysis solution to complex the likely minimal trace metal contamination and to again not affect the absorbance reading.

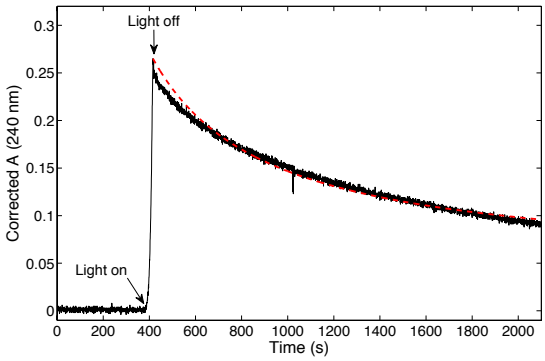

Figure B1. Absorbance (A) at 240 nm, subtracted by that at 400 nm, of the photochemical O_2^- standard after a typical 30 second irradiation. Dashed red line is modeled A.

Superoxide Decay Kinetics

Kinetics of Superoxide Decay following Standard Spikes

Throughout the text (Chapters 3 – 5), superoxide decay is described by the following equation

$$\frac{d[O_2^-]}{dt} = -k_{pseduo}[O_2^-] - 2k_d[O_2^-]^2 \qquad \text{B1}$$

where k_{pseudo} (s^{-1}) is the pseudo-first order rate constant and k_d is the second order dismutation rate constant, defined by Zafiriou (1990) as $(5 \pm 1)\times[H^+]\times10^{12}$ M^{-1} s^{-1}. Integrating equation B1 and solving for $[O_2^-]$ then gives the following equation

$$[O_2^-] = \frac{k_{pseduo}[O_2^-]_0}{k_{pseduo}e^{k_{pseudo}t} + 2k_d[O_2^-]_0(e^{k_{pseudo}t} - 1)} \qquad \text{B2}$$

where $[O_2^-]_0$ is the concentration of the O_2^- superoxide spike. Because FeLume signal (S; counts) is a linear function of O_2^- concentration, we can substitute S for O_2^- in Equation B2, as in Heller and Croot (2010b) and Garg et al. (2011)

$$S = \frac{k_{pseduo}S_0}{k_{pseduo}e^{k_{pseudo}t} + 2k_d[O_2^-]_0(e^{k_{pseudo}t} - 1)} \qquad \text{B3}$$

where S_0 is the FeLume signal at time zero, in other words, when the superoxide standard was spiked into unirradiated seawater. Before each superoxide addition, background signal was monitored and subtracted from the FeLume signal following each superoxide spike to correct for background chemiluminescence due to the autooxidation of $MCLA^-$. S (corrected) was then modeled by a nonlinear regression of S versus t, typically over the first 60 seconds of decay (Rose et al., 2008), as described in Chapters 3 and 4, using S_0 and k_{pseduo} as fitting parameters (Figure B2). S has also been modeled by a linear regression of log-linearized FeLume data vs. time (Rose et al., 2008), and S_0 determined

by extrapolation of modeled *S* to time zero. Both the nonlinear and linear methods are in good agreement (Figure B2). Calibration curves were constructed by a linear regression of $[O_2^-]_0$ versus S_0 (e.g. Figure B3).

All superoxide standards were performed on unirradiated seawater samples containing ~30 μM DTPA to remove any metal catalyzed decay and therefore have a larger amount of the spiked superoxide present by the time the sample reached the detector (about 10 second transit time from the sample container to the spiral flow cell). Loss of superoxide was greatest for the largest spike concentrations (50 – 60% loss for 25 – 40 nM) and negligible to about 10% loss for spike concentrations ≤10 nM. Pseudo-first order rate constants determined from these spikes ranged from $12 – 35 \times 10^{-3}$ s^{-1} and were in good agreement for each sample.

Kinetics of Superoxide Decay following Seawater Irradiations

Typical seawater irradiations for O_2^- under the solar simulator are shown for an oligotrophic station (bottom water collected from Station 29, Chapter 4) and compared to that for a coastal tidal creek (Chapter 5) in Figure B4. In the example here, it took about 10 minutes for superoxide to reach steady state concentrations in the oligotrophic sample whereas superoxide reached steady state in less than 30 seconds in the tidal creak sample. Post irradiation, O_2^- decay was also faster in the tidal creek sample. Decay kinetics reported in Chapters 3 – 5 are based on the superoxide decay Equation B1, using the known second order rate constant for superoxide disproportionation (k_D) and unknown sinks, represented by pseudo-first order rate constant (k_{pseudo}). This model predicts superoxide decay observed in our experiments fairly well, but occasionally was not able to model the entirety of measured decay (e.g. post the first irradiation in Figure B4).

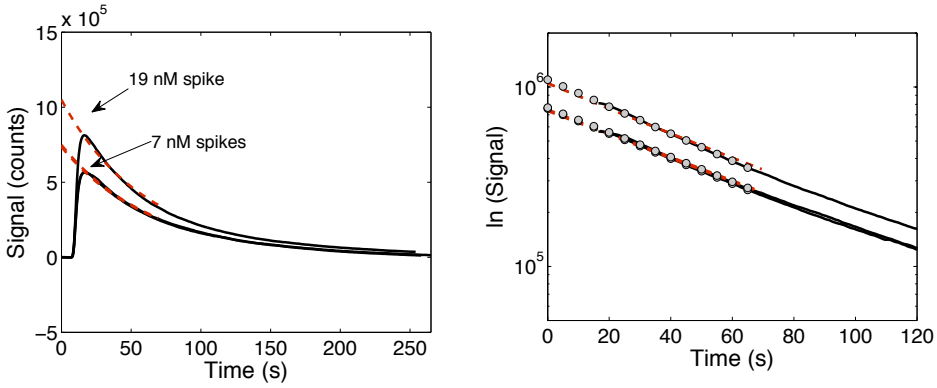

Figure B2. Example photochemical standard spike signals in 0.2 µm filtered seawater solutions (black lines; left). Signal at time zero (S_0) and k_{pseudo} (s^{-1}) are determined from a nonlinear regression of signal (S) versus time (e.g. Equation 3.10 and 4.10). Modeled decay fits over the first 60 seconds are shown with red dashed lines. Log-linearized S and log-linearized model fits (red dashed lines) are compared to a linear regression of ln(S) versus time (gray circles; right).

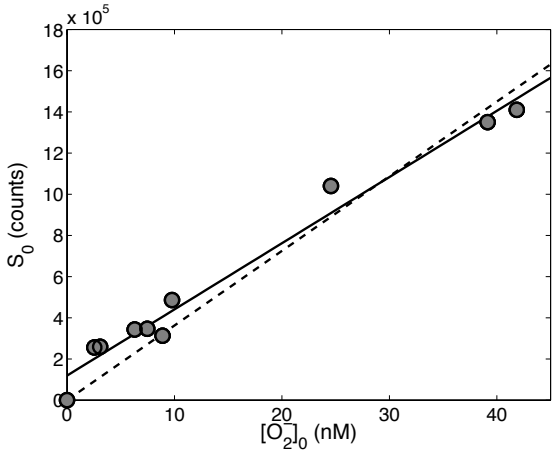

Figure B3. Typical calibration curve for modeled S_0, modeled as described above, versus the superoxide spike concentration ($[O_2^-]_0$, nM). The solid line is a linear regression giving a slope, $C = S_0/[O_2^-]_0$, of $(3.21 \pm 0.18)\times10^4$ counts nM^{-1} and an r^2 of 0.98. The dashed line is a linear regression with the x-intercept set to zero, giving a C value of $(3.62 \pm 0.57)\times10^4$ counts nM^{-1} and an r^2 of 0.94. Either regression gives the same C value, within error.

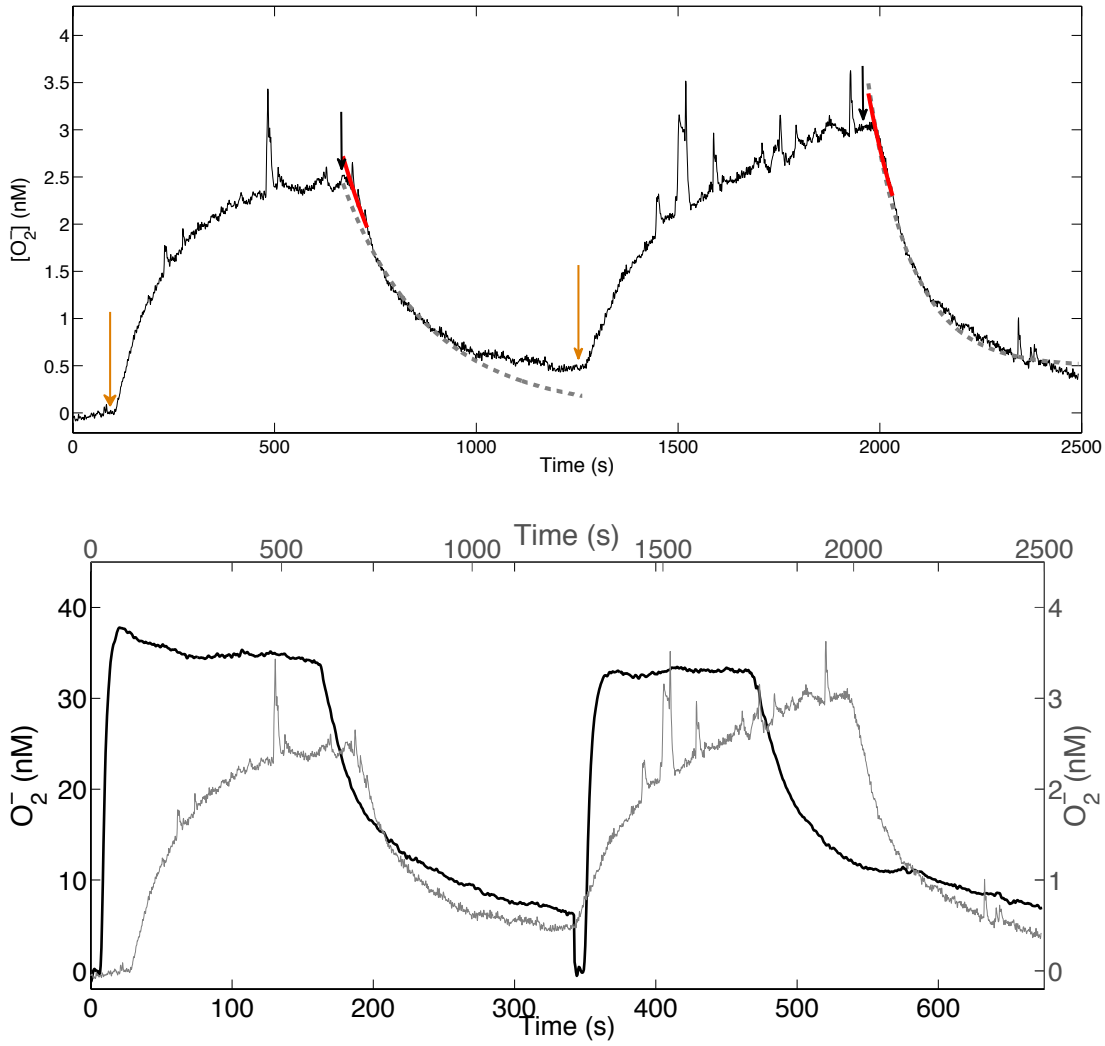

Figure B4. Superoxide measured during and after repeat irradiations of bottom water collected at Station 29 (Chapter 4; top). Orange arrows mark the start time of the irradiation and black arrows mark when the solar simulator was turned off. Modeled superoxide decay according to equation B2 are shown for fits over the entire curve (Gray dashed lines) and over the first 60 seconds of decay (red lines). The bottom graph compares Station 29 irradiations (gray lines, concentration data on the right axes, time data on the top axis) to those for a coastal tidal creek (Chapter 5; black lines, concentration data on the left axis and time data on the bottom axis).

Purely first order decay and purely second order decay equations were also fit to superoxide data (Table B1). First order decay follows the equation

$$\frac{d[O_2^-]}{dt} = -k_1[O_2^-] \quad \text{B4}$$

and was determined by a nonlinear regression according to

$$[O_2^-] = [O_2^-]_0 e^{k_1 t} \quad \text{B5}$$

or a linear regression of log-transformed O_2^- decay data over time. Second order decay follows

$$\frac{d[O_2^-]}{dt} = -k_2[O_2^-]^2 \quad \text{B6}$$

and was determined by a linear regression of the reciprocal of the superoxide signal over time, according to

$$\frac{1}{[O_2^-]} = \frac{1}{[O_2^-]_0} + k_2 t \quad . \quad \text{B7}$$

For decay models, FeLume S and S_0 were substituted for $[O_2^-]$ and $[O_2^-]_0$, respectively, so all regressions were again of S versus t and the rate constant (k_1 or k_2) and S_0 were used as fitting parameters using *nlinfit* or the curve fitting tool box in Matlab®. S_0 was then converted to $[O_2^-]_0$ using the appropriate calibration constant (C; counts nM^{-1}). Results from Station 10 and 29 (Chapter 4) are listed in Table B1. First order decay constants (k_1 or k_{pseudo}) were either faster when determined over the first 60 seconds of decay (Station 10) than that determined for the entire decay curve, or similar (Station 29) over both ranges. Additionally, first-order rate constants were similar between the model including the dismutation reaction (k_{pseduo}; Equation B2) and the model that excluded the dismutation reaction (k_1; Equation B5), confirming that dismutation is not the dominant

Table B1. Results of model fits for $[O_2^-]_0$ (nM) and first order (k_1 and k_{pseudo}; s^{-1}) and second order (k_2 M^{-1} s^{-1}) rate constants determined over the entire superoxide decay data (A) or over the first 60 seconds of decay (B).

(A) Models for O_2^- steady-state and rate constants determined over at least 500 seconds of decay

		$[O_2^-]_0$ (nM)			k_1 (10^{-3} s^{-1})	k_2 (10^6 M^{-1} s^{-1})	k_{pseduo} (10^{-3} s^{-1})
Station	Sample	1st order	2nd order	Both	1st order	2nd order	Both
10	bottom	2.30 ± 0.41	2.66 ± 1.14	1.23 ± 0.19	1.29 ± 0.40	1.03 ± 0.19	1.86 ± 0.95
	1000 m	1.75 ± 0.29	1.75 ± 0.29	1.73 ± 0.26	1.34 ± 0.40	1.19 ± 0.16	1.76 ± 0.57
	surf	2.61 ± 0.49	5.17 ± 4.19	2.85 ± 0.41	1.94 ± 0.55	1.87 ± 0.26	1.53 ± 0.60
	50/50 surf/bot	3.20 ± 0.84	n.d.	3.08 ± 0.47	7.57 ± 2.69	n.d.	7.33 ± 2.59
29	deep	2.43 ± 0.38	2.75 ± 1.16	2.43 ± 0.38	4.15 ± 0.11	3.37 ± 0.72	4.09 ± 1.02
	surf	2.46 ± 0.42	2.82 ± 1.74	2.44 ± 0.37	4.65 ± 0.12	3.96 ± 1.05	5.12 ± 1.06

(B) Models for O_2^- steady-state and rate constants determined over the first 60 seconds of decay

		$[O_2^-]_0$ (nM)			k_1 (10^{-3} s^{-1})	k_2 (10^6 M^{-1} s^{-1})	k_{pseduo} (10^{-3} s^{-1})
Station	Sample	1st order	2nd order	Both	1st order	2nd order	Both
10	bottom	3.02 ± 0.65	3.03 ± 0.11	1.45 ± 0.22	4.48 ± 0.02	1.70 ± 0.17	4.02 ± 0.62
	1000 m	2.20 ± 0.39	2.23 ± 0.06	2.20 ± 0.41	3.84 ± 0.47	2.10 ± 0.30	3.53 ± 0.49
	surf	3.34 ± 0.26	3.42 ± 0.29	3.81 ± 0.58	4.34 ± 1.52	1.66 ± 0.45	3.97 ± 0.40
	50/50 surf/bot	4.08 ± 0.52	4.54 ± 0.47	3.88 ± 0.72	13.5 ± 3.54	5.33 ± 0.47	12.1 ± 2.92
29	deep	2.62 ± 0.17	2.66 ± 0.34	2.72 ± 0.47	4.68 ± 1.67	2.12 ± 0.78	5.19 ± 1.98
	surf	2.71 ± 0.42	2.80 ± 0.13	2.70 ± 0.42	5.80 ± 0.69	2.78 ± 0.39	5.37 ± 0.75

pathway of superoxide decay following these solar simulator exposures. Furthermore, second order decay constants (k_2) were on the order of 10^6 M^{-1} s^{-1}, well above that determined for superoxide dismutation in seawater (e.g. $k_D \sim 50{,}000$ M^{-1} s^{-1} at a pH of 8; Zafiriou, 1990), arguing that additional pathways of superoxide decay must be included in these models. In our opinion, Equation B2 best represents our knowledge of superoxide chemistry in natural waters, and was therefore used exclusively throughout Chapters 3 – 5 of this dissertation.

References

Ong, T., 2007. Detailed mechanistic and optimization of the photochemical production method of superoxide. In: *Department of Chemistry*, Colby College, Waterville, ME.

Garg, S., Rose, A.L., Waite, T.D., 2011. Photochemical production of superoxide and hydrogen peroxide from natural organic matter. Geochim. Cosmochim. Acta. 75, 4310–4320. doi:10.1016/j.gca.2011.05.014

Heller, M.I., Croot, P.L., 2010a. Application of a superoxide (O_2^-) thermal source (SOTS-1) for the determination and calibration of O_2^- fluxes in seawater. Anal. Chim. Acta. 667, 1–13. doi:10.1016/j.aca.2010.03.054

Heller, M.I., Croot, P.L., 2010b. Superoxide decay kinetics in the southern ocean. Environ. Sci. Technol. 44, 191–196. doi:10.1021/es901766r

McDowell, M.S., Bakac, A., Espenson, J.H., 1983. A Convenient Route to Superoxide Ion in Aqueous Solution. Inorg. Chem. 22, 847–848.

Metsärinne, S., Rantanen, P., Aksela, R., Tuhkanen, T., 2004. Biological and photochemical degradation rates of diethylenetriaminepentaacetic acid (DTPA) in the presence and absence of Fe(III). Chemosphere. 55, 379–388. doi:10.1016/j.chemosphere.2003.10.062

Rose, A.L., Miller, C.J., Fujii, M., Waite, T.D., 2011. Comment on "Application of a superoxide (O_2^-) thermal source (SOTS-1) for the determination and calibration of O_2^- fluxes in seawater" by Heller and Croot. Anal. Chim. Acta 702, 144–5; discussion 146–147. doi:10.1016/j.aca.2011.05.022

Rose, A.L., Moffett, J.W., Waite, T.D., 2008. Determination of superoxide in seawater using 2-Methyl-6-(4-methoxyphenyl)-3,7-dihydroimidazo[1,2-a]pyrazin-3(7H)-one chemiluminescence. Anal. Chem. 80, 1215–1227.

Zafiriou, O.C., 1990. Chemistry of superoxide ion-radical (O_2^-) in seawater. I . pK*a_{sw} (HOO) and uncatalyzed dismutation kinetics studied by pulse radiolysis. Mar. Chem. 30, 31–43.